University of Strathclyde

Department of Physics

COLLOIDAL SEMICONDUCTOR NANOCRYSTALS FOR COLOUR CONVERSION AND SELF-ASSEMBLED LASERS

BY

PEDRO URBANO DOS SANTOS ALVES

A thesis presented in fulfilment of the

requirements for the degree of

Doctor of Philosophy

September 2022

Declaration of Authorship

This thesis is the result of the author's original research. It has been composed by the author and has not been previously submitted for examination which has led to the award of a degree.

Signed: _____

Date: _____

Frontispiece

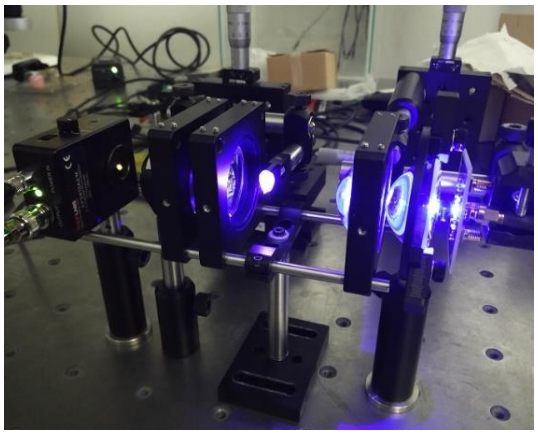

Blue LED set-up optically exciting a ceasium lead bromide composite (saturated white in the centre) for bandwidth measurements.

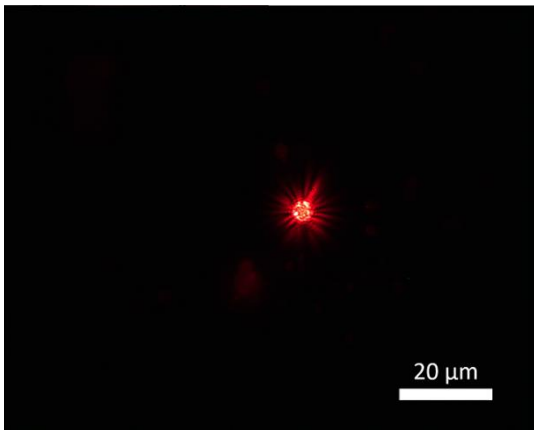

Laser action in a self-assembled microsphere of red quantum dots.

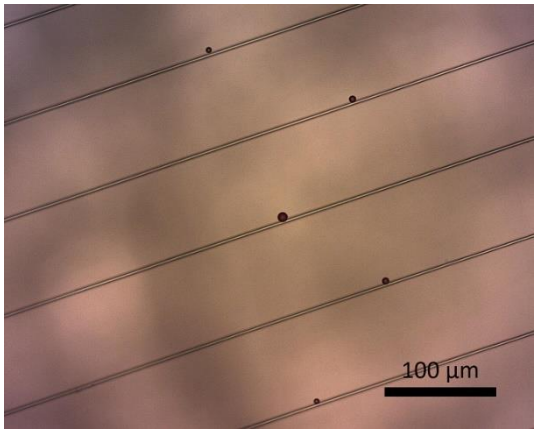

Self-assembled microspheres of red quantum dots coupled to waveguides via transfer printing.

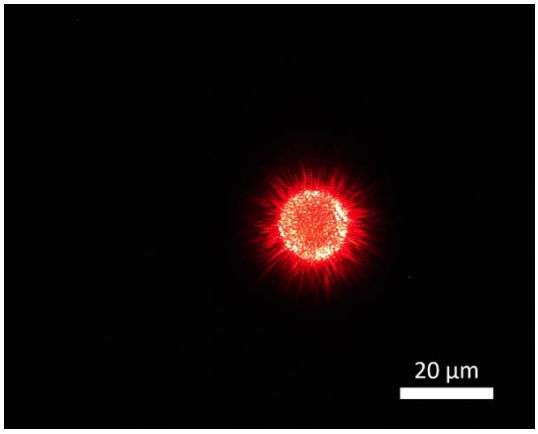

Enhanced self-assembled microsphere of red quantum dots by adding blue quantum dots to its structure.

Abstract

Nanocrystals have been at the forefront of technological developments in photonics thanks to their unique optoelectronic properties. In this thesis, different types of luminescent semiconductor nanocrystals have been studied, improved, and implemented towards novel applications. The topics of research discussed are: (i) II-V colloidal quantum dots as the building blocks of novel lasers via self-assembly from the bottom up (the fabrication and study of these are in fact the main focus of the thesis), and (ii) a perovskite quantum dot-based structure as a robust colour-converter of LEDs.

(i) II-VI alloyed core-shell $Cd_xS_{1-x}Se/ZnS$ quantum dots are nanosized colloids (dispersed in solution) with excellent optical properties in the visible spectrum. These Cd-based colloidal quantum dots represent the most mature colloidal quantum dot technology and their use as light emitters and laser gain material is being intensely pursued. To date, colloidal quantum dot (and related nanocrystal) lasers have been made from the top down with the quantum dots deposited into an optical resonator fabricated separately. Departing from this standard approach and fully capitalizing on the solution processability of colloids, this work uses quantum dots as nanobricks to create supracrystal/supraparticle microspheres that self-assemble from a bottom-up approach. These supraparticles act simultaneously as the gain material and the optical microcavity. In addition to that they are capable of laser emission under optical excitation. Using red-emitting $Cd_xS_{1-x}Se/ZnS$ quantum dots, laser oscillation between the 625 and the 655 nm is obtained from single quantum dot spheres with diameters of 5.6 ± 3.2 μm and energy threshold of 4.7 ± 2.1 nJ for a 532 nm pump source with a beam spot size of approximately 6 μm in diameter.

The possibility of making hetero-supraparticles by selecting and self-assembling together quantum dots with different emission and absorption spectra is also demonstrated. When carefully selected, these combinations can enhance the quality factor of the sphere. As an example, microspheres of red quantum dots and green quantum dots had an increase in the quality factor from 135 ± 19 to 340 ± 60, when compared to red quantum dot microspheres of the same size (6.0 ± 0.5 μm in diameter). Microspheres with quantum dots of red and higher band gap species also maintain similar laser threshold energies to their red quantum dot microsphere counterparts. In the example mentioned above, both

microspheres reached laser threshold at 12 – 14 $mJ.cm^{-2}$, for a beam spot size of 2.88×10^{-7} cm^2. In addition to that, microspheres with higher bandgap quantum dots in their composition have also reported laser for cavities of sizes 3 – 4 times bigger, further suggesting that the increase in the quality factor and decrease in self-absorption is promoted by the addition of higher bandgap quantum dots.

Synthesis of microspheres with different bandgap quantum dots also allow for simultaneous multicolor lasing in a single sphere. Stable dual laser emission of yellow (575 nm) and red (630 nm) is shown in a microsphere of 6.0 ± 0.5 μm in diameter, for energy thresholds between 13.3 and 45.6 nJ and for a spot size of approximately 4.85×10^{-7} cm^2.

The integration of supraparticle lasers to other devices is demonstrated via transfer printing. This method can move them reliably between substrates, and this was done to successfully couple them to waveguides. This demonstration paves the way to more complex designs and applications in integrated photonics.

In addition to quantum dots, the self-assembly procedure was also tested and adapted to other types of semiconductor nanocrystals, including nanoplatelets and tetrapods, in a collaboration work with Nanyang Technological University (LUMINOUS! group).

(ii) A different material was studied for colour conversion. Ceasium lead bromide perovskite nanocrystals have up to date the fastest luminescent dynamics of all known nanocrystals and are therefore appealing for light communication applications. However, they are not stable in the presence of heat and humidity. Different coatings using two different polymers (PDMS and PMMA) have been studied as a way of protecting and increasing the stability of $CsPbBr_3@Cs_4PbBr_6$ crystals. While PDMS samples were not stable upon immersion in water, PMMA composites showed little to no trace of degradation when immersed in water under vigorous stirring for up to 72 hours. Bandwidth measurements with PMMA samples have given similar results to the current state of the art, showing that PMMA is an effective matrix host for $CsPbBr_3@Cs_4PbBr_6$ against moisture and water.

Contents

List of Figures

List of Tables

List of Publications

- **P. U. Alves**, I. M. Watson, N. Laurand and M. D. Dawson, "Water Resistant Caesium Lead Bromide Crystal Composites," *2018 IEEE British and Irish Conference on Optics and Photonics (BICOP)*, 2018, pp. 1-4, doi: 10.1109/BICOP.2018.8658335*.

- **P. U. Alves**, N. Laurand and M. D. Dawson, "Multicolor laser oscillation in a single self-assembled colloidal quantum dot microsphere," *2020 IEEE Photonics Conference (IPC)*, 2020, pp. 1-2, doi: 10.1109/IPC47351.2020.9252438*.

- **P. U. Alves**, D. Jevtics, M. J. Strain, M. D. Dawson, N. Laurand, " Enhancing self-assembled colloidal quantum dot microsphere lasers," 2021 IEEE Photonics Conference (IPC), 2021, pp. 1-2, doi: 10.1109/IPC48725.2021.9592976*

- **P. U. Alves**, P. Edwards, R. Martin, M. J. Strain, M. D. Dawson, N. Laurand "Self-assembled colloidal nanocrystal microsphere lasers – device performance and integration with optical waveguides via transfer printing," drafted and in preparation for submission

*Both journal publications and conference presentations. The published papers can be found in Annex C.

Abbreviations

APD – Avalanche Photo Diode

AR – Auger Recombination

CC – Colour Conversion

CCD - Charge-coupled device

CL - Cathodoluminescence

CQD – Colloidal Quantum Dot

DBR – Distributed Bragg Reflector

DC – Direct Current

DFB – Distributed Feedback

EQD – Epitaxial Quantum Dot

FWHM – Full Width Half Maximum

FRET – Förster Resonant Energy Transfer

FSR – Free Spectral Range

LD – Laser Diode

LED – Light Emitting Diode

NA – Numerical Aperture

NC - Nanocrystal

NPL – Nanoplatelet

NR - Nanorod

OFDM - Orthogonal Frequency Division Multiplexing

PDMS - Polydimethylsiloxane

PL – Photoluminescence

PLQY – Photoluminescence Quantum Yield

PMMA – Poly(methyl methacrylate)

PVA – Poly(vinyl alcohol)

QD – Quantum Dot

Q-factor – Quality factor

QY – Quantum Yield

RF – Radio Frequency

SNR – Signal to Noise Ratio

SP – Supraparticle

SEM – Scanning Electron Microscopy

TIR – Total internal reflection

TE – Transverse Electric

TM – Transverse Magnetic

TP – Tetrapod

TfP – Transferprinting

UV – Ultraviolet

VLC – Visible Light Communication

WDM - Wavelength Division Multiplexing

WGM – Whispering Gallery Mode

XRD - X-Ray Diffraction

Dedicado à minha família

Part I

Introduction

Chapter 1. Semiconductor Nanocrystals for Lasers and Colour Conversion

The research of this thesis focuses on luminescent semiconductor nanocrystals (NCs) for the development of novel, self-assembled lasers and for the robust colour-conversion of light-emitting diodes (LEDs). This introduction chapter starts by giving a quick overview and background of NCs, highlighting the types of NCs relevant to this work in Sections 1.1 and 1.2. Sections 1.3 and 1.4 state the motivations and give the outline of the thesis. As detailed in Section 1.4, the rest of this chapter covers in more detail further aspects of the materials and the relevant physics concepts.

1.1 Background on Nanocrystals

NC is the nomenclature given to organic and inorganic crystals with sizes ranging approximately between 1 and 20 nm. They can be made of metal, semiconductor, or magnetic materials, and many are synthesized in solution with the possibility of custom optimizations such as their size and shape [1]. NCs have found a wide range of applications, ranging from biochemistry (e.g.: bio-imaging, sensing and bio-assays) [2], to optics (e.g: LEDs and laser gain materials [3]–[6]), energy (e.g.: light harvesting in photovoltaics [7]) and other optoelectronic and magnetic applications (eg.: photodetectors, field effect transistors, memory elements [1], [7]–[12]).

NCs made of semiconductors as used in this work are particularly attractive for photonic applications thanks to the flexibility for fine tuning and control of their optical and electronic properties through quantum confinement, and, for some of them, their solution processability. Quantum confinement is the spatial confinement of charge carriers in a material at the scale of the wavefunction of the carriers. This restriction results in a modification and quantization of the electronic levels (as explained in Section 1.2 in the case

of quantum dots) and of the density of states of the material as illustrated in Figure 1-1. According to their degree of quantum confinement, which depends on size and shape [13], semiconductor NCs can be sub-categorized into 3 main types: nanoplatelets (NPLs), nanorods (NRs) and quantum dots (QDs), all of which have prompted intense research and development over the last two decades [14], [15].

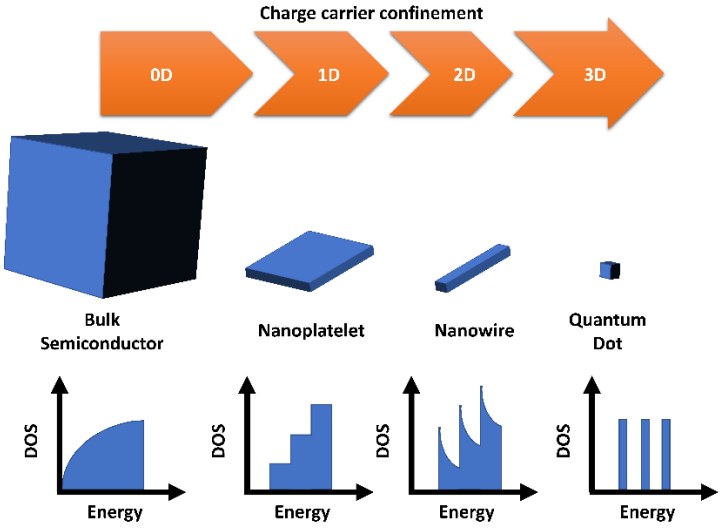

Figure 1-1. Effect of shape and size on nanomaterials on the charge carrier confinement, where the density of states as function of the energy evolves from a square root dependency in bulk (3D), to a step-like function in quantum wells (2D), a negative square root dependency in quantum rods (1D), and a Dirac-δ function in quantum dots (0D).

Light emitting semiconductor NCs are of course of special interest for light-emitting devices. Different semiconductor alloys combined with the quantum confinement effect enables a wide wavelength coverage from the UV to the mid-infrared [16]. For example, Cd-based NCs or metal-halide perovskite-based NCs (both used in this thesis), make coverage of the full visible spectrum with a single material system possible.

The reduced dimensionality in NCs, and QDs in particular, increases the electron-hole wavefunction overlap, which typically increases the radiative quantum efficiency. Furthermore, the discretized density of states of QDs leads to a reduced thermal spread of carriers within bands – in principle this means that light emitted by a QD can be made to more efficiently match the energy of resonating modes in a cavity. These are all attractive attributes for the realization of lasers. Indeed, several types of QDs possess optical

characteristics that make them suitable for the development of lasers [17]. Moreover, solution processed QDs are compatible with almost all kinds of laser cavities and substrate materials as they allow the fabrication of devices by solution-based methods, such as spin-coating and inkjet printing [17].

QDs can also provide colour conversion as efficiently as rare-earth phosphor materials[10], [18], [19], and their solution processability, high photoluminescence quantum yield (PLQY), broad absorption and narrow emission spectrum have already enabled their incorporation in the latest generations of high-definition LCD screens and white light illumination [10], [18]. NCs are also contributing to new lighting applications. QDs have significantly faster luminescence dynamics than phosphors. Combined with micro-sized LEDs and their capability of being modulated at high-speeds speed [20]–[22], QDs have been shown to be an attractive solution as colour-converters in sources for Visible Light Communication [23], and by extension LiFi [12]. They are seen as a fundamental element of the next generation of communication technology [12], [24], [25], as they provide modulation and multiplexing in the visible spectrum at higher frequencies than the current rare-earth phosphor materials [25]–[28].

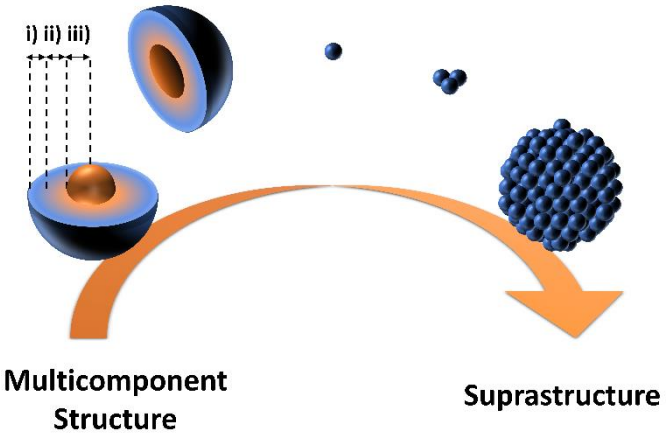

Figure 1-2. Example of a multicomponent structured NC (QD) and a suprastructure made of many of these QDs. The multicomponent structure illustrates an alloyed core-shell QD, such as CdSe (iii); $Cd_xZn_{1-x}Se$ (ii); $ZnSe_{0.5}S_{0.5}$ (i), and the suprastructure can be fabricated via self-assembly of many of these QDs.

NCs are often made into a multicomponent structure at the nanoscale (Figure 1-2) using different types of materials or alloys, which confers additional design parameters with which

to tune their properties. For example, the shell encapsulation of a core QD uses crystalline lattices with different element combinations to tailor and improve the electronic and optical properties (see Section 1.2.2 for more details). This is particularly common in colloidal NCs, where ligands play an important role by assisting the synthesis process and functionalizing the surface for target applications [1]. Adding more components to the initial structure allows the manipulation of several material properties of NCs, such as wave functions, plasmon resonances, spins, and others [1], [29].

Colloidal NCs can also be themselves part of crystalline suprastructures (feature size tens of nm up to several hundreds of micrometers), in which case the NC can be seen as a building block or brick (Figure 1-2). Such suprastructures can be synthesized by a self-assembly process which results in densely packed superlattices (Figure 1-2) that can also give additional properties [30]–[32]. As will be seen later, in this work suprastructures are capitalized upon in order to control the light emission by acting as optical resonators, thereby bridging the gap between the electronic structure (controlled at the NC scale) and the photonic scale.

1.2 Quantum Dots

The majority of the work presented in this thesis is based on quantum dots of two different types and therefore some background information on these materials is given in this section. More information on these materials will be given later in this chapter and in other relevant chapters.

QDs are semiconductor nanoparticles with feature sizes that can go below 10 nm. They can be subdivided in two main classes: epitaxial QDs (EQDs) and colloidal QDs (CQDs). Although EQDs are not the focus of this thesis, they are briefly introduced below.

EQDs are formed by growth or deposition of a crystalline structure on an appropriate substrate and comprise a whole variety of dot structures, such as QDs based on lithographic patterning of epitaxial quantum wells, QDs defined by gates applied to a 2D structure, droplet-epitaxy QDs fabricated by filling of nano-openings patterned into a planar surface, self-assembled QDs fabricated by Stransky–Krastanow growth mode, etc. [33]. EQDs are already commercially available in light sources and have high fidelity performance, but require cleanroom equipment during their fabrication and their accessible wavelength range is restricted to 0.9 – 1.3 µm, which currently limits some of their applications [33].

When QDs are fabricated via a colloidal synthesis process, they can also be called CQDs as they possess surface ligands that prevent aggregation and enable dispersion in different solvents.

As briefly mentioned in Section 1.1, because the particle diameter of QDs in general is of the same magnitude as the de Broglie wavelength of the electron wave function, these particles are said to be quantum confined in all three dimensions [34]. Spatial confinement promotes the enhancement of Coulomb interactions between charge carriers due to a forced overlap of electronic wave functions and reduced dielectric screening. These interactions have important spectral and dynamical implications such as size-tuneability of emitted spectrum, excited state lifetimes, and carrier multiplication [35]–[37].

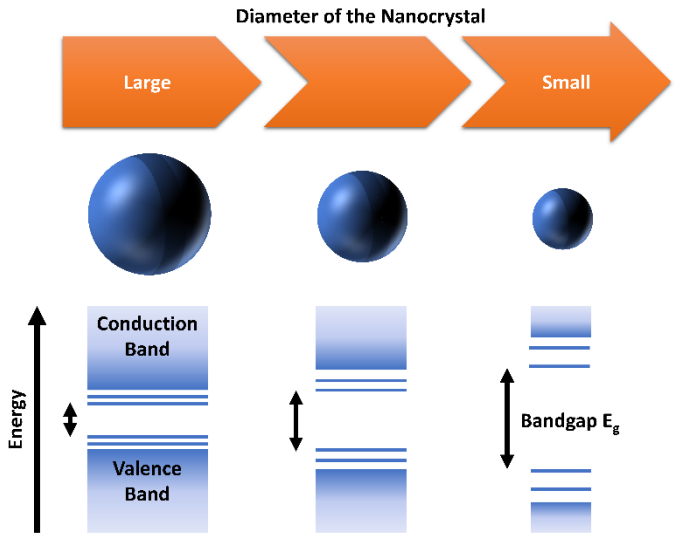

Figure 1-3. Illustration of the size-tuneability in QDs. The smaller the QD is, the wider the bandgap of these 0D semiconductors gets. Emission resulting from radiative decay between conduction and valence bands can therefore be tuned according to the size of QDs.

Similarly to bulk semiconductors in general, the valence band and conduction band of QDs are the bands closest to the Fermi level, which is the highest energy level that an electron can occupy at the absolute zero temperature. These bands determine the optoelectronic properties of QDs [38]. The valence band is the highest range of electron energies in which electrons are normally present at absolute zero temperature, while the conduction band is the lowest range of vacant electronic states. On a graph of the electronic band structure of a (undoped) semiconductor, the bandgap (E_g) is the minimum energy required to promote an

electron from the valence band to the conduction band and the Fermi level sits between these two bands [38]. Figure 1-3 illustrates how the size of a QD impacts its electronic structure, and therefore its optoelectronic properties, through the effect of quantum confinement. As the strength of the latter increases (for a diminishing size of the semiconductor crystal) the transition from a band structure characteristic of the bulk to discrete electronic levels (akin to those in atoms) becomes more pronounced. The bandgap energy (the lowest transition energy) increases for smaller QD sizes of a same constituent material.

QDs have inherited unique properties between bulk materials and their discrete molecules or atoms. Optical properties such as the direct photogeneration of multiexcitons by single photons and broadband absorptions below the optical band gap and narrow emissions show the capability of stimulated emission and optical gain in QDs [4], [39] and light down conversion [40], respectively.

Core/shell Cd-based CQDs and a type of all-inorganic halide perovskite QDs were the main materials used in this thesis, for colour conversion and lasing applications, respectively. These families of materials are briefly presented below. More details are given later in the thesis (particularly in Chapter 2).

1.2.1 Cd-based CQDs

One of the most established categories of multicomponent structured QDs belongs to the family of II–VI heterostructures [41] and these account for a large variety of different carrier localization regimes (Figure 1-4). The QDs in this family consist of a CdSe or CdTe core (or an alloy related to these) overcoated with one or several shells of another material alloy – creating a heterostructure. The shell passivates the surface of the core, increasing the luminescence quantum efficiency and enabling control of the carrier localisation.

Type-I core/shell heterostructures, have both electron and hole charge carriers localised in the core [41]. Quasi-type-I and II heterostructures have one charge carrier delocalised and the other localised in either the core or the shell [41]. Finally, type-II heterostructures, have one charge carrier localised in the core and the other in the shell [41]. The synthesis of multicomponent structured CQDs has opened the way towards engineering of band offsets at the NC scale, which can be modified by strain and changes in the crystalline structure [41].

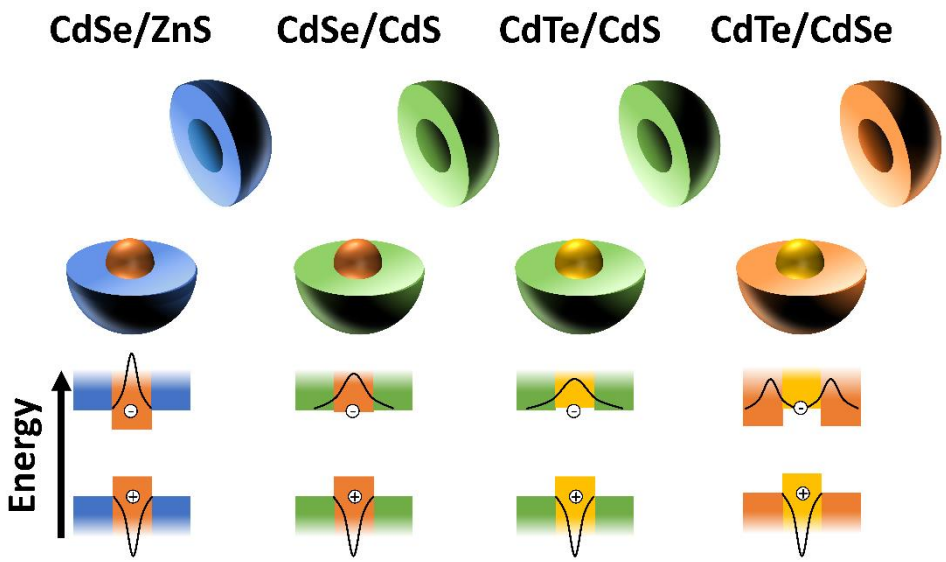

Figure 1-4. Schematic band diagrams of examples of different II-VI core/shell QD heterostructures: type-I (CdSe/ZnS), with the electron and hole wavefunctions localised in the core of the QD; quasi-type-I (CdSe/CdS) and quasi-type-II (CdTe/CdS), with the electron wavefunction delocalised and hole function localised in the core; and type-II (CdTe/CdSe), with the electron wavefuntion localised in the shell and the hole wavefunction localised in the core.

In this thesis, alloyed core/shell CdSSe/ZnS NCs, which are type I or quasi type I depending on their wavelengths, have been used for the self-assembled microlasers described in Chapters 2 to 4.

1.2.2 All-inorganic Halide Perovskite QDs

Perovskites are a class of compounds with a crystalline structure in the form of ABX_3,(Figure 1-5) where A and B are cations (with A usually larger than B) and X is an anion that binds them together [34], [42]. All-inorganic ceasium lead halide perovskite colloidal QDs were first reported in 2015 [43] to improve the stability problems [44] and sensitivity to oxygen and moisture [45] of hybrid organic-inorganic perovskite materials. These possess a cubic or orthorhombic structure and their emitting spectrum depends on the anion used to bind them (Figure 1-5) [43]. In addition to that, they feature large absorption cross-sections, high PLQY, and defect-tolerant properties.[46] They also exhibit strong nonlinear absorption and thus two-photon pumped lasing has been achieved with relatively low threshold [46]. Moreover,

unlike the more established Cd-based QDs, $CsPbBr_3$ QDs show nearly temperature-independent PL peak position between the 20 and 100 °C due to their unique electronic structure [46]. For CdSe-based QDs, the expansion of the crystal lattice and electron-phonon interactions induced by temperature decrease the bandgap energy and red-shift the emission. However, the bandgap of $CsPbBr_3$ QDs originates from the interaction between different orbitals and an increase in temperature changes the interaction between these orbitals. Such changes compensate the electron-phonon interactions and enable a nearly temperature-independent emission between the 20 and 100 °C [46].

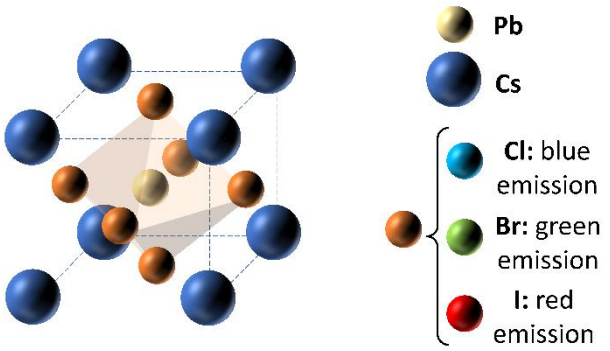

Figure 1-5. Crystalline structure of all-inorganic ceasium lead halide perovskites is predominantly face-centered cubic or orthorhombic. The anions on the faces of the cube (Cl, Br or I) dictate the emission wavelength of the NC (blue, green and red, respectively).

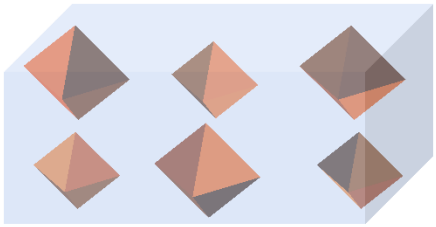

Figure 1-6. $CsPbBr_3$-in-Cs_4PbBr_6 crystals: structure inclusion schematic where $CsPbBr_3$ phases with up to tenths of nm in size (represented in orange) grow inside the Cs_4PbBr_6 phase represented in blue [47], [48].

$CsPbBr_3$-in-Cs_4PbBr_6 (Figure 1-6) exhibits highly efficient green luminescence and enhanced thermal stability [46]. Cs_4PbBr_6 does not have a perovskite structure but can be considered a 0D perovskite by analogy because $[PbX_6]^{4-}$ octahedrons are isolated in the crystal. This structure results in a higher bandgap than $CsPbX_3$, shifting the band edge emission more towards the UV [49]. The origin of the green luminescence is thought to come from the formation of $CsPbBr_3$ QDs with a crystalline structure as seen in Figure 1-5, within the Cs_4PbBr_6 host crystalline structure [47], [48] during the growth of large Cs_4PbBr_6 crystals [47]–[50], as illustrated in Figure 1-6. When compared to CQDs, $CsPbBr_3$-in-Cs_4PbBr_6 QDs have a more efficient luminescence in the green and enhanced thermal stability. The latter is tied to the 'ligand-free' nature of the embedded $CsPbBr_3$ in a higher-bandgap semiconductor material (Cs_4PbBr_6). Unlike the organic ligands of CQDs, this encapsulation can withstand elevated temperatures [49].

$CsPbBr_3$-in-Cs_4PbBr_6 is the material utilized for the work on colour conversion described in Chapter 5.

1.3 Motivation

Despite the advantages of QDs and CQDs described above, all-inorganic halide perovskite NCs continue to have problems with moisture which limits their usage in applications that cannot avoid exposure to humidity. Likewise, in terms of laser applications CQDs are usually combined with an optical cavity that is fabricated separately and many times require additional lithography steps to be integrated in photonic circuitry. QD lasers would benefit from photonic structures that do not rely on any form of lithography either during fabrication or in terms of implementation in integrated photonics. This thesis focuses on the challenges above. It addresses the fabrication complexity of CQD microlasers discussed in Section 1.6 by exploring the self-assembly of suprastructures with the well-established Cd-based CQDs as light emitters for a new class of lasers (see Section 1.6 and Chapter 2) that are both the gain material and an optical cavity. In addition to that, it explores ways of using all-inorganic halide perovskite crystals for colour conversion of LEDs, while protecting them against humidity. As it will be seen in Section 1.9, sensitivity to humidity is one of the main disadvantages of these materials and a simple encapsulation solution could enable their usage in smart lighting applications, such as visible light communications (VLC), also known as Li-Fi.

1.4 Thesis Outline

In addition to this chapter, where the framework of the thesis is presented and main topics are approached, this work comprises five other chapters where the problems stated above are individually studied. Chapter 2 discusses Cd_xSe_{1-x}/ZnS QDs and their applications to microsphere lasers by taking advantage of bottom-up self-assembly of the alloyed CQDs to synthesize suprastructures (microspheres). The work on these micro lasers fabricated from the bottom up is then branched out in two different topics: the addition of higher bandgap CQDs to the synthesis of microspheres, which enable additional properties (Chapter 3) and the integration and coupling of individual microlasers to other devices via transfer printing (Chapter 4). Work on other types of NCs are presented in Chapter 5. This work includes a study of in-house synthesized $CsPbBr_3$-in-Cs_4PbBr_6 crystals, which provide further photo and

thermal stability [46] for applications in colour-converting composites, and studies on more exotic NCs (doped QDs, NPLs and tetrapods) for self-assembly into microspheres and the study of their properties, initiated during a 3-month internship at Nanyang Technological University. Finally, Chapter 6 contains the concluding remarks of this work and gives an outlook for further studies.

Some information on the synthesis and a general overview on the physics of the CQDs, including electronic states, optical gain, their dynamics for light communication and lasing applications, and the thermodynamics behind the process of self-assembly will now be explored in more detail. The focus is placed on Cd-based dots as this is the material technology predominantly utilized in this research, although all inorganic perovskite NCs (the family of the material used in the colour converter study) are also discussed.

1.5 Fundamentals of CQDs

1.5.1 Synthesis

Like most colloidal QDs, CdSe-based QDs are usually synthesized via hot injection [51]. This method takes advantage of thermally decomposed organometallic cationic precursors in a hot reaction medium which anionic precursors are rapidly injected into (Figure 1-7). The hot injection facilitates the instantaneous supersaturation of reactant, promoting a fast nucleation and growth of monodispersed QDs.

To produce monodisperse colloids, the hot-injection method needs to have the nucleation and growth stages of the colloid temporally separated [52], [53]. The nucleation is promoted by injecting one reagent into a heated reaction mixture and supersaturating the solution. This initial period of supersaturation leads to a short nucleation phase, which in turn decreases the solute in solution. Once the concentration of solute falls below the nucleation threshold, the nucleation phase ends and the controlled growth phase begins (Figure 1-8). Here, the initial size distribution is mainly determined by the time it takes to fully inject and mix the added precursor.

During the growth of colloidal QDs, the high surface energy of the smallest NCs in solution will usually encourage their dissolution in the solvent. This allows other crystals in solution to assimilate the dissolved material and grow even further, increasing the

average NC size as the reaction time goes on. This mechanism, also referred to as 'Ostwald ripening', allows the size of NCs to be tuned according to the duration of the growth phase. In the particular case of CQDs, it also enables control over the band gap of the material. The PL of CQDs is shifted to longer wavelengths as they grow in size, until the growth phase is quenched through rapid cooling.

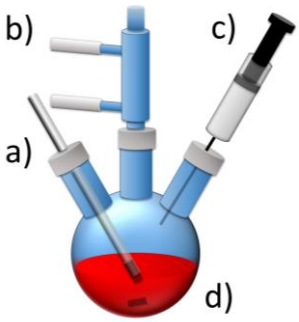

Figure 1-7.Example of a typical hot-injection setup using a thermometer (a), a temperature regulator system (b), and syringe with anionic organometallic precursors (c) to control the synthesis on a 3-necked flask with thermally decomposed organo-metallic cationic precursors (d) at the required temperature and magnetic stirring conditions.

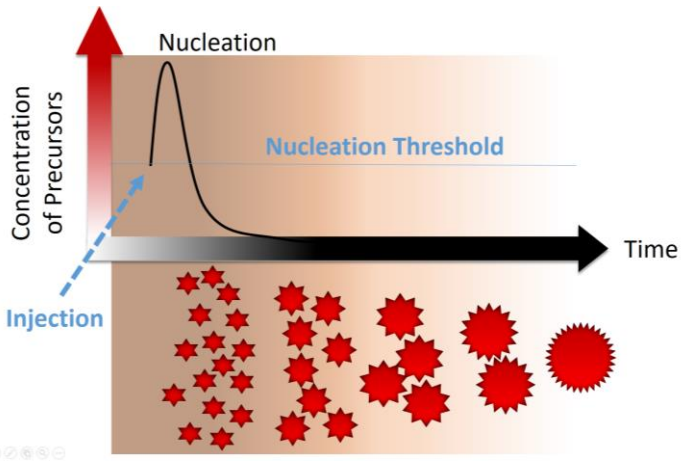

Figure 1-8. Depiction of the nucleation and growth phases over time, during the hot-injection method.

The kinetics of hot-injection methods may depend on several parameters such as the reactivity of precursors, reaction variables (i.e., temperature and concentration), and surfactants used during the process [51]. In addition to CQDs, this flexibility allows the synthesis of several other types of NCs by adjusting the hot-injection recipes, as will be seen in Chapter 5. The perovskite crystals studied in this thesis are the only crystals that follow a different procedure, which is covered in Section 5.2.1.

It is also worth noting that while hot-injection techniques excel at tuning the diameter of CQDs as a function of the reaction time, there are other methods, namely heat-up (or non-injection) synthesis techniques, that produce larger scales of CQDs with identical sizes.

In heat-up methods, all reagents are mixed in the reaction flask at the beginning of the synthesis. In this stage, the monomers required for nucleation are either bound to ligands or part of a larger complex that prohibits or lowers their reactivity. Once the solution is heated, the precursors transform into free monomers and begin to nucleate. Here, the nucleation rate and supersaturation of monomers is controlled by temperature [54].

1.5.2 Energy States – Optical transitions

In general, spherical semiconductor CQDs have carrier motion spatially constrained in all three dimensions (regime of 0D confinement seen in Figure 1-1) and therefore they have discrete electronic states. These discrete electronic states are labelled according to their principal (n = 1, 2, 3, …) and orbital angular momentum (L = 0, 1, 2, …) quantum numbers, and are usually denoted as nL [35], [55]. In this notation, the quantum number L is replaced by the letter of the corresponding atomic-like progression (S for L = 0, P for L = 1, D for L = 2, etc.) [35], [56]. For regimes of 0D confinement in spherical QDs, the Brus equation can be used to find the bandgap Energy, $E_g(QD)$ [35], [55]–[57], where the bandgap is approximated to the sum of the bulk bandgap of the material, $E_g(bulk)$, and the size-dependent confinement energies of the band-edge electron ($1S_e$) and hole ($1S_h$) states. The bandgap (Figure 1-3) for the three degenerate lowest states (n = 1), namely 1S, 1P and 1D, can then be estimated as follows [35]:

$$E_g(QD) = E_g(bulk) + \frac{\hbar^2\pi^2}{2m_{eh}R^2} \quad \text{(Eq. 1)}$$

with $\hbar$ as the reduced Planck constant, R the QD radius, m_e and m_h the effective electron and hole masses, respectively, and $m_{eh} = m_e.m_h/(m_e + m_h)$.

In addition to the types of semiconductors used during the synthesis, it can be seen from Eq. 1 that the emission of QDs can also be tuned according to their size, as the bandgap of QDs is inversely proportional to their size. This continuous spectral tunability can be exploited in a wide range of applications in lighting and laser technologies, and it also fills spectral gaps currently not accessible with traditional semiconductor lasers [55]. The size tunability overviewed in Figure 1-3 can be complemented with Figure 1-9, where it is shown that an increase in size of CdSe/ZnS CQDs (and consequent bandgap decrease) results in PL emission spectra of higher wavelengths and solutions of distinct colours.

In these CQDs, the relatively narrow PL spectra come mainly from the lowest transition (continuous lines), while the absorption spectra (dashed lines) are composed of a multitude of transitions that combine to give an overall increasing absorption as wavelength shortens. This illustrates one of the attractive properties of CQDs as luminophores, as they possess a broad absorption for photons above the bandgap and a narrow emission that can be tuned during their synthesis.

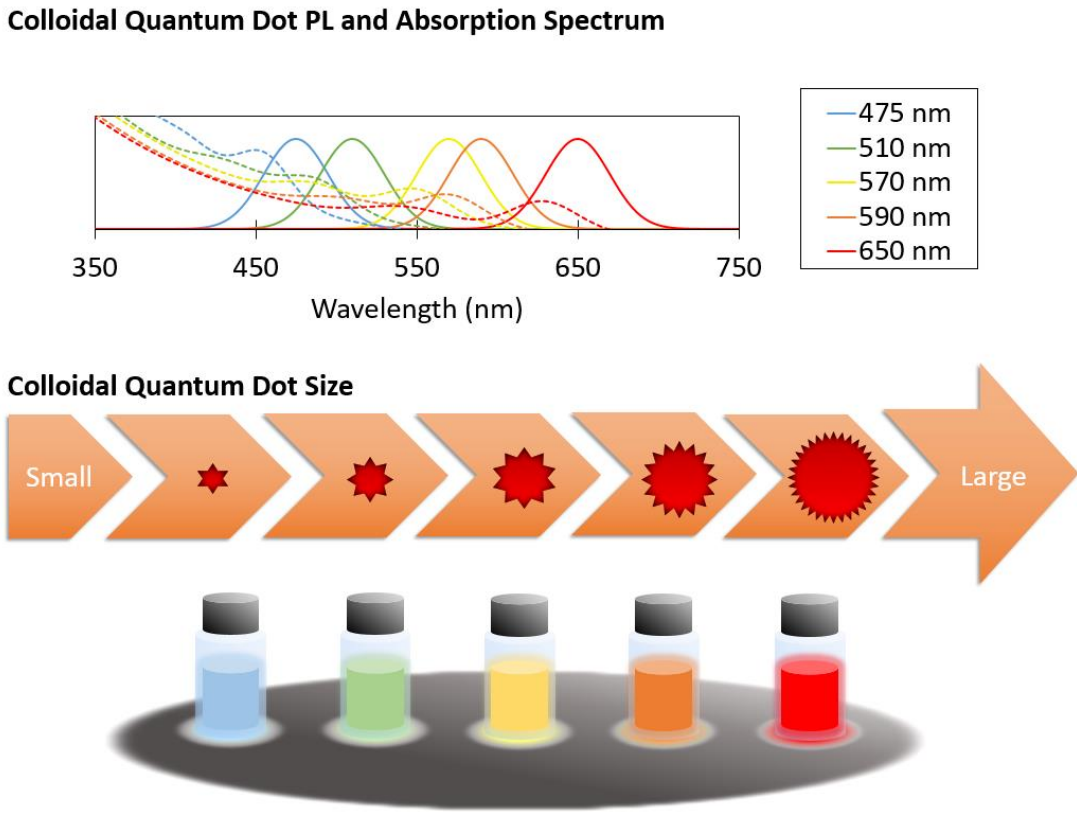

Figure 1-9. Illustration of typical PL (continuous lines) and absorption spectra (dashed lines) of CQDs, according to their different sizes and corresponding wavelength emissions.

The optical properties of CQDs can also be tuned by changing the semiconductor material or alloy composing the CQDs. This effect is linked to the dependence of the bulk bandgap energy $E_{g,0}$ on the material and its effect can be understood by looking at Eq. 1. The alloyed core CdSSe/ZnS CQDs utilized in the laser experiments of Chapters 2 to 4 all have the same sizes (around 6nm in diameter) and the wavelength is set by changing the ratio of S/Se in the alloy of the core (Figure 1-10).

While the simple model described by Eq. 1 explains the concept for size tunability of CQDs and provides a reasonable description of the NC conduction band, the physics behind the

valence band is more complicated but it helps to better understand the absorption spectra of CQDs.

Figure 1-10. Picture of green (530 nm), yellow (575 nm) and red (630 nm) CQDs in solution taken from the laboratory. These CQDs all have nominally the same size (6 nm) but differ in alloy composition in the core.

For the valence band, the Hamiltonian or total energy of the system contains both the crystal-lattice and NC-confinement potentials. As a result, it needs to be described by the total angular momentum, F, which is given by the sum of the Bloch-function angular momentum, J, and the orbital momentum of the hole envelope function, L [35]. Here, the total angular momentum is usually denoted in the form of nL_F [35].

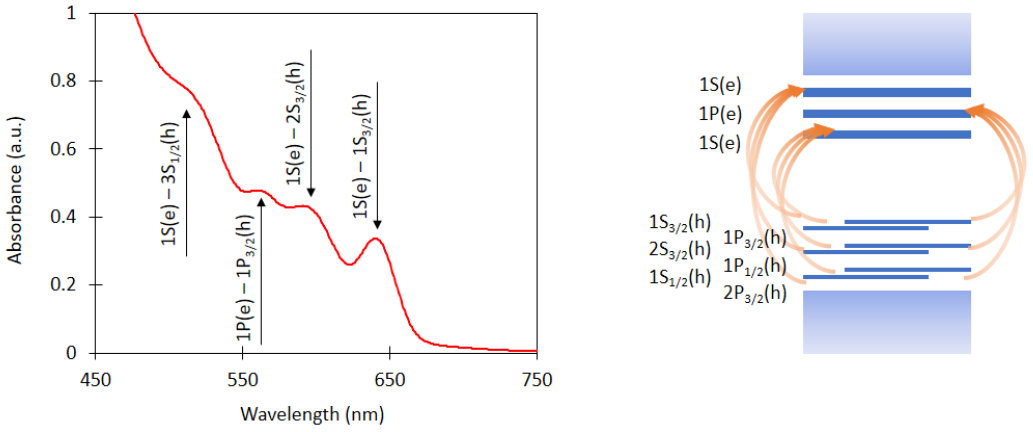

Figure 1-11. Illustration of a typical absorption spectrum of CdSe NCs (left), with the 4 lowest interband transitions involving either 1S or1P electron states marked, and of a 6-fold degenerate valence band representation (right) with the allowed optical interband transitions indicated by arrows.

Some exceptions aside, most III-V and II-VI semiconductor compounds (including CdSe) have a 6-fold degenerate valence band like the one represented in Figure 1-11. Note that the valence bands can be different for some CQD semiconductors (e.g.: PbS, PbSe [58]) but for relevance the CdSe 6-fold degeneracy was focused on here. When considering this subband degeneracy, the overall structure of CQD absorption spectra (Figure 1-11) becomes much more obvious [35].

The emission spectrum of NCs and CdSe CDs in particular is explained by the fine structure of the band-edge 1S(e) – $1S_{3/2}$(h) transition. This fine structure arises from the electron-hole (e-h) exchange interaction and the crystal field and shape asymmetry (Figure 1-12).

The e-h exchange interaction is enhanced in NCs compared to the bulk material due to the increased overlap between electron and hole wavefunctions. Due to that overlap, the band-edge electron 1S(e) and the hole states $1S_{3/2}$(h) must be treated as a combined state with total angular momenta $N = F_e + F_h$, where $F_e = 1/2$ and $F_h = 3/2$ are electron and the hole total angular momentums. Following from that, N has two possible state outcomes: N=1 or N=2. These two states are split by the exchange interaction and can either be high-energy, optically active bright excitons (N=1) or lower-energy, optically passive dark excitons (N=2).

The e-h exchange interaction states are then further split into 5 sub-levels due to the crystal field and the shape asymmetry of CQDs, forming 2 upper states (U) and 3 lower (L) states. These so called fine-structure states are labelled according to the magnitude of the projection of the exciton total angular momentum, N_m, along the unique crystal axis (Figure 1-12). Here, the lowest-energy state ($N_m = 2$; dark state) remains optically passive regardless of the effect of additional level-splitting and is separated from the next higher-energy state ($N_m = 1^L$; bright state) by several meV, depending on the CQD size.

At lower temperatures, the exciton recombination occurs via the optically forbidden low energy dark state, which leads to long radiative lifetimes. These long radiative lifetimes are determined by spin-flip processes that transfer dark excitons (e – h parallel spins) into radiative bright excitons (e – h antiparallel spins), namely the short-range e – h exchange interaction, acoustic phonons and semiconductor – air interfaces [59].

As the temperatures increase, the thermal redistribution of the exciton population mixes the dark state with the higher bright states with higher energies, leading to shorter radiative

lifetimes. This happens because bright excitons already have e – h antiparallel spins and are therefore ready to recombine radiatively.

At sufficiently high temperatures, the exciton population becomes equally distributed between bright and dark states, leading to the saturation of the decay constant. Typically in CQDs (including the CdSSe/ZnS CQDs used in Chapters 2 – 4), this decay saturation point sits between a few to a few tens of nanosecond, a range that is suitable for VLC (see Section 1.9).

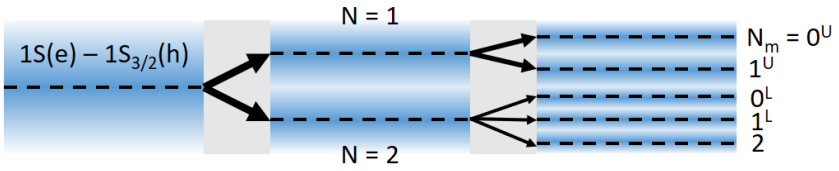

Figure 1-12. Schematics of the fine-structure splitting of the band-edge 1S(e)-1S3/2(h) transition in CdSe NCs.

The band-edge exciton fine structure can also partially explain the Stokes shift, i.e. the difference between the maximum absorption wavelength and the photoluminescence peak (e.g. Figure 1-9). For CdSe CQDs of most sizes, the band-edge absorption is dominated by the superposition of two upper-manifold strong optical absorbing states (1U and 0U excitons). However, emission tends to occur at the lower energy emitting states (N_m = 2 and 1L), which are separated from the absorption states by tens of meV. The transition from these higher states to lower states is allowed by the non-radiative release of energy via the generation of longitudinal optical phonons. This interaction of energy states with longitudinal optical phonons, the band-edge exciton fine structure and the size dispersion of CQDs are the main causes for the global Stokes shift observed in NC samples [35].

1.5.3 Optical gain in CQDs

Before discussing the conditions to achieve laser with CQDs, it is important to overview the main relaxation pathways of CQDs [13]. Charge carriers can recombine radiatively in CQDs either by spontaneous emission (Figure 1-14i) or by stimulated emission, which is necessary for lasers (Figure 1-14ii). In addition to that, they can also recombine non-radiatively through several different processes (e.g. Auger recombination, thermalisation by coupling to

vibrations, multiexciton generation, ejection of a hot charge carrier and trap-assisted non-radiative recombination either at the surface of the QD or via an impurity (Figure 1-14ii – vii). Trap assisted radiative recombination (see Section 5.1) and energy transfer between QDs (studied in Chapter 3. and Chapter 5.) can also occur, but were left out of Figure 1-14 for simplification purposes.

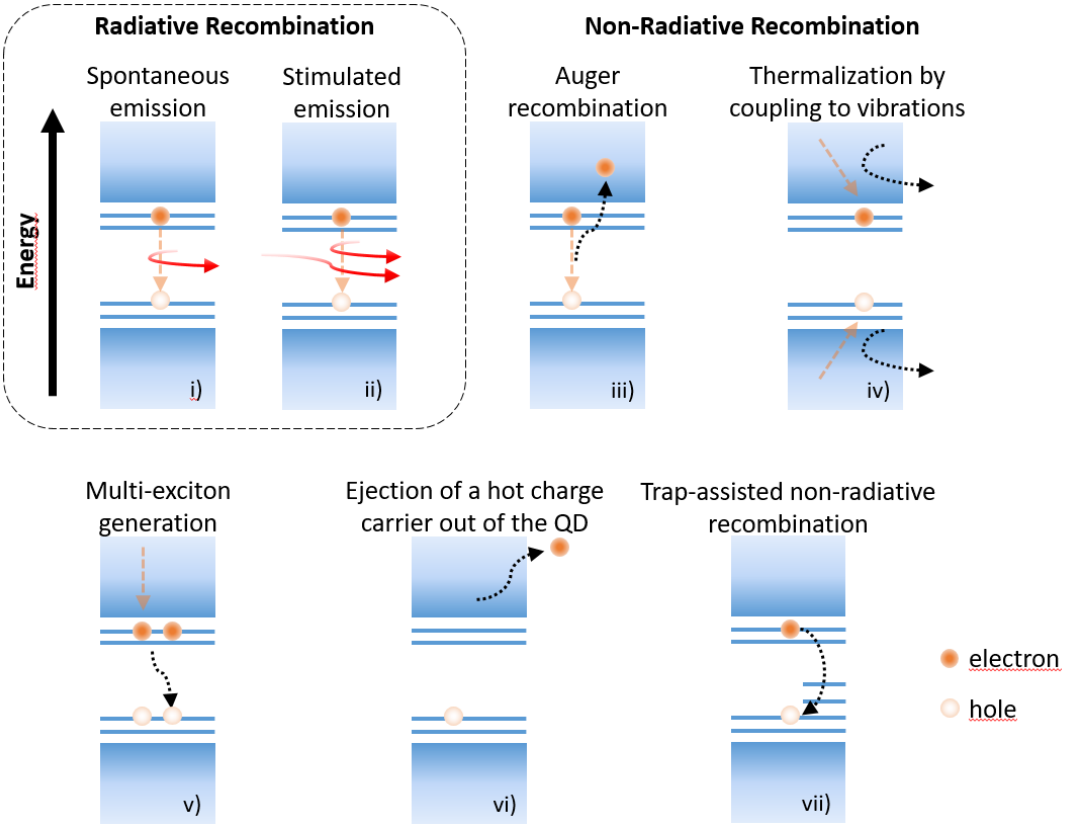

Figure 1-13. Schematic of the main relaxation pathways for carrier states in CQDs: i) spontaneous emission of a photon through the recombination of an electron-hole pair; ii) stimulated emission of a photon by another photon, through the recombination of an electron-hole pair; iii) Auger recombination, where the excess energy from the electron-hole recombination is transferred to another charge carrier that is subsequently excited to higher energy states; iv) energy dissipation via coupling to phonons; v) multi-exciton generation, where the hot-carrier energy is converted into an additional electron–hole pair; vi) ejection of a hot charge carrier to the environment of the CQD; vii) trap-assisted electron-hole recombination via coupling to phonons. Red wavy arrows depict photons.

Optical gain is one of the prerequisites to build a laser [4], [60]. This is attained when the light generation by stimulated emission in the laser material dominates over the light absorption. However, as seen above and in the previous section, CQDs have quantized atomic-like energy levels with multifold degeneracy of electron and hole states and non-radiative recombination

from multiexciton states [4], [60]. This can increase the gain threshold and complicate the optical gain process of CQDs [17].

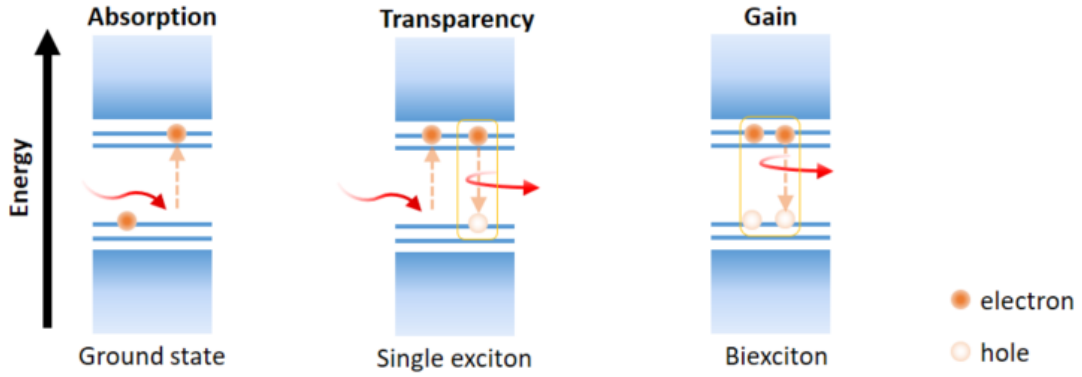

Figure 1-14. The 3 main transition state types in QDs for a 2-fold degeneracy and 2-level system (top). Ground state regime can only form excitons when electrons in the valence band absorb energies equal or superior to the bandgap. Transparency state regimes include a single exciton and can either absorb energy to generate a second exciton or decay and emit a photon, assuming that the recombination is radiative. Gain occurs in the presence of biexcitons, where their annihilation results into a free exciton and the emission of a photon. Red wavy arrows depict photons and yellow boxes represent exciton and biexciton states in the transparency and gain regime, respectively.

However, in most cases Cd-based QDs have the degeneracy (at least partly) lifted by a variety of parameters, such as the crystal structure, the shape of the NC and core/shell structure (see previous section). In certain cases, thanks to this lifting of degeneracy, the system can be considered as a simple 2 level for the lowest transition. For clarity, this is the assumption taken in the following explanation of gain in CQDs. Figure 1-14 shows the simplified optical transition state in CdSe CQDs with a 2-fold degeneracy and 2-level system [17]. Here, the states of the quantum mechanical system are said to be degenerate if they yield the same value of energy for different quantum numbers (spin up and spin down), and the 2-level system implies that the system in consideration only has two energy levels (ground state and excited state).

The ground state is characterized by two electrons located in the bottom level (valence band) that can only absorb energy. Optical transparency can occur when an incident photon at the transition energy has an equal chance to trigger recombination of the excited electron via stimulated emission and to be absorbed by the other electron in the ground state [61]. The

condition for optical gain is verified when both electrons are excited and stimulated emission dominates over optical absorption. Note that spontaneous and non-radiative emission can also occur during these recombinations.

In such QDs, biexciton states and higher order multiexciton states are responsible for optical gain, which can only happen for $\langle N \rangle$ >1, where $\langle N \rangle$ is the average number of excited excitons per CQD [55][4], [55]. The state filling leads to a Poissonian exciton population, where the probability of a given number of excitons being generated for a fixed pump energy is given by the Poisson distribution [62]. It is important to note that while the simplified model of CQD electronic states discussed above provides a reasonable description of the CQD conduction band, the valence band has usually a more complex, multi-subband character that takes into consideration both the crystal-lattice and CQD-confinement potentials [35], as was discussed in the previous section. For QDs whose degeneracies are distinct from 2, the conditions for optical transparency increase, and so does $\langle N \rangle$ for gain threshold [35], [55]. It can be shown that for an inhomogeneously broadened ensemble of CQDs the condition for transparency, given by the average number exciton per dot at transparency, $\langle N \rangle_{tr}$, is given by Eq. 2 [63]:

$$\langle N \rangle_{tr} = \frac{\gamma}{\gamma + 1 - (\gamma - 1).e^{-\frac{\Delta_{XX}^2}{\Gamma^2}}} \qquad \text{(Eq. 2)}$$

where γ is the level of degeneracy for the transition, Γ is the inhomogeneous linewidth and Δ_{XX} the exciton-exciton interaction energy. For a degeneracy of 2 and type I CQDs where the biexciton interaction energy is negligible with respect to the linewidth, the previously discussed result is found: $\langle N \rangle_{tr} = 1$. For a degeneracy of 3, that value increases to $\langle N \rangle_{tr} = 1.5$. For the alloyed core CQDs used in Chapters 2 – 4, if they are considered as quasi-type I and of degeneracy of 3, the expected value of $\langle N \rangle$ at transparency is likely to be between these two values.

From a laser engineering point of view, most CdSe-based CQDs can be seen as a 3-level pumping scheme (Figure 1-15); or possibly a quasi-3 level system. This is because there is still some absorption at the wavelength at which emission and optical gain develops. As a result, they require pumping energies higher than the bandgap to allow population inversion and consequently stimulated emission. Population inversion occurs when the population of excited electrons (N_2) is higher than those at ground state (N_1). Upon pumping CQDs, electrons transit to E_3 and usually decay to E_2 non-radiatively via emission of phonons. They

can then decay radiatively from E_2 to E_1, by releasing a photon. Because the transition E_{21} takes longer than E_{32} ($\tau_{21} >> \tau_{32}$), N_3 will be close to zero. If $\langle N \rangle_{tr} = N_2 > N_1$, population inversion between level 1 and 2 is achieved and optical amplification at the respective frequency can be obtained [38]. This condition is equivalent to the one derived previously for the exciton with $\langle N \rangle > 1$. The quasi-3 level nature of some CQDs comes from the Stokes shift caused by the fine structure of the lowest hole state as explained in Section 1.5.2.

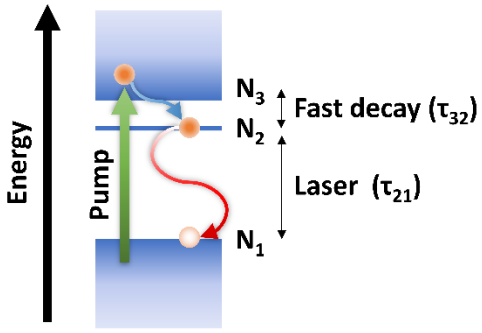

Figure 1-15. 3-level pumping scheme.

The laser rate equation of a 3-level semiconductor laser system can be modeled assuming that the three energy levels E_1, E_2 and E_3 are nondegenerate. If N_1, N_2 and N_3 represent the population densities of the three levels and the pump is assumed to excite electrons from level 1 to level 3 that decay to level 2 through a nonradiative process, then the pump effectively transfers electrons from level 1 to level 2. Assuming that the nonradiative relaxation from level 3 to level 2 is faster than from level 2 to level 1, the population of electrons will accumulate in level 2. If the transitions take place exclusively between these three levels, then the population of electrons per unit volume, N, can be written as the sum of the populations in each of its levels (Eq. 3):

$$N = N_1 + N_2 + N_3 \qquad \text{(Eq. 3)}$$

The rate equations that describe the evolution of N_1, N_2 and N_3 as a function of time are then (Eq. 4):

$$\begin{cases} \frac{dN_3}{dt} = \underbrace{-W_p(N_3 - N_1)}_{stimulated\ transitions\ 3\leftrightarrow 1} - \underbrace{T_{32}N_3}_{spontaneous\ transitions\ 3\rightarrow 2} \\ \frac{dN_2}{dt} = \underbrace{-W_1(N_2 - N_1)}_{stimulated\ transitions\ 2\leftrightarrow 1} + \underbrace{T_{32}N_3 - T_{21}N_2}_{spontaneous\ transitions\ 3\rightarrow 2\ and\ 2\rightarrow 1} \\ \frac{dN_1}{dt} = \underbrace{W_p(N_3 - N_1) + W_1(N_2 - N_1)}_{stimulated\ transitions\ 3\leftrightarrow 1\ and\ 2\leftrightarrow 1} + \underbrace{T_{21}N_2}_{spontaneous\ transitions\ 2\rightarrow 1} \end{cases} \quad \text{(Eq. 4)}$$

Where W_p is the rate of pumping per electron from level 1 to level 3, which depends on the pump intensity, W_1 is the stimulated transition rate per electron between levels 1 and 2, and the spontaneous transition rates T_{32} and T_{21} are given by (Eq. 5):

$$\begin{cases} T_{32} = A_{32} + S_{32} \\ T_{21} = A_{21} + S_{21} \end{cases} \quad \text{(Eq. 5)}$$

Where A_{32}/A_{21} and S_{32}/S_{21} correspond to the radiative and nonradiative transition rates between levels 3 and 2 or levels 2 and 1, respectively. The spontaneous transitions between levels 3 and 1 are neglected in $\frac{dN_3}{dt}$ since most electrons on level 3 are assumed to transit to level 2 rather than to level 1.

The stimulated transition rate between levels 1 and 2 can be written as (Eq. 6):

$$W_1 = \frac{\pi^2 c^2}{\hbar\omega^3 {n_0}^2} A_{21} g(\omega) I_1 \quad \text{(Eq. 6)}$$

With I_1 as the intensity of the radiation in the 2 → 1 transition, $g(\omega)$ as the lineshape function describing the transitions between levels 1 and 2, ω as the frequency of the pump and n_0 as the refractive index of the medium [64].

At steady state (Eq. 7):

$$\frac{dN_1}{dt} = \frac{dN_2}{dt} = \frac{dN_3}{dt} = 0 \quad \text{(Eq. 7)}$$

Eq. 4 yields (Eq. 8):

$$\frac{N_2 - N_1}{N} = \frac{[W_p(T_{32} - T_{21}) - T_{32}T_{21}]}{[3W_pW_1 + 2W_pT_{21} + 2T_{32}W_1 + T_{32}W_p + T_{32}T_{21}]} \quad \text{(Eq. 8)}$$

And in order to obtain population inversion between levels 2 and 1 ($N_2 - N_1 > 0$), $T_{32} > T_{21}$ and $W_p \geq \frac{T_{32}T_{21}}{T_{32} - T_{21}}$ are conditions that need to be verified.

Laser rate equations can also be modelled for pumping schemes of other levels (e.g.: 2-level system or 4-level system)[64], and be used to model semiconductor microlasers, including the microsphere resonators covered in Chapters 2 and 3 [65].

So far, non-radiative processes that compete with light emission and can increase the excitation power needed to reach a given exciton population were not considered. The main non-radiative processes in CQDs, and ways to overcome them, are discussed in the following section.

1.5.4 Challenges underlying the optical gain in CQDs

Although surface-trapping [66], [67] and photo induced absorption [68] can hinder optical gain in CQDs, these problems were solved by adopting core-shell structures [66], [69] and engineering the surface and environment of the CQDs [4], [17]. The rapid carrier cooling processes (carrier-carrier and carrier-phonon) in CQDs [70], [71] are also comparable to those in bulk semiconductors [72] and the hot carrier relaxation does not limit optical gain in CQDs [72], [73].

The limiting factor against the development of stimulated emission and lasing in CQDs is Auger recombination (AR), a nonradiative many-body carrier decay process where the energy released by the annihilation of a pair of electron and hole is used to stimulate the other electron or hole to a higher energy state (see Figure 1-14) [17]. This process is more efficient in CQDs than in their bulk counterparts [74], [75] because the spatial and dielectric confinement strengthen carrier-carrier interaction in CQDs and the conservation for translational momentum responsible for mitigating AR in bulk semiconductors is attenuated in CQDs.

The AR lifetime in CdSe CQDs falls between several to tens of picoseconds, which is three to four orders of magnitude shorter than their spontaneous emission lifetime [74]. The AR rate has also been investigated in CQDs as a function of the photoexcited exciton number [74], [76] and monotonously accelerates with the increase of exciton number. The AR lifetime is found to be inversely proportional to the square of the average number of excitons, which indicates that the AR in the quantum confined CQDs is dominated by energy transfer from the annihilation of an exciton to an electron or a hole [77]. The AR is also size dependent: It

greatly increases with the reduction of the dot size and its lifetime shows a linear dependence on the volume of the CQDs [74], [76].

1.5.5 Optimizing CQDs for optical gain

One way of mitigating AR in CQDs and facilitating their use as the active medium of optical amplifiers and lasers is by weakening the carrier-carrier interaction in CQDs through spatial decoupling of electron and hole wave functions. As mentioned earlier, this can be done by engineering a type of heterostructure that promotes spatial decoupling through selective coating of shell semiconductors [13] (Figure 1-4). Heterostructures of type-I trap simultaneously electrons and holes, while those of type-II attract charge carriers of one type and repel the other [78]. Suppressed AR has been observed in type-II heterostructures, such as CdSe/ZnTe and ZnTe/CdSe CQDs, due to the level of spatial separation between electron and hole wave functions. However, they also showed a reduced optical oscillator strength which hinders stimulated emission [41], [79], [80]. On the other hand, the quasi-type-I band alignment observed in CdSe/CdS CQDs allows simultaneously for a suppressed AR and a strong oscillator strength. In these structures, holes are confined in the core and electrons are delocalized over the entire CQDs due to the smaller conduction-band offset when compared with the valence band [81]. As a consequence, overlap between the electron and hole wave functions is effectively reduced and CQDs benefit of a lower-threshold optical gain. Such a phenomenon becomes more pronounced for CQDs with the same heterostructure but having thicker shells [82]–[85].

Another way of reducing AR is by engineering the shape of the confinement potential. Theoretical [86], [87] and experimental work [29], [88] have confirmed that an alloyed interface with smoothed confinement potential in the heterostructure can decrease the AR rate by more than three orders of magnitude when compared to heterostructures with an abrupt interface (Figure 1-16). AR and interfacial or surface trap states are known to cause random fluctuations in the QD PL, a phenomenon termed blinking [89]. An alloyed interface significantly decreases the overlap between the initial and the final state involved in the AR process [86], [90], [91]. CQDs with alloyed interfaces showed reduced optical gain thresholds, highlighting the importance of surface/interface engineering towards CQDs for solution-processed lasers. The type of CQDs used in our laser experiments are related to the structure seen in Figure 1-16.

AR can also be removed in single-exciton gain CQDs, when the carrier-induced Stark effect is taken into consideration [92], [93]. This happens when the photoexcited single exciton state generates a local electric field which lifts the transition energy of the ground-state absorption [92], as opposed to the situation of optical transparency typically found where the stimulated emission is completely consumed by the ground-state absorption. For example, engineered type-II CdS/ZnSe core-shell CQDs with strong repulsive exciton-exciton interaction hinder absorption from singly excited CQDs and enable single-exciton gain with average exciton per CQD of $\langle N \rangle < 1$ [92].

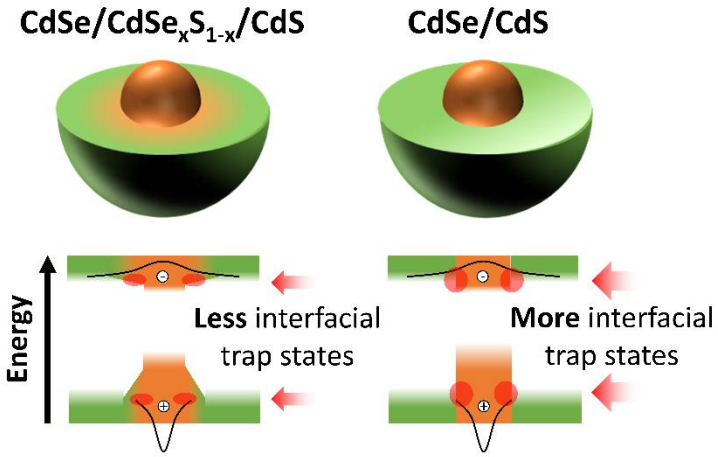

Figure 1-16. Alloyed CdSe-based CQDs (such as the example on the left) have a reduced number of interfacial trap states when compared to their abrupt core-shell counterparts (right), which contributes to the decrease of non-radiative AR [90], [91].

1.6 CQDs for laser applications

This section makes the link between discussions of optical gain in CQDs given previously and the laser threshold, and gives a summary of CQD laser structures and of the state of the art of these types of lasers. Although there are several different types of semiconductor NCs with combined emission tunability ranging from infrared (e.g.: PbS, PbSe QDs) to ultraviolet (UV), namely in the long and middle wave UV (ZnO QDs) [94], in this thesis special attention is given to CdSe-based CQDs with a tunable emission exclusively in the visible [94].

1.6.1 Colloidal nanostructures for lasing

It is worth noting that aside from CQDs, there are also other non-spherical colloidal nanostructures advantageous for lasing applications, such as NRs, NPLs and nanotetrapods (TPs). Colloidal NRs have a 2D confinement, which significantly impacts the multiexcitonic AR, leading to the prolonged optical gain duration, anisotropic optical gain and occurrence of stimulated emission from higher-order multiexcitons [77], [95]. Similarly to NRs, colloidal NPs (or colloidal quantum wells) have also a large aspect ratio, which suppresses the mutiexcitonic AR [96], [97] and are capable of functioning as favourable lasing materials [98], [99], including under continuous-wave lasing [100]. Colloidal TPs can also be exploited for photonic applications, such as providing simultaneous dual-colour emission [101]. CdSe/CdS dot-in-rod and CdSe/CdS dot-in-TP are the most representative NCs of mixed dimensionality that provide simultaneous dual-colour emission [102]–[104]. Such materials are able to serve as a light antenna, which significantly enhances the effective absorption cross-sections of the CdSe/CdS heterostructures while suppressing the reabsorption effect, therefore contributing to low-threshold stimulated emission and lasing [104]–[106].

1.6.2 Requirements for laser emission

The condition for optical gain in CQDs was discussed in 1.5.3. However, optical gain is not the only requirement to achieve laser emission. Optical gain must be combined with optical feedback, which is usually obtained with a cavity or resonator. There are several possible resonator configurations and the most common for CQD lasers are described in the next section (Figure 1-17). However, regardless of the resonator design, in order to reach the threshold for laser oscillation the overall gain for an optical mode needs to compensate the overall loss experienced by it.

A laser requires 3 main components to operate: the gain medium, in this case CQDs, which act as an amplifier for light; a pump source, to excite the gain medium; and a cavity, to provide optical feedback and promote stimulated emission [107]. To explain the optical feedback process, let us consider a simple cavity design, such as the Fabry-Perot cavity. This type of resonator uses two mirrors to create the optical cavity and when energy is given to the CQD gain medium (for example via optical pumping) some of the light emitted by the CQDs couples into the cavity modes (Figure 1-17b). The light from these modes bounces back and forth between the 2 mirrors, providing optical feedback at given resonances and promoting stimulated emission by the CQDs. Some of this light eventually escapes the cavity

through the output coupling, which can be provided by one of the mirrors with a non-unity reflectivity, or through other loss processes such as scattering or absorption.

If L corresponds to the distance between these 2 mirrors with reflectivities R_1 and R_2, α to the distributed loss and g the modal gain, the condition for laser oscillation requires a mode to repeat itself after one-round trip (Eq. 9):

$$R_1 R_2 e^{2(g-\alpha)L} \geq 1 \qquad \text{(Eq. 9)}$$

Here, the modal gain g is linked to the gain material region g_m by Eq. 10:

$$g = \Gamma . g_m \qquad \text{(Eq. 10)}$$

with Γ corresponding to the fraction of photons in the cavity interacting with the gain material region, g_m [108]. If the dependence of the gain material region on $\langle N \rangle$ is approximately the same as in bulk active layers, g_m becomes directly proportional to the population inversion (Eq. 11) [64], [109]:

$$g_m = a(\langle N \rangle - \langle N \rangle_{tr}) \quad \text{(Eq. 11)}$$

where a corresponds to the differential gain in the gain material [109]. If the mode is fully confined in the gain medium, then $\Gamma = 1$. However, in the case of CQDs, the fraction of the CQDs also needs to be considered as CQD cannot occupy all the space. This leads to $\Gamma < 1$. For highly packed CQDs, one can expect $\Gamma \approx 0.7$ or lower depending on the packing fraction and the nature and size of the ligands [110].

The material (CQD) gain at threshold is given by Eq. 12:

$$g_m = \frac{1}{\Gamma}\left[\frac{1}{2L} ln\left(\frac{1}{R_1 R_2}\right) + \alpha\right] \qquad \text{(Eq. 12)}$$

And from Eq. 11 and 12, the population inversion necessary for laser threshold is then given by (Eq. 13):

$$\langle N \rangle - \langle N \rangle_{tr} = \frac{1}{\Gamma a}\left[\frac{1}{2L} ln\left(\frac{1}{R_1 R_2}\right) + \alpha\right] \qquad \text{(Eq. 13)}$$

As the cavity will never be perfect (the reflectivities will be lower than 1 and α is non zero), the laser threshold happens at a higher value of $\langle N \rangle$ than for transparency.

1.6.3 Resonator configurations of CQD lasers

Unlike EQDs, CQDs have no substrate requirements and their solution processibility makes them compatible with almost all types of cavity structures. Typical laser cavities include Fabry-Perot cavities [111], microring resonators [112], vertical cavities implemented with distributed Bragg reflectors [98], [111], [113], distributed feedback cavities (DFB) [114], [115] and cavities that benefit from whispering gallery mode (WGM) optical feedback, such as microsphere [116]–[118], cylindrical [119], [120] or toroidal [121] cavities. WGMs in microspheres can be tuned to have single or multimode lasing [65], [118], [122]. CQD liquid droplets can also act as WGM laser cavities when levitated [123]. WGM lasers allow evanescence pumping with tapered optical fibres for efficient in-coupling and out-coupling of the pumping and emitting light – an interesting feature for integrated laser systems [117]. Close-packed CQD films can achieve random lasing by introducing suitable scattering centers [124]–[126]. Photonic crystals can also be used as cavities in CQD-based nanolasers, which benefit from low gain thresholds and enhanced spontaneous emission coupling into the cavity mode by Purcell effect [127].

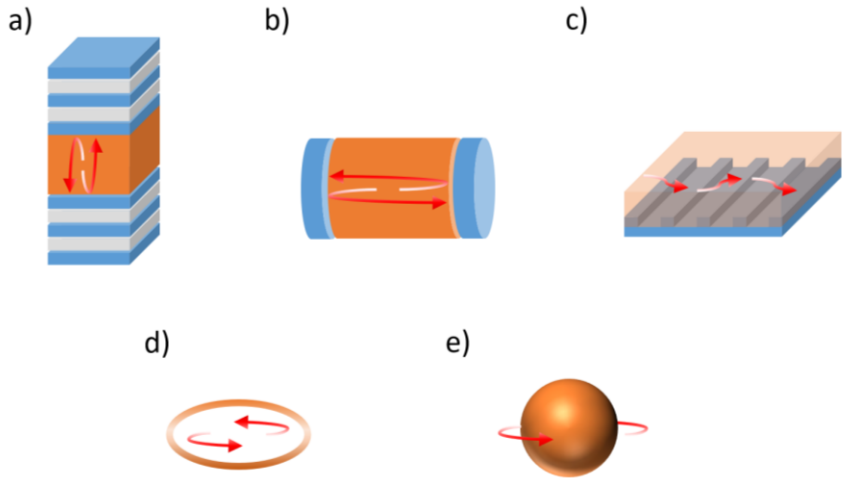

Figure 1-17. Different types of NC laser geometries: (a) vertical cavities implemented with distributed Bragg reflectors [98]*, (b) Fabry-Perot cavities* [111]*, (c) distributed feedback cavities* [114]*, (d) microring resonators* [112]*, and (e) microsphere cavities where dielectric spheres are doped or coated with NCs* [116], [117].

1.6.4 Types of Lasing in CQDs

The CQD lasers described above emit either in a single or multi-mode, and most are optically pumped by a pulsed laser source. These pulsed laser sources can have different pump pulse durations, ranging from a few nanoseconds to several femtoseconds, which in turn can impact the laser emission threshold of CQD lasers. Figure 1-18 compiles the laser threshold fluence for CdSe-based CQD lasers of different configurations in the state of art, according to the pump pulse duration. Table 1-1 summarises the details of each reference used in Figure 1-18.

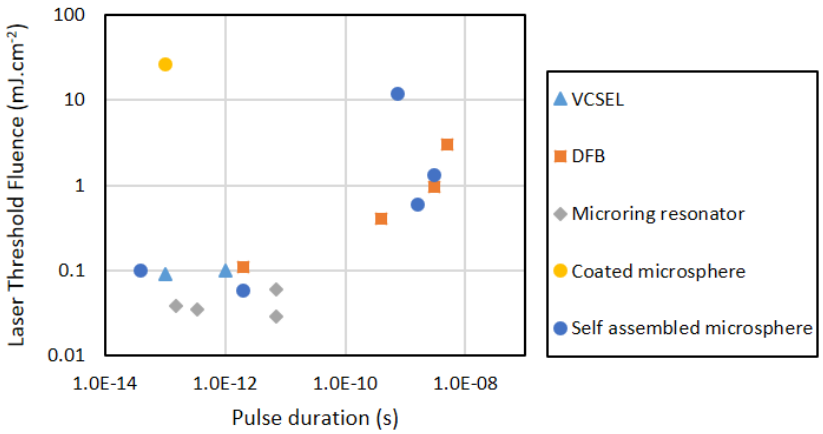

Figure 1-18. Laser cavities based on CdSe CQDs and respective pump fluences at laser threshold as a function of the pump pulse duration. The references used in this figure can be found on Table 1-1.

Although there are several different factors that can impact the threshold fluence (e.g.: emission of the CQD, Quality factor of the laser cavity, repetition rate of the pump, wavelength of the pump, density of CQDs, etc.), the pulse duration of pulsed laser sources has a major impact on the required fluence to achieve lasing emission: the longer the pulse is, the higher the laser threshold will be. Pulsed laser sources are necessary for this type of device to mitigate the effect of the slow optical gain lifetime limited by the fast AR in CQDs [4]. This mitigation occurs because for a given intensity, a pulsed laser source will deliver periodic but strong bursts of energy that will generate more excitons than a weak but continuous wave laser source.

Nevertheless, the realization of other forms of lasing could also be beneficial for practical applications in various fields [17].

Table 1-1. Reference details of Figure 1-18.

Cavity Type	Pulse Duration (s)	Pump Repetition Rate (s^{-1})	Threshold Fluence ($mJ.cm^{-2}$)	Reference
VCSEL	1.00E-13	1.00E+05	9.00E-02	[128]
	1.00E-12	4.90E+06	1.00E-01	[129]
DFB	2.00E-12	4.90E+06	0.108	[83]
	5.00E-09	1.00E+01	3.00E+00	[130]
	4.00E-10	1.00E+03	4.00E-01	[131]
	3.00E-09	1.00E+01	9.52E-01	[132]
Microring resonator	7.00E-12	2.00E+02	2.90E-02	[133]
	7.00E-12	1.00E+02	6.00E-02	[134]
	1.50E-13	1.00E+03	3.87E-02	[135]
	3.40E-13	1.00E+04	3.50E-02	[112]
Coated microsphere	1.00E-13	1.00E+03	2.60E+01	[136]
Self-assembled microsphere	2.00E-12	1.00E+03	0.058	[118]
	3.00E-09	20	1.3	[122]
	4.00E-14	1.00E+04	1.00E-01	[65]
	7.60E-10	7.10E+03	1.20E+01	[31]
	1.60E-09	1.00E+04	6.00E-01	[137]

Continuous-wave (CW) lasing on CdSe CQDs has been realized by decreasing the level degeneracy using strain. The strain engineering, which had already been shown to reduce pump threshold in epitaxial quantum well lasers [138]–[140], was employed by growing asymmetric compressive shells on CdSe cores so that the splitting of the band-edge states can be larger than the thermal energy and introduce biaxial strain [140]. This decreases the effective level degeneracy of the CQDs and consequently the optical gain threshold. Optically pumped CW lasing was achieved by coating these biaxially strained CQDs onto a 2D-DFB optical cavity.

Electrically pumped CQD lasers present even more challenges. Since optical gain is originated from the multiexciton states due to the double degeneracy of the band-edge level, Auger recombination is more likely to occur in electrically pumping due to the 1-by-1 carrier injection into CQDs [4], [141]–[143]. Organic ligands of CQDs also exhibit poor electrical conductivity, acting as an insulating layer around the CQDs and hindering the carrier injection and transportation [142], [143]. Even if electric current could be properly injected into CQDs, the flowing current necessary for population inversion in CQDs would probably overheat and damage the laser device [144]. A first step has been taken towards electrically pumped CQD

lasers by achieving optical gain in CQDs under electrical pumping [145], [146]. Alloyed core-shell CdSe/$Cd_xZn_{1-x}Se$/$ZnSe_{0.5}S_{0.5}$ CQDs with extremely long biexciton Auger lifetimes (2.4 ns) have shown optical gain when pumped electrically when used in a p-i-n architecture with optimized organic/inorganic charge transport layers and an insulating spacer for heat dissipation [145]. Following on from that, devices using CQDs with very similar structures (CdSe/$Cd_xZn_{1-x}Se$/$ZnSe_{0.5}S_{0.5}$/ZnS) have been reported to operate as LEDs if pumped electrically, or as lasers if pumped optically [146]. Nevertheless, the implementation of such architecture in a cavity to provide the optical feedback and lasing by electrical means is yet to be researched [55].

Multi-photon pumped QCD lasers are also an interesting type of laser as they use absorption of several photons with sub-band gap energy for optical gain and lasing action [17]. Here, the pump photons have longer wavelengths (infrared range) and exhibit a super-linear dependence of absorption on incident power, which results in a larger penetration depth into samples and a higher spatial resolution [17], [147].

1.7 All-inorganic perovskite NCs for lasing applications

Unlike other CQDs, the all-inorganic ceasium lead halide NCs do not need the additional shell coating to ensure a high ratio of photons emitted over photons absorbed, or PLQY [43], [148], [149]. In addition to that, perovskite NCs also exhibit better optical properties in the blue-green spectral regime than CdSe-based CQDs, as unlike CdSe CQDs they do not suffer from photodegradation and poor PLQY in that short visible wavelength range [17], [150], [151], and their large absorption cross-section, suppressed reabsorption due to the large biexciton binding energy and high PLQY confer them low-threshold stimulated emission in pulsed regimes [45], [152]. Moreover, stimulated emission and lasing in perovskite NCs can be easily tuned between blue, green, and red colours [45], [153]. Similarly to CQDs, many resonator configurations in Section 2.2.5 have also been demonstrated with perovskite NCs, such as cylindrical WGM resonators [45], spherical resonators [154] and distributed Bragg reflectors for vertical cavity surface emitting lasers (VCSELs) [155]. However, despite the advantages stated above, $CsPbX_3$ NCs continue to have much faster AR rates than CdSe-based heterostructures, which makes them unfavourable for applications in long pulse duration and continuous wave mode lasing [17], [156]. Moreover, they suffer from relatively poor stability against moisture and heat [157].

1.8 Self-assembly of Nanocrystals

Self-assembly of CQDs was here exploited to fabricate a new type of microsphere lasers, as will be reported and discussed in Chapters 2-5. Therefore, some background on the physics of self-assembly of NCs are presented in the following sections.

Self-assembly is a bottom-up process where individual components rearrange into an ordered structure by themselves [158]. Self-assembly of nanosized objects allow the fabrication of higher level structures, with the nano-objects playing the role of "bricks", at micro- and nano-scales that would otherwise be much more difficult to fabricate with top-down techniques, such as electron beam lithography or dip-pen nanolithography [158], [159]. In addition to that, self-assembly processes are carried out with equipment of much lower complexity when compared to the aforementioned top-down techniques [158].

1.8.1 Preparation of nanocrystal superlattices

Ordered structures of colloidal NCs are prepared mainly via three different processes, namely: solvent evaporation (Figure 1-19), gravitational sedimentation (Figure 1-20) and solvent destabilization (Figure 1-21) [158]. Evaporation-based assembly is usually employed to self-assemble superlattice thin films. Here, particles begin nucleation at the late stages of solvent drying and the amount of excess surfactant offers a degree of control over the thickness of the superlattice [158]. Destabilization-based assembly exploits attractive interactions between NCs when solvent intermingling in NC capping layers becomes less favourable than overlap of ligands between neighbouring NCs. This is done by adding an interface of nonsolvent to the solution, where destabilization can happen by nonsolvent diffusion or nonsolvent enrichment, both promoting gradual clustering of NCs in solution. Another way of creating destabilization is by adding small, noninteracting cosolutes to the solution that act as depletants. In these so called entropic destabilizations, the cosolutes are preferentially excluded from the vicinity of the large colloidal NCs, causing an attractive depletion force that pushes NCs together. The third and last process here introduced, gravitational sedimentation, is used in large or dense NCs where crowding-induced self-assembly can occur via sedimentation in the bottom of solvent [158].

In addition to these processes, there are several other factors that can impact the ordering of NC superlattices, such as choices of solvent, temperature, and shapes of NCs and substrates [158].

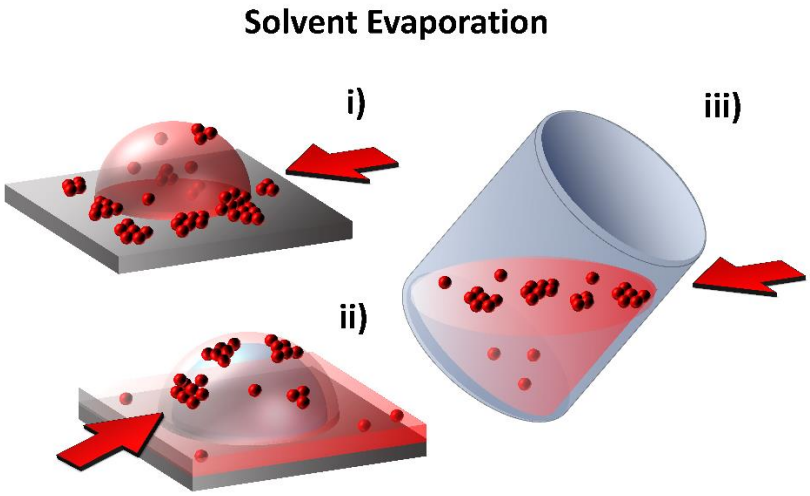

Figure 1-19. Preparation of NC superlattices by solvent evaporation using different techniques, such as drop casting on a solid substrate (i), evaporating over a polar liquid (ii) or evaporating from a tilted vial (iii).

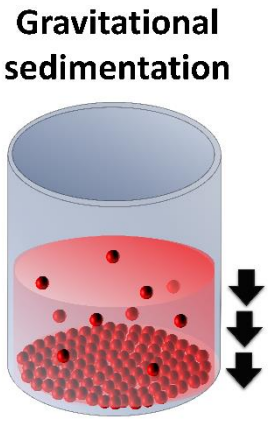

Figure 1-20. Preparation of NC superlattices by gravitational sedimentation. This can be used in large and dense NCs, which is when gravity predominates over thermal motion.

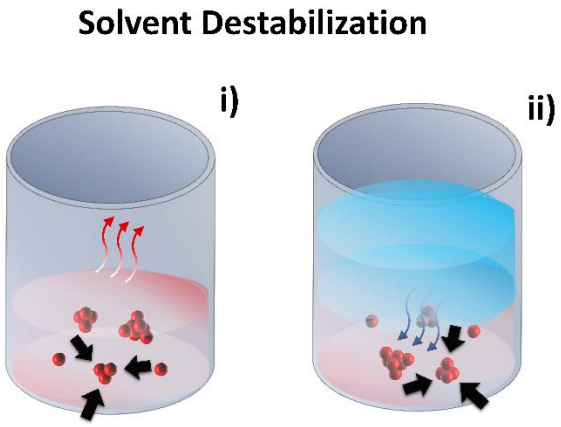

Figure 1-21. Preparation of NC superlattices by solvent destabilization using different techniques, such as non-solvent enrichment (i) and non-solvent diffusion (ii).

The syntheses of microspheres in this thesis use a combination of solvent evaporation and solvent destabilization, where the non-solvent enrichment (CQDs) caused by the slow evaporation of solvent in an oil-in-water emulsion leads to the self-assembly of CQD supraparticles. The full self-assembly process is described in Chapter 2.

1.8.2 Nanocrystal interactions and thermodynamics

During self-assembly, it is important to consider the various contributions to the NC–NC interactions to better understand and control the process. These interactions include van der Waals forces between inorganic cores and surface ligands as well as via osmotic, electrostatic, and elastic contributions [158].

During evaporation, colloidal NC solutions remain in the dispersed state as long as the pair potential $U(r)$ at interparticle separation distance r is dominantly repulsive (Figure 1-22, top). This happens because molecular chains (e.g. hydrocarbon surfactants, neutral polymers, ionic ligands) tethered to the NC surface can enable steric and/or electrostatic stabilization of NCs according to the solvent and application [160]. The forces acting on the particles, $F_{U(r)}$, and pair potential are related through the following expression: $F_{U(r)} = \frac{\mathrm{dU(r)}}{\mathrm{dr}}$. From this relationship, it can also be seen that the shorter the distance between two particles, the more negative the slope in the pair potential is and the stronger the forces repelling these two particles from each other will be.

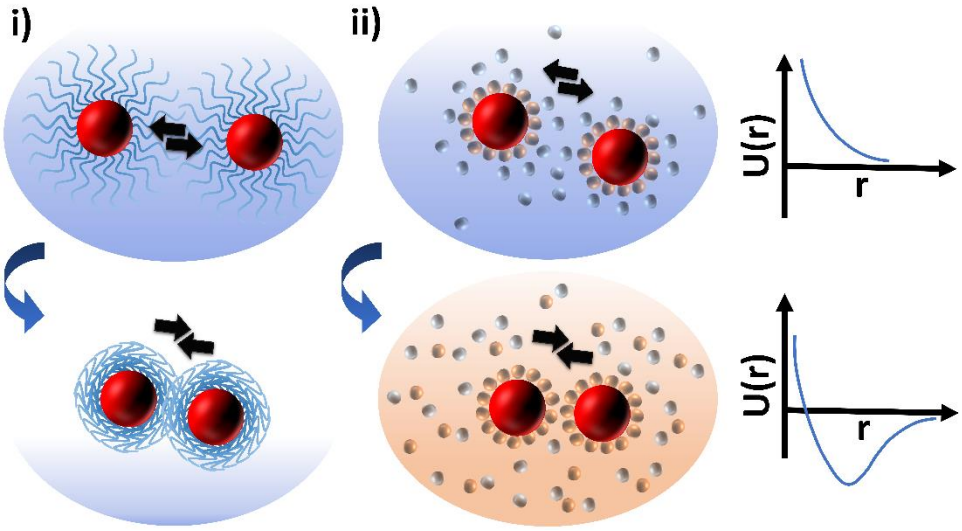

Figure 1-22. Sketch of a pair of interacting NCs with neutral (i) and ionic (ii) surface ligands. The top illustrations show the NCs sterically stabilized, together with the exclusively repulsive pair interaction potential U at interparticle separation distance r for NCs. The bottom illustrations demonstrate examples of destabilization by solvent evaporation (i) and solvent diffusion (ii), which lead to changes in the pair potential U and consequent aggregation of NCs [158], [161].

Without the presence of ligands on colloidal NCs, the van der Waals interaction between inorganic cores is typically attractive. Intermolecular forces of such interaction come from transient fluctuations in the distribution of electrons and usually favour flocculation of the colloid (Figure 1-22, bottom). To prevent aggregation in apolar solvents, surface ligands such as hydrocarbons are typically used. The osmotic and elastic repulsion between chains in solvent form the basis of steric stabilization, where van der Waals attraction forces are screened by the ligand elastic repulsions upon compression [158]. In a similar fashion, ionic ligands are used to prevent NCs from aggregating in polar solvents by adsorbing charged species. The adsorbed charged species gives rise to osmotic pressure between surfaces of neighbour NCs and prevents them from aggregating, leading to electrostatically stabilized colloids [158].

Destabilizations of the colloid favourable to aggregation of NCs (e.g. via removal of solvent, reduction of solvent quality via nonsolvent addition or cooling the solution, and desorption or crosslinking of capping ligands) cause a drop in the pair potential that was shielding NCs. Two particles affected this way will be attracted to each other if the slope is positive and repelled if the slope is negative. This causes them to aggregate at an interparticle distance corresponding to the minimum of the potential if this minimum far exceeds the characteristic thermal energy of the system [158]. The higher the magnitude of the slope is, the higher the speed of the destabilization and aggregation will be and the more defects the superlattice structure will have [162], [163]. Low defect superlattices are more likely to occur under destabilizations near equilibrium conditions, where self-assembly occurs at a slow pace [164].

The aggregation of NCs into a superlattice is a phase transition that proceeds via nucleation and growth. Regarding the nucleation process, it can be homogeneous if it takes place in solution and the nucleus is approximately a sphere, the geometry with the lowest surface energy. Such process requires overcoming a Gibbs free energy nucleation barrier. The Gibbs free energy corresponds to the work done or received by the system to its surroundings, minus the work of the pressure forces. To overcome the nucleation barrier, this transient state between the initial (non-aggregated) and final (aggregated) states needs to receive external work, which can be provided by inducing the processes in Figure 1-19, Figure 1-20 and Figure 1-21. Reducing solvent quality by adding impurities or other interfaces turns the

nucleation heterogeneous. These changes lower the nucleation barrier and increase the nucleation rate [158].

While the considerations mentioned above give a general idea of the various factors governing NC self-assembly, other factors might be present depending on the chemistry of the system and the experimental setup [165]–[167].

1.8.3 Shape of the self-assembled structures

Under thermodynamic control, supraparticles (SPs) adopt an equilibrium structure that exhibits a minimized Gibbs free energy (G) defined as $G = G_b + S.\gamma$, where G_b is the bulk Gibbs free energy and S and γ are the surface area and surface tension of the SP, respectively [168]. The surface tension is a positive term determined by the repulsive solvophobic interactions between the SP and the surrounding molecules, whereas the bulk Gibbs free energy is a negative term determined by interparticle interactions between neighboring NCs, such as van der Waals interactions between their inorganic cores and interactions between their surface ligands [168]. Here, the balance between the bulk and surface free energy terms in minimizing the overall Gibbs free energy dictates the equilibrium shape of SPs [168]. The SPs made of CQDs in Chapters 4, 6 and 7 adopt a close-packed superlattice structure to minimize the bulk free energy and a spherical shape to minimize the surface free energy. However, SPs could potentially be tuned into other shapes by varying the values of G_b, γ,and S. This can be done for example by changing the shape of the NC, type of non-solvent and shape of the emulsion, respectively [158], [168].

1.9 NC-based colour converter for Visible Light Communications

In Sections 1.6 and 1.7, the applications of CQDs as laser materials was discussed. Another application of CQDs is as colour converters. In such cases, they are used (typically in the spontaneous emission regime) in conjunction with a pump light source (e.g. shorter wavelength LEDs or micro-LEDs, laser diodes), absorbing light from this pump source and re-emitting the energy as luminescence in a process termed downconversion (upconversion is not discussed here), for applications such as displays, lighting and illumination, and VLC [169], [170]. The study of a perovskite QD-based color-converters is reported in Chapter 5. To place this into context, we give below some information on colour conversion and VLC.

Regarding VLC, CQDs are attractive alternatives to the rare-earth and transition metal phosphors used in commercial display and lighting technologies as their enhanced density of states and electron/hole wavefunction overlap [13] contribute to narrower emission linewidths and faster dynamics [22], [171]–[174].

VLC is typically implemented using high-speed optical modulation LEDs and received using photodiodes (PDs) [175]. VLC systems only allow real-valued and positive signals for data modulation because of the incoherent light output of the LED, which limits the usage of several data modulation protocols [175]. To achieve high-speed data transmission in VLC, optical orthogonal frequency division multiplexing (O-OFDM) is often used. Common O-OFDM schemes include DC-biased optical OFDM (DCO-OFDM), asymmetrically clipped optical OFDM (ACO-OFDM), non-DC- biased OFDM (NDC-OFDM) and unipolar OFDM (U-OFDM) [175]. The choice of protocol and setup, as well as the distance between transmitter and receiver play a role in the data transmission speed [175], [176]

1.9.1 Time dynamics of colour conversion

Gallium nitride (GaN) based light emitting diodes (LEDs) and micro-LEDs have been replacing traditional incandescent or fluorescent lamps due to their more robust, efficient and spectrally defined output of UV and visible light [177], [178].

In particular, micro-LEDs have lateral dimensions lower than 100μm and can be arranged in arrays with densities up to many hundreds of pixels per inch [178]. In addition to that, unlike more conventional LEDs, the bandwidth of micro-LEDs is not RC-limited due to their small area. Instead, the limiting factor is the carrier lifetime, τ, which corresponds to the average time it takes for electrical carriers injected into the device to recombine [178]. Thanks to that, optical modulation bandwidths around a GHz have been reported for micro-LEDs [21], [179], which are up to 3 orders of magnitude faster than standard broad area LEDs [178]. These factors make micro-LEDs especially attractive in VLC to help meet the rapid increase in wireless data traffic [180].

InGaN-based LEDs can in principle emit in the UV, visible and near infrared by changing the alloy composition. However, in practice they are the most efficient in the blue-violet and have reduced emission efficiencies at longer wavelengths. On the other hand, red emitting LEDs, which are typically based on the AlInGaP alloy, have their efficiency significantly

reduced for wavelengths near and below 600 nm. This means there is a 'yellow-green gap' around 560 nm where there is currently no efficient LED. The same is true for laser diodes (LDs). The emission of LEDs is also single wavelength due to the fabrication process, which is done by growing the LED structure, including the active quantum well structure region, on a single wafer [178], [181]. Therefore, when used in lighting and digital lighting applications, efficient blue or UV GaN LEDs and LDs are often combined with colour converters in order to emit light at different wavelengths in the visible, or to produce white light [22].

The standard approach uses a UV or blue LED chip to photo-pump the colour converting material, which absorbs the LED photons and re-emits at longer wavelengths. In turn, the colour converting material enables emission across the visible spectrum [181].

Figure 1-23 demonstrates the colour conversion concept for VLC, where a µLED is modulated to carry a signal (represented by 1 and 0 in the schematic) and the modulated light is absorbed and reemitted at a longer wavelength by the colour converter (CC) material [181]. Practical implementation of colour conversion with µLEDs intended for VLC has already been demonstrated [170]. Moreover, CC composites can be designed with a wide array of characteristics for this purpose [22].

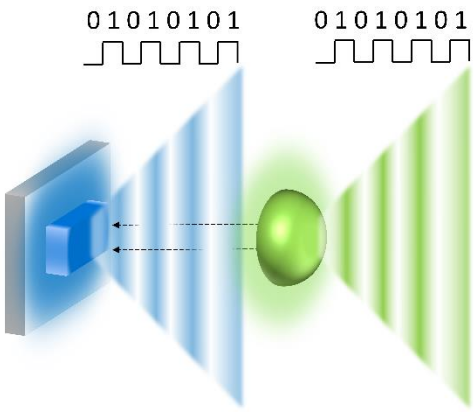

Figure 1-23. Principle of time-dependent color conversion, where data encoded through modulation of a source is transferred to another wavelength via a color converter [181]*. Here, a blue LED is schematically shown to be down converted to green emission.*

One aspect to take into consideration while implementing CCs for VLC is their time dynamics. Colour conversion requires excitation of the CC material, which in this case is done by

absorbing the micro-LED light and generating, for QDs, electron-hole pairs (excitons). This step is then followed by radiative emission of the CC material, where excitons decay through spontaneous emission at the designated wavelength [181]. The time dynamics are therefore set by the rate of radiative transition between the lowest excited state and the ground state of the colour-converting material. The longer the excited state lifetime is, the longer the CC material takes to go through spontaneous emission. This in turn impacts the maximum response time of CCs without loss of information, hereby defined as the frequency for which the modulated part of the optical power drops to half its DC value, or bandwidth (BW). The relation between the BW of the CC and its luminescence lifetime (τ) is given by $BW = \frac{\sqrt{3}}{2\pi\tau}$ [157], [182].

CCs for VLC applications should therefore ideally combine a short luminescence lifetime and a high efficiency [22], [157]. Furthermore, a narrow emission linewidth could also enable wavelength division multiplexing (WDM) in VLC [22], [183]. Reabsorption in any CC material where the intrinsic emission overlaps the absorption [184], [185] should also be taken into consideration, as it lengthens the effective luminescence lifetime of the medium and therefore decreases the BW. Colour converted micro-LEDs devices using phosphors are limited by the BW of phosphors, which are at least 3 orders of magnitude lower than the ones of micro-LEDs [23]. For this motive, faster CCs are worth being explored. There are several types of such colour converters currently under research (e.g. Inorganic semiconductors, organic semiconductors, epitaxial quantum well NPLs) [181]. In this thesis, particular attention is given to one type of inorganic semiconductors, all-inorganic metal halide perovskite NCs (Chapter 5) although background on Cd-based CQDs for VLC is also summarized below for completeness.

1.9.2 All-inorganic perovskite NCs for VLC

All-inorganic metal halide perovskite CQDs have been demonstrated as colour converters for VLC [49], [150], [172], [173] and have the fastest known luminescence dynamics among CQDs [186]. However, they present some disadvantages such as limited thermal and moisture stability, even though several approaches have been explored to mitigate these issues [187]. With such CQDs, bandwidths around 85MHz can attained for white-light sources combining a micro-LED and yellow-emitting $CsPbBr_{1.8}I_{1.2}$ perovskite CQDs (blended in resin), achieving

VLC links of 300Mb/s [173]. $CsPbBr_3$-in-Cs_4PbBr_6 crystals consisting of $CsPbBr_3$ QDs formed within a Cs_4PbBr_6 matrix (see Section 1.2.2 and Chapter 5 for more details), have been shown to improve thermal stability significantly and demonstrated as a laser gain material [188]. Such crystals have also been studied as fast CCs emitting in the green (520 nm) for VLC [49]. Their optical properties were studied at different pump power density regimes (from 0.7 mW/cm^2 to 7.15 kW/cm^2) using either micro-LEDs or LDs. Bandwidths between 22 MHz (average lifetime of 13 ns) and 41MHz (average lifetime of 7 ns) were achieved for pump densities of 3 W/cm^2 and 7 kW/cm^2, respectively. The corresponding VCL links (DCO-OFDM) achieved data rates of 380-560 Mb/s for the CCs alone, and 1.14 and 1.5 Gb/s for both pump light and colour converted light. Such speeds match those of organic semiconductors [189], which have the faster dynamics in general, while keeping the typical absorption spectra and narrow emission wavelength characteristic of CQDs [181].

1.9.3 CQDs for VLC

Core-shell CQDs have excited electrons and holes confined mainly in the core of the NCs and fast dynamics due to the strong electron-hole spatial overlap. Because of that and the high luminescence efficiency with a narrow emission spectrum [186], they are among the most suitable CQDs for VLC.

These NCs can be designed to emit at a certain wavelength, within a broad wavelength spectrum ranging from UV to mid infrared [186]. They also have a broad and efficient absorption in the emission spectrum of GaN micro-LEDs and LDs (UV and blue wavelengths). Moreover, their solution processability allows for a flexible integration in different setups [22], [170].

In the visible spectrum, the expected radiative lifetimes and BW for metal-halide, Cd-based CQDs range from ones to tens of ns and 10 to 100MHz, respectively [181]. Reports regarding data transmission rates using VCL links (OFDM modulation protocol) for these NCs show values between 300 and 600Mb/s for the colour-converted light alone [170], which are close to those discussed in Section 2.3.

Current results show that CQDs also have potential as colour converters for VLC. They have data transmission rates close to Gb/s and their tuneability, stability and solution

processability allows further applications in WDM and micro-scale integration using a vast array of fabrication techniques [169], [190]–[193].

1.10 Summary

This chapter has given an overview of the fundamentals of NCs – in particular CdSe-based CQDs and all-inorganic ceasium lead halide perovskite NCs – and has highlighted their properties for laser applications, self-assembly into superlattices, and for colour-converting technology applied to micro-LED based VLC. The topics above provide a theoretical background for the research presented on the remaining chapters of this thesis.

Part II

Results

Chapter 2. Self-Assembly of Semiconductor Nanocrystals for Lasers

In this chapter, colloidal semiconductor quantum dots are self-assembled into micron-scale spherical supraparticles (SPs) that act as both the gain medium and the optical cavity of miniature lasers. These microlasers promise exciting applications in sensing and integrated photonics and are also attractive for studying laser physics at small dimensions. The chapter reports on the concept, fabrication and characterization of these lasers, including an analysis to extract the average exciton numbers per NC at threshold under optical pumping.

2.1 Introduction

As discussed in Chapter 1, colloidal semiconductor NCs are known for their size-tunable electronic and optical properties, discrete density of states, and low temperature solution processing [35], [194]–[196], which make them very attractive as the gain medium of lasers [17]. Additionally, NCs can be used in many different material platforms and have great prospects for integrated optics applications [197]. Several different NC laser geometries have been reported, e.g. Fabry-Perot cavities [111], microring resonators [112], vertical cavities implemented with distributed Bragg reflectors [98], distributed feedback cavities [114], and microsphere cavities where dielectric spheres are doped or coated with NCs [116], [117]. These examples can be found in Figure 1-17 (Chapter 1).

However, while the field of NC lasers has made tremendous progress, NCs have so far been used almost exclusively as the gain material. Fabrication of laser devices still requires top-down patterning of the NCs at a sub-micron level (e.g. using photo or contact lithography), or a way to combine NCs with an optical microcavity that is fabricated separately. Designing such devices becomes challenging when approaching the micro or nanometre scale, as it is difficult to keep a low level of defects especially on complex devices.

An elegant alternative is to use the bottom-up self-assembly of NCs into SPs the form of microspheres with a crystalline structure [118]. Due to the high refractive index of semiconductor NCs and of the sphericity of the self-assembled structure, a SP can form whispering gallery mode (WGM) cavities [118] and efficiently trap light. Because SPs consist of NCs that can work as an optical gain material when optically excited, SPs are by themselves miniature laser sources. Note that such lasers were reported first in [118] but in this work, another initial demonstration had been independently made in our laboratory around the same time.

In contrast to the standard approach where NCs are coated onto, or use as dopants within microspheres made of another material and fabricated separately, SPs are both the gain material and the cavity; the fabrication is therefore simplified [118]. The self-assembly of SPs is based on an oil-in-water emulsion technique, where one of the phases contains CQDs diluted in a non-polar solvent and the other contains water and a surfactant acting as emulsifier. The nucleation and quality of the SP can be controlled with temperature, solvent selection, and interfacial tension between the two phases according to the requirements [198]. Polydispersity can also be precisely controlled depending on the application. While the dispersity of macro-processed syntheses can go as low as 22% - 13%, it can be further lowered to approximately 5% with the help of microfluidics [118].

SPs made of CdSe/CdS CQDs have been reported with quality factors (Q-factors) up to 320 [118]. Their lasing oscillation under optical pumping is evidenced by a clear threshold behaviour, coherent emission and emission lifetime shortening due to the stimulated emission process. In that report, experiments used a frequency – doubled regenerative amplifier seeded by a mode-locked Ti: sapphire laser (with laser pulses of 100−200 fs at a repetition rate of 1 kHz and a spot size of 10 μm at FWHM) to enable laser emission from their CdSe/CdS microspheres at threshold fluences of approximately 100 $\mu J/cm^2$ [118]. SPs have also exhibited a predominantly linear polarization [118] and enhanced resonant optical behaviour resulting in an increase in absorption efficiency in the visible range by more than 2 orders of magnitude when compared to dispersed quantum dots [14]. Enhanced excitonic coupling has been observed in ligand-exchanged SPs which leads to the formation of a free biexciton system on sub-picosecond time scales [32]. More recently, single-mode laser emission has also been reported on compact microspheres with diameters between 1.5 to 5 μm, via ligand exchange, and tested in vitro and in vivo [122]. In addition to that, the photon-

stimulated amplification process in these microspheres can be simulated with precision by the rate equations [65].

While SPs combine the advantages of microsize and simple, potentially low-cost, fabrication, some laser parameters are challenging to extract, at least under free space optical excitation. This is particularly true for the average number of excitons $\langle N \rangle$ per QD in the microlaser as a function of the pump intensity. The average number of excitons is a parameter that relates to the population inversion (see Chapter 1) within the SP and knowing its value at threshold is important for comparing the performance of microlasers post-fabrication and before utilization. It is difficult to determine the pump power coupled into and absorbed by the microsphere, and therefore $\langle N \rangle$, due to scattering and a non-homogeneous pump profile.

In the following sections, and after explaining the concept of WGM and describing the experimental methods, SPs made of CdS_xSe_{1-x}/ZnS CQDs and ranging approximately between 4 and 20 μm in diameter are studied individually according to their size, with their below threshold emission intensities modelled to a Poissonian function in order to extract $\langle N \rangle$ at different excitation levels. Laser emission (above threshold) for SPs of different sizes is also presented and discussed. SPs reported in this chapter had similar Q-factors to those reported in [118]. In Chapter 3 the SP properties are further explored by selecting their building blocks for laser oscillation at several wavelengths simultaneously [30] and to increase their Q-factor [31].

2.2 Characterization of Quantum Dots

SPs synthesized in this work used cadmium selenide sulfide (Core) zinc sulfide (Shell) Trilite™ fluorescent QDs, with alkyl ligands. These QDs were ordered from Cytodiagnostics (Cytodiagnostics, Canada). The average diameter of these QDs ranged between 5.5 and 6.5 nm. The corresponding absorption and emission spectra (in solution) can be seen in Figure 2-1 and Figure 2-2, respectively. The emission peak is located at 630 ± 5 nm and the PL has a full width at half maximum (FWHM) of 30-40 nm. The Stokes shift is between 10 and 15 nm.

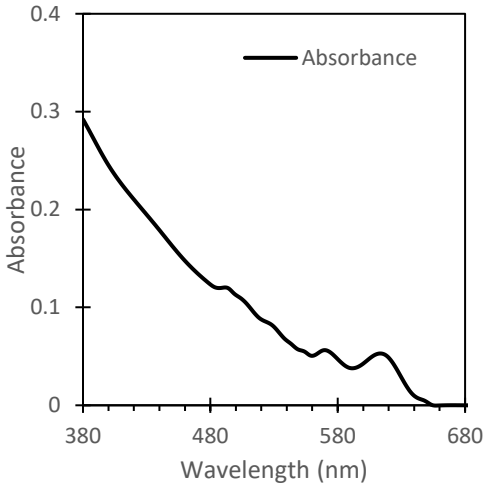

Figure 2-1. Absorbance spectrum of the used commercial NCs.

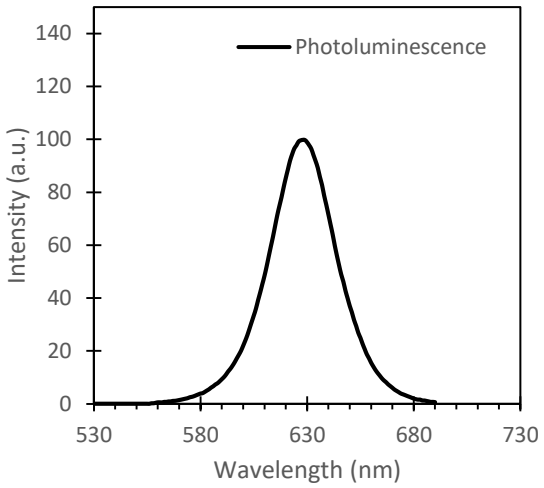

Figure 2-2. PL spectrum of the used commercial NCs. Emission peak is measured at 628.1 nm. FWHM is approximately 37.9 nm.

2.3 Microsphere resonators and Whispering Gallery Modes

SPs in this work operate as microsphere lasers because CQDs provide optical gain and the spherical shape acts as a WGM resonator. The concept and basic theory of WGM is introduced in this section.

WGMs are associated with electromagnetic oscillations in a spherical, disk or ring-shaped optical cavity. These modes correspond to the closed trajectory rays trapped in the cavity by almost total internal reflection. In case of constructive interference, a WGM is formed and creates the feedback loop required for lasing applications at the WGM resonance.

The damping of these modes depends on the surface roughness and internal absorption. The Q-factor, defined as $Q = \lambda/\Delta\lambda$, is the dimensionless parameter that characterizes this damping and corresponds to the ratio of a resonator's centre wavelength to its bandwidth when subject to an oscillating driving force. The higher the Q-factor is the lower the losses in the resonator are.

Figure 2-3 illustrates how a ray striking the surface at near glancing incidence ($\theta_i \approx \pi/2$) can propagate inside a spherical resonator. Assuming that the dielectric sphere has a refractive index N, radius r >> photon wavelength λ, and is in vacuum, if the ray hits the surface with an angle of incidence $\theta_i > \theta_c = arcsin(1/N)$, total internal reflection (TIR) occurs.

Due to the spherical symmetry, all subsequent angles of incidence are the same, and the ray is trapped. In the near glancing incidence scenario, the trapped ray will propagate close to the surface of the sphere and take a path γ similar to the equatorial line of the sphere, which corresponds to $\gamma \approx 2\pi r$ for a round trip. When constructive interference occurs, this round trip also corresponds to a multiple of the ray's wavelength in the medium, $\gamma \approx l\lambda$, which is to say, $\frac{2\pi r}{\lambda} \approx \frac{l}{N}$. The number of wavelengths, l, can be identified as quantum number of the angular momentum of the ray, as the angular momentum L is denoted as $\mathrm{L} \approx rp = \frac{2\pi r\hbar N}{\lambda} = \hbar l$, where the linear momentum is $p = \hbar k = \frac{2\pi\hbar N}{\lambda}$, and k is the wave number [199].

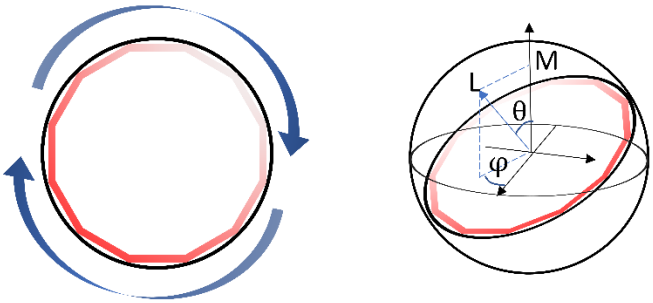

Figure 2-3. Ray of light propagation by TIR in a spherical cavity. (left) and angular momentum L associated with WGM and its M projection on the polar axis (right).

The pseudo-Free Spectral Range (pseudo-FSR) of spherical resonators can be deduced from Lorentz-Mie theory to a first approximation as $\Delta\nu_{n,l}^{\Delta l} \approx \frac{c}{2\pi Nr}$, where *c* is the speed of light in vacuum, *N* is the refractive index and *r* is the radius of the sphere [199]. The FSR corresponds to the spacing between two modes with the same polarization and with the same n, only differing by one unit in their quantum number l. Here, the principal quantum number n corresponds to the radial index ($n \in \mathbb{N}$), the mode number l indicates the order of the spherical harmonic that describes the angular momentum field distribution ($0 \leq l \leq n-1$, represented by L in Figure 2-3) and the index m is the azimuthal mode number, which is given by the projection of the angular momentum on the polar axis ($-l \leq m \leq l$, represented by M in Figure 2-3).

The Lorentz-Mie theory can also be used to calculate the absorption, reflection and extinction coefficients of spherical resonators [200], which follow the same trend as SPs of CdSe-based QDs [32], and the volume computation of WGMs in microspheres [201].

2.4 Synthesis of Quantum Dot Microspheres

The self-assembly of SPs followed an oil-in-water emulsion prepared at room temperature. The oil phase solution, with a total volume of 115 µl, was prepared by redispersing QDs in a compatible solvent that is also immiscible in water (e.g. chloroform or toluene) at a concentration of approximately 250 mg/ml. This process is done under the fume cupboard for safety reasons, and a 2ml glass vial was used for the purpose. The final concentration of QD solution can be prepared in one of two ways: solvent evaporation or precipitation of QDs. Both techniques require measuring the weight of the glass vial before the addition of the QD solution with the help of a pipette and after this process is completed. The solvent evaporation process is done by attaching the 2ml vial with the QD solution to a vacuum pump, which promotes a quick evaporation of the solvent and leaves QDs in the vial. The vial is then weighed again and the mass of QDs is roughly calculated by subtracting the initial measurement (weight of the vial) from the final. This process is repeated until the mass of QDs is such that after redispersing it in 115 µl of solvent, the final solution ends up with the desired concentration (250 mg/ml). The other possible technique is the precipitation of QDs. This is done by destabilizing the solution, in this case with the addition of a slightly polar solvent. As seen in Chapter 1, such addition will neutralize the pair potential that was shielding QDs from aggregating with each other and enable their precipitation. Destabilization is done by adding an alcohol (e.g. ethanol or methanol) to the solvent where QDs are dispersed. The added alcohol should be at a minimum volume ratio of 1:1 or more, for efficient precipitation. Once these two are mixed, the final solution is vortexed for 1 minute and left resting for 10 minutes. After 10 minutes, the solution is centrifuged at 10 000 g for another 10 minutes. The supernatant is then removed, and the sample is placed under vacuum for 10 minutes, to evaporate any remaining solvent. The final weight of the sample is measured and the mass of QDs obtained. Once the mass is known, the chosen solvent is added to the QDs until the final solution ends up with the desired concentration (250 mg/ml). The pellet of precipitated QDs can then be easily redispersed placing the sample in ultrasound for 5 to 10 seconds.

The water phase solution has Polyvinyl Alcohol (PVA) dissolved in milli-Q water at a mass ratio of 1.25 %. PVA is an amphiphilic compound with a stronger polar or hydrophilic part and a weaker non-polar part. Because of this, PVA tends to have more solubility in water and can

therefore be used as an oil-in-water emulsifier. The non-polar component of PVA helps with the dispersion of the oil phase solution in the water phase solution.

The recipe could be prepared with slightly different volumes assuming the ratio between oil and water phases is kept approximately the same.

The emulsion was prepared by vortexing 115 µl of the QD solution with 450 µl of the water solution for 10 minutes and stirring the mixture for approximately 2 hours at 750 rpm and room temperature to evaporate the solvent of the oil phase. Once the stirring is completed, self-assembled SPs were diluted in water at a volume ratio of 1:50 and vortexed again to remove traces of PVA on their surfaces. Samples in this work were prepared by drop-casting 10 µl of purified SPs onto a glass substrate. Chloroform (anhydrous, 99.5 %) and Polyvinyl alcohol (average Mw 85,000-124,000, 87-89% hydrolyzed) were ordered from Merck and used as received. Water was purified with Milli-Q water purification system. The magnet used for stirring was washed in toluene (10min), acetone (10min) and IPA (10min) and rinsed with water before its usage and before it was stored again. All the contaminated waste was disposed appropriately in their respective containers.

The critical stage of the self-assembly occurs while mixing the two phases, where chloroform begins to evaporate from the dispersed phase and QDs inside the emulsions begin to nucleate and grow into SPs [118], [198] (Figure 2-4).

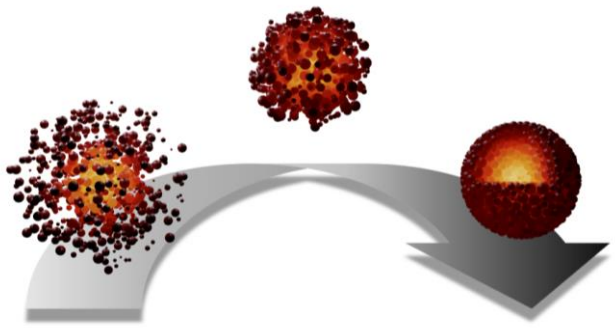

Figure 2-4. Illustration of the nucleation process occurring inside the emulsions that lead to SPs.

To characterize the size of SPs, after the self-assembly process, a sample solution of synthesized SPs was drop cast on glass and observed under the microscope. Figure 2-5 shows a scaled picture of SPs, and Figure 2-6 the histogram of their measured radius (right). The radius was measured automatically using a custom-made algorithm on Wolfram

Mathematica™ software. The algorithm follows steps similar to others already reported [202], combined with image processing functions from the software. A sample of SPs measured this way (N = 221) had an average radius of 2.8 µm ± 1.7 µm and a polydispersity of approximately 60%. The polydispersity (PD) is given by $PD = \frac{r_\sigma}{r_\mu}.100\ \%$, where r_μ is the average radius of SPs and r_σ is their standard deviation. Sub-micron SPs are also present in these samples, but could not be detected on the microscope due to the limitations in its resolution. These were instead seen in SEM.

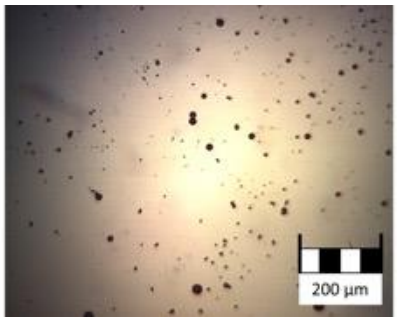

Figure 2-5. Size distribution of SPs: microscope image.

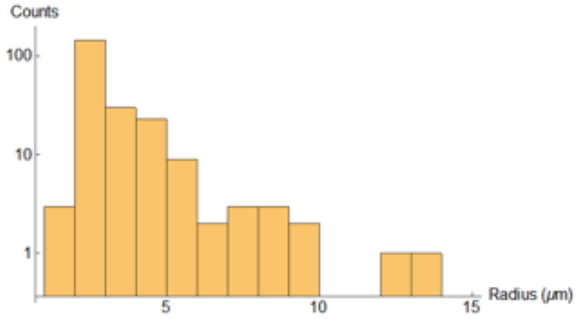

Figure 2-6. Histogram of the radius of SPs in Figure 2-5. Average radius size: 2.8 µm ± 1.7 µm; Sample size: 221.

2.5 Experimental Setup

The µ-PL setup design used to characterize SPs is represented in Figure 2-7. This setup is based on a previous design [203] and operates with a 0.76 ns pulse width microchip pulsed laser (λ = 532 nm, MNG-03E-100, Teem Photonics) at a repetition rate of 7.1 kHz and with a beam spot area of approximately 2.88×10^{-7} cm^2 at FWHM. The energy of this laser is attenuated by a waveplate (λ/2), polarizer and neutral density filter. This setup uses a custom-made beam expander with two plano-convergent lenses (focal lengths f_1 = 12.5 cm and f_2 = 2.5 cm). An attenuator wheel is incorporated within the beam expander to allow fine control of the pump intensity during experiments. A set of beam splitters is used to guide light into an objective lens (4×/0.13, Nikon), in order to focus the pump light onto the sample.

At focus, the beam spot size had a diameter of 6 µm. Samples are placed on an xyz stage that gives full control on their positioning. The light emitted by the sample is collected by the same objective and sent via a set of beam splitters onto the fiber coupled spectrometer (AvaSpec-2048-4-DT with 0.7 nm of spectral resolution between 220-1100 nm using an

optical fibre with a core of 50 µm in diameter, Avantes) and CCD camera (DCC1645C, Thorlabs).

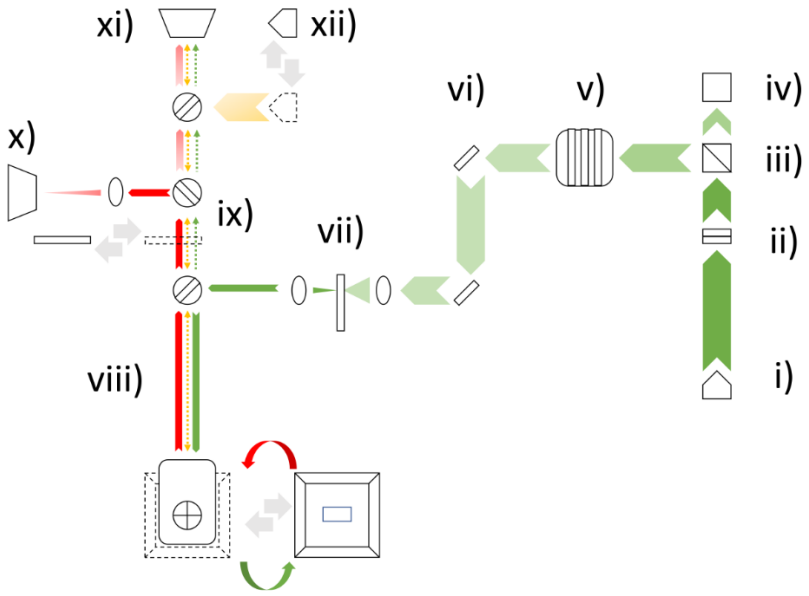

Figure 2-7. Schematic of the µ-PL setup: i) Pump source (532 nm laser); ii) Waveplate; iii) Polarized beam splitter; iv) Beam dump; v) set of neutral density filters; vi) mirrors; vii) beam expander with attenuator wheel incorporated; viii) setup with a mounted objective lens (4×/0.13, Nikon) and a xyz stage where the sample is placed; ix) set of 3 beam splitters and a long pass filter (550 nm); x) Spectrometer fiber-coupled to the setup; xi) CCD camera; xii) lamp. Green arrows represent the path of the laser from the pump, red arrows represent the path of the laser from the SP and yellow arrows represent the light path of the lamp.

A long pass filter (FEL0550, Thorlabs) is placed between the first two beam splitters when needed (either during the acquisition of measurements or camera capture). A lamp, also coupled to the set of beam splitters, can be switched on to help visualizing features on camera. A powermeter was used to calibrate the output energy as a function of the attenuator filter before each experiment.

2.6 Q-factor

The WGMs of a typical SP were observed below threshold using a scanning electron microscopy (SEM) technique named cathodoluminescence (CL), while imaging the SP at the same time (Figure 2-8a). These measurements were done with the help of Dr. Paul Edwards from the Physics department. CL emission is enabled by the absorbed energy from electrons

hitting the SP, which leads to the subsequent emission of photons. The CL spectrum in Figure 2-8b was acquired with a spectrometer coupled onto the SEM (Scanning Electron Microscope). This process proved to be less noisy than with the PL setup to observe WGMs below threshold because of the higher contrast between the WGM signature and the background luminescence. The periodicity of the WGMs was measured by doing a Fourier analysis of the CL spectrum (Figure 2-8c). Such analysis provides details on the distance between consecutive angular modes of the SP. This distance can be correlated to the pseudo-FSR of spherical microresonators, $\Delta\nu_{n,l}^{\Delta l} \approx \frac{c}{2\pi N a}$, where again the number indexes n and l correspond to the order of the spherical harmonic that describes the radial and angular field distribution, respectively, *c* is the speed of light in vacuum, *N* is the refractive index and *a* is the radius of the sphere [199]. From the SEM image, the diameter of the SP in Figure 2-8a was estimated to be approximately 14.0 ± 0.5 µm. This value is relatively close to the 13.7 ± 0.5 µm calculated using the pseudo-FSR correlation for consecutive modes [199], and a refractive index of *N* = 1.7, the latter corresponding to the expected value of Cd-based CQDs [204]. The Q-factor of the modes can also be calculated from Figure 2-8b as $Q = \lambda/\Delta\lambda$, where λ corresponds to the wavelength of the mode propagated in the cavity and $\Delta\lambda$ to the full width half maximum of that mode.

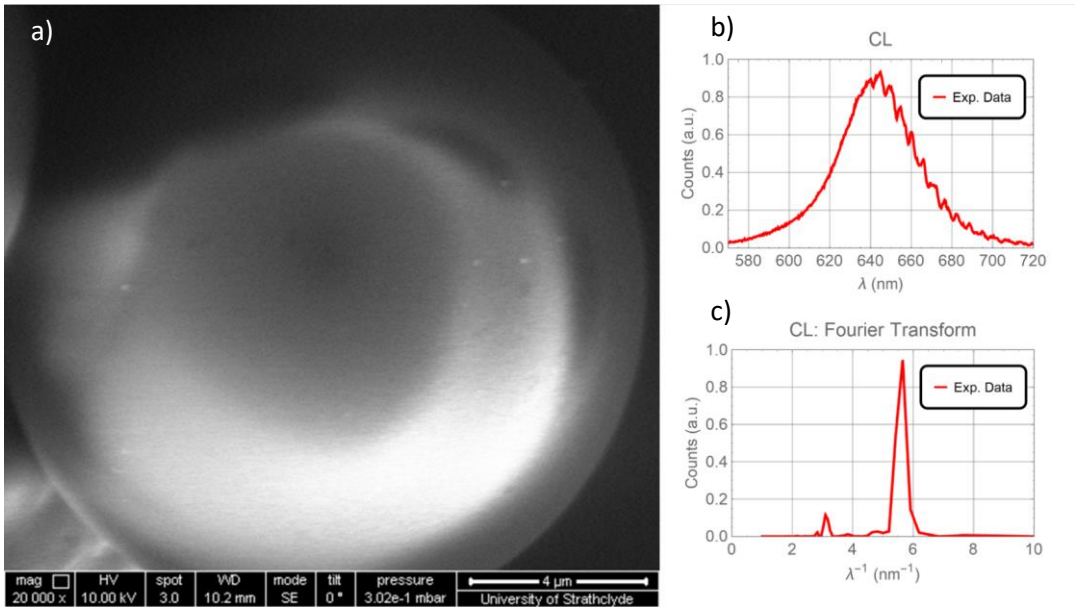

Figure 2-8. SEM image of a SP of approximately 14 µm in diameter (a) and its CL (b) and Fourier analysis (c). The Q factor estimated from the WGMs was 294 ± 15.

Here, the Q-factor is estimated as 294 ± 15. This value falls within the range of measurements for other SPs in this work and is consistent with the Q-factors previously reported on SPs of approximately the same size and composition synthesized using microfluidics [118]. These Q-factors are expected to be dependent on the limited Stokes shift of QDs, which causes reabsorption losses from the overlap between the absorption and emission (Figure 2-1 and Figure 2-2). In addition to that, other parameters such as the shape and surface roughness of SPs may limit the Q-factor even further.

2.7 Optical pumping results

SPs of different sizes were characterized individually in the µPL setup. Typical PL spectra and the laser transfer function of an SP (radius of 4.9 µm) can be seen in Figure 2-9 and Figure 2-10, respectively. Here, the regime below threshold spanned approximately between 0 and 7 nJ and the above threshold regime for pump energies higher than 7 nJ.

The main PL peak, around 630 nm, corresponds to the exciton and biexciton emissions of the QDs and is the first to be detected at lower pump energies (Figure 2-9, red spectrum). The exciton and biexciton emissions come from the electron-hole recombination in CQDs, more specifically from the fine structure of their band-edge to the ground state (as seen in Chapter 1). Regarding the biexciton emission, biexcitons are formed from two excitons. When they are annihilated, they disintegrate into a free exciton and a photon. Here, the energy of the photon is smaller than that of the exciton by the biexciton binding energy. This leads to a red-shift of the biexciton emission in such CQDs and that makes the differentiation between exciton and biexciton emissions peaks difficult to read in the PL spectrum, due to their proximity.

At higher energy pump levels, a higher energy transition corresponding to multiexcitonic emission (see Chapter 1, Section 1.5.2) can also be detected around 580 nm [95], [205] (Figure 2-9, green and blue spectra). Above threshold, the SP oscillates on multiple laser modes whose wavelengths range between 625 nm and 650 nm (Figure 2-9, blue spectrum). Each lasing peak has a linewidth limited by the resolution of the spectrometer used.

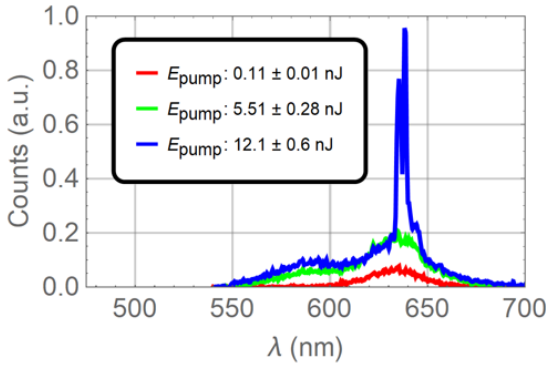

Figure 2-9. Typical PL spectra shown for a SP with 4.9 ± 0.5 µm in radius at different energy pump levels.

The typical laser transfer function (emission intensity versus pump intensity) of a SP can be seen in Figure 2-10, where lasing threshold occurs at a pump energy of around 7 nJ in this device. Spontaneous emission and lasing emission curves occur below and above this threshold, respectively.

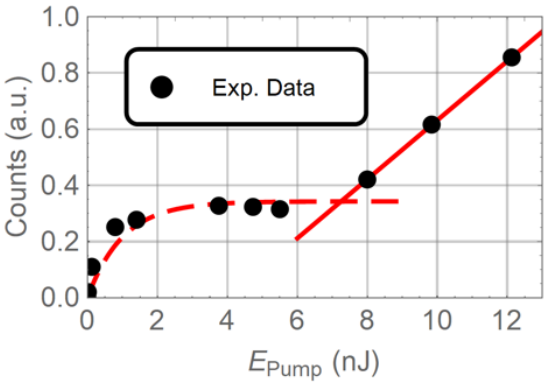

Figure 2-10. Typical transfer function shown for a SP with 4.9 ± 0.5 µm in radius at different energy pump levels. Two red curves (dashed and continuous) were added as guides to the eye to differentiate the emission below and above laser threshold, respectively.

In addition to the clear threshold behaviour observed both in Figure 2-9 and Figure 2-10, the differences between SPs below and above the lasing regime can also be observed under the microscope with an evident transition in intensity and the arising of a WGM lasing pattern characterized by the deep red corona on the SP periphery (Figure 2-11 and Figure 2-12).

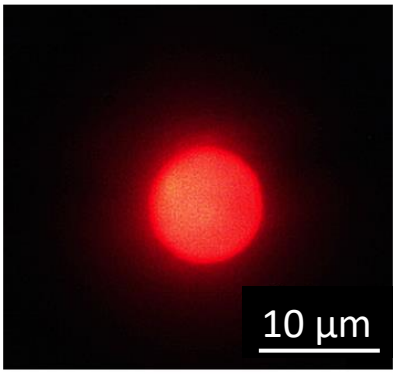

Figure 2-11. Microscope image of the SP with 4.9 ± 0.5 µm in radius under optical pumping below lasing threshold.

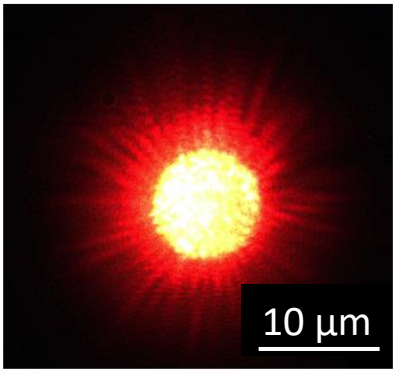

Figure 2-12. Microscope image of the SP with 4.9 ± 0.5 µm in radius under optical pumping above lasing threshold.

When above threshold, this SP oscillates due to the WGMs. These are characterized by three parameters referred to as n, l and m [24], which correspond, respectively, to the number of maxima of the radial, angular and azimuthal field distribution (as explained in Section 2.3).

To have a better understanding of this phenomenon, the expected WGMs of a microsphere with the same characteristics (i.e. radius and refractive index) as in Figure 2-9 to Figure 2-12 were calculated theoretically, and the results were compared to the WGM lasing pattern observed under the microscope (Figure 2-12). The algorithm used to calculate the modes above can be found in Annex A.

For this numerical experiment, the sphere was considered to have the same radius as the characterised SP, 4.9 µm, and a refractive index of *N* = 1.7 [204]. The modal equations (see Appendix A) for the electric field (transverse electric – TE and transverse magnetic – TM) [201] were solved for a wavelength close to the resonant peaks found experimentally (λ = 636 nm) to determine the values of l for which the resonances occur, or in other words, the values for which the modal equations are equal to zero (Figure 2-13a for TE modes and Figure 2-13b for TM modes). Once the values of l are known, the exact resonance wavelengths located within the laser emission range observed in the PL spectrum of the SP can then be found using the modal equations again, this time using the l values determined above and finding for which wavelengths the modal equations are equal to zero (Figure 2-13b for TE modes and Figure 2-13d for TM modes). Table 2-1 shows the resonance wavelengths found

for this numerical experiment in the region of interest, i.e. the wavelengths at which the lasing peaks of Figure 2-13 show up.

Table 2-1. Radial index, angular field distribution and resonant wavelengths in the region of interest for a SP with a radius of 4.9 μm and refractive index of N *= 1.7.*

	TE		TM	
n	l	λ (nm)	l	λ (nm)
1	75	636	74	635
2	69	636	68	638
3	64	638	63	640
4	60	635	59	638
5	56	637	56	632
6	53	632	52	637
7	49	637	49	635

The spacing between resonant wavelengths falls below the resolution of the spectrometer, and therefore it is difficult to identify the exact TE and TM modes. Nevertheless, the range of resonant frequencies found in this numerical experiment (mainly between the 635 nm and the 640 nm) match those observed experimentally (Figure 2-13i). Small deviations between the numerical and laboratorial measurements can be assigned to the not perfectly spherical shape of the SPs and small fluctuations in the refractive index.

Once the parameters above are found, the norm of electric field (real component) for TE and TM modes can be evaluated and plotted. Figure 2-13e – h illustrate an example of such intensity maps in the xy and xz plane for a TE (n = 1, l = 75, λ = 636, m = 20; Figure 2-13e and g) and TM mode (n = 1, l = 74, λ = 635, m = 20; Figure 2-13f and h). Despite the impossibility of filtering and isolating each mode from Figure 2-13j alone, the spatial periodicity between maxima of intensity is similar in both cases for an azimuthal field distribution of 20 (m = 20). Figure 2-13j shows roughly 11 maxima of intensity in a quarter of the sphere, which match the number of maxima observed on Figure 2-13e and f. For higher radial field distribution numbers (n > 1) evidenced in Table 2-1 and Figure 2-13i, the mode volumes expand towards the core of the SP regardless of the high absorption coefficient found in CQDs [204].

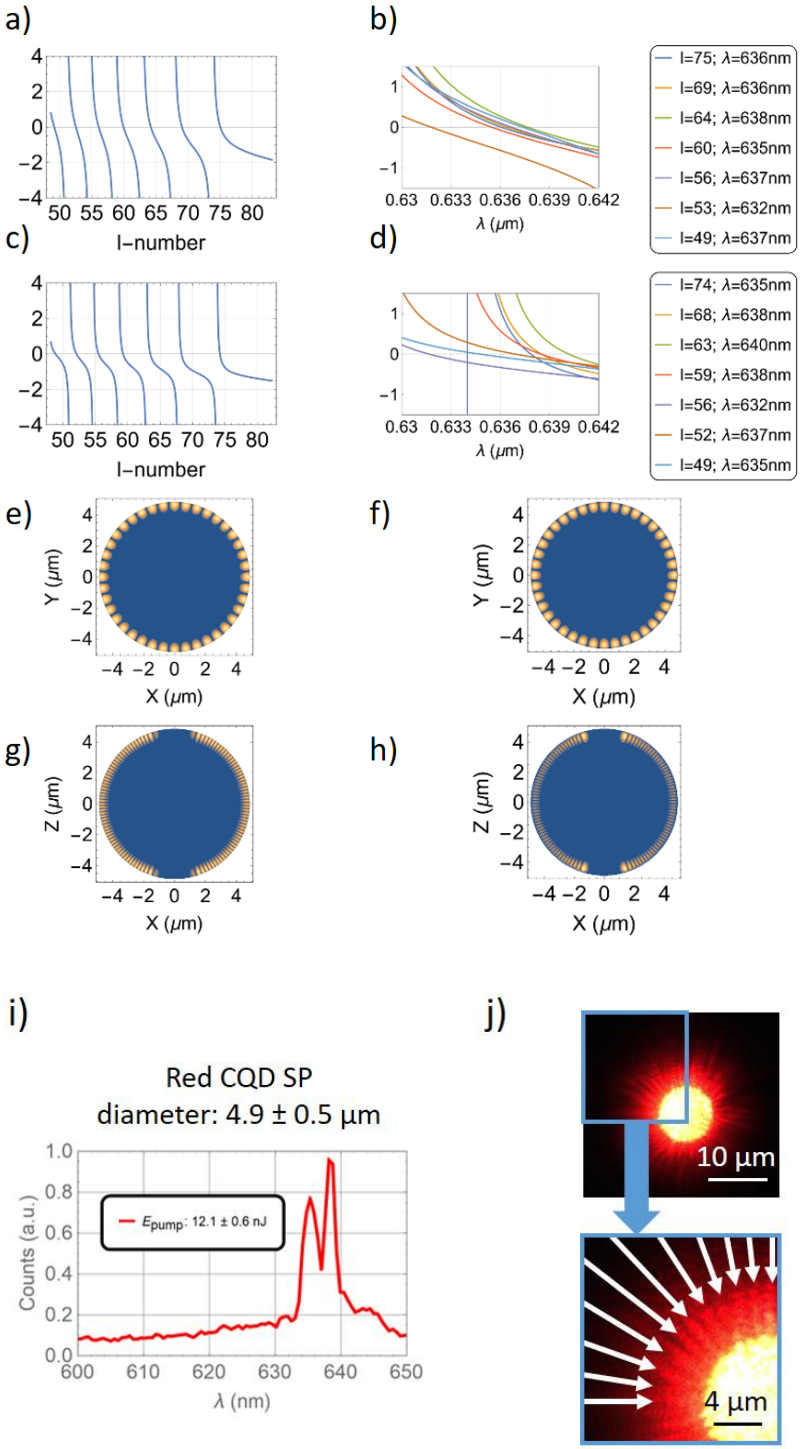

Figure 2-13. Study on the modes of a SP. The mode number l (a; b) and resonant frequencies (c; d) were calculated by solving the modal equations [201] *for TE and TM fields, respectively. The numerical experiment uses a SP with the same radius as the one measured experimentally (2.45 μm) and a refractive index of 1.7* [204]. *These results were then compared with the emission spectrum of the experimental measurements (e). Modes evaluated in the xy-plane for both TE (f: $n = 2$, $l = 31$, $m = 20$; h: $n = 3$, $l = 27$, $m = 20$) and TM (f: $n = 1$, $l = 35$, $m = 20$; h: $n = 2$, $l = 30$, $m = 20$) had their periodicity compared to those counted experimentally (j).*

In general, the different SPs measured in this work display multimode lasing with spectrometer-resolution-limited peaks ranging between 625 nm and 655 nm. They tend to oscillate on one or several angular modes, depending on the SP size and pumping levels (see Figure 2-17 to Figure 2-21 and Table 2-2). There is a trend of the threshold pump energy increasing with the size of the SP (Figure 2-14), which is attributed to the pump spot (and energy) overlap with the SP – SPs with sizes close to or higher than the pump spot size are illuminated by lower and less homogeneous pump intensities at the edges.

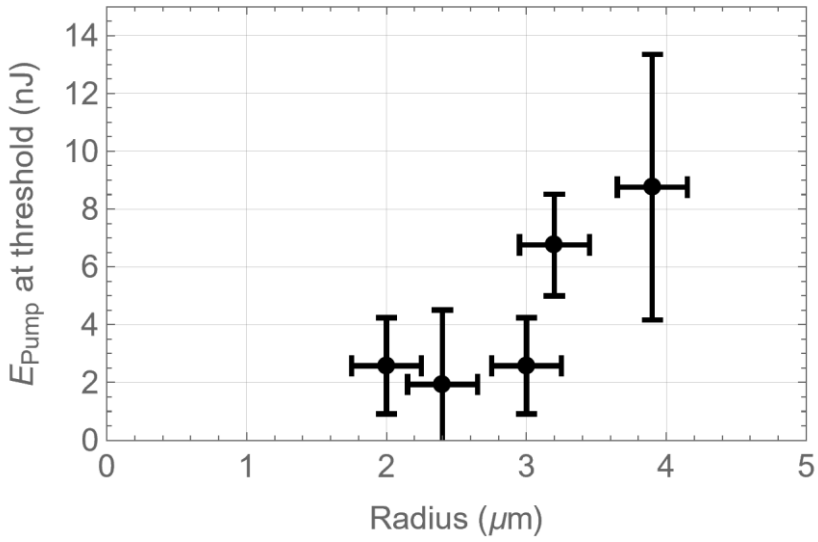

Figure 2-14. Energy threshold as a function of the size of the SP (for red CQDs). More information on the spectrum and characteristics of these SPs can be found in Table 2-2 and Figure 2-17 to Figure 2-21. The error in the x-axis is given by the measurement error in the size of the SP (minimum scale bar of 1 µm in diameter, which corresponds to 0.5 µm in radius). The error in the y-axis is given by the average and standard deviation of the two closest data points below and above laser threshold.

2.7.1 Regime Below Laser Threshold

The sub-linear evolution of the microsphere emission intensity versus pump energy below threshold (Figure 2-10) indicates that lasing oscillation is reached in a regime where there is more than one exciton per CQD on average. Extracting this value at different pump levels and in particular at threshold is interesting in order to assess the performance of SP lasers and the excitation level of the gain medium. However, it is difficult and certainly more challenging than for lasers based on planar CQD films due to the spherical geometry of SPs and the overlap with the pump laser. This section details a model used to obtain such values.

The spontaneous emission of the k^{th}- exciton in a QD has been experimentally observed to follow a Poisson distribution [111], [140], [206], [207]. In the case of CdSe-based QDs, the exciton and biexciton emissions are also known to be of similar wavelength and, in our case, close to 630 nm, whereas the next multiexciton emission shows up near 580 nm [95], [205]. To model the spontaneous emission of SPs, the problem was approached by generalizing the spontaneous emission of a QD to the SP and solving the following multi-nonlinear model fit (Eq. 14 – 16):

$$\begin{cases} Data_{630nm} = A.P(k_1;\langle N\rangle),\ 1 < k_1 < 2; \\ Data_{580nm} = A.P(k_2;\langle N\rangle),\ k_2 > 3; \end{cases} \quad \text{(Eq. 14)}$$

$$P(k;\lambda = \langle N\rangle) = \frac{\Gamma(k+1,\langle N\rangle)}{\Gamma(k+1)} - \frac{\Gamma(k,\langle N\rangle)}{\Gamma(k)} \quad \text{(Eq. 15)}$$

$$\langle N\rangle = \beta.E_{pump}^{\alpha} \quad \text{(Eq. 16)}$$

Where the data acquired by the spectrometer (Eq. 14) is proportional to the probability of a QD to emit from the k^{th}- exciton, $P(k;\langle N\rangle)$, in a SP with a given average number of excitons per QD, $\langle N\rangle$. Since not all the QDs in the ensemble will contribute the same exciton emission, mainly due to the absorption of the material, different quantum efficiencies and differences between the size of SPs and pump spot size overlap, the probability mass function $P(k;\langle N\rangle)$ was approximated to a continuous probability density function Poisson distribution $P(k;\lambda)$ [208], where $\Gamma(k)$ and $\Gamma(k,\lambda)$ are the Euler and incomplete gamma functions, respectively (Eq. 15). The average number of excitons $\langle N\rangle$ is given as the power law of the pumped energy, E_{pump} (Eq. 16) [206], [207]. The unknown parameters *A*, β, and α were left as free parameters and are studied below. More details on the algorithm used to compute the fit above can be found in Annex B.

To study how this set of parameters (*A*, β, and α) behave, fifteen SPs of different sizes ranging approximately between 4 and 20 µm in diameter were randomly chosen and had their spectra recorded at different values of the pump energy E_{pump} below the laser threshold (Figure 2-15).

A set was then estimated for each SP, by fitting the experimental data peaks around 580 nm and 630 nm to Eq. 14. Since the emission peak at 630 nm comes from exciton and biexciton emissions, k_1 was constrained between 1 and 2. Likewise, the multiexciton parameter k_2 was constrained to be equal or higher than 3 [95], [205]. The data from the fifteen sets was then

split according to each parameter (A, β, and α) and analyzed as a function of the size of SPs (Figure 2-16a, b, and c, respectively).

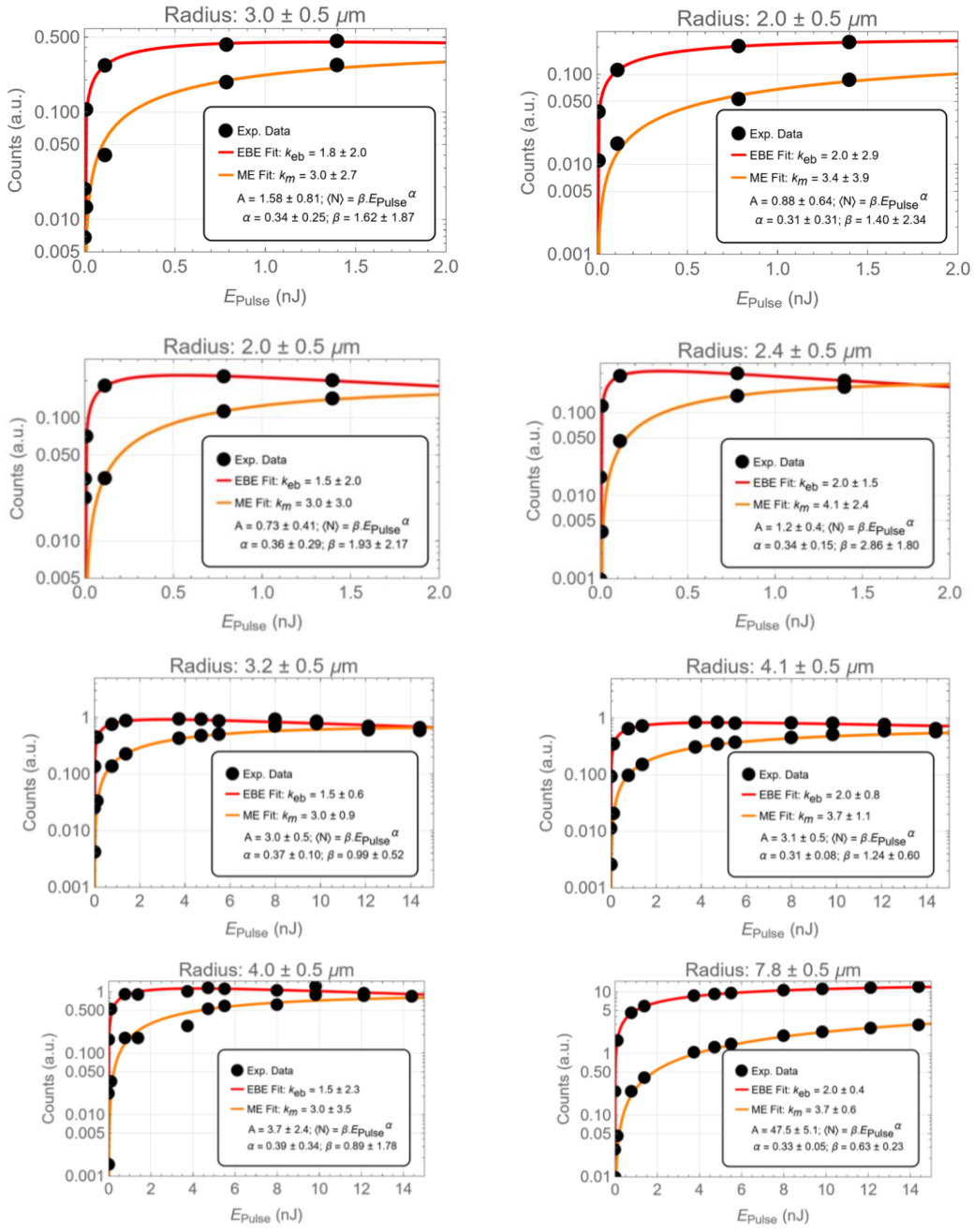

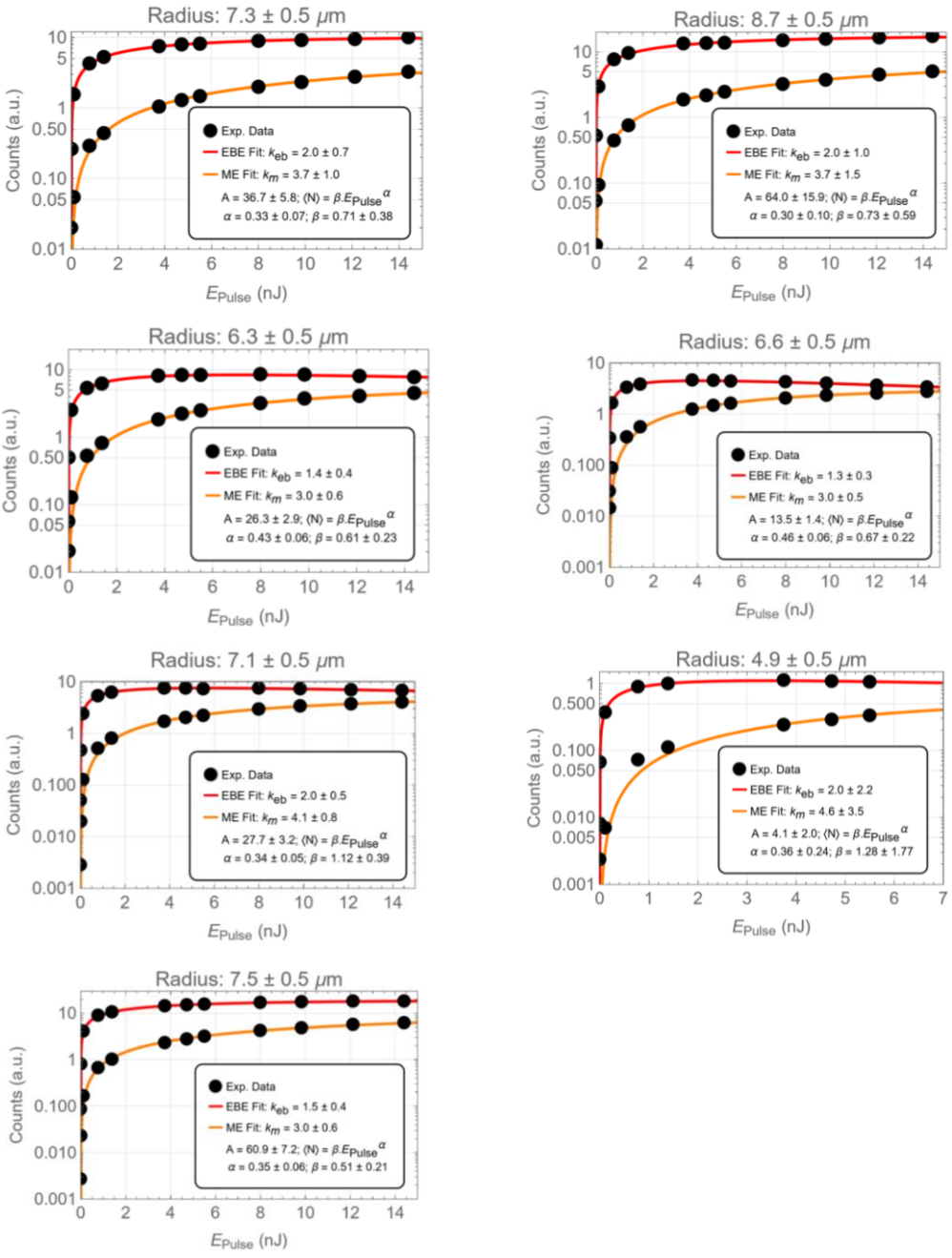

Figure 2-15. Fit of Eq. 14 to the Exciton/Biexciton (EBE) and Multiexciton (ME) peaks for SPs of different sizes.

It is worth noting that some of the fits have estimated parameters with large errors. This is mainly due to the lack of data points caused by small samplings on SPs with low energy lasing thresholds, or the lack of data points in the higher end of energies, which is limited by the laser and setup.

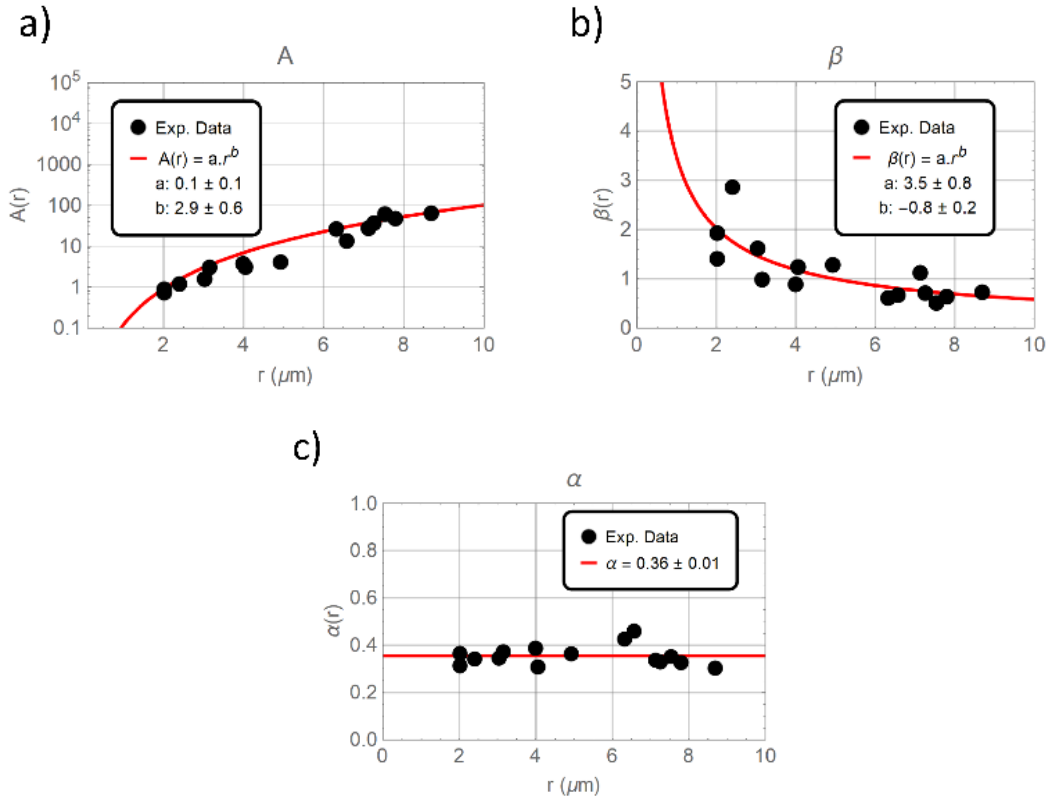

Figure 2-16. Study on the free parameters A (a), β (b) and α (c) of SPs in Eq. 14 (and Eq. 16), as a function of their radius. The dots correspond to the parameters extracted from the experimental data for each of the fifteen SPs. This data was then analyzed by fitting the parameters to their most likely trends (expressions and fit results in caption).

Regarding $\langle N \rangle$, the results suggest that the coefficient α is intrinsic to the QDs used in this experiment and does not depend of the size of the SP as it is constant with the radius (Figure 2-16c). In other words, whenever the E_{pump} is doubled, the $\langle N \rangle$ of QDs in the SPs increase by a factor of approximately 1.3β. On the other hand, the coefficient β accounts for mechanics extrinsic to QDs as it is inversely proportional to the size of SPs (Figure 2-16b). The fact that this proportionality is very close to the inverse of the radius of the SP might be related with the ratio between the pump fluence across the surface of a SP and the total number of QDs in its volume, which follows the same trend.

Coefficient *A* accounts for the detected emission of SPs, which is proportional to the number of QDs emitting light (active QDs) and the collection efficiency of the setup. Assuming that the efficiency of the setup is a constant, *A* simply becomes proportional to the number of active QDs. Figure 2-16a suggests that *A* is indeed proportional to the volume of SPs, which

is also consistent with the existence of modes deep in the SP (Figure 2-13). The light emission of a SP (Eq. 14) can then be simply put as the number of active QDs times the average emission of an active QD in the SP, according to *k* and $\langle N \rangle$.

Once β and α are known, $\langle N \rangle$ can be estimated from the results in Figure 2-16. On average, the threshold fluence corresponded to $\langle N \rangle \approx 2.3$. This value is higher than the expected value of $\langle N \rangle \approx$ 1-1.5 for transparency (the onset of optical gain) in CQDs of this type [111], as was discussed in Chapter 1, but close to the value found in the literature for Cd-based SPs [118], of $\langle N \rangle$ = 2.5, obtained via numerical gain modelling [140]. The higher $\langle N \rangle$ is expected in order to reach lasing condition as was explained in 1.6.2. Ultimately, it is limited by the Q-factor. These limitations could come either from defects intrinsic (e.g. surface roughness) or extrinsic (e.g. debris on the surface, non-homogeneous pump fluence) to SPs. A further reduction of $\langle N \rangle$ at threshold would require an increase of the Q-factor by reducing self-absorption in the SP and guaranteeing smoothness of the SP.

2.7.2 Regime Above Laser Threshold

Figure 2-17 – Figure 2-21 and Table 2-2 show a compilation of the 5 SPs from Figure 2-16 that were capable of laser emission, including their PL spectra at different energies (below and above lasing threshold), estimated threshold energies, radius and calculated average number of excitons per QD in the SP using both the results from the individual fits (Figure 2-15) and the results in Figure 2-16.

The reason why not all the SPs can reach laser emission might be bound to several factors. Surface roughness or debris on the SPs might hinder the WGMs. Likewise, a non-homogeneous pump fluence or a partial overlap between the pump and the SP can impact the energy threshold. These factors could explain why SPs of similar sizes can have different energy thresholds and estimated average number of excitons, $\langle \mathrm{N} \rangle$.

While the individually fitted parameters may give more precise $\langle N \rangle$ (from Figure 2-15), the calculation of $\langle N \rangle$ referenced to the parameters in Figure 2-16 can give a reasonable estimation that only depends on the size and pump energy of the SP. The mean value of $\langle N \rangle$ for the sample in Table 2-2 was similar for both cases ($\langle N \rangle \approx 2.3$).

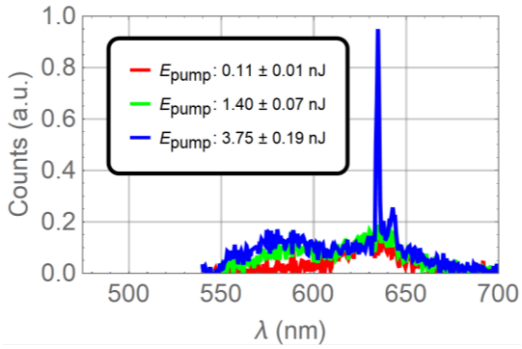

Figure 2-17. PL spectra shown for a red SP with 2.0 ± 0.5 µm in radius at different energy pump levels.

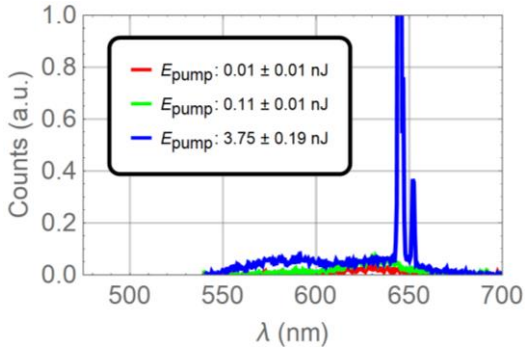

Figure 2-18. PL spectra shown for a red SP with 2.4 ± 0.5 µm in radius at different energy pump levels.

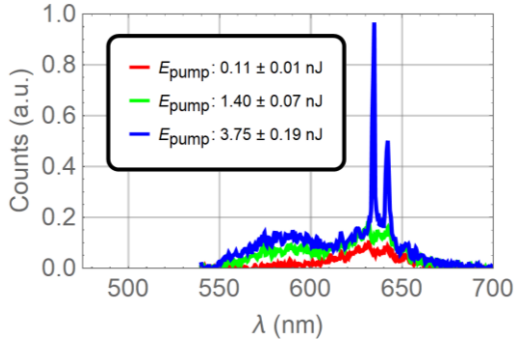

Figure 2-19. PL spectra shown for a red SP with 3.0 ± 0.5 µm in radius at different energy pump levels.

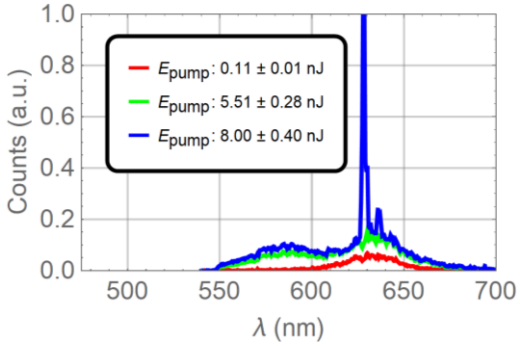

Figure 2-20. PL spectra shown for a red SP with 3.2 ± 0.5 µm in radius at different energy pump levels.

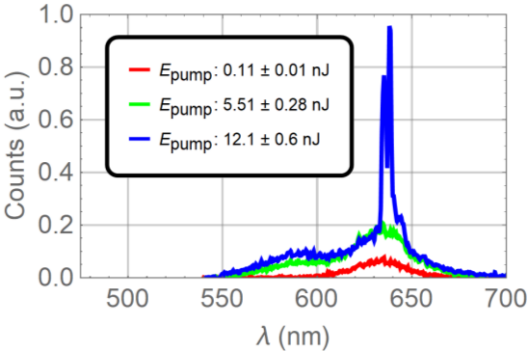

Figure 2-21. PL spectra shown for a red SP with 4.9 ± 0.5 µm in radius at different energy pump levels.

Table 2-2. List of the SPs that went above the lasing threshold for the range of studied E_{pump}. The counting of SPs in Figure 2-15 (SP nr) is made from left to right and top to bottom.

	Radius (μm)	E_{pump} at threshold (nJ)	$\langle N \rangle$ (Figure 2-15)	$\langle N \rangle$ (Figure 2-16)	SP nr
Figure 2-17	2.0 ± 0.5	2.6 ± 1.1	2.7	3.1	3
Figure 2-18	2.4 ± 0.5	0.5 ± 0.3	2.2	1.4	4
Figure 2-19	3.0 ± 0.5	2.6 ± 1.1	2.2	2.1	1
Figure 2-20	3.2 ± 0.5	6.8 ± 1.2	2.0	2.7	5
Figure 2-21	4.9 ± 0.5	6.8 ± 1.2	2.6	1.8	14

2.8 Conclusion

In this chapter red-emitting SP lasers based on CQDs have been demonstrated. This chapter has also provided an in-depth study on the modelling for emission below threshold and determination of $\langle N \rangle$ using fifteen randomly chosen SPs ranging between approximately 4 and 20 μm in diameter.

The SPs had a Q-factor of 294 ± 15, which was estimated from the CL measurements on SEM. The CL measurements proved to be more accurate than the PL measurements most likely due to the setup conditions and methods behind each of them. CL measurements on SEM use a continuous electron beam flow suggesting that the dynamics of the system are kept constant over time and WGMs were easily observed. On the other hand, the μPL setup operates at a 532 nm wavelength with a 0.76 ns pulse width laser at a repetition rate of 7.1 kHz (see Section 2.5), and these parameters already seem to introduce noise in the PL measurements, even at low fluences. The previous report on PL measurements and similar CdSe-based SPs has shown low noise and clear WGMs for a continuous wave (CW) excitation source at 405 nm wavelength [118]. The above seem to imply that clearer WGMs are more evident in the spectra when using continuous pump sources. The Q-factors here obtained via CL on SEM were consistent with those obtained via PL using a CW laser as pump source in the state of art [118].

SPs in this work achieved multimode lasing between the 625 and the 655 nm when pumped above the threshold fluence, which was on average estimated for $\langle N \rangle \approx 2.3$ according to the emission model introduced in this work. These results were also consistent with the current

state of the art [118] and the emission model here introduced could help with the characterization of SPs in future works.

Chapter 3. Blends of Nanocrystals

3.1 Introduction

An optimal design of spherical microresonators requires the tuning of several parameters to minimize the loss of stored energy [199]. In spherical SPs the parameters that determine their Q-factor not only depend on the shape, size, and average refractive index of the SP, but also on their building blocks - the CQDs. In the solid state, CQDs can suffer from self-absorption, exciton diffusion and nonradiative recombination [209]. In combination, these factors dampen the oscillations of whispering gallery modes (WGMs) and decrease their Q-factor and this has in turn a detrimental effect on the properties of SP lasers, namely it increases the threshold.

In this chapter, CdSSe/ZnS CQDs with higher bandgaps (green CQDs emitting at 540 nm and blue CQDs emitting at 490 nm), which are close to or above the pump photon energy, were added to the fabrication of red (630 nm) CQD SPs (same as in Chapter 2) and studied as a way of minimising such losses. The hypothesis is that decreasing the density of 'active' CQDs (active in the sense that the CQDs emit the laser light) should also decrease the self-absorption and non-radiative transfer processes within active CQDs, which in turn increases the Q factor.

Here it is important to note that the different types of alloyed CdSSe/ZnS CQDs were all of the same nominal size, and that the bandgap was set by alloying the core of CQDs at different density rates, instead of tuning their size. Since their size remains constant, the self-assembly process of different types of CQDs remains unaffected. In fact, a blend of CQDs at different bandgaps within a single SP such as these can also be likened to a heterostructure: in this case a heterostructure SP.

CQDs with bandgap higher than the pump photon will not have a direct role on the emission, but they will help maintain the overall SP structural properties while reducing the density of active CQDs. However, this is not true if the added CQDs have a bandgap lower than the

energy of the pump photons. In the latter case, the added CQDs can absorb, transfer and even re-emit light themselves. The blue emitting CQD are definitely inactive in that sense, while the green CQDs might be at the limit between the two regimes. In addition to these, yellow-emitting CQDs (575nm), with a bandgap between the emission of the pump and the bandgap of red CQDs, were also tested in combination with red CQDs - these definitely take part in the emission processes as is seen later in the chapter with the demonstration of multicolour laser emission.

The mixing of blue and green-emitting types of CQDs with red CQDs is characterized, and the self-absorption is studied, for SPs of different sizes and pumped at different intensities in Sections 3.2 and 3.3, respectively. The emission below threshold of SPs are analysed using the approach described in the previous chapter. Section 3.4 demonstrates how mixing higher bandgap CQDs can indeed improve the Q-factor in a CQD SP microsphere. Lastly, Section 3.5 shows how multicolor lasing can be achieved in SPs.

3.2 Synthesis of Blended Quantum Dot SP Microspheres

The synthesis process follows the same steps as in Section 2.4. The new SPs were synthesized using the standard recipe with CQDs mixed at different ratios according to Table 3-1:

Table 3-1. Percentage of CQDs used for each batch.

	Batch						
CQDs	1	2	3	4	5	6	7
Red	100%	25%	50%	75%	25%	50%	75%
Green	-	75%	50%	25%	-	-	-
Blue	-	-	-	-	75%	50%	25%

A SP from the 1st batch and a SP from the 4th batch were used in Section 3.4, due to their similar sizes and relatively low noise WGM measurements.

In addition to the 1st batch in Table 2-2 (100% red SPs), two additional batches were used in Section 3.5: yellow SPs made of CQDs emitting at approximately 575 nm and SPs with a 50:50 ratio of red and yellow CQDs.

All the SPs were drop-cast onto a glass substrate and, with the water evaporated, optically-pumped individually.

3.3 Optical Characterization

Similarly to Section 2.5, SPs were selected and optically pumped one at a time with a 0.76 ns pulse width microchip pulsed laser (λ = 532 nm) at a repetition rate of 7.1 kHz and with a beam spot area of approximately 2.88×10^{-7} cm^2. The only exception is Section 3.6, where we used a 1.6 ns pulsed frequency-doubled Nd:YAG laser at 532 nm, at a repetition rate of 10 kHz with a beam spot area of 1.9×10^{-5} cm^2. The beam intensity was controlled by a variable wheel neutral density attenuator and focused on the sample with an objective lens (Section 3.3-3.4: N PLAN EPI 50×/ 0.75, Leica; Section 3.5: 4×/ 0.13, Nikon). A spectrometer (AvaSpec-2048-4-DT, Avantes) was used to acquire the spectral data [30]. The size of the SPs was measured by both optical microscopy and SEM.

The following sub-sections present the results and analysis of the blended SPs for their below and above threshold regimes.

3.3.1 Regime Below Laser Threshold

The characterization process of the blended SPs in Table 3-1 followed the same steps as in Section 2.7.1, where a sample of SPs was randomly selected from each blend and individually characterized as a function of their radius and optical pump energies. This characterization was performed to test the impact of mixing CQDs of different bandgap in the SPs.

Red – Green

25%-75%

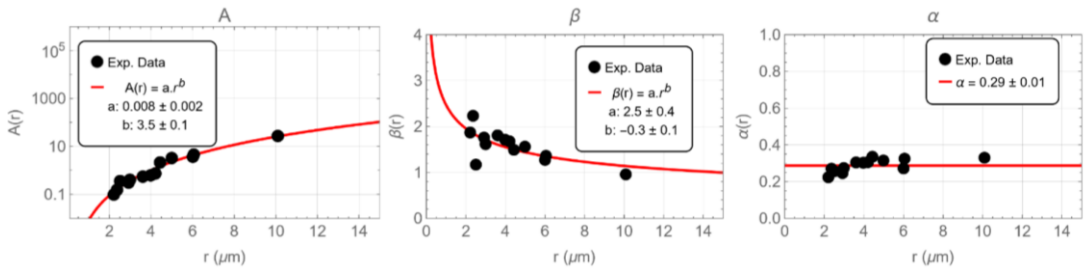

50%-50%

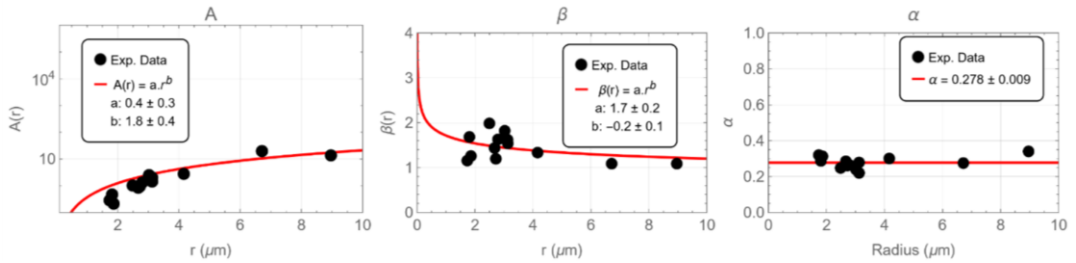

75%-25%

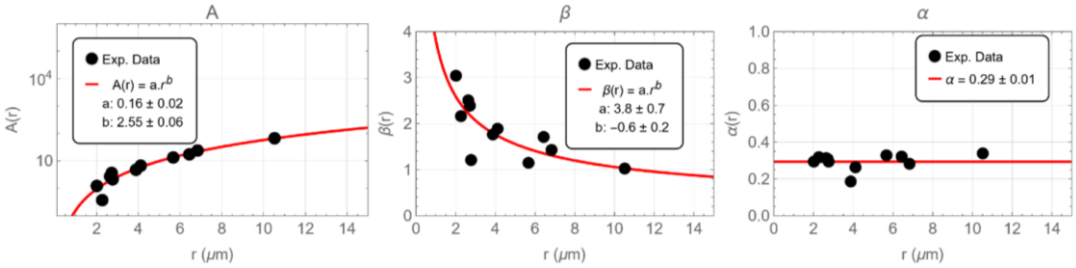

Red – Blue

25%-75%

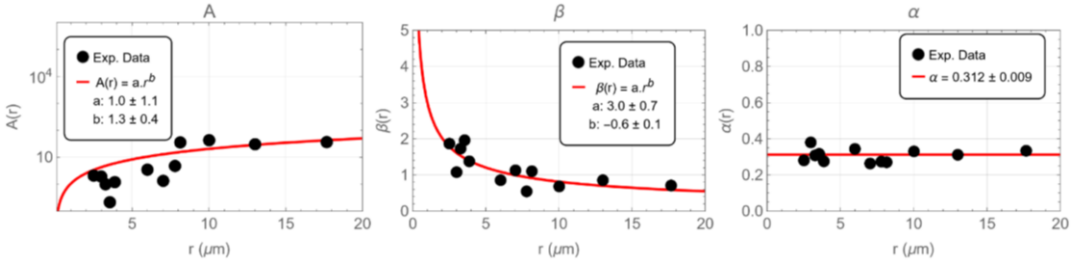

50%-50%

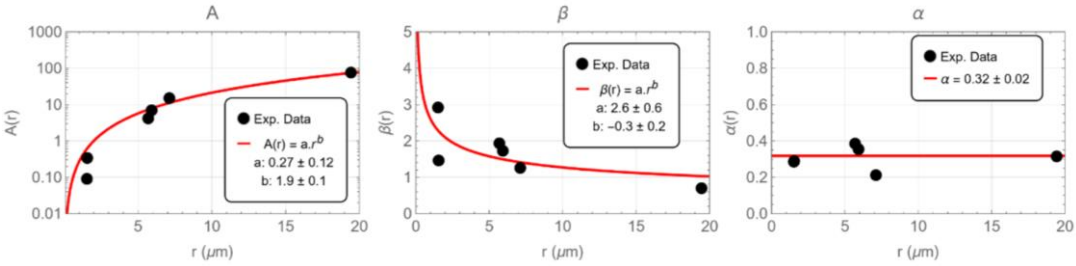

75%-25%

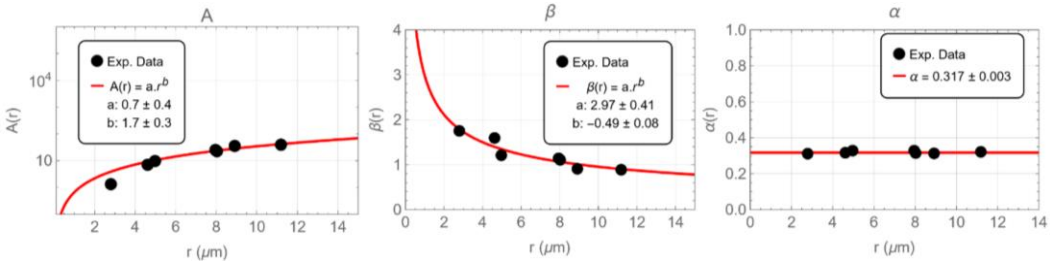

Figure 3-1. Study on the below laser threshold characteristics of SPs of different blends.

Figure 3-1 displays the parameters A, β, and α as a function of the SP radius for different blends (Red-Green and Red-Blue) and different ratios, along with the fits. Results for the red samples (100%) are those of Chapter 2. For completeness, more details on the sample size and individual characterization of SPs can be seen in Figure 3-4 to Figure 3-9 (from which Figure 3-1 was obtained). The fitted parameters obtained from Figure 3-1 are compiled in Table 3-2:

Table 3-2. Compiled fitted parameters from Figure 3-1, sorted by type of blend.

		Red	Red - Green			Red - Blue		
		100%	75%-25%	50%-50%	25%-75%	75%-25%	50%-50%	25%-75%
$A(r) = a.r^b$	a	0.1 ± 0.1	0.2 ± 0.0	0.4 ± 0.3	0.01 ± 0.0	0.7 ± 0.4	0.3 ± 0.1	1.0 ± 1.1
	b	2.9 ± 0.6	2.6 ± 0.1	1.8 ± 0.4	3.5 ± 0.1	1.7 ± 0.3	1.9 ± 0.1	1.3 ± 0.4
$\beta(r) = a.r^b$	a	3.5 ± 0.8	3.8 ± 0.7	1.7 ± 0.2	2.5 ± 0.4	3.0 ± 0.4	2.6 ± 0.6	3.0 ± 0.7
	b	-0.8± 0.2	-0.6± 0.2	-0.2± 0.1	-0.3± 0.1	-0.5± 0.1	-0.3± 0.2	-0.6± 0.1
α		0.36	0.29	0.28	0.29	0.32	0.32	0.31

Here, the parameter A is proportional to the number of QDs in the volume of the SP contributing to the emission detected on the spectrometer (see Section 2.7.1). By looking at Figure 3-2, the red and green blend ($A_{Red-Green:\,75-25}$) of SPs present similar or slightly higher emissions than red SPs (A_{Red}) most likely due to the reduction of self-absorption in the red emission enabled by a smaller concentration of red QDs in the SP, and compensation of red emission either by energy transfer between green QDs to red QDs or by higher absorption rates from red QDs, as in this case they can absorb light both from the pump and green QDs.

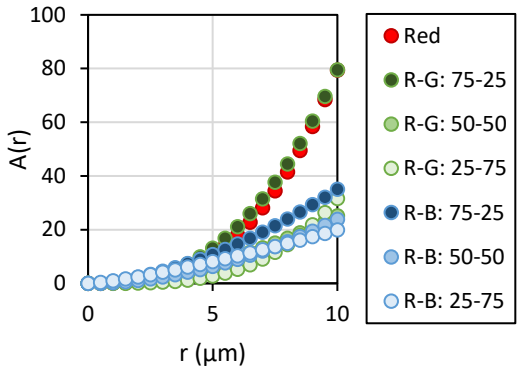

Figure 3-2.Parameter A as a function of the radius of a SP.

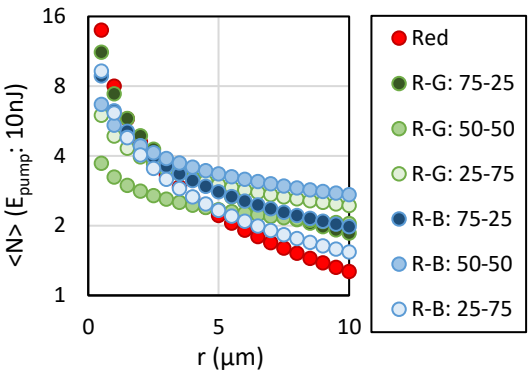

Figure 3-3. $\langle N \rangle$ as a function of the radius of a SP.

For the blend of red and blue QDs ($A_{Red-Green:\,75-25}$), blue QDs can inhibit reabsorption of red photons by red QDs, but they do not contribute for energy transfer or emission that can be absorbed by red QDs. These factors decrease the overall emission of SPs when compared to the other two types of SPs. For blends with either blue or green QDs but lower ratios of red QDs, the lack of red QDs eventually outweighs the advantages of adding a second type of QD and the emissions drop when compared to SPs of red QDs.

Regarding the average number of excitons, the registered values for both blends were in general higher than in red SPs, specially for large SPs.

Assuming SPs under a 10 nJ pump source and using the fitted parameters in Table 3-2, the average number of excitons for the red blends ($\langle N \rangle_{Red}$) is higher for small SPs, but it quickly drops as the radius of the SP increases and is eventually surpassed by the $\langle N \rangle$ of blended SPs (Figure 3-3). These results suggest that the increased interaction between QDs promoted in larger SPs (volume >> surface) leads to energy transfer and non-radiative recombination which in turn causes a drop of $\langle N \rangle$ for every type of SP. However, these phenomena are more likely to happen in red SPs because red QDs have no neighbour higher bandgap QDs capable of slowing this process.

The addition of higher bandgap QDs on the SP clearly slows these phenomena to some degree, resulting in SPs with an higher $\langle N \rangle$. In these experiments, the blends of Red-Green ($\langle N \rangle_{Red-Green:\,25-75}$) and Red-Blue ($\langle N \rangle_{Red-Blue:\,50-50}$) showed the highest $\langle N \rangle$ for larger SPs. Nevertheless, for these devices to reach laser threshold the density of active QDs is also

important to stimulate emission, implying that there is a trade-off between this and the use of higher bandgap QDs in SPs to minimize unwanted energy transfer or non-radiative recombination.

The following section covers the studies on SPs above laser threshold and these implications in more detail.

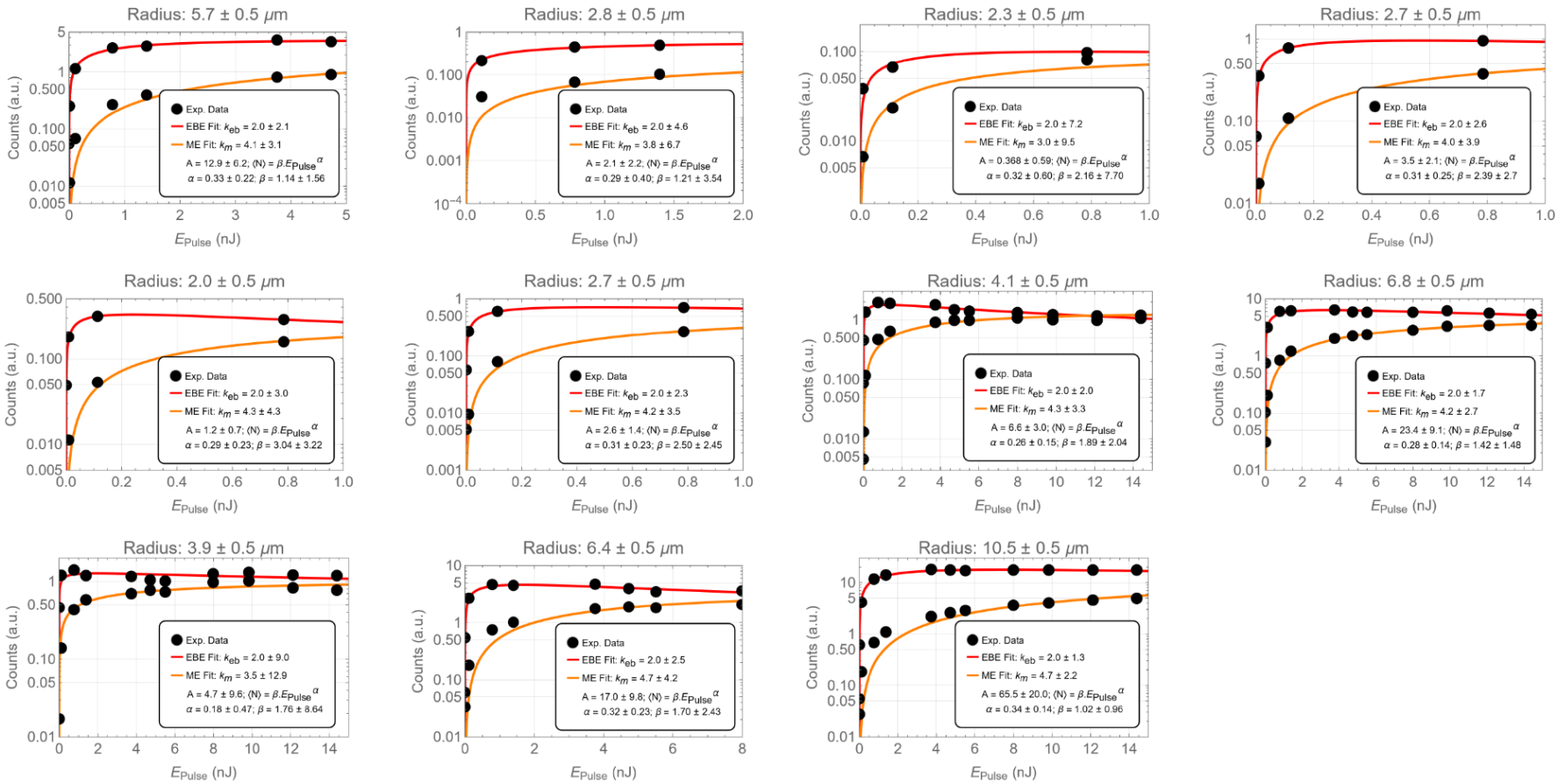

Figure 3-4. Red -Green blend SPs (75% – 25%): Fit of Eq. 2 to the Exciton/Biexciton (EBE) and Multiexciton (ME) peaks for SPs of different sizes.

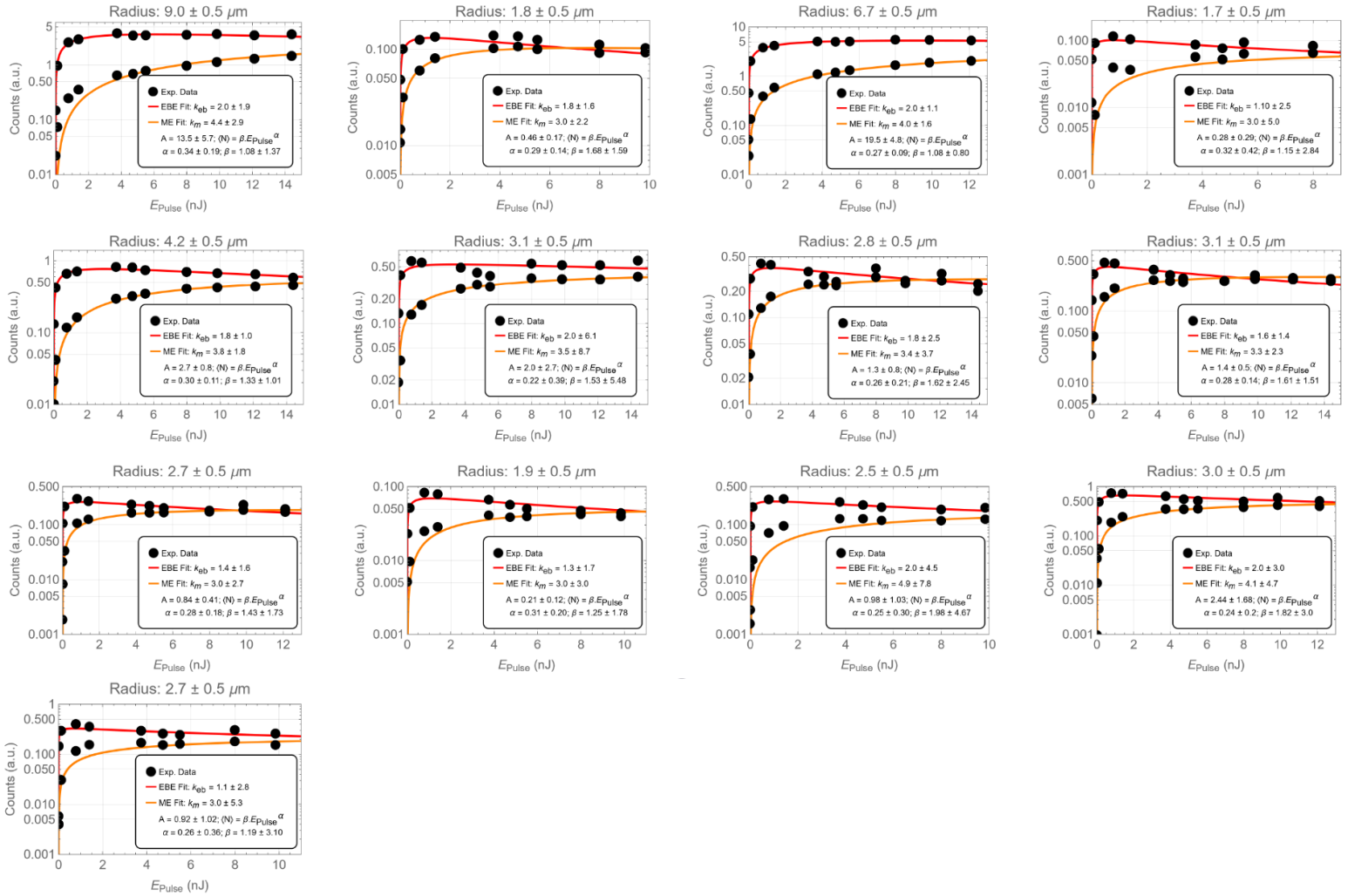

Figure 3-5. Red -Green blend SPs (50% – 50%): Fit of Eq. 2 to the Exciton/Biexciton (EBE) and Multiexciton (ME) peaks for SPs of different sizes.

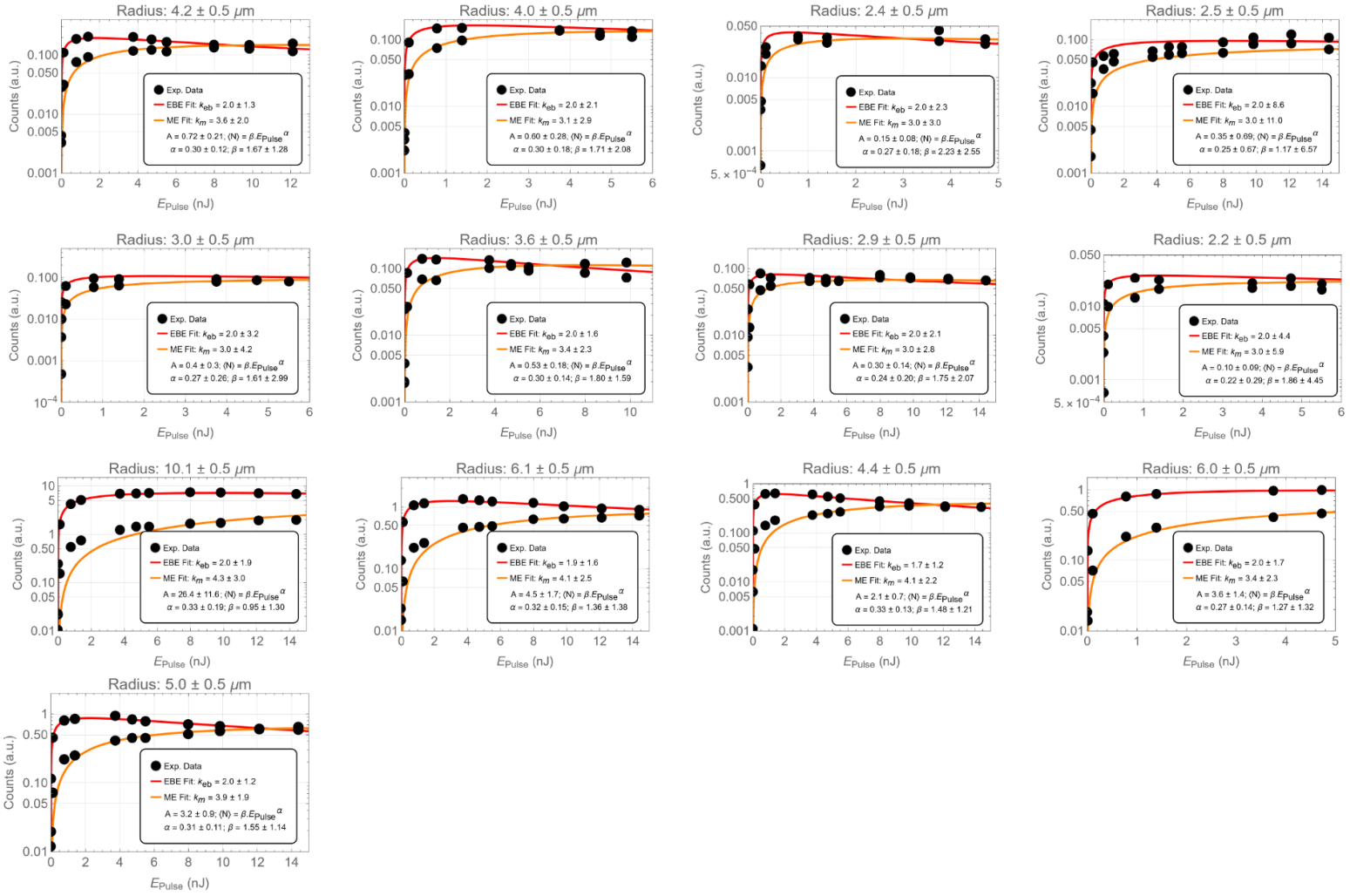

Figure 3-6. Red -Green blend SPs (25% – 75%): Fit of Eq. 2 to the Exciton/Biexciton (EBE) and Multiexciton (ME) peaks for SPs of different sizes.

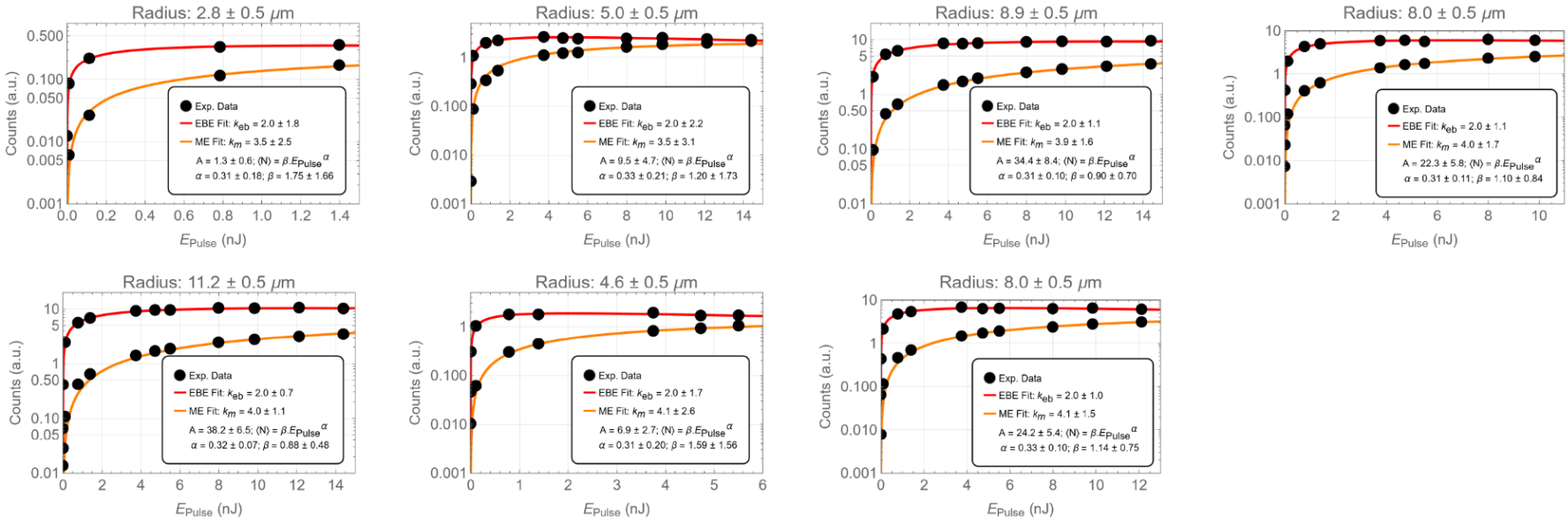

Figure 3-7. Red -Blue blend SPs (75% – 25%): Fit of Eq. 2 to the Exciton/Biexciton (EBE) and Multiexciton (ME) peaks for SPs of different sizes.

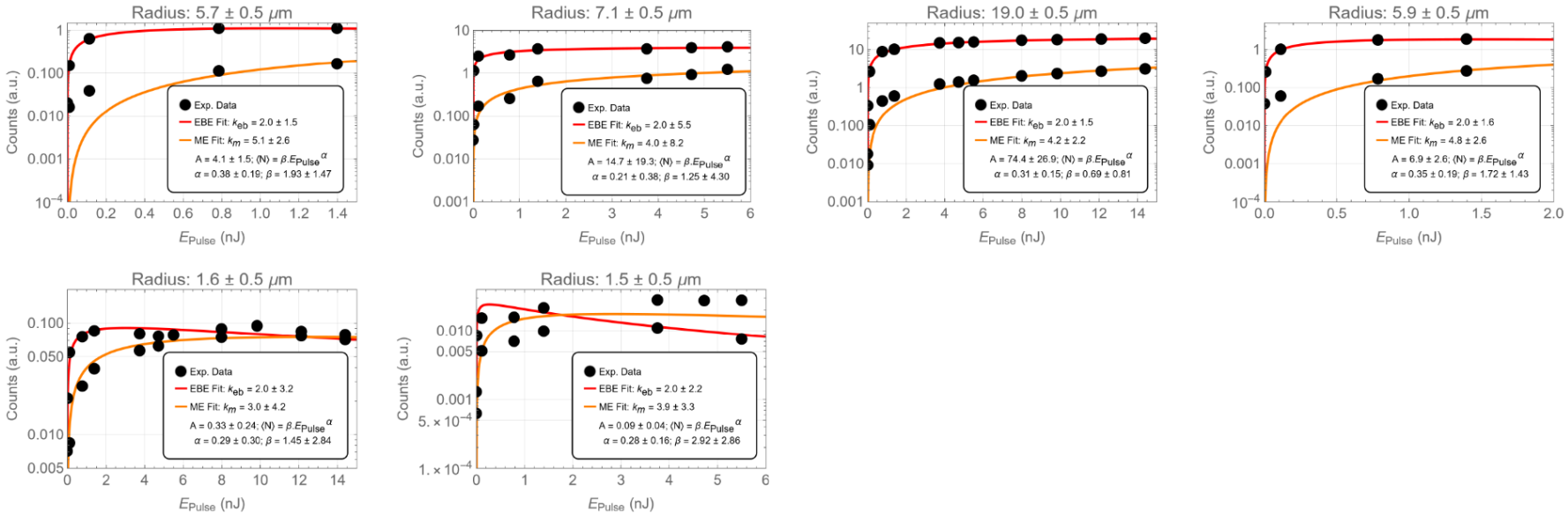

Figure 3-8. Red -Blue blend SPs (50% – 50%): Fit of Eq. 2 to the Exciton/Biexciton (EBE) and Multiexciton (ME) peaks for SPs of different sizes.

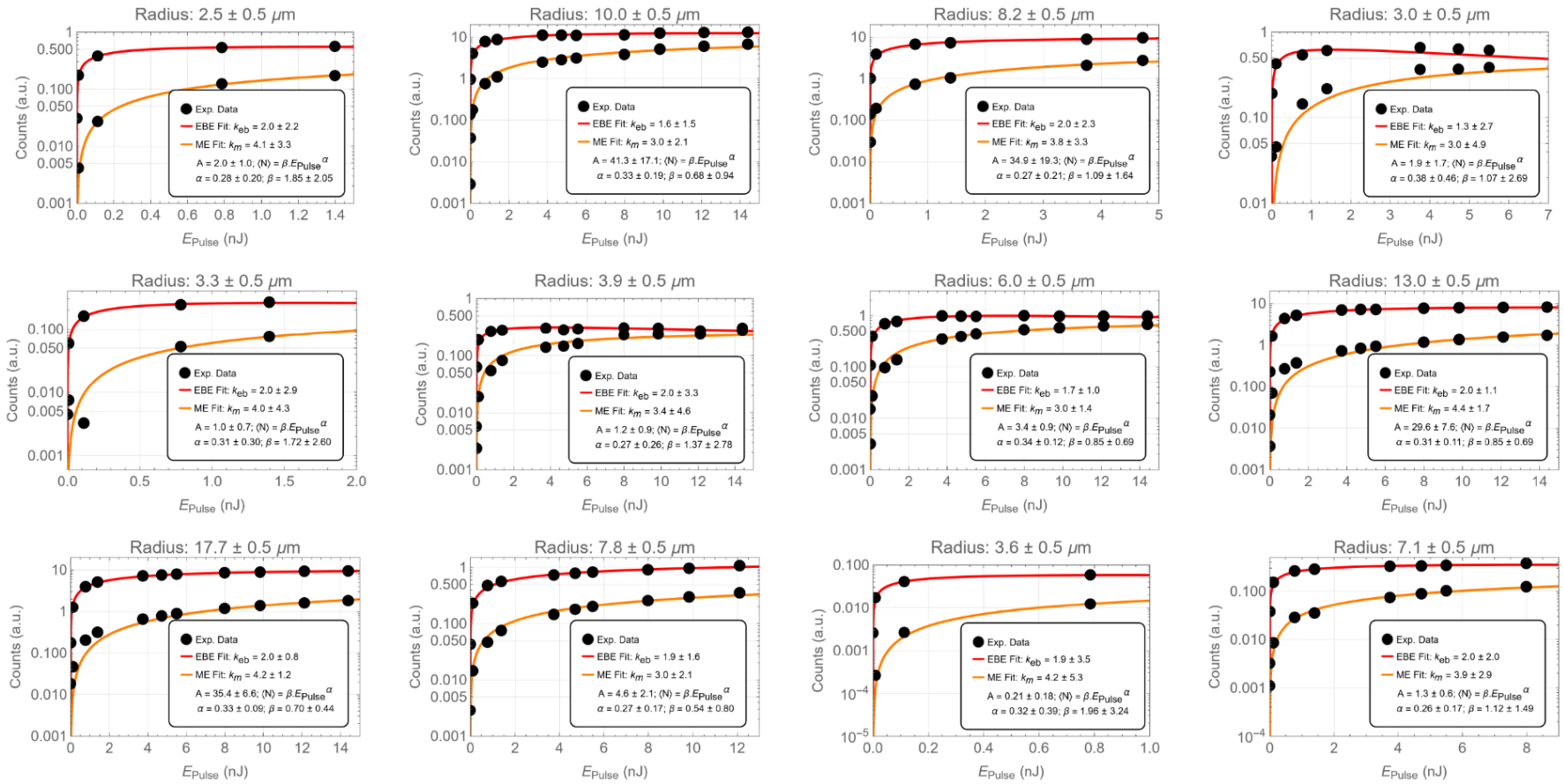

Figure 3-9. Red -Blue blend SPs (25% – 75%): Fit of Eq. 2 to the Exciton/Biexciton (EBE) and Multiexciton (ME) peaks for SPs of different sizes.

3.3.2 Regime Above Laser Threshold

Now that the blended SPs have been characterised below threshold and the fitting parameters are known, the next step is to look at their behavior above threshold. Table 3-3 toTable 3-8 show a compilation of the SPs made of blends that were capable of reaching laser threshold, together with their emission spectra at different energies (below and above lasing threshold: Figure 3-10 to Figure 3-33), estimated threshold energies, radius and calculated average number of excitons per QD in the SP using both the results from the individual fits (Figure 3-4 to Figure 3-9) and the results in the previous section (Figure 3-1). The regime above laser threshold is focused on the red emission. To simplify the readings, the emission of green QDs was cut by plotting the spectra of Red-Green SP for wavelengths above 580 nm. Just like the SPs of red QDs, the SPs of blends studied in this section above threshold oscillate on multiple laser modes whose wavelengths range between 625 nm and 650 nm and each lasing peak had a linewidth limited by the resolution of the spectrometer used.

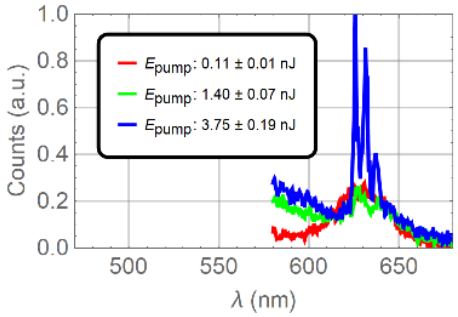

Figure 3-10. PL spectra shown for a Red – Green (75% - 25%) SP with 2.0 ± 0.5 μm in radius at different energy pump levels.

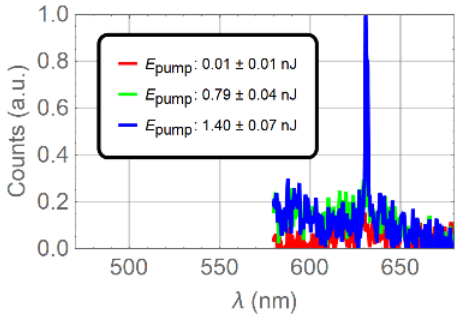

Figure 3-11. PL spectra shown for a Red – Green (75% - 25%) SP with 2.3 ± 0.5 μm in radius at different energy pump levels.

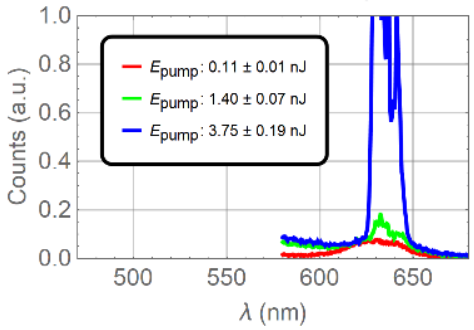

Figure 3-12. PL spectra shown for a Red – Green (75% - 25%) SP with 2.7 ± 0.5 μm in radius at different energy pump levels.

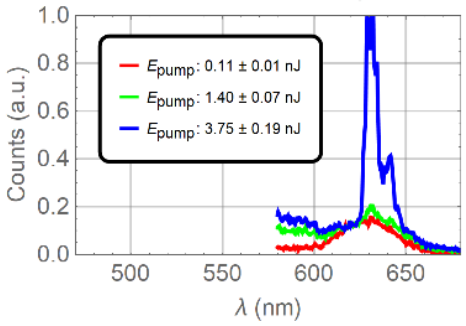

Figure 3-13. PL spectra shown for a Red – Green (75% - 25%) SP with 2.7 ± 0.5 μm in radius at different energy pump levels.

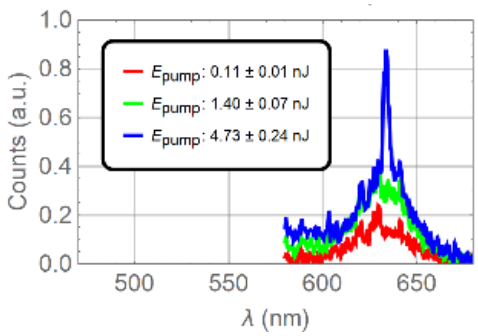

Figure 3-14. PL spectra shown for a Red – Green (75% - 25%) SP with 2.8 ± 0.5 µm in radius at different energy pump levels.

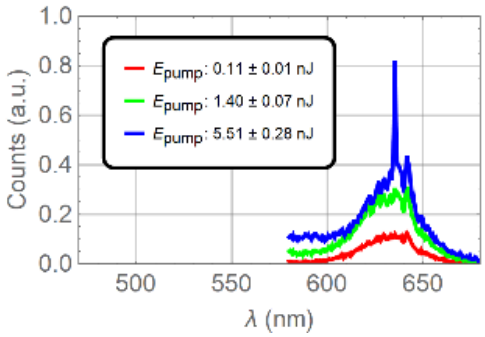

Figure 3-15. PL spectra shown for a Red – Green (75% - 25%) SP with 5.7 ± 0.5 µm in radius at different energy pump levels.

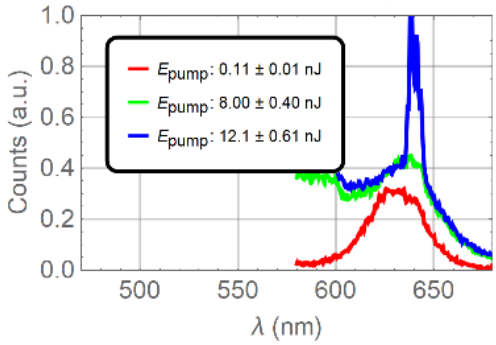

Figure 3-16. PL spectra shown for a Red – Green (75% - 25%) SP with 6.4 ± 0.5 µm in radius at different energy pump levels.

For similar motives to those highlighted in Section 2.7.2, the reason why not all the SPs showed lasing might be related to several factors. Surface roughness or debris on the SPs might hinder the WGMs. Likewise, a non-homogeneous pump fluence or a partial overlap between the pump and the SP can impact the energy threshold. These factors could explain why SPs of similar sizes can have different energy thresholds and estimated average number of excitons, ⟨N⟩.

To simplify the reading of the estimated $\langle N \rangle_{Threshold}$ according to the type of blend, this information has been compiled in Figure 3-34 and Figure 3-35.

Table 3-3. List of Red – Green (75% - 25%) SPs that went above the lasing threshold. The counting of SPs (SP nr) from their lists in Figure 3-4 is made from left to right and top to bottom.

Red – Green: 75% - 25%					
	Radius (μm)	E_{pump} at threshold (nJ)	$\langle N \rangle$ (Figure 3-1)	$\langle N \rangle$ (Figure 3-4)	SP nr
Figure 3-10	2.0 ± 0.5	2.6 ± 1.2	4.0	3.3	5
Figure 3-11	2.3 ± 0.5	1.1 ± 0.3	2.2	2.4	3
Figure 3-12	2.7 ± 0.5	1.4 ± 0.5	2.7	2.3	4
Figure 3-13	2.7 ± 0.5	2.6 ± 1.2	2.4	2.2	7
Figure 3-14	2.8 ± 0.5	3.1 ± 1.7	1.7	2.8	2
Figure 3-15	5.7 ± 0.5	3.5 ± 2.1	1.7	1.9	1
Figure 3-16	6.4 ± 0.5	10.1 ± 2.1	2.2	1.8	11

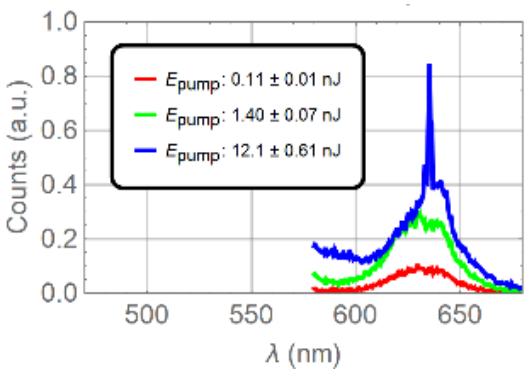

Figure 3-17. PL spectra shown for a Red – Green (50% - 50%) SP with 9.0 ± 0.5 μm in radius at different energy pump levels.

Table 3-4. List of Red – Green (50% - 50%) SPs that went above the lasing threshold. The counting of SPs (SP nr) from their lists in Figure 3-5 is made from left to right and top to bottom.

Red – Green: 50% - 50%					
	Radius (μm)	E_{pump} at threshold (nJ)	$\langle N \rangle$ (Figure 3-1)	$\langle N \rangle$ (Figure 3-5)	SP nr
Figure 3-17	9.0 ± 0.5	10.1 ± 2.1	2.3	2.1	1

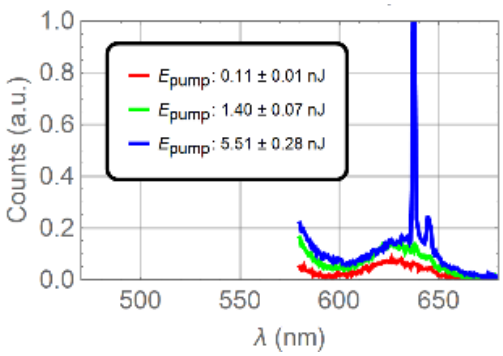

Figure 3-18. PL spectra shown for a Red – Green (25% - 75%) SP with 6.0 ± 0.5 μm in radius at different energy pump levels.

Table 3-5. List of Red – Green (25% - 75%) SPs that went above the lasing threshold. The counting of SPs (SP nr) from their lists in Figure 3-6 is made from left to right and top to bottom.

Red – Green: 25% - 75%					
	Radius (μm)	E_{pump} at threshold (nJ)	$\langle N \rangle$ (Figure 3-1)	$\langle N \rangle$ (Figure 3-6)	SP nr
Figure 3-18	6.0 ± 0.5	3.5 ± 2.1	1.8	2.1	15

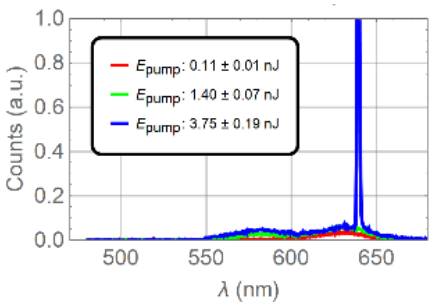

Figure 3-19. PL spectra shown for a Red – Blue (75% - 25%) SP with 2.8 ± 0.5 μm in radius at different energy pump levels.

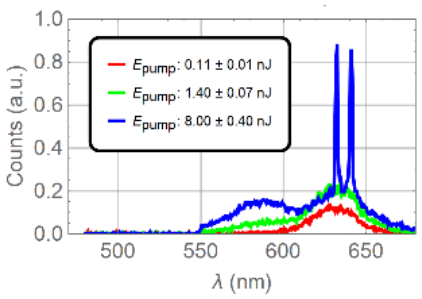

Figure 3-20. PL spectra shown for a Red – Blue (75% - 25%) SP with 4.6 ± 0.5 μm in radius at different energy pump levels.

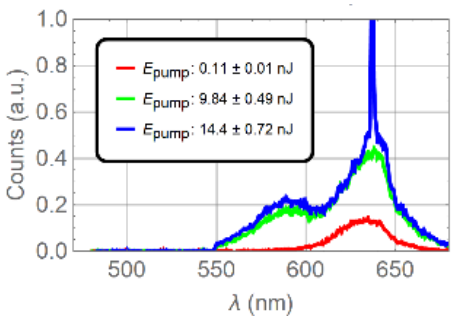

Figure 3-21. PL spectra shown for a Red – Blue (75% - 25%) SP with 8.0 ± 0.5 μm in radius at different energy pump levels.

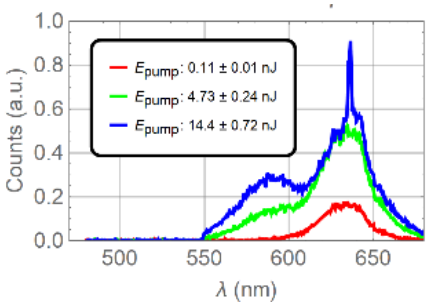

Figure 3-22. PL spectra shown for a Red – Blue (75% - 25%) SP with 8.0 ± 0.5 μm in radius at different energy pump levels.

Table 3-6. List of Red – Blue (75% - 25%) SPs that went above the lasing threshold. The counting of SPs from their lists in Figure 3-7 is made from left to right and top to bottom.

Red – Blue: 75% - 25%

	Radius (μm)	E_{pump} at threshold (nJ)	⟨N⟩ (Figure 3-1)	⟨N⟩ (Figure 3-7)	SP nr
Figure 3-19	2.8 ± 0.5	2.6 ± 1.2	2.4	2.4	1
Figure 3-20	4.6 ± 0.5	4.7 ± 3.3	2.6	2.3	6
Figure 3-21	8.0 ± 0.5	12.1 ± 2.3	2.4	2.4	4
Figure 3-22	8.0 ± 0.5	12.1 ± 2.3	2.6	2.4	7

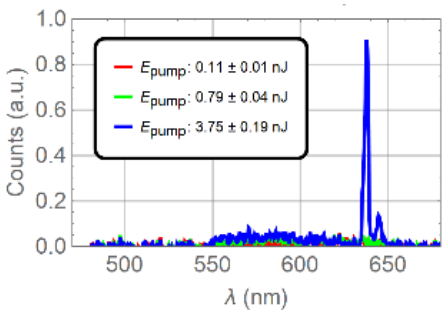

Figure 3-23. PL spectra shown for a Red – Blue (50% - 50%) SP with 1.5 ± 0.5 μm in radius at different energy pump levels.

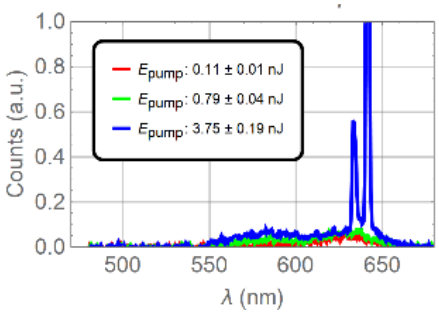

Figure 3-24. PL spectra shown for a Red – Blue (50% - 50%) SP with 3.1 ± 0.5 μm in radius at different energy pump levels.

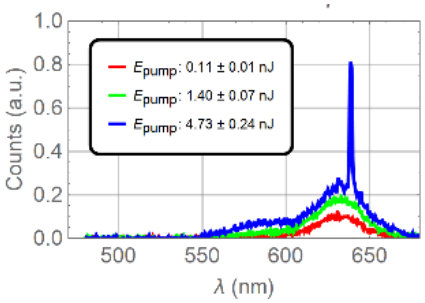

Figure 3-25. PL spectra shown for a Red – Blue (50% - 50%) SP with 5.7 ± 0.5 μm in radius at different energy pump levels.

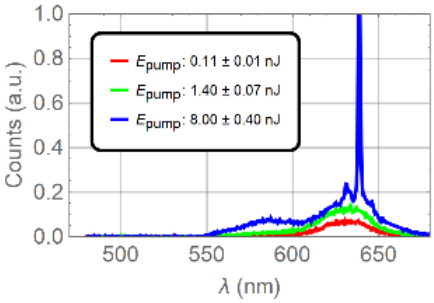

Figure 3-26. PL spectra shown for a Red – Blue (50% - 50%) SP with 5.9 ± 0.5 μm in radius at different energy pump levels.

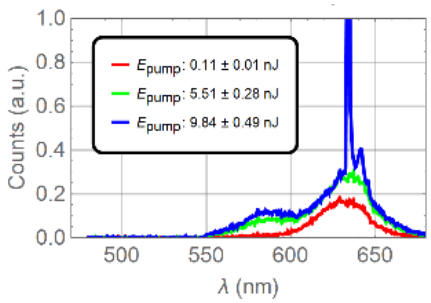

Figure 3-27. PL spectra shown for a Red – Blue (50% - 50%) SP with 7.1 ± 0.5 μm in radius at different energy pump levels.

Table 3-7. List of Red – Blue (50% - 50%) SPs that went above the lasing threshold. The counting of SPs from their lists in Figure 3-8 is made from left to right and top to bottom.

Red – Blue: 50% - 50%

	Radius (μm)	E_{pump} at threshold (nJ)	⟨N⟩ (Figure 3-1)	⟨N⟩ (Figure 3-8)	SP nr
Figure 3-23	1.5 ± 0.5	2.3 ± 1.5	3.7	3.0	8
Figure 3-24	3.1 ± 0.5	2.3 ± 1.5	---	2.4	13
Figure 3-25	5.7 ± 0.5	3.1 ± 1.7	3.0	2.2	1
Figure 3-26	5.9 ± 0.5	4.7 ± 3.3	3.5	2.5	4
Figure 3-27	7.1 ± 0.5	7.7 ± 2.2	1.9	2.8	2

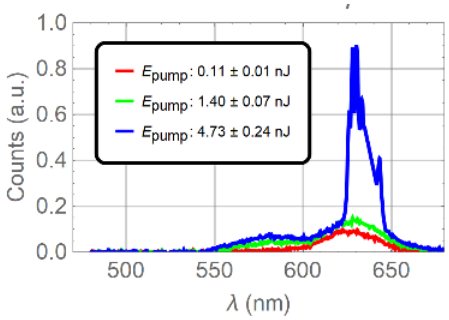

Figure 3-28. PL spectra shown for a Red – Blue (25% - 75%) SP with 2.5 ± 0.5 μm in radius at different energy pump levels.

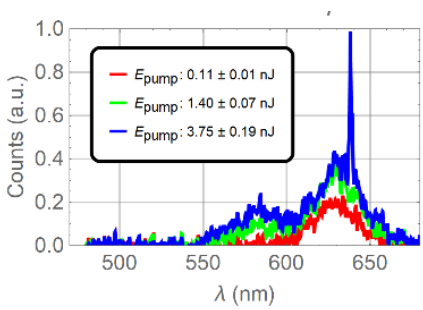

Figure 3-29. PL spectra shown for a Red – Blue (25% - 75%) SP with 3.3 ± 0.5 μm in radius at different energy pump levels.

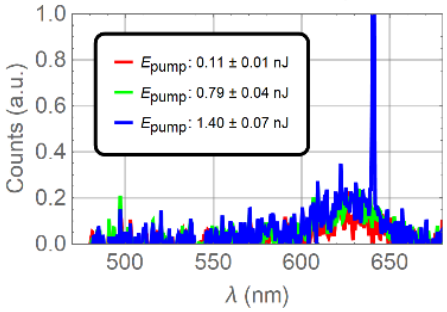

Figure 3-30. PL spectra shown for a Red – Blue (25% - 75%) SP with 3.6 ± 0.5 μm in radius at different energy pump levels.

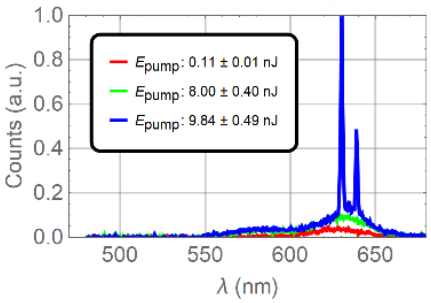

Figure 3-31. PL spectra shown for a Red – Blue (25% - 75%) SP with 7.1 ± 0.5 μm in radius at different energy pump levels.

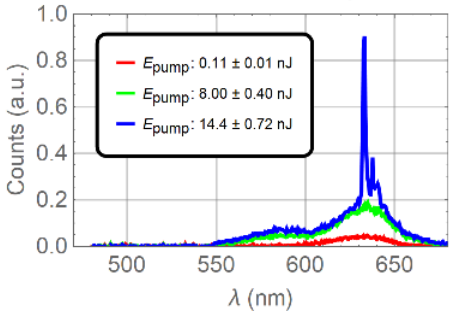

Figure 3-32. PL spectra shown for a Red – Blue (25% - 75%) SP with 7.8 ± 0.5 μm in radius at different energy pump levels.

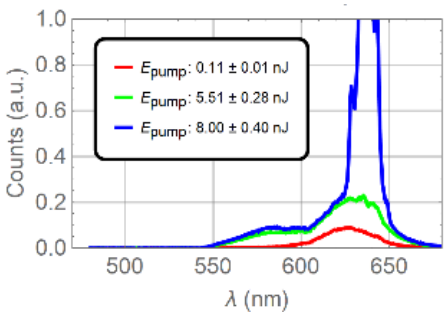

Figure 3-33. PL spectra shown for a Red – Blue (25% - 75%) SP with 8.2 ± 0.5 μm in radius at different energy pump levels.

Table 3-8. List of Red – Blue (25% - 75%) SPs that went above the lasing threshold. The counting of SPs from their lists in Figure 3-9 is made from left to right and top to bottom.

Red – Blue: 25% - 75%					
	Radius (μm)	E_{pump} at threshold (nJ)	⟨N⟩ (Figure 3-1)	⟨N⟩ (Figure 3-9)	SP nr
Figure 3-28	2.5 ± 0.5	3.1 ± 1.7	2.5	2.5	1
Figure 3-29	3.3 ± 0.5	2.6 ± 1.2	2.3	2.0	5
Figure 3-30	3.6 ± 0.5	1.1 ± 0.3	2.0	1.4	11
Figure 3-31	7.1 ± 0.5	8.9 ± 0.9	2.0	1.8	12
Figure 3-32	7.8 ± 0.5	11.2 ± 3.2	1.0	1.8	10
Figure 3-33	8.2 ± 0.5	6.8 ± 1.2	1.8	1.5	3

Under the same pump conditions, the $\langle N \rangle_{Threshold}$ behaves differently for blended SPs and the red SPs studied in Chapter 2. Figure 3-34 shows a compilation of the data in this work (red and blended SPs, Table 2-2 and Table 3-3 to Table 3-8, respectively). For small spheres, the $\langle N \rangle_{Threshold}$ is relatively high in both cases ($2 < \langle N \rangle_{Threshold} < 3.5$). This could be due to the lower Q-factors associated to smaller spherical cavities, where the WGM optical path lengths are closer to the resonance wavelengths, the chances of coupling photons are lower, and therefore on average QDs need higher populations of excitons to achieve laser conditions.

For larger SPs, the $\langle N \rangle_{Threshold}$ decays slower in blended SPs when comparing to the red SPs. This led to the observation of larger SPs capable of laser emission in the case of blended SPs. Red SPs in these experiments have only reached laser threshold for radius up to approximately 5 μm, whereas blends of SPs reached laser threshold for sizes of approximately 10 μm (radius 2× bigger) and this value was only limited by the size of the SPs during their synthesis. Syntheses yielding larger blended SPs could potentially produce bigger SPs capable of reaching laser threshold. The slower $\langle N \rangle_{Threshold}$ decay in blended SPs could be due to a lower density of red QDs in the SP that in turn requires more excitons per each of those QDs to reach laser threshold. Red SPs possess the highest density of red QDs so their $\langle N \rangle_{Threshold}$ decays quicker as the sphere becomes bigger and the Q-factor increases.

Nevertheless, once red SPs get close to 4 µm in radius, internal factors (i.e. self-absorption, non-radiative recombination processes) and external factors (i.e. pump conditions such as the spot size) overcome the gain in the material and prevent them from achieving lasing.

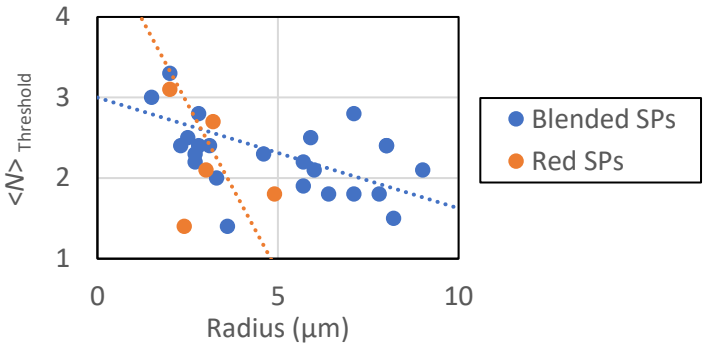

Figure 3-34. Average number of excitons per QD in the SP at laser threshold, $\langle N \rangle_{Threshold}$, as a function of the SP radius. The plot compares the results for red and blended SPs. Data on the red and blended SPs can be found in Table 2-2 and Table 3-3 to Table 3-8, respectively. The $\langle N \rangle_{Threshold}$ was calculated from the individual spectra of each SP and the dashed lines are linear regressions for each set of data, simply to help visualizing the trends.

Data suggests that using a second higher bandgap type of CQD in the synthesis of SPs inhibits non-radiative recombination of electron-hole pairs in QDs and self-absorption of red emission. These deductions derive from the fact that blended SPs were able to reach laser threshold for larger radii, where the WGMs occur for longer optical paths and processes such as self-absorption or non-radiative recombination interfere with the gain of the material required for laser.

Having a closer look exclusively at the blended SPs (Figure 3-35), the data suggests that for SPs of blends with higher ratios of red QDs (75% and 50%), those with blue QDs need higher $\langle N \rangle_{Threshold}$ to achieve lasing, when compared to blends with green QDs. This could be due to the passive behaviour of blue QDs (slow self-absorption in the red and scatter light) when compared to the active and passive behaviour of green QDs (not only do they slow self-absorption in the red and scatter light, but they also contribute to the pumping of red QDs via energy transfer or radiatively).

For lower ratios of red QDs (25%), blue blends become the SPs with lower $\langle N \rangle_{Threshold}$, likely because their passive behaviour is more efficient that the partial absorption and active behaviour of blends with green QDs.

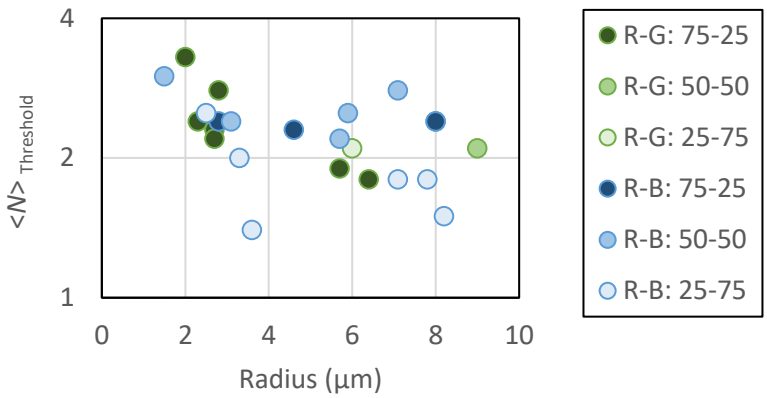

Figure 3-35. Average number of excitons per QD in the SP at laser threshold, $\langle N \rangle_{Threshold}$, as a function of the SP radius. The plot compares the results between blended SPs. Data on the blended SPs can be found in Table 3-3 to Table 3-8, respectively. The $\langle N \rangle_{Threshold}$ was calculated from the individual spectra of each SP.

The next two sections look at the effects blending QDs with other higher bandgap QDs have on the self-absorption of SPs (Section 3.4) and their implications on the Q-factor of SPs (Section 3.5).

3.4 Reduction of Self-Absorption in SPs

Self-Absorption in SPs was evaluated by measuring the PL peak in the red spectrum of each SP in the sample, for a given blend and for a given pump energy. These measurements were done on the same µPL setup as in Section 2.5. A representation of the distribution of PL peak values as a function of the pump energy can be seen below (Table 3-9). The red CQDs used in this experiment are the same as those in Chapter 2 and have a peak emission in dilute solution of 630 nm. Due to the overlap between emission and absorption in these CQDs (small Stokes shift), self-absorption occurs. This is exacerbated when at high concentrations, when non-radiative energy transfer can also take place, like in solid-state thin films or in SPs. The result is a shift of the PL spectrum towards higher wavelengths.

Table 3-9. Representation of the PL peak distribution in the red spectrum for red CQDs and its blends of green and blue at different ratios.

Batch 1: Red CQDs

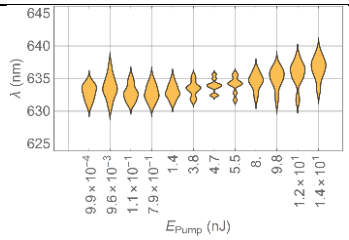

Batch 2, 3 and 4: Red - Green CQDs

25%-75%	50%-50%	75%-25%
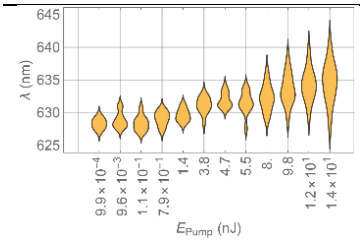	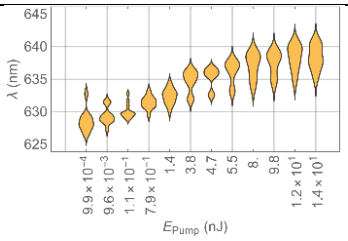	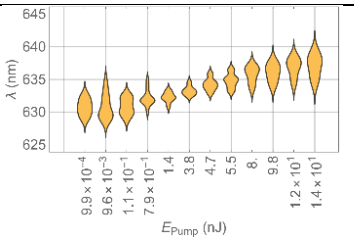

Batch 5, 6 and 7: Red - Blue CQDs

25%-75%	50%-50%	75%-25%
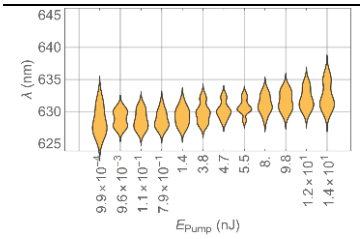	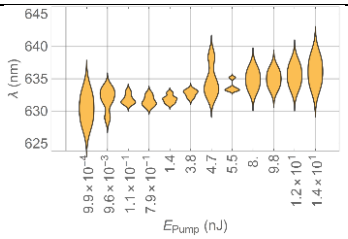	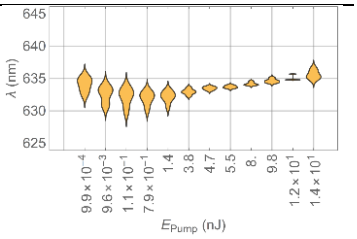

The 1st batch, which includes SPs exclusively of red CQDs, demonstrates that shift in the solid state. For low pump energies, the PL peak is approximately at 634 nm. As the pump energy is increased, self-absorption (or radiative energy transfer) should diminish due to filling of the lower energy states. However, for higher pump energies it goes up to almost 640 nm. This effect could be explained by the volume of the SP. At low pump energies, emission from the surface of the SP dominates and self-absorption of light by CQDs at the surface or near it is minimal – the red-shift in the emission of these SPs when compared to the emission of CQDs in diluted solution is then mostly caused by non-radiative energy transfer. As the pump energy is increased, emission of CQDs deeper within the SP contributes more and more to

the detected PL spectrum. Emission of such CQDs has a higher chance of interacting with CQDs from the outer layers and therefore it increases the likelihood of self-absorption. Non-radiative energy transfer and self-absorption should explain, at least partially, the red shift dynamics according to the pump energy.

The addition of green CQDs reduces the density of red CQDs and therefore the self-absorption of red photons. For low energies, there is a noticeable impact as the PL peaks registered almost no shift when compared to the emission of red CQDs in solution. This shows that non-radiative energy transfer is reduced. Nevertheless, for higher pump energies, these tend to the same peak values as in red SPs. Therefore, while the density is lowered, self-absorption is still significant for light emitted from within the SP. The 2nd batch (red-green 25%-75%) was able to maintain the PL peak value around 630 nm up to approximately 2 nJ. By increasing the red CQD percentage to 50, the 3rd batch had this value decreased to approximately 0.1 nJ. For SPs with only 25% of green CQDs, the PL peak in the 4th batch already starts slightly shifted for the lowest energy pump measurements.

The blend of blue and red CQDs is decreasing self-absorption even further. This is because blue CQDs do not absorb pump light nor the emission of red CQDs, increasing the chances of this red emission to escaping the SPs without being self-absorbed. In contrast, green CQDs can absorb some of the pump light and transfer this absorbed energy (radiatively and non-radiatively) to red CQDs; in a way this improves the emission of red CQDs and therefore enhances the emission from CQDs deeper in the SP structure that is detected. As discussed before, this emission is likely to be reabsorbed before it leaves the SP, leading to a red-shift. The 5th batch showed no signs of self-absorption up to 5 nJ, and the 6th batch up to approximately 1 nJ. Although the 7th batch showed signs of self-absorption for low energies, the rate at which the peak is shifted is slower that the red SPs or the blends of red and green SPs.

3.5 Enhancement of the Q-factor

This section covers the effect blends have on the Q-factor of SPs. To study this effect, two SPs (both 6.0 ± 0.5 µm in diameter) were selected from the synthesized batches, one containing exclusively red CQDs (batch 1) and the other containing the blend of red-green CQDs (batch 4)[31]. The size of the SPs was measured optically with a microscope and verified

by the pseudo FSR of their cavities, $\Delta\nu_{n,l}^{\Delta l} \approx \frac{c}{2\pi.N.a}$, where the radius a of a sphere with refractive index N can be expressed by the spacing between two consecutive modes with the same polarization [199]. The Q-factor, $Q = \frac{\lambda}{\Delta\lambda}$, was calculated from the resonance centre wavelength, λ, and the resonance peak width at full width half maximum, Δλ, below lasing threshold [199].

Emission below and above lasing threshold of the red SP is shown in Figure 3-36, together with the respective micrographs in Figure 3-37. The red SP had its Q-factor estimated from the modes highlighted in grey on the normalized emission below threshold and its Fourier transform ($Q \approx 135 \pm 19$). As seen in Chapter 2, the Fourier transform is used to decompose the spectrum of a SP (e.g. Figure 2-8b) into their spatial frequency within the range of interest (Figure 2-8c). This helps with the reading of the spacing between modes, which can then be individually analysed to calculate the Q-factor. The lasing threshold of this red SP was around 12 mJ.cm^{-2} (Figure 3-38), but for fluences above 20 mJ.cm^{-2} the emission rolls over, likely due to electron–hole separation, charge diffusion and nonradiative recombination [209].

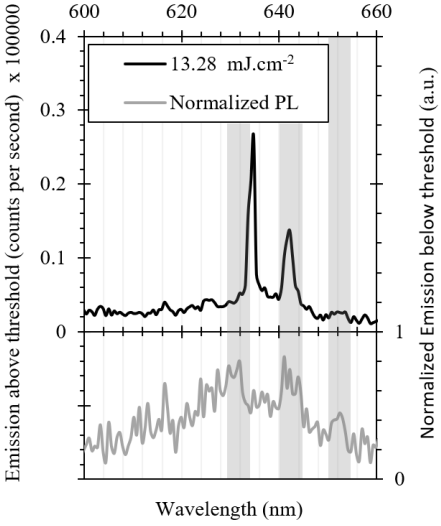

Figure 3-36. Emission of the red SP above (13.3 mJ.cm^{-2}) and below (normalized PL) lasing threshold.

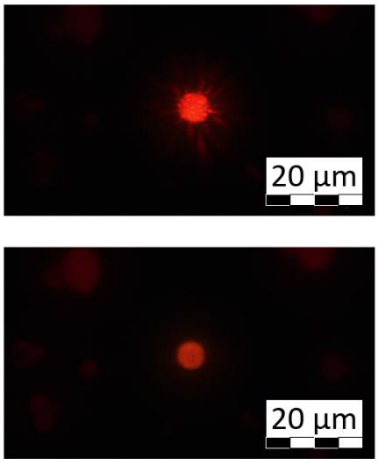

Figure 3-37. Microscope images of the red SP below and above lasing threshold.

Emission data above and below lasing threshold for the blended SP are shown in Figure 3-39 to Figure 3-41. The presence of green CQDs reduces the density of red CQDs and therefore

diminishes exciton diffusion and self-absorption at the laser transition as discussed previously. The enhanced Q-factor ($Q \approx 340 \pm 60$) extracted for this blended SP is ascribed to this reduction in energy transfer and self-absorption.

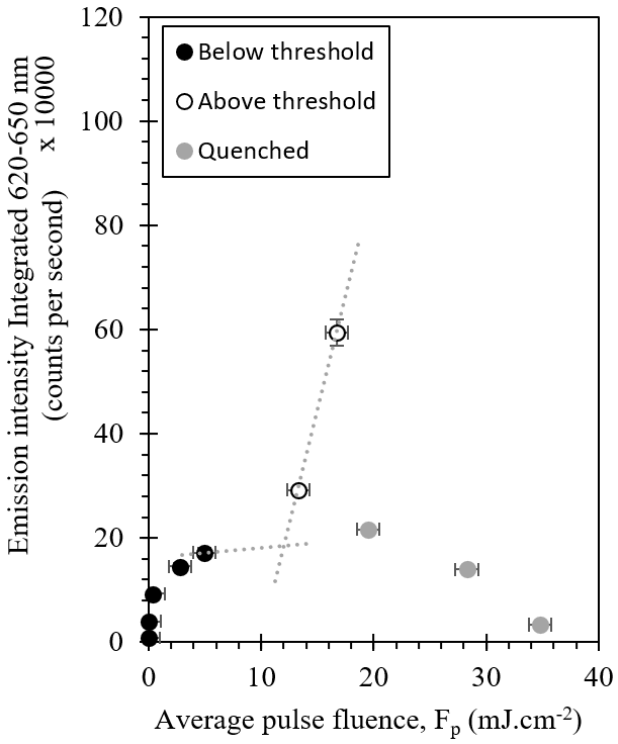

Figure 3-38. Laser transfer function of the red SP.

The higher Q of the blend SP is also reflected in the lower slope above threshold (Figure 3-41). The effect of a lower density of the red CQDs on the modal gain is not only mitigated by the lower exciton diffusion but also by the fact that green CQD can act as donors. In turn the lasing threshold is not affected significantly (12 – 14 mJ.cm^{-2}), and the SP laser is able operate at higher intensity without rolling over (Figure 3-41).

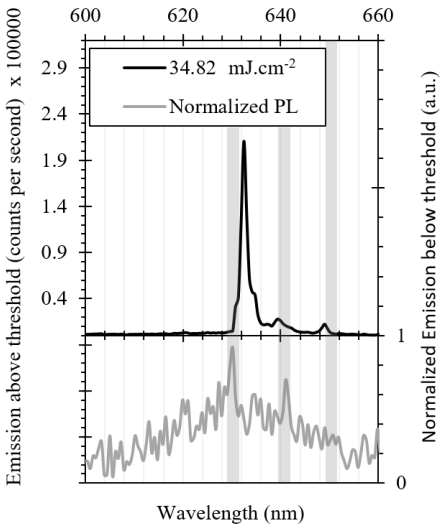

Figure 3-39. Emission of the blended SP above (34.8 mJ.cm^{-2}) and below (normalized PL) lasing threshold.

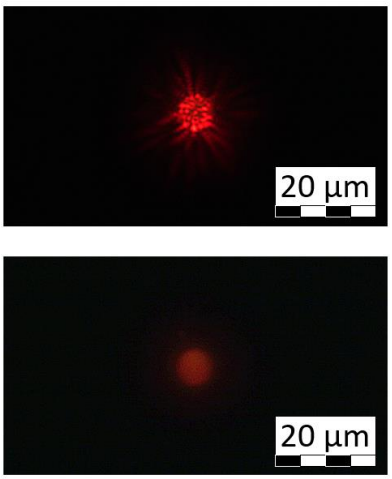

Figure 3-40. Microscope images of the blended SP below and above lasing threshold.

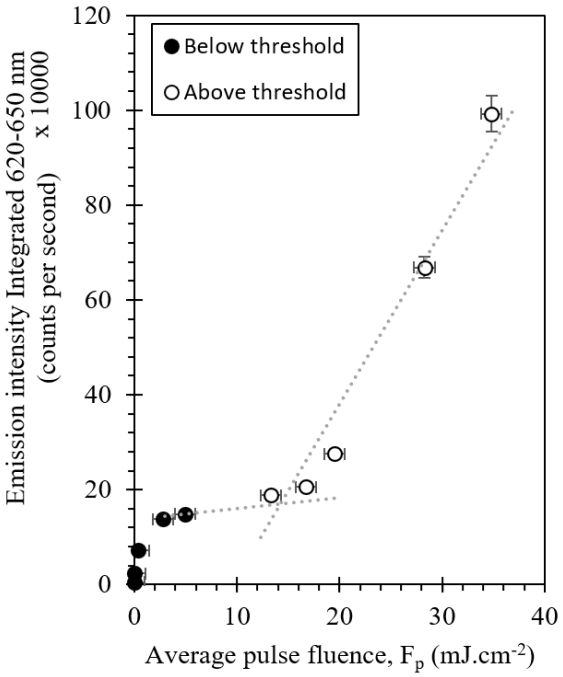

Figure 3-41. Laser transfer function of the blended SP.

3.6 Multicolour Lasers

Studies on blended SPs presented in previous sections include blending red CQDs with CQDs of higher bandgaps (green; blue) that are also higher or very close to the emission of the

optical pump (green). However, it would also be interesting to study if multicolour lasing can be observed when the higher bandgap CQDs also absorb in the optical pump wavelength (e.g. yellow CQDs).

Single colour laser oscillation has been demonstrated with CQDs, but prior to this work no reports had been made regarding multicolour laser oscillation on self-assembled SPs. Such multicolour lasers could pave the way for a broad range of applications including miniature tunable lasers, high density colour displays and sensing devices [210].

In this section, a heterostructure SP made with an appropriate blend of yellow-red CQDs is used to demonstrate multicolour lasing in individual SPs and its optical properties are compared to SPs of exclusively yellow or red CQDs.

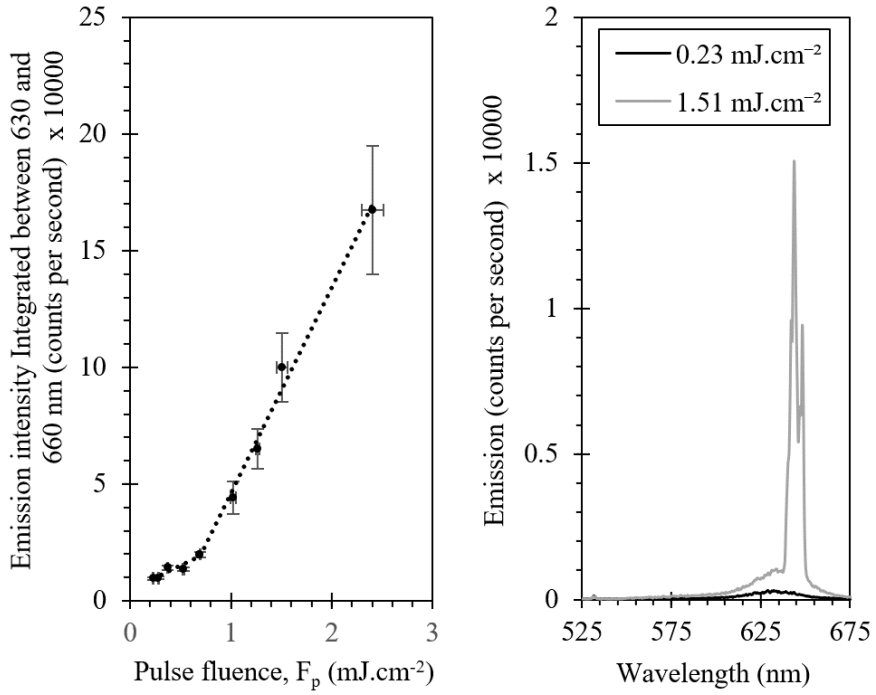

Figure 3-42. Laser transfer function of a red SP (diameter: 7.6 µm) and its typical spectrum below and above threshold.

Figure 3-42 and Figure 3-43 show the typical emission intensity responses of a red SP laser (intrinsic CQD emission at 630 nm, laser emission at 640 nm) and a yellow SP laser (intrinsic CQD emission at 575 nm, laser emission in the orange at 590 nm-595 nm) as a function of the pump fluence, as well as their characteristic PL below and above threshold.

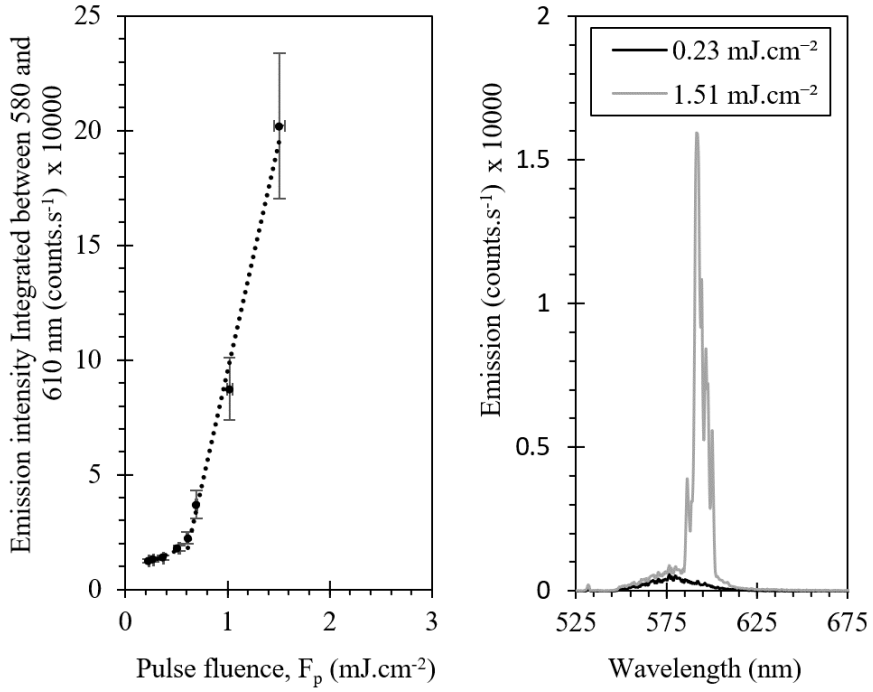

Figure 3-43. Laser transfer function of a yellow SP (diameter: 6.8 µm) and its typical spectrum below and above threshold.

For both single colour lasers, the threshold fluence was between 0.5 and 0.7 mJ.cm^{-2}. Note that the lowest fluence at threshold here is attributed to the different setup and beam spot size (see Section 3.3), which led to a better pump and SP overlap, leading to more efficient pumping. It is not because these SP have lower threshold intrinsically.

To test if multicolour laser oscillation could be obtained with a single SP, the third batch of SPs was prepared with 50 % of red CQDs and 50 % of yellow CQDs (Figure 3-44).

Depending on the pump fluence, three laser regimes were observed. In the first regime, the first modes to go above the lasing threshold were in the red band and this happened approximately at the same fluence as their single wavelength counterparts (0.5 to 0.7 mJ.cm^{-2}). For the second regime, at around 2.0 mJ.cm^{-2}, modes in the yellow band started to oscillate while the modes in the red band started to lose energy. Stable dual colour lasing was obtained at approximately 2.4 mJ.cm^{-2} (Figure 3-44). The third regime, at higher fluences, had the modes in the yellow band dominating the emission spectrum whilst modes in the red returned to their below threshold state.

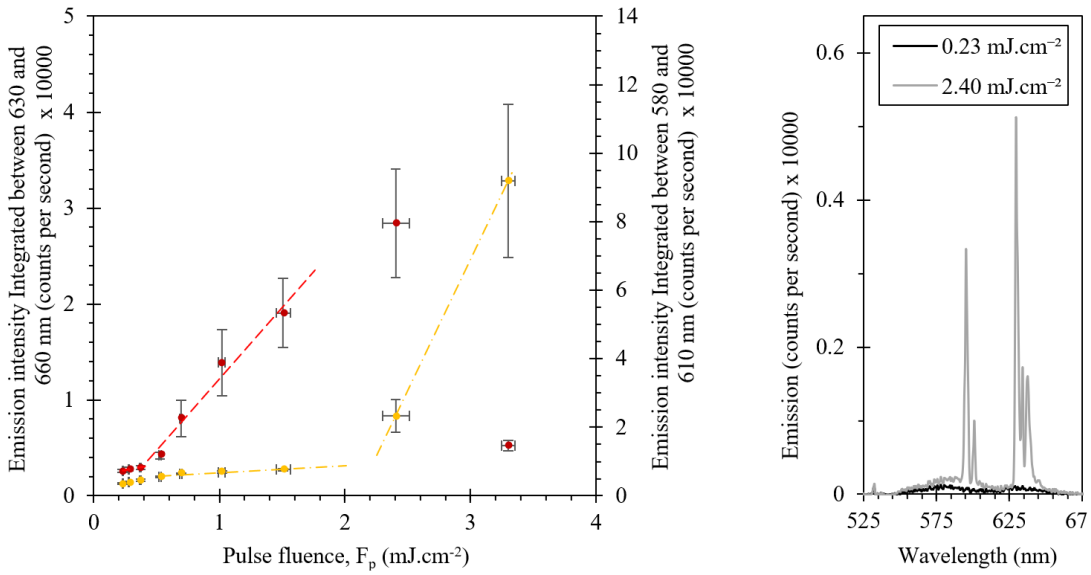

Figure 3-44. Laser transfer function of a multicolour SP (diameter: 6.4 µm) and its typical spectrum below and above threshold. The laser transfer function of the multicolour SP has the red emission (630 – 660 nm) plotted on the left y-axis and the yellow emission (580 – 610 nm) plotted on the right y-axis.

3.7 Conclusion

It has been shown that blending CQDs during the synthesis of SPs is a way to control, in some cases enhance, the properties of these sources.

Self-absorption of red CQDs in SPs has decreased by blending them with higher bandgap CQDs. This allowed an enhancement of the Q-factor, an increase in the cavity size, and an increase in the emission intensity per QD in self-assembled microsphere CQD lasers.

If the bandgaps of the CQDs present in a SP are lower than the emission of the pump, multicolour lasing can also be observed. Three lasing regimes were successfully demonstrated in a single SP, as a function of the pump fluence (namely single colour red, single colour yellow and simultaneous dual colour red and yellow).

These findings represent important steps towards the design of higher quality CQD microcavities with multicolour lasing capabilities and have great application potential for integrated circuits, imaging, sensing and novel photonic materials [30], [198].

Chapter 4. Integration of Nanocrystal Microspheres in Optical Systems

Moving and integrating SPs into other devices is a required step to use SPs to their full potential. This chapter covers a successful way of doing so via transfer-printing (TfP), a "pick up and release" approach where a stamp retrieves loosely bound samples from a donor substrate and places them onto the receiving substrate [203], [211]–[213]. The term TfP was chosen over the traditionally used TP or μTP to avoid confusion with acronym already given in this thesis to tetrapods. As proof of concept of integration of SPs into other devices, TfP was used to couple a SP onto a waveguide and this coupling was optically studied.

4.1 Mechanics of Transfer Printing

Kinetically controlled transfer printing is described by the interaction between two interfaces: the interface between the stamp and the ink and the interface between the ink and the substrate.

Although the term 'ink' is usually associated to a liquid substance, it is here used to denote the material to be transferred with the TfP equipment, in this case the SPs.

The TfP reported here used a custom-made polymer μ-stamp of PDMS in a modified dip-pen nano-lithography system to pick up and move SPs with sub-micron resolution [214]. An auxiliary camera embedded in the system allowed the user to control the TfP process [215].

4.1.1 Physics of Transfer Printing

The μ-stamp of PDMS is applied onto an ink on a donor substrate which leads to conformal contact and adhesion driven by van der Waals interactions. Here, the adhesion between the ink and the stamp is sensitive to the rate at which the stamp separates from the donor, to

the temperature and to its viscoelasticity. Polymers like PDMS exhibit viscoelasticity (an elastic and viscous behaviour) when subjected to stress. This means that when PDMS or similar materials are no longer under stress, their elasticity allows molecules to slowly recover their former spatial arrangement and the strain slowly returns to zero. Their viscosity implies that these materials exhibit a time-dependent strain [216].

When the µ-stamp is peeled from the donor substrate with enough velocity, the adhesion is strong enough to lift the ink from the donor onto the surface of the µ-stamp (Figure 4-1a). Likewise, when the µ-stamp is brought into contact with the receiving substrate and removed with a lower velocity, the adhesion between the ink and the µ-stamp becomes relatively weak and allows the ink to adhere preferentially to the receiving substrate (Figure 4-1b) [217].

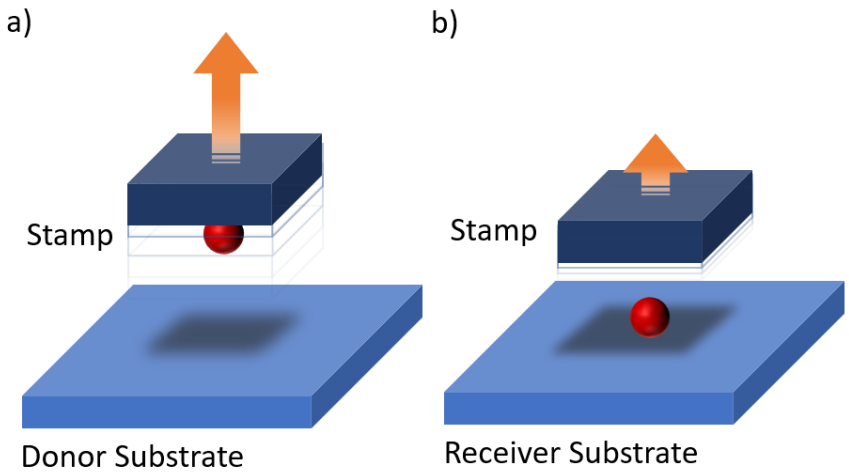

Figure 4-1. Schematic of the "retrieval" (a) and "printing" or "releasing" (b) of a SP (ink), which correspond to the two process flows for kinetically controlled transfer printers [218].

The energy release rate G for steady-state velocity is often measured experimentally and is related to the peel force F and µ-stamp width, w, [217]:

$$G = \frac{F}{w} \qquad \text{(Eq. 17)}$$

If the donor and receiver substrates are the same, then the energy release rate between the µ-stamp and ink ($G^{stamp\&ink}$) must be higher than the energy release rate between the ink and substrate ($G^{ink\&substrate}$) for retrieval, and lower than the energy release rate between the ink and substrate ($G^{ink\&substrate}$) for releasing [217]:

Retrieval: $G^{ink\&substrate} < G^{stamp\&ink}(v)$ (Eq. 18)

Release: $G^{ink\&substrate} > G^{stamp\&ink}(v)$ (Eq. 19)

In this case, the elastic nature of both the rigid ink and the substrate implies that $G^{ink\&substrate}$ is independent of the μ-stamp peeling velocity. On the other hand, due to the viscoelastic properties of the μ-stamp, the μ-stamp energy release rate $G^{stamp\&ink}$depends on the peeling velocity. The critical peel velocity for each μ-stamp/ink/substrate system that separates the retrieval and releasing regimes and determines the direction of transfer can be expressed as [217]:

$$G^{stamp\&ink}(v) = G_0\left[1 + \left(\frac{v}{v_0}\right)^n\right] \qquad \text{(Eq. 20)}$$

where G_0 is the critical energy release rate when the peeling velocity v approaches zero, v_0 is the reference peeling velocity at which the critical energy release rate doubles to G_0, and the exponent n is a scaling parameter determined experimentally. This equation has been shown to hold for either low or high peel velocity, for a wide range of temperatures, and for different types of interfaces [217].

The critical velocity, v_c, that separates the retrieval and release regimes in the kinetically controlled transfer printing can be determined from the following two-equation system:

$$\begin{cases} G_{crit}^{ink\&substrate} = G_{crit}^{stamp\&ink}(v) \\ G_{crit}^{stamp\&ink}(v) = G_0\left[1 + \left(\frac{v_c}{v_0}\right)^n\right] \end{cases} \qquad \text{(Eq. 21)}$$

This happens when the energy release rate between the ink and substrate matches the energy release rate between the μ-stamp and the ink (Eq. 21, 1st equation). As mentioned before, assuming that the elastic behaviour between the ink and substrate does not depend on the peeling velocity ($G^{ink\&substrate} = cte$), and the viscoelastic behavior between the μ-stamp and ink is given by Eq.21, 2nd equation, then the critical peeling velocity, v_c, is found by solving Eq. 21:

$$v_c = v_0\left(\frac{G_{crit}^{ink\&substrate} - G_0}{G_0}\right)^{\frac{1}{n}} \qquad \text{(Eq. 22)}$$

Until here, the ink has been considered as a solid thin film. However, this is not the case when working with SPs or similar structures, as they do not cover the full surface between μ-stamp and substrate. If the fraction f, ranging between 0 and 1, ($0 < f < 1$) accounts for the portion of surface on the μ-stamp that is covered by SPs, then the steady state peel forces and energy release rates are given by:

$$\text{Retrieval:} \qquad F_{retrieval} = w.G_{retrieval}^{average}(v) \quad \text{(Eq. 23)}$$

$$\text{With} \quad G_{retrieval}^{average}(v) = f.G^{ink\&substrate} + (1-f).G^{stamp\&substrate}(v) \quad \text{(Eq. 24)}$$

And:

$$\text{Release:} \qquad F_{release} = w.G_{release}^{average}(v) \quad \text{(Eq. 25)}$$

$$\text{With} \quad G_{release}^{average}(v) = f.G^{stamp\&ink}(v) + (1-f).G^{stamp\&substrate}(v) \quad \text{(Eq. 26)}$$

It is also interesting to note that the comparison between the average energy release rates for retrieval and release, $G_{retrieval}^{average}(v) = G_{release}^{average}(v)$, is independent of the microstructure size, shape, spacing or distribution, and yields the same results as Eq. 18 – 19.

Figure 4-2 illustrates an example of energy release rates $G^{ink\&substrate}$ and $G^{stamp\&ink}(v)$ as a function of the peeling velocity. The critical velocity (Eq. 22) is here represented at the intersection between the two energy release rates. Higher velocities than the point of intersection promote retrieval of ink and lower velocities promote release of ink [217].

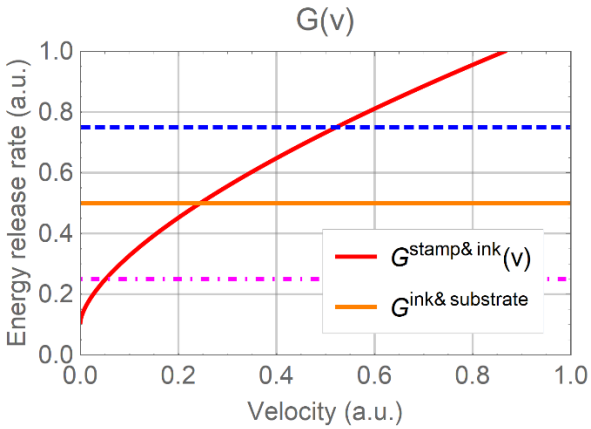

Figure 4-2. Schematic diagram of critical energy release rates for the ink&substrate interface and for the stamp&ink interface. The intersection of the horizontal line in the middle with the curve represents the critical peel velocity for the kinetically controlled transfer printing. Velocities below this point promote the "retrieving" of the object, and velocities above this point promote the "release" of the object. The horizontal lines at the bottom and top represent very weak and very strong ink/substrate interfaces, respectively. Adapted from [217].

Another important parameter is the influence of temperature on the viscoelasticity of the μ-stamp, which changes its peeling velocity. The dependence of the energy release rate on the temperature can be expressed as $G^{stamp\&ink} = G^{stamp\&ink}(v.\alpha_T)$ [217], where α_T corresponds to a temperature shift factor given by [219]:

$$log\ _{10}\alpha_T = -c_1 \frac{T-T_g}{c_2+T-T_g} \qquad \text{(Eq. 27)}$$

Where T and T_g are the current and glass transition temperatures of the μ-stamp, and c_1 and c_2 correspond to fit parameters that depend on the type of polymer the stamp is made [219]. This expression tends to be very accurate specially for temperature values close to the glass transition temperature [217].

Figure 4-3 illustrates how much of an impact temperature can have on the energy release rate, and therefore consequences on the retrieval and release processes.

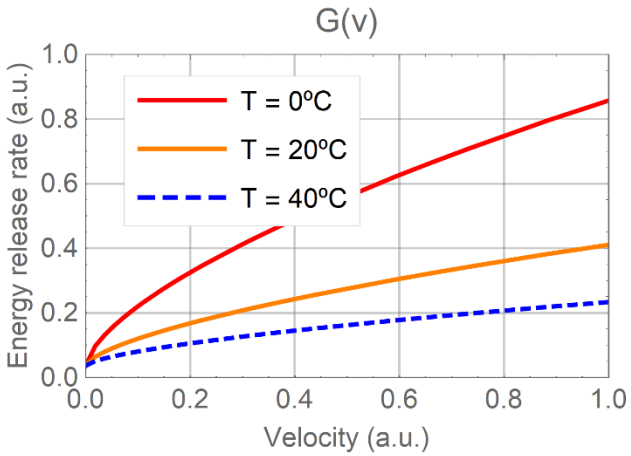

Figure 4-3. Illustration of energy release rates for three different temperatures (0, 20 and 40 °C). Adapted from [217].

Similarly to what has been done by solving Eq. 21, the critical peeling velocity can also be estimated as a function of the temperature by taking into account the temperature shift factor. Figure 4-4 illustrates the impact the temperature has on the critical peeling velocity.

The temperature has a strong influence in the dynamics of kinetically controlled transfer printing and shows that it is advantageous to retrieve objects at a lower temperature and release them at an elevated ones.

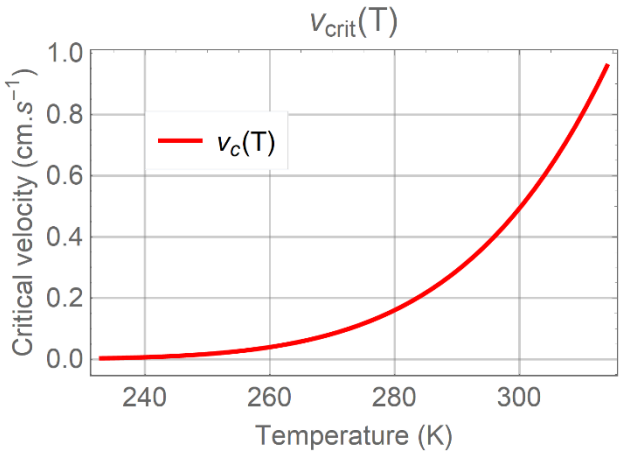

Figure 4-4. Critical velocity as a function of the temperature. Velocities higher than the critical velocity promote the retrieval of objects and velocities lower than the critical velocity promote the release of objects. Adapted from [217]

4.1.2 Stamp Fabrication

The TfP of SPs used a customized PDMS stamp cast from a mould using silicon elastomer and curing agent at a ratio of 10:1 (Figure 4-5).

The tip in the centre, which was used to pick-up and drop-off SPs, corresponds to a small extrusion of the main block of PDMS with a length × width × height of 10 × 30 × 5 μm^3.

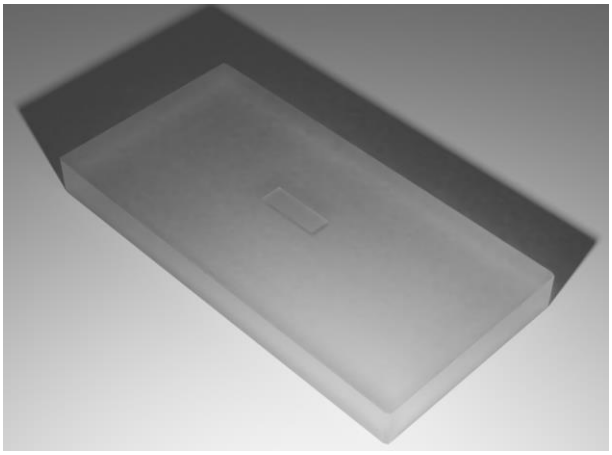

Figure 4-5. The PDMS stamp (length × width: 100 × 200 µm) used in the transfer printing process was cast from a mold using silicon elastomer and curing agent at a ratio of 10:1. The tip in the centre, used to pick up and drop SPs, corresponds to a small extrusion of the main block of PDMS (length × width × height: 10 × 30 × 5 µm).

4.1.3 Transfer-Printing of Microspheres

Figure 4-6 shows a picture of the TfP system, an adapted NanoInk NLP 2000. This dip-pen nanolithography instrument is capable of depositing a wide variety of materials with sub-micron accuracy and precision. It uses sets of individual pen tips (atomic force microscope tips) to create multi-component patterns of inks with feature sizes on the order of micrometres to sub-100 nm (when using dry ink) and can sweep areas as large as 10 × 10 cm^2. Its axis system is composed of xyz piezo-driven linear stages and T_x, T_y encoded goniometer stages with accuracies of ±25 nm and ±0.00025°, respectively. This system was adapted by replacing the pen tips by a stamp holder (Figure 4-7) and the ink reservoir by a donor substrate made here of SPs on a glass substrate. The imaging software interface enables control of the digital zoom, focus positioning and light intensity. It also allows toggling between different image planes by storing in memory different focal points. The process can be visualized, captured and recorded in real time with the in-built microscope of NanoInk. This is done through the μ-stamp, and it is possible thanks to its optical transparency.

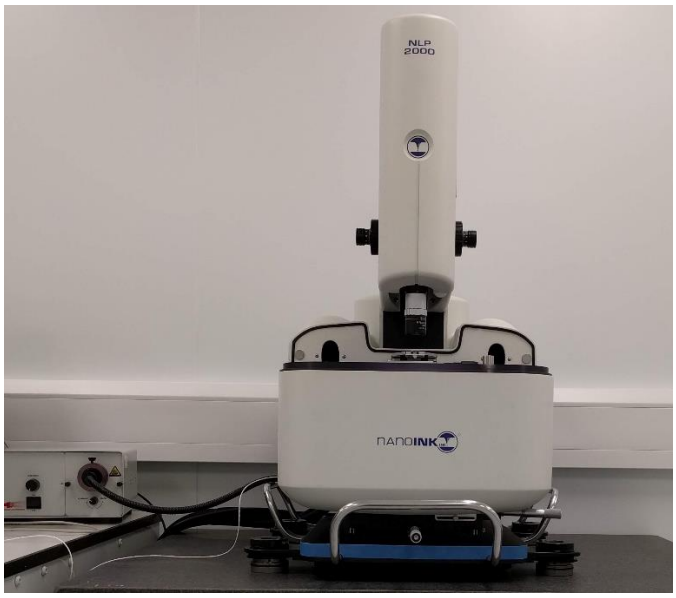

Figure 4-6. Picture of the adapted NanoInk NLP 2000 system for TfP.

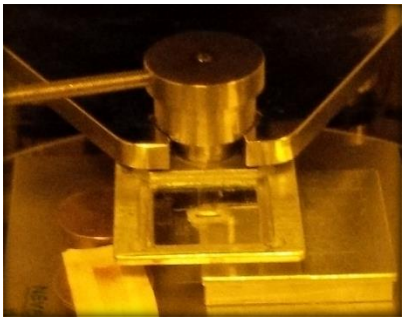

Figure 4-7.Picture of NanoInk NLP 2000 stamp holder.

The TfP process can be explained in 5 steps (Figure 4-8a). First, the user chooses the SP they want to transfer (i). Once this is done, the system uses its stamp to pick up the desired SP by getting in contact with it (ii). After the pick-up, the user selects the desired location for the drop-off (iii). Once the SP is put into contact with the substrate, it is released (iv), and the process can be repeated (v). Regarding the drop-off of SPs, two substrates were tested. Figure 4-8b shows the drop-off of 15 SPs on a PDMS substrate, positioned in the shape of

University of Strathclyde logo. Figure 4-8a illustrates the drop-off on a glass substrate where the SP was released by coupling it to a waveguide (with microscope image shown in Figure 4-10b). Although no estimations on the energy release rates and peeling forces were done, SPs showed to be easy to pick up from glass substrates using the PDMS µ-stamp. Regarding the release of SPs, in the case of the PDMS substrate the drop-off occurred by contact alone. For the glass substrate the drop-off was more difficult, but the topology of the waveguide assisted with the drop-off process by enabling the SP to be slid into place.

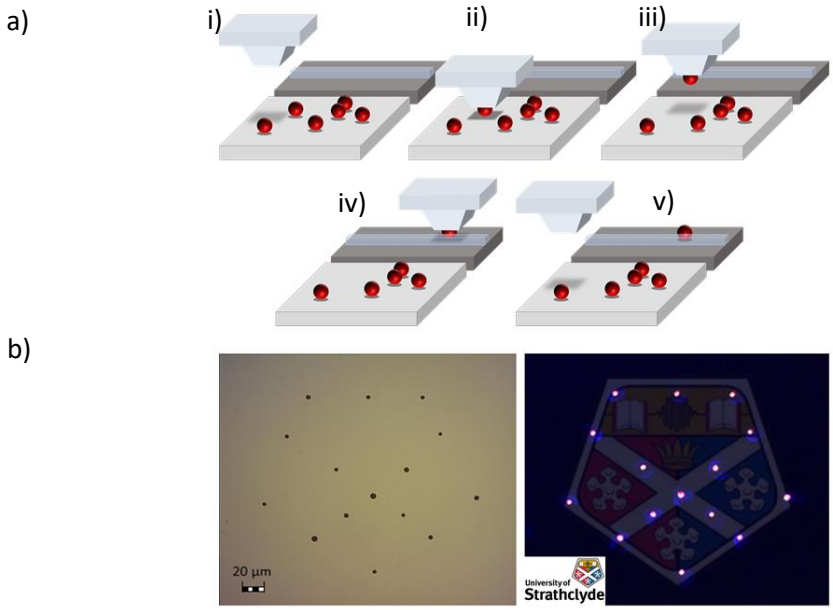

Figure 4-8. Illustration of the transfer-printing process applied to the coupling of a SP to a waveguide (a): a SP is selected with the stamp (i). Once it is picked up (ii-iii), the stamp moves it to the target destination (iv). The SP is dropped (v) by being put in contact with the substrate. Another example is given below (b) where 15 SPs were moved to a PDMS substrate (left). The right image shows the overlapping between the University of Strathclyde logo and the SPs under UV light.

4.2 Experimental Setup

To visualize if light from the SPs was being coupled into waveguides, an extra camera (DCC1645C, Thorlabs) was installed on the µPL setup of Section 2.5 (Figure 2-7). The beam spot area was also changed to approximately 4.85×10^{-7} cm^2.

Regarding the sample, waveguides were fabricated through laser lithography. A 2 µm layer of SU-8 was spin-coated onto a glass substrate and exposed with a custom maskless laser lithography tool (λ = 370 nm). After developing the SU-8, the waveguides were cleaved at

both ends. Resulting waveguides were 8.0 ± 0.5 mm in length with a cross-section of 2 µm × 2 µm, which makes them multimode at the wavelength of interest (visible light spectrum) with a high numerical aperture (NA) for input coupling and compatible with several optical interconnect techniques [220]. The propagation losses were measured with a narrow linewidth tunable laser (λ = 1550 nm). Propagation loss of the waveguides was measured using the Fast Fourier Transform method and estimated to be less than 3 $dB.cm^{-1}$ for the fundamental mode [221]. These waveguides were made by Dr. John Mcphillimy and the SP, made of red Cd_xSe_{1-x}/ZnS CQDs (Section 2.2), were transferred with the help of Dr. Benoit Guilhabert and Matěj Hedja.

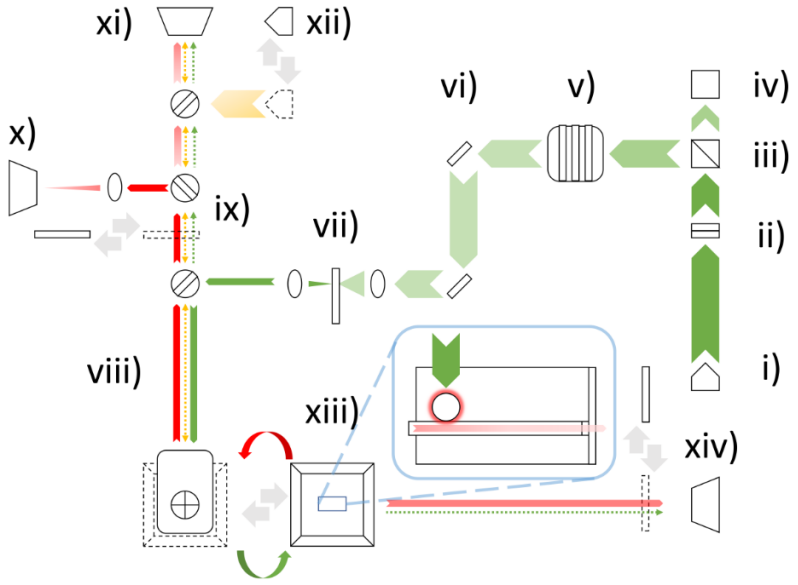

Figure 4-9. Schematic of the µ-PL setup with edge detection: i) Pump source (532 nm laser); ii) Waveplate; iii) Polarized beam splitter; iv) Beam dump; v) set of neutral density filters; vi) mirrors; vii) beam expander with attenuator wheel incorporated; viii) setup with a mounted objective lens (4×/0.13) and a xyz stage where the sample is placed; ix) set of 3 beam splitters and a long pass filter (550 nm); x) Spectrometer fiber-coupled to the setup; xi) CCD camera; xii) lamp; xiii) detail of SP-waveguide coupling; xiv) CCD camera with a long pass filter incorporated (550 nm). Green arrows represent the path of the laser from the pump, red arrows represent the path of the laser from the SP and yellow arrows represent the light path of the lamp.

Measurements were taken in the dark and a long pass filter (FEL0550, Thorlabs) was attached to the camera to cut off stray light from the pump. SPs were coupled and pumped on one end of the waveguide and the camera was focused on the facet of the other end. When the SP is pumped, if emitted light is coupled onto the waveguide, it will travel all the way through and be visible at the end, at the furthest facet, where the camera was placed for the facet

imaging. Images were acquired and processed for different pump fluences. The updated setup is shown in Figure 4-9, and the experimental results in the following section.

4.3 Optical Coupling of SPs to Waveguides

The illustration of the device during the measurements can be seen in Figure 4-10a. The SP was placed near one of the two extremities of the waveguide (Figure 4-10b), and the detection took place on the facet of the other extremity (Figure 4-10c), approximately 8 mm away. Insets i) and ii) of Figure 4-10a are zoomed images that illustrate the device operating and correspond to the microscopic image in Figure 4-10b and added CCD camera view in Figure 4-10c, respectively.

In dark room conditions, the SP was excited at different optical pulse energies and the CCD camera acquired a micrograph of the facet for each one of these energies while the emission spectrum of the SP was being recorded through the µPL setup. The top emission data acquired from the spectrometer and the corresponding facet emission data acquired by the CCD camera can be seen in Figure 4-11.

Images acquired by the CCD camera were then processed by calculating the signal-to-noise ratio (SNR) between the pixel intensity with the laser off (noise) and laser on (signal), given by Eq. 28.

$$SNR = 10Log_{10}\left(\frac{signal}{noise}\right)^2 \qquad \text{(Eq. 28)}$$

The collected spectra were split between the modes in intervals of 3.5 nm and compared with the SNR from the images. Results show that the waveguide output is strongly correlated to the longest wavelength modes (644 - 647.5 nm), whereas modes emitted at lower wavelengths are barely coupled into the waveguide. The exact reasons for this are still under investigation but could be explained by the geometry of the system and the region of the WGMs. The diameter of the SP (7.7 ± 0.5 µm) is bigger than the cross-section of the waveguide (2 µm × 2 µm). Once the SP reaches laser threshold, the first modes are likely confined to the equatorial region. However, higher pump energies may enable higher azimuthal modes that overlaps more and are more easily coupled to the waveguide (Figure 4-12). These have a higher threshold because of coupling with and scattering from the

waveguide. Their higher wavelength is also probably, at least partly, caused by the interaction with the waveguide, which breaks the symmetry and contribute to lifting the mode degeneracy.

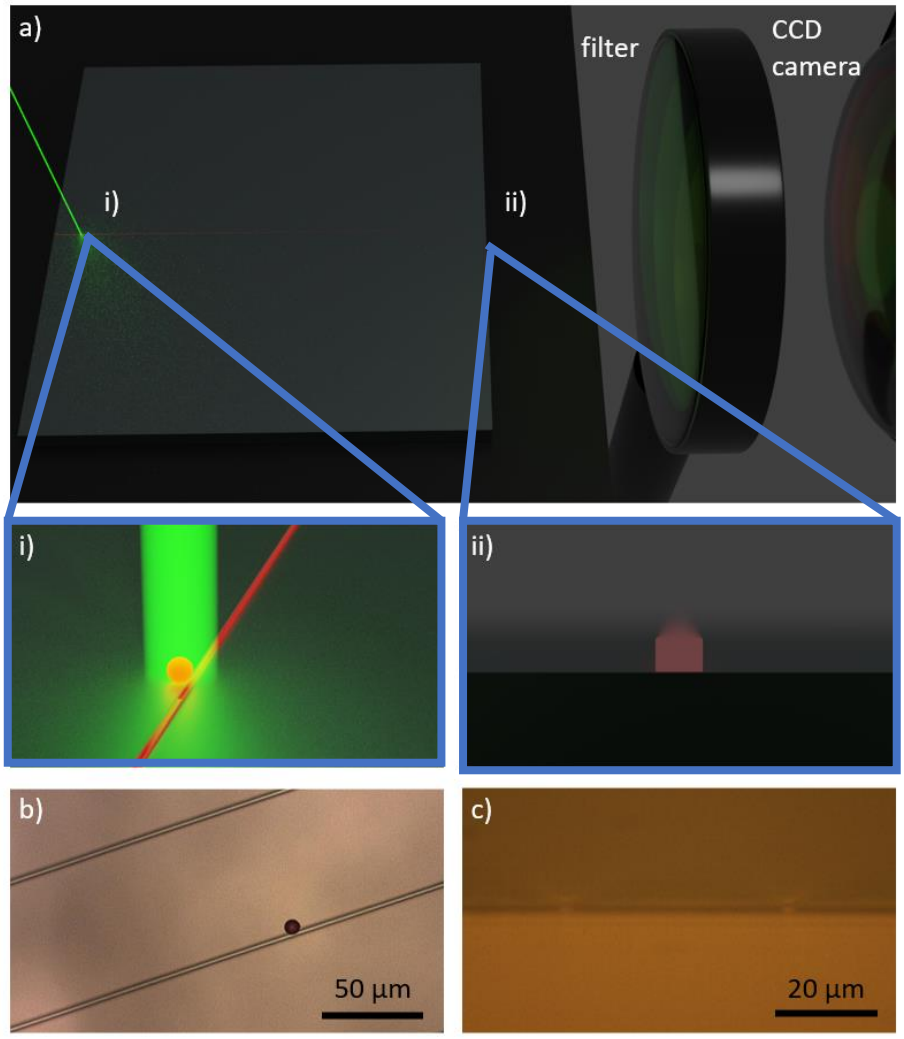

Figure 4-10. Illustration of the SP – waveguide coupling setup (a), where the sample is simultaneously aligned with the laser pump (a-i) and the CCD camera (a-ii). The SP (radius ≈ 3.9 ± 0.3 µm) is being pumped on one edge of the waveguide, and the other edge the facet is being monitored by the CCD camera, which is preceded by a long pass filter (550 nm) to cut any light from the pump (532 nm). Figures b) and c) show microscope and CCD camera views and correspond to illustrations a-i) and a-ii), respectively.

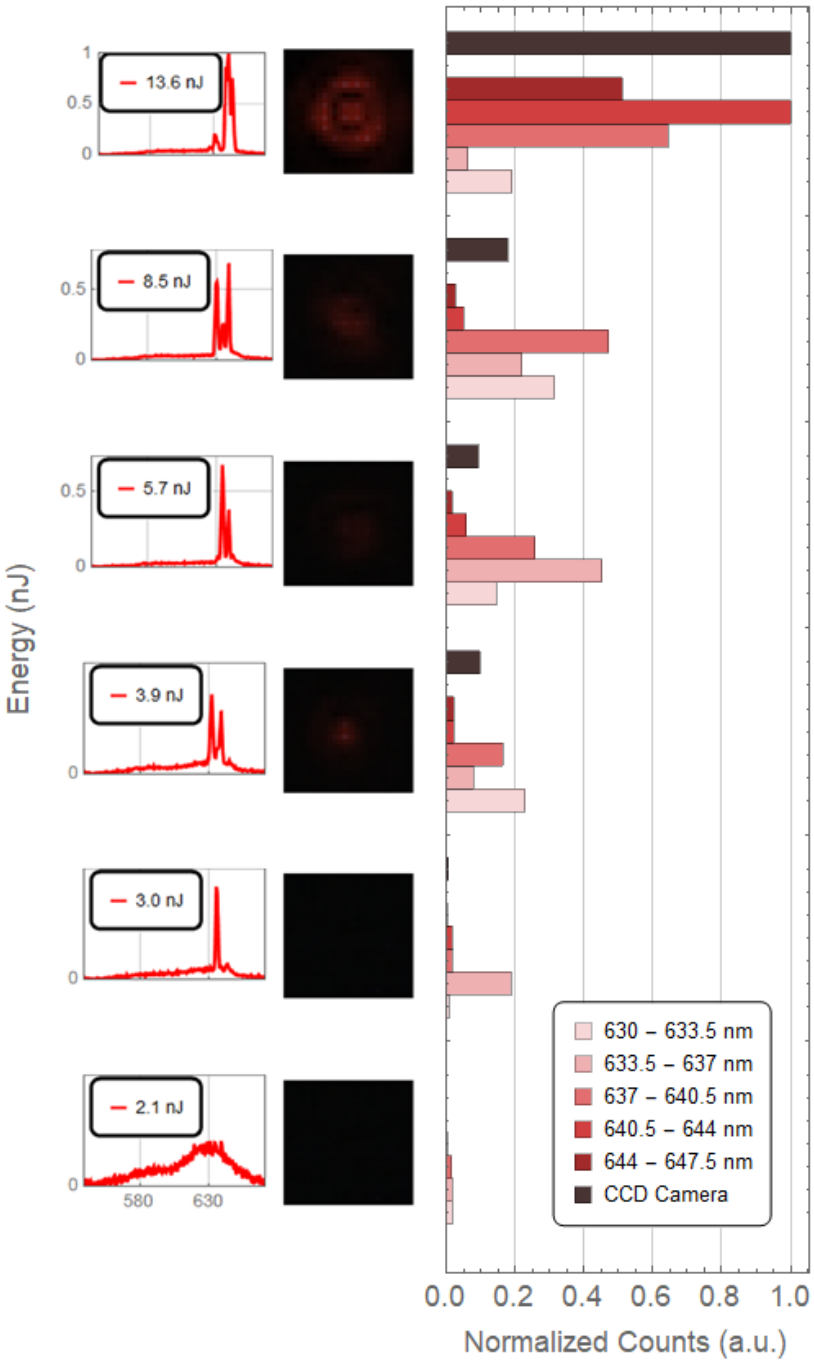

Figure 4-11. Readings from the spectrometer and CCD camera as a function of the optical pump energy. Acquisitions were made simultaneously and compared with each other to verify which modes were coupled into the waveguide. This compound figure compiles the spectra of the SP at different optical pump energies acquired on the spectrometer (left column) and the images obtained at the end of the cleaved facet of the waveguide where light is being coupled (mid column). For each of those energies, the column on the right shows the normalised counts integrated over the highlighted wavelengths (labelled in a range of red colours) using the data from the spectrometer (left column), and the normalised signal to noise ratio pixel intensity of the image (mid column) labelled in black. Labels on the axes of the spectra in the left column were left out to

simplify the figure (the x-axis corresponds to the wavelength in nm, and the y-axis to the counts normalised to the maximum intensity obtained at 13.6 nJ).

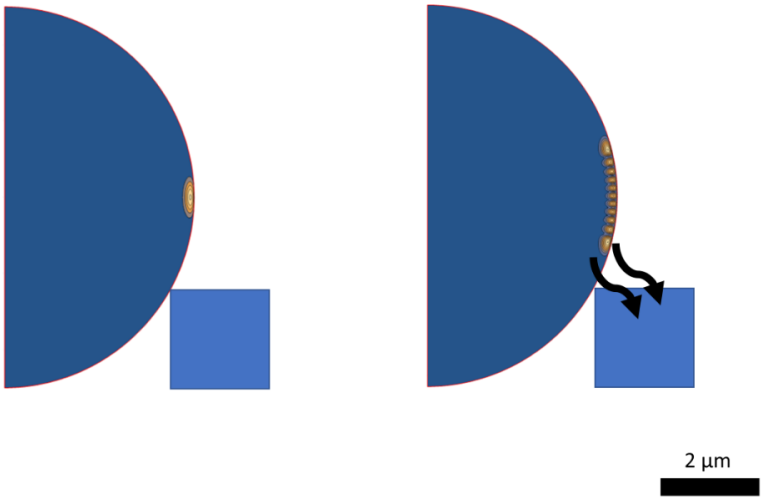

Figure 4-12. Representation of two different WGMs for a given wavelength propagating in a SP and how it can affect the coupling between a SP and waveguide (the waveguide being 2 × 2 µm² in cross-section).

4.4 Conclusion

In this chapter, the basics of kinetically controlled TfP were covered. These included a brief description of the equipment, the mechanics behind it and the physics involved in retrieving and releasing objects.

The TfP technique was shown to be a reliable way of transferring SPs between substrates and printing them at a desired location without affecting their emission below and above lasing threshold. For this purpose, a customized µ-stamp with a small extrusion was fabricated to transfer SPs individually.

As proof-of-concept, an integrated application was demonstrated by successfully coupling modes of a SP to a waveguide.

The results above have shown that the transfer printing method is a strong contender for future integrated photonic applications of SPs. The successful coupling of SPs to waveguides has shown that SPs have potential for integrated applications, paving the way to more complex designs with them.

Chapter 5. VLC and Self-Assembly Studies on Exotic Nanocrystals

The research presented in this chapter is a compilation of studies done on more exotic NCs. These studies can be subdivided in two parts. The first half summarized work initiated during a 3-month collaboration with the Nanyang Technological University (LUMINOUS! Research group, under supervision of Prof. Hilmi Volkan Demir). It comprises the study of three other main classes of NCs: Copper-doped quantum dots, tetrapods and nanoplatelets (Cu-doped QDs, TPs and NPLs, respectively) for the self-assembly of SPs. The second half comprises work on the synthesis and analysis of $CsPbBr_3@Cs_4PbBr_6$ crystals, as well as studies of the luminescence and bandwidth properties of related composite samples before and after being placed in contact with water [222].

5.1 Self-Assembly Studies using Exotic Nanocrystals

The three classes of NCs studied here were copper doped CdSe QDs, CdSe TPs, and CdSe NPLs. Their syntheses follow procedures similar to those already published by the LUMINUOUS! Group [223]–[227].

In terms of morphology, doped QDs do not differ much from the regular QDs shown in Chapter 2. On the other hand, TPs and NPLs are NCs with non-spherical configurations, which can potentially affect their self-assembly into microspheres.

The motivation behind this research was to assess if such nanomaterials were capable of self-assembling into SP microspheres and thus create whispering gallery mode (WGM) resonators. Successful results would allow one to explore the lasing of such SPs. Other properties such as Förster Resonance Energy Transfer (FRET) could also be studied by enabling the mixing of different NCs with synergistic characteristics during self-assembly.

The following sections summarize a general background on these types of materials and the self-assembly results with each one of them.

5.1.1 SP Microspheres of doped Quantum Dots

When doped with metal ions, QDs and other NCs can benefit from unique optical and photophysical properties over their undoped counterparts, such as large Stokes shift to avoid self-absorption or energy transfer, longer excited-state lifetimes, wider spectral window, and improved chemical and thermal stability [228], [229]. These properties and their high QY in the infrared have motivated the study of doped CQDs in several different applications (e.g.: solar cells, photovoltaics, lasers, passive heaters, etc.) [229].

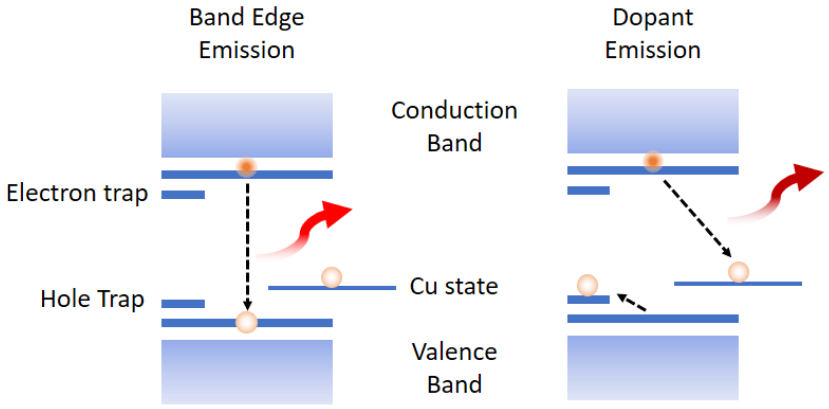

Figure 5-1. Illustration of the two typical pathways of radiative recombination in Cu-doped QDs. Band edge emission prevails in the presence of a hole in the valence band (left diagram). If the Cu state is optically active (Cu^{+2}) and there are no holes present in the valence band (or they have been captured by hole traps), then the dopant emission takes place (right diagram).

In this section, Cu-doped CQDs were used in the self-assembly of SPs and therefore a more in-depth explanation of their radiative recombination mechanism is given below [230].

The emission of Cu-doped CQDs has been attributed to the optical transition that couples the electron band-edge state to the Cu impurity state (Cu state). If the Cu state is in its +1 oxidation state (Cu^{+1}), then activation of the impurity band occurs via non-radiative capture of a hole from the valence band $Cu^{+1} \longrightarrow Cu^{+2}$. Otherwise, the Cu state can be considered as occupied with a permanent hole if the copper ion is in its +2 oxidation state (Cu^{+2}), and

therefore only a conduction band electron is required for the dopant emission to happen. After this emission process, the electron ends up decaying non-radiatively from the Cu state to the valence band [230].

An exception to the dopant emission occurs if in the addition of a conduction band electron there is also a photogenerated hole in the valence band. In this case, the fast recombination time scales of the band edge emission (30 – 60 ns) compared to those of the Cu-dopant emission (up to 1000 ns) favour the band edge emission [230].

In addition to Cu^{+1} states, surface treatment of the CQDs can also help with the capture of holes from the valence band. For example, ligands can add fast hole traps that will capture additional holes, and therefore further enhance the dopant emission and suppress the band edge emission [230]. Figure 5-1 illustrates the 2 pathways of radiative recombination in Cu doped QDs mentioned above (band edge emission and dopant emission) [229].

The typical emission and absorption spectra of these NCs can be seen in Figure 5-2 and Figure 5-3.

5.1.1.1 Synthesis of Cu-doped CdSe QDs

The synthesis of Cu-doped CdSe QDs follows similar steps to those of regular QDs seen in Section 1.5.1, but requires special care during the nucleation and growth of QDs to guarantee the incorporation of Cu ions in CdSe QDs and avoid the separate formation of $Cu_{2-x}Se$ particles [231]. Methods to prepare such QDs include colloidal precipitation with proper tuning of reagent and surfactant concentrations [231] or cluster-seeded synthesis, a method that uses organometallic clusters as nucleation centers for QDs [232].

For this case study, core-only CQDs (CdSe, Cu-doped, approximately 3 nm in diameter), and core (CdSe, Cu-doped)/ shell (CdS) CQDs, approximately 5 nm in diameter, were synthesized at NTU and used here. Both have a signature emission with two peaks, at approximately 600 nm corresponding to the first excitonic transition, and the other in the infrared, at approximately 800 nm coming from the Cu dopant. Their respective emission and absorption spectra measured in solution can be seen in Figure 5-2 and Figure 5-3.

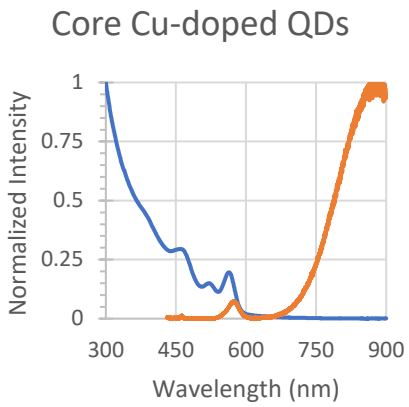

Figure 5-2. PL spectrum of Cu-doped core and core/ shell quantum dots.

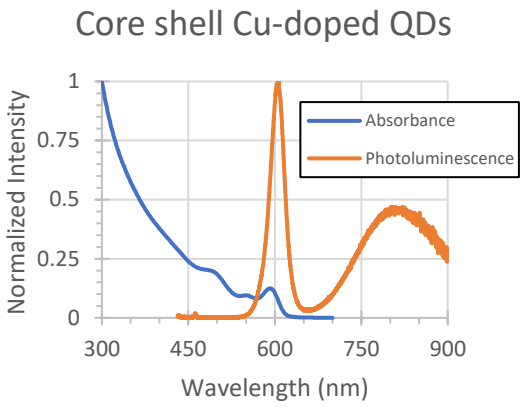

Figure 5-3. Absorbance spectrum of Cu-doped core and core/ shell quantum dots.

5.1.1.2 Synthesis of Cu-doped CdSe Microspheres

The recipe described in Section 2.4 was applied to synthesize SPs of core and core/shell Cu-doped QDs.

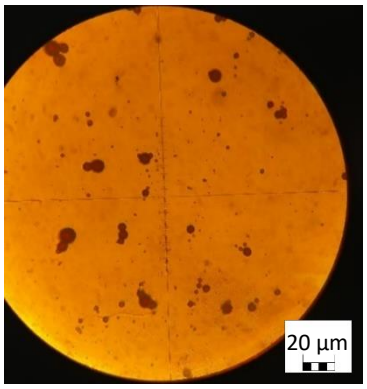

Figure 5-4. Core Cu-doped microsphere solution diluted in water (1:50). Microscope objective: ×20.

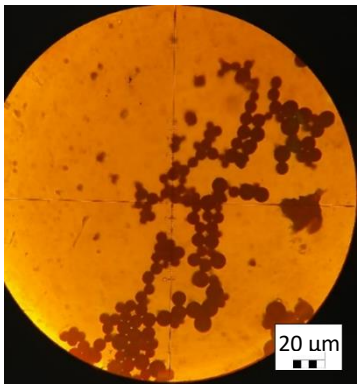

Figure 5-5. Core Cu-doped microsphere solution (initial solution). Microscope objective: ×20.

Characterization of the size and shape of the resulting SPs was done under the microscope. Figure 5-4 and Figure 5-5 display SPs of core Cu-doped QDs, with sizes ranging between 5 and 10 µm, approximately. Figure 5-6 and Figure 5-7 display SPs of Cu-doped core/ shell QDs, with sizes ranging between 3 and 7 µm, approximately.

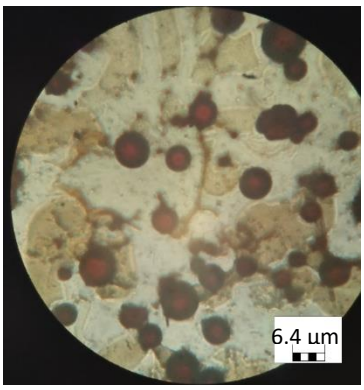

Figure 5-6. Core shell Cu-doped QD microspheres (initial solution). Microscope objective: ×63.

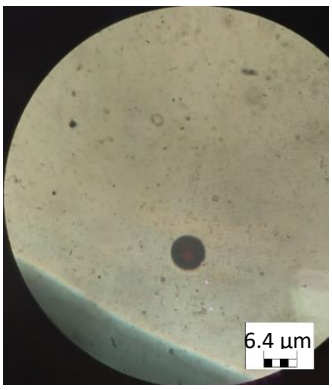

Figure 5-7. Core shell Cu-doped QD microspheres diluted in water (1:50). Microscope objective: ×63.

5.1.2 Microspheres of Tetrapods

TPs are nanocrystals made of a core from which four arms are grown, hence the name. Their geometry helps a more efficient capture of photons, and allows the self-assembly into percolating networks, providing an efficient way to create electronic pathways in devices that rely upon charge transport [233], [234]. Moreover, they can also allow higher energy radiative transitions via spatially indirect recombination [235]. Similarly to other NCs, TPs can also be found in a range of applications such as photovoltaics, optoelectronics, and mechanical devices [233].

5.1.2.1 Synthesis of CdSe Tetrapods

The synthesis of TPs relies mainly on the precise control of mechanisms such as polymorphism, twinning, oriented attachment, splitting crystal and tailored growth during formation of NCs to promote the characteristic branched growth [233], [236], [237].

The colloidal TPs used for this experiment were core Cu-doped CdSe TPs and core Cu-doped CdSe/ shell CdS TPs with a core of approximately 4 nm and arms of approximately 25 nm. Similarly to Cu-doped QDs, these also have a signature emission with two peaks, at approximately 600 nm corresponding to the first excitonic transition, and the other in the infrared, at approximately 800 nm coming from the Cu dopant. Their emission and absorption spectra can be seen in Figure 5-8 and Figure 5-9.

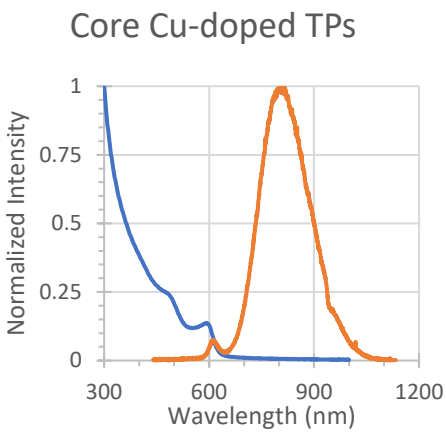

Figure 5-8. PL and absorbance spectra of Cu-doped core TPs.

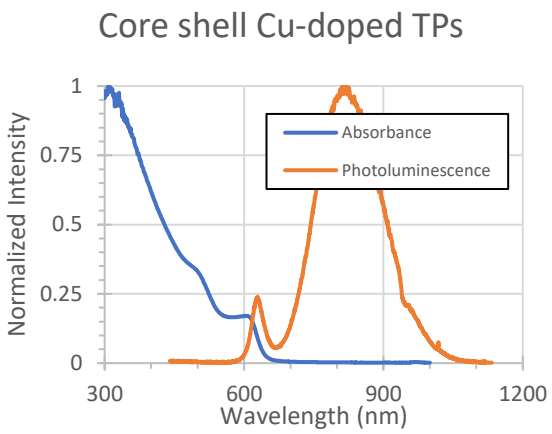

Figure 5-9. PL and absorbance spectra of Cu-doped core/ shell TPs.

5.1.2.2 Synthesis of Tetrapod Microspheres

The recipe in Section 2.4 was here applied to successfully synthesize SPs of core Cu-doped CdSe TPs and core Cu-doped CdSe/ shell CdS TPs.

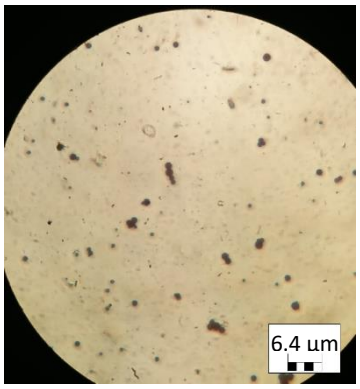

Figure 5-10. Core Cu-doped TP microspheres diluted in water (1:50). Microscope objective: ×63.

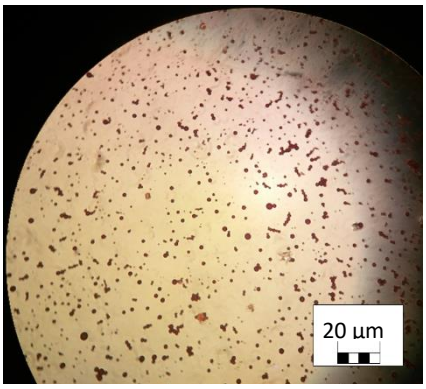

Figure 5-11. Wider view of Fig. 40. Microscope objective: ×20.

Figure 5-10 and Figure 5-11 display SP microspheres of core Cu-doped TPs seen under different objectives. The size of these microspheres ranged between 1 and 2 µm, approximately. Figure 5-12 shows microspheres of core/ shell Cu-doped TPs with sizes ranged between 2 and 4 µm, approximately.

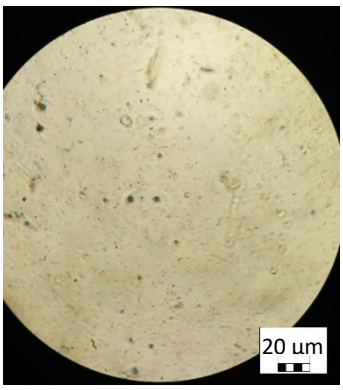

Figure 5-12. Core/Shell Cu-doped TP microsphere (solution diluted in water-1:50). Microscope objective: ×20.

5.1.3 Microspheres of Nanoplatelets

In general and due to their quantum confinement properties, NPLs tend to present narrower emission linewidths, higher oscillator strengths, larger exciton binding energies, and higher absorption cross-sections when compared to QDs due to their geometry [238]. CdSe-based NPLs are of particular interest as their findings comprise lasing research outputs on undoped core NPLs, with their possible heterostructures [239]. Undoped core-shell and core-crown/shell NPLs have ultralow optical gain thresholds and show FRET, as a function of the crown/shell enclosure [240], [241] and NPL orientation [242], respectively. For optoelectronic applications, it is also worth noting that NPLs can have up to near-unit FRET efficiencies [243]. Regarding electric injection, namely for LED applications, NPLs display a narrow electroluminescence and tuneablity [244]. This class of new materials shows promise for developing new high-performance LEDs [245]. Doped core NPLs display a largely Stokes-shifted PL emission peak with near-unity quantum yields, which arises from the intermediate energy band gap level introduced by the dopant ions [226]. Properties such as these make them useful for energy transfer applications, such as luminescent solar cell concentrators.

5.1.3.1 Synthesis of Nanoplatelets

Colloidal CdSe-based NPLs are typically synthesized in two different crystal structures, namely hexagonal wurtzite CdSe nanoribbons or quantum belts, and cubic zinc blende CdSe NPLs [246]. NPLs with a wurtzite crystal structure form by low-temperature based lamellar-like template growth, whereas their cubic zinc blende counterparts form either by oriented attachment, soft templated formation, growth driven by precursor insolubility or syntheses

without short ligands [246]. Posterior growth of different layers, such as CdS shells on CdSe NPLs, can also be done with atomic layer precision via colloidal atomic layer deposition [227].

When NPLs are synthesized with only a few monolayers thickness, and grown by extending exclusively their lateral size, they can lead to the formation of multiwall rolled-up nanostructures where the spontaneous folding can be induced by chiral ligands and the nanostructure characteristics [247].

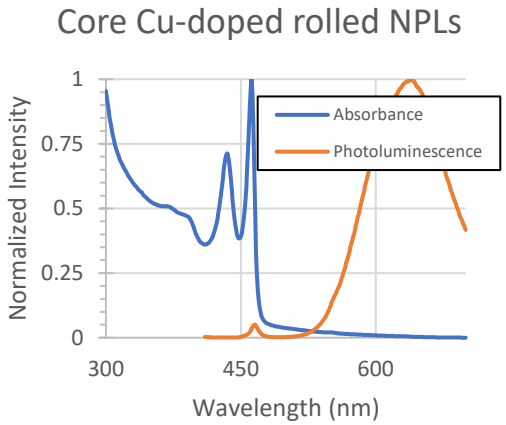

Figure 5-13. PL and absorbance spectrums of Cu-doped core rolled NPLs.

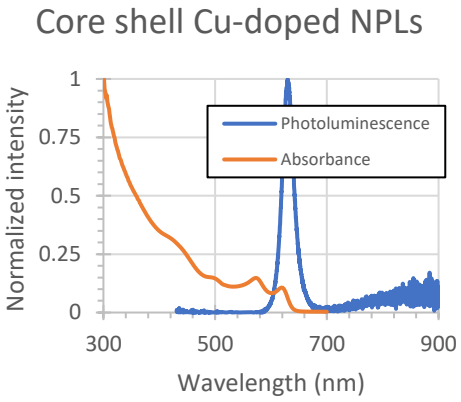

Figure 5-14. PL and absorbance spectrums of Cu-doped core/ shell flat NPLs.

In this section, two different types of NPLs were tested for self-assembly into microspheres: 2D flat (rectangle-shaped) and rolled (cylinder-shaped) NPLs. The PL and absorbance spectra of rolled NPLs, made of core Cu-doped CdSe, and flat NPLs, with a Cu-doped CdSe core and CdS shell can be found in Figure 5-13 and Figure 5-14, respectively. Rolled NPLs and flat NPLs asymmetry could prove particularly challenging for the self-assembly process, especially in the case of flat NPLs where the surface to volume ratio is high and can therefore lead to a preferential assembly orientation.

5.1.3.2 Synthesis of rolled Nanoplatelet Microspheres

The rolled NPs in this section were approximately 2.5 ML thick and after rolling themselves, they were approximately 100 × 40 nm^2 in size. Again, the same recipe as above and as in Section 2.4 was applied to synthesize SPs of core Cu-doped CdSe NPLs and core Cu-doped CdSe/ shell CdS NPLs. Figure 5-15 displays microspheres of rolled Cu-doped NPLs successfully

self-assembled, as seen under the microscope. The size of these microspheres ranged between 3 and 5 µm, approximately.

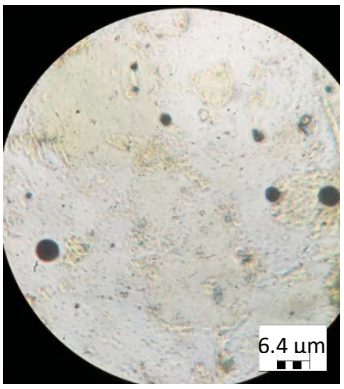

Figure 5-15. SPs of Cu-doped rolled NPLs (Microscope objective ×63).

5.1.3.3 Synthesis of flat Nanoplatelet Microspheres

Flat NPLs used in this section were approximately 14 × 15 nm^2 in width × length. They did not self-assemble into SPs with the standard protocol of Section 2.4. Instead, they showed a tendency to stack with each other. The resulting stacks formed micro-sized clusters, but not spherical enough to have WGMs (Figure 5-16).

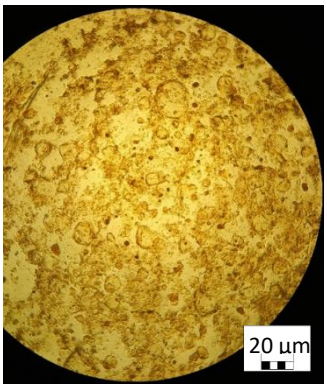

Figure 5-16. SPs of Cu-doped NPLs. Microscope objective ×20.

To avoid stacking and compensate for the difficulty flat NPLs have in forming a spherical SP structure, an additional transparent polymer (PMMA) was added to the recipe as buffer. The recipe in Section 2.4 was tested again with 4 different percentages of PMMA (5%, 10%, 30%

and 50%) added to the 'oil solution'. Here, the PMMA percentage is relative to the mass of NPLs used.

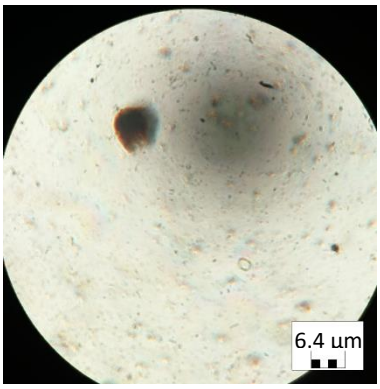

Figure 5-17. SPs of Cu-doped NPLs. PMMA: 5% of NPLs by mass. (Microscope objective ×63).

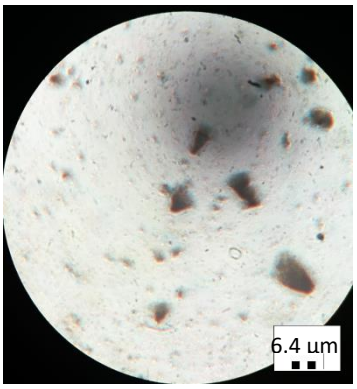

Figure 5-18. SPs of Cu-doped NPLs. PMMA: 10% of NPLs by mass. (Microscope objective ×63).

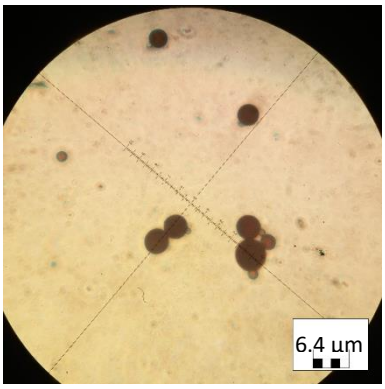

Figure 5-19. SPs of Cu-doped NPLs. PMMA: 30% of NPLs by mass. (Microscope objective ×63).

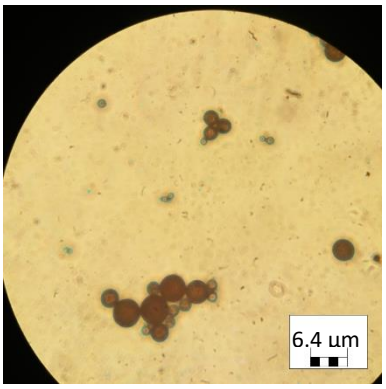

Figure 5-20. SPs of Cu-doped NPLs. PMMA: 50% of NPLs by mass. (Microscope objective ×63).

The addition of PMMA contributed to the assembly for better SP microspheres. From these four experiments, the mass ratio of NPLs: PMMA to achieve the best results was 3: 10. Lower ratios (5% and 10%) also formed SPs, but their shape was far from the desired result (Figure 5-17 and Figure 5-18). The transition from 10% to 30% of PMMA proved to be significant. Figure 5-19 shows microspheres which are now well defined and have a closer size distribution. Higher amounts of PMMA, such as the example of 50% depicted in Figure 5-20, show the same self-assembly improvements but at the cost of lower optical properties due to higher amounts of buffer material (PMMA) and lower amounts of active material (NPLs).

The overall size of microspheres in these experiments was between 1 and 5 µm, approximately.

5.1.4 Microspheres of Nanoplatelets and QDs

This experiment comprised the preparation and study of 5 different types of microspheres made of Cu-doped CdSe/ shell CdS rolled NPLs and QDs. The goal was to observe how the self-assembly behaves with two distinct components, with different shapes, to further study energy transfer between them. The samples were self-assembled with the following ratios (NPLs: QD): 100:0; 75:25; 50:50; 25:75 and 0:100.

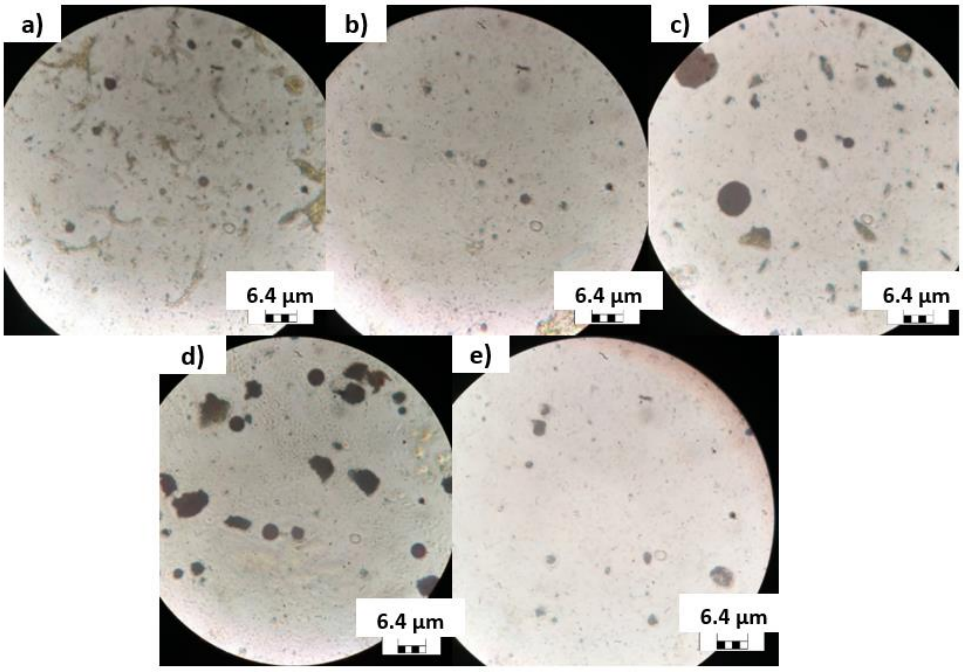

Figure 5-21. SPs of Cu-doped rolled NPLs and QDs. Ratio between NPLs and QDs, from a) to e): 100:0; 75:25; 50:50; 25:75; 0:100 (Microscope objective ×63).

Although SPs varied in size from synthesis to synthesis, microspheres were observed in all the 5 syntheses (Figure 5-21). These results could be promising for further experiments and characterizations as they could enable synergy between WGMs and FRET.

5.1.5 Summary on SP assembly using exotic NCs

During this work, self-assembly of different exotic NCs into microspheres has been successfully demonstrated.

Results suggest that QDs, TPs and rolled NPLs have the ability to self-assemble into well-defined microspheres without the help of additional buffers. On the other hand, due to their tendency to stack, flat NPLs required a percentage of PMMA to achieve the same results.

The small shifts in size of the SPs observed between experiments can be explained by fluctuations in the concentration of surfactant (PVA) and solute (NCs). The accuracy of the measurements to estimate the concentration of NCs and the evaporation rate of Chloroform during the process might also affect the final size of the microspheres.

Regarding the next steps, testing the SPs studied in the sections above under optical pumping is one of the main priorities. SPs made of Cu-doped NCs do not reabsorb the emitted infrared light and should therefore provide cavities with high Q-factors in the infrared with potential applications as biosensors. Likewise, NPLs benefit from narrower emission linewidths, higher oscillator strengths, larger exciton binding energies, higher absorption cross-sections and lower Auger recombination rate when compared to colloidal quantum dots and could therefore improve current QD based SPs.

5.2 Water Resistant All Inorganic Halide Perovskite Composites for VLC

Solid-state lighting and display technologies rely on UV/blue GaN LEDs, or in some special cases laser diodes, to optically pump phosphors [248], [249]. For the purpose of high light quality and/or wide colour gamut, a combination of narrow-band red and green phosphors are often used [250]. For device processing and operation stability, phosphors are also required to be heat and water resistant [250], [251]. However, the very long PL lifetime of phosphors precludes their utilization in applications requiring high speed modulation of the light, e.g. VLC [25], [26].

As seen in Chapter 1, Perovskite QDs of the form $CsPbX_3$, where X corresponds to a halide ion [151], represent an alternative to phosphors for such applications and are particularly attractive because they have the fastest dynamics of all known QDs [13], [252]. Despite these advantages, Perovskite QDs have limitations in terms of stability. Several approaches have

been reported to improve their thermal stability [253], [254], but their sensitivity to oxygen and moisture continues to be a problem and few solutions have been reported to address this [254]–[256].

A promising material for narrow-band green colour conversion is the so-called $CsPbBr_3@Cs_4PbBr_6$ [46] (see Section 1.2.2). It consists of $CsPbBr_3$ QDs formed within the wide band gap material $Cs4PbBr_6$, which acts as a host matrix for the QDs [47], [257]. As opposed to CQDs, these $CsPbBr_3$ QDs are inherently included within Cs_4PbBr_6 and have no organic ligands on their surfaces, which is beneficial for thermal stability and photostability. The band edge emission of such material has been shown to be practically temperature invariant [46]. However, a low-cost method to enhance the stability of $CsPbBr_3@Cs_4PbBr_6$ upon water exposure remains a challenge.

To shield the $CsPbBr_3@Cs_4PbBr_6$ crystals, two common polymeric materials soluble in the same solvent as the crystals, namely poly(methyl methacrylate) (PMMA), and polydimethylsiloxane (PDMS) were here studied as encapsulating matrices hosting the $CsPbBr_3@Cs_4PbBr_6$ crystals. The following sections report the synthesis of these samples and the methods for PL. These are followed by the results of PL measurements prior to and after immersion in water are discussed. Initial characterization of the optical bandwidth of the samples is also presented at the end of this study.

5.2.1 Synthesis of Ceasium Lead Bromide Crystals

The synthesis of ceasium lead bromide crystals was prepared by our colleague Dr. Ian Watson. Stoichiometric amounts of ceasium bromide and lead bromide at a 4:1 mole ratio were dissolved together in a minimum quantity of dimethylsulphoxide solvent for the $CsPbBr_3@Cs_4PbBr_6$ preparation. This precursor solution was placed in an open inner vial inside a sealed outer jar containing chloroform. Vapour diffusion of the chloroform into the metal salt solution was completed over about 24 hours and caused formation and precipitation of the crystalline solids.

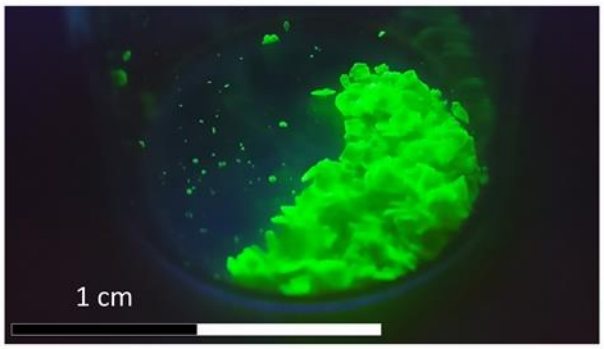

Figure 5-22. Synthesized bulk $CsPbBr_3@Cs_4PbBr_6$ crystals under UV illumination.

This method follows previously reported preparations, but with chloroform acting as an antisolvent [46]. The collected crystals, with sizes ranging from a few hundreds of µm to mm, were washed with chloroform and dried under atmospheric pressure at 60 ºC (Figure 5-22). Manual grinding was done with an agate pestle and mortar.

5.2.2 Preparation of Samples

Two PMMA samples were fabricated by dissolving and stirring PMMA (Sigma-Aldrich) in toluene, together with ground $CsPbBr_3@Cs_4PbBr_6$. A mass ratio of 3:1 was used for PMMA and crystals. The solvent was left to evaporate over time, under atmospheric pressure and temperature. One of the PMMA samples, a slab with a thickness of approximately 1 mm, was tested as it was after the PMMA polymerization (PMMA slab). The second sample, also a slab with a thickness of approximately 1 mm, was additionally encapsulated in PDMS (PMMA slab encapsulated in PDMS). Both PMMA slides were cast in a mould made of PDMS (Sylgard 184, Dow Corning) with a mass ratio between elastomer and curing agent of 10:1 and cured at room temperature.

Two other PDMS samples were prepared by stirring PDMS (Sylgard 184, Dow Corning) with ground $CsPbBr_3@Cs_4PbBr_6$. A mass ratio of 3:1 was used between PDMS and crystals, and a mass ratio of 5:1 between elastomer and curing agent. These composites were cast in a mould made of PDMS (Sylgard 184, Dow Corning) with a mass ratio between elastomer and curing agent of 10:1 and cured at 60°C. One of the samples was molded in the shape of a slab, approximately 1mm thick (PDMS slab), and the other in the shape of a thicker composite, approximately 3mm thick (PDMS thick). Crystal sedimentation was observed

during the preparation of PDMS samples. This led to a heterogeneity in the concentration of $CsPbBr_3@Cs_4PbBr_6$ in the PDMS slab and to a lower effective concentration of $CsPbBr_3@Cs_4PbBr_6$ in the PDMS thick sample.

The PDMS and PMMA slabs with ground $CsPbBr_3@Cs_4PbBr_6$ were tested to see how these encapsulation methods would protect the NCs when in the presence of water. The PMMA slab encapsulated in PDMS was studied to see if there were any benefits in using a PDMS coating, when compared to the bare PMMA slab. Finally, the thick PDMS sample was made to test if the surface area could make a difference during the exposure to water. PDMS is a flexible material and the PDMS slab can bend and be exposed to different amounts of water. A thick and bulk sample will minimize that exposure difference. The four samples above can be seen in Figure 5-27.

5.2.3 Sample Characterization – Methods

5.2.3.1 Phase Analysis of Perovskite Crystals

X-Ray Diffraction (XRD) analysis was performed on ground $CsPbBr_3@Cs_4PbBr_6$ crystals using a Bruker D8 Discover diffractometer (GX000915), and Copper radiation at a wavelength of 1.5406 Å.

5.2.3.2 Set-up for PL and Absorption Measurements

A 100×100 μm^2 450 nm-emitting µLED was used as pump source to measure the PL of all samples. Two sets of two lenses each (aspheric lenses, Numerical Aperture, NA=0.621 and diameter of 45 mm, Thorlabs) were used to, respectively, image the µLED light onto the samples, and to collect the sample's emission onto the detector. A fibre-coupled CCD spectrometer (Ocean Optics, USB 4000; resolution: 2 nm at full width half maximum) was used to acquire the emitted spectral data (Figure 5-23).

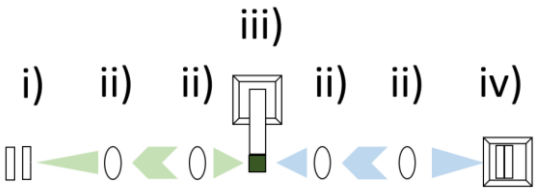

Figure 5-23. Schematic of the PL setup used to characterize the composites: i) fiber coupled CCD spectrometer with long pass filter (λ=500 nm) connected to the PC; ii) plano convex lenses; iii) sample holder; iv) µLED

The absorbance was measured by replacing the pump source in the setup described above by a tungsten halogen lamp (Ocean Optics, HL-2000). Blank composite samples (i.e. with no $CsPbBr_3$@Cs_4PbBr_6 crystals) of PDMS and PMMA were used as reference samples.

5.2.3.3 Bandwidth Setup

The frequency response and bandwidths of colour converters are important characteristics for their use in VLC (see Chapter 1). The optical bandwidth measurements for the perovskite samples here studied will be now covered in detail. Regarding the optical setup, a network analyzer (Hewlett Packard 8753ES) was employed to produce a radio frequency (RF) electrical signal. A bias-T compatible with the bandwidth range of the RF signal is then used to insert DC power from a DC source (TENMA 72-10480) into the RF signal. First, this setup is calibrated by measuring the reference of the added signal directly onto the network analyzer, with the DC source off. Then, the modulated signal is plugged to a light source (µLED), and all the measured signals that go through the optical circuit with the DC source on have the reference subtracted from them.

The optical setup (Figure 5-24) uses a set of lenses to converge light from the µLED onto the sample and a second set of lenses to focus the PL onto the avalanche photo detector (APD430A2/M, Thorlabs), APD, covered by a Long Pass Filter (500nm) to cut the blue light coming from the light source. The photo receiver sends an electrical response back to the network analyzer where the data is processed and saved on a floppy disk. Two sets of measurements are done. A first one, that measures the background ($Bandwidth_{Background}$), and a second one, that measures the sample's response and the background ($Bandwidth_{Total}$). Responses are acquired for a range of different input currents.

The bandwidth measurements have a range of frequencies being swept while recording the detected light intensity. The component of the frequency response of the sample at each frequency is given by:

$$Response_{Sample} = Bandwidth_{\ Total} - Bandwidth_{\ Background} \qquad \text{(Eq. 29)}$$

The response of the sample can be modelled, as a first approximation, to a low pass filter with a mono-exponential decay of the excited state:

$$Normalized\ electrical\ response\ (\nu) \equiv M(\nu) = (1 + (2\pi\nu)^2\tau_{av}^2)^{-1} \qquad \text{(Eq. 30)}$$

where ν corresponds to the frequency at which the response was taken, and τ_{av} to the effective lifetime of the sample [26].

Readings from this network analyzer come in dB, therefore the acquired response as a function of the frequency is given by:

$$M_{dB}\ (\nu) = \mathrm{k} - 10\mathrm{Log}_{10}(1 + (2\pi\nu)^2\tau_{av}^2) \qquad \text{(Eq. 31)}$$

Where k corresponds to the frequency response when the frequency tends to 0.

As the signal is provided by an electrical source, the data from the network analyser is the electrical power spectrum, which is proportional to the square of the photocurrent. The optical bandwidth is therefore given by the frequency at which the signal drops by 6 dB [258].

The average lifetime and the optical bandwidth of the sample are related by [49]:

$$f_{-6dB} = \frac{\sqrt{3}}{2.\pi.\tau_{av}} \qquad \text{(Eq. 32)}$$

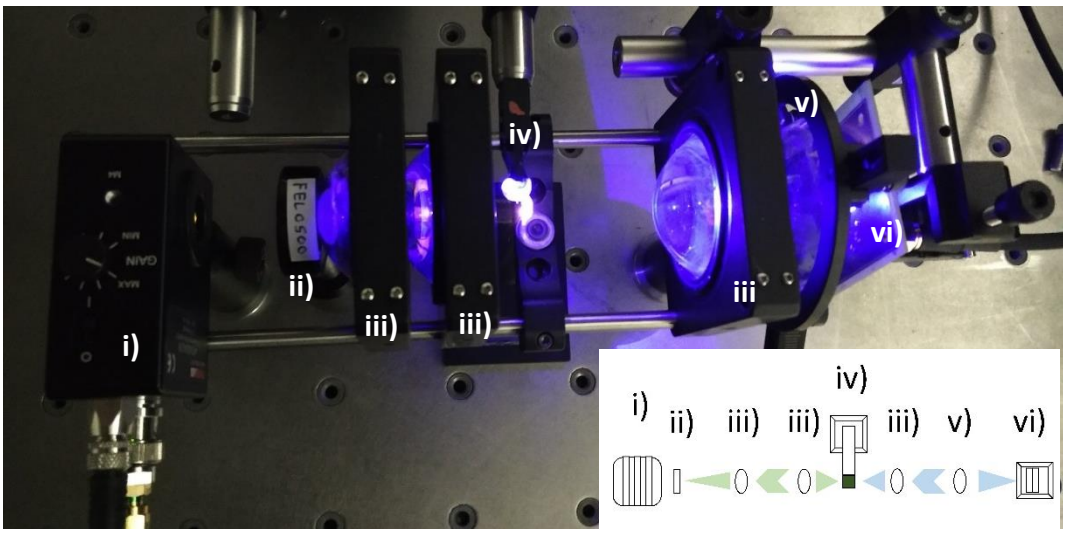

Figure 5-24. Bandwidth measurement setup with the inset schematic: i) photoreceiver; ii) long pass filter (λ=500 nm); iii) plano convex lenses; iv) sample holder; v) positive meniscus lens; vi) µLED.

5.2.4 XRD on $CsPbBr_3$@Cs_4PbBr_6 Crystal Samples

Figure 5-25 shows a powder diffraction pattern from a ground portion of the $CsPbBr_3$@Cs_4PbBr_6 crystal preparation with nominal Cs_4PbBr_6 stoichiometry, compared with a stick-plot representation of the literature pattern of rhombohedral Cs_4PbBr_6 [46]. A log scale has been used for clear presentation of weaker peaks. Positions of stronger peaks from our preparation match those expected from the Cs_4PbBr_6 phase, although there is evidence of preferred orientation effects on relative peak intensities, and one peak attributable to the CsBr starting material. Figure 5-25 is also labelled with peak positions calculated for cubic, perovskite-phase $CsPbBr_3$ with a lattice constant of 5.84 Å, and there are clear matches for the 100, 110 and 210 reflections. The $CsPbBr_3$ 111 reflection cannot be observed, but is weak in reported powder patterns of bulk material [259]. The findings just discussed are consistent with those of previous authors who have presented XRD evidence for spontaneous formation of $CsPbBr_3$ NCs within a bulk crystalline Cs_4PbBr_6 host, and attributed green luminescence to this nanophase [46], [47], [257].

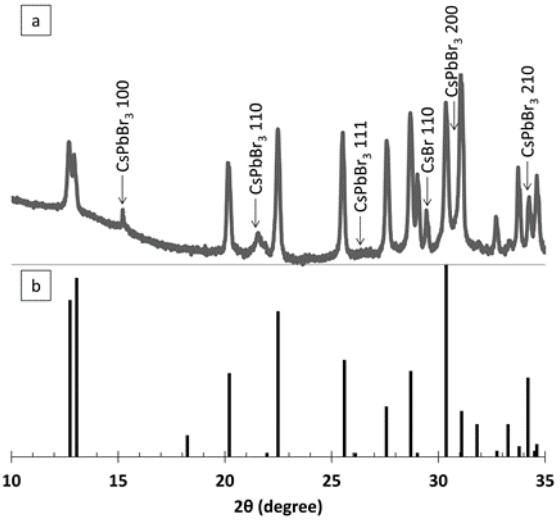

Figure 5-25. a) Log-scaled powder XRD pattern from the $CsPbBr_3$@Cs_4PbBr_6 crystal preparation with nominal Cs_4PbBr_6 stoichiometry (the intensity range in the original dataset was 1-100 counts per second); b) Stick plot representation of literature data for the bulk Cs_4PbBr_6 phase [188].

5.2.5 Water Exposure

Four different samples, using PMMA or PDMS host matrices, had their PL and absorbance measured before full immersion in deionized water. The PL spectrum of each sample prior to immersion in water can be seen in Figure 5-26. There are differences in the initial maximum intensity peaks and respective emission wavelengths between samples. This is explained by intrinsic variations in the concentration of $CsPbBr_3$@Cs_4PbBr_6 crystals and the different thickness of samples. Because the intrinsic PL overlaps with the absorption spectrum, such differences lead to different amounts of reabsorption, hence different intensities and red shifts in the PL spectrum. The PDMS thick, which has the least re-absorption, has a PL peak very close to the intrinsic $CsPbBr_3$ emission at 520 nm. The typical PL linewidth is 17 ± 2 nm at full width half maximum. PL and absorbance acquisitions were repeated 1, 4 and 72 hours after the samples had been thoroughly stirred underwater.

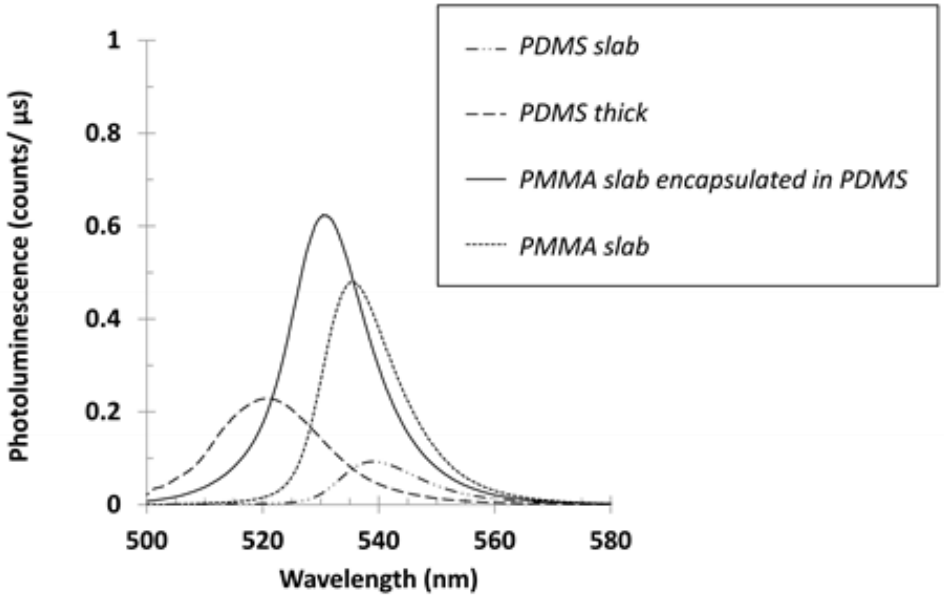

Figure 5-26. PL measurements of each of the fabricated samples prior to their submersion in water. Pumping was by a 450 nm µLED.

The PL intensity of PMMA composites was constant over time, and its subsequent encapsulation with PDMS showed little to no extra improvement (Figure 5-27).

On the other hand, the PDMS samples showed an adverse effect. After 4 hours underwater, the PDMS slab (PDMS thick) had its PL intensity reduced by almost two orders (one order) of magnitude. These results suggest that water was able to reach and affect most of the crystals in the PDMS samples, despite the hydrophobicity of PDMS.

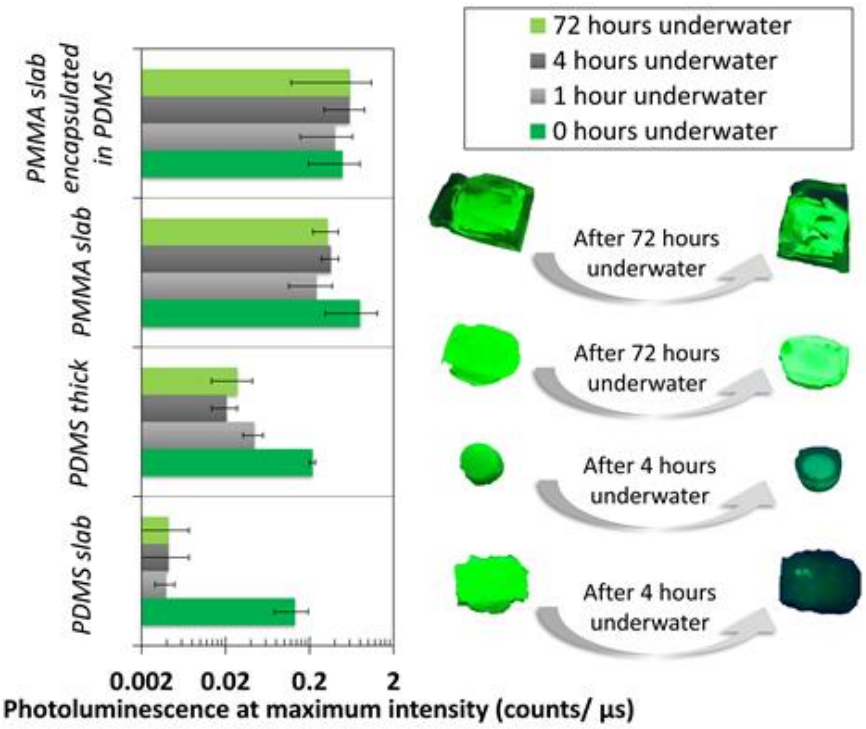

Figure 5-27. PL at maximum intensity over time, for each of samples studied. Samples are presented in the same order as in the bar plot.

The shifts in the PL peak and in the absorption spectrum after 1, 4 and 72-hour of immersion in water (with respect to the data before immersion) are plotted for all samples in Figure 5-28. The PL and absorption spectra of PDMS samples are red shifted by approximately 8 nm. This significant shift corroborates the compositional changes in this type of sample. The same was not observed in PMMA samples, where the shifts were close to the measurement error.

A possible explanation for the different results between PDMS and PMMA matrices might arise from the differences in polymer chain arrangements and consequent water insulation. While PMMA has predominantly linear chains, and forms a dense, glassy microstructure after solvent evaporation, the PDMS used is engineered to partially cross-link during curing, to give an elastomeric end product [260], [261]. This characteristic appears to allow more permeation of water into the PDMS composites, which in turn causes degradation of the luminescent $CsPbBr_3$ QDs. Water permeation in PDMS [260] and PMMA [262] has been extensively studied in different contexts, but is in agreement with these findings.

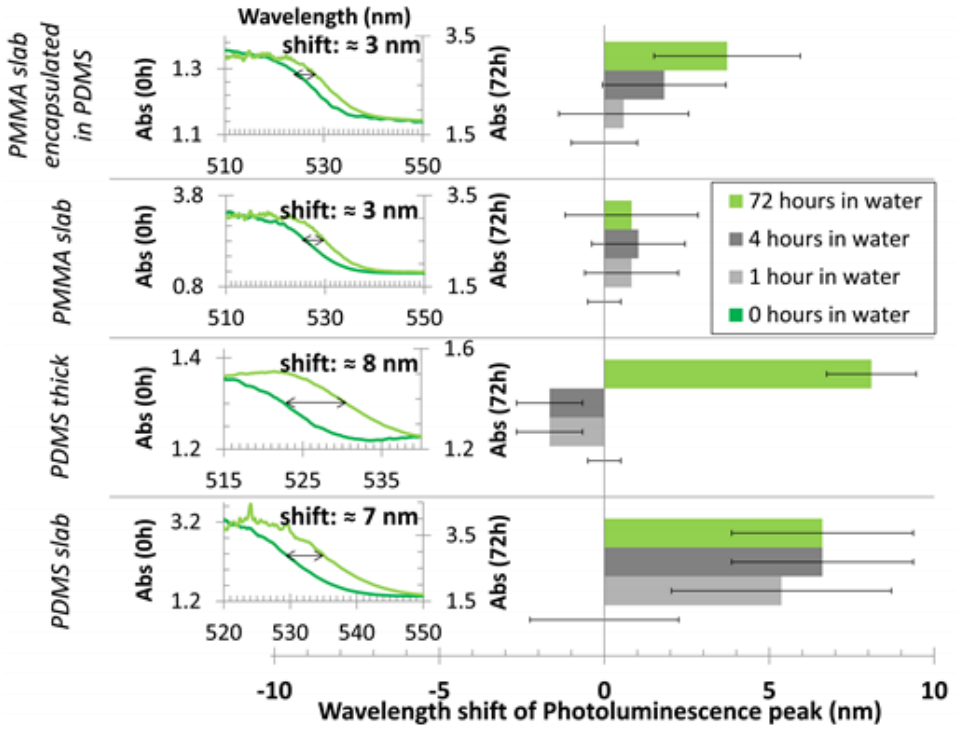

Figure 5-28. Shift in wavelength of the PL peak of each sample after 0, 1, 4 and 72 hour-immersion in water (right) with (left) absorbance spectra before and after immersion in water for 72 hours.

5.2.6 Bandwidth Measurements

This experiment comprised a bandwidth study on PMMA Perovskite composites of different ratios optically pumped at different intensities. The PMMA matrix was selected due to its higher resistance to water. The two composites of $CsPbBr_3$@Cs_4PbBr_6 crystals in PMMA were prepared at a mass ratio of 1:2 (Figure 5-29) and 1:3 (Figure 5-30), respectively, and exposed to a µLED powered at 10 (left) and 200 mA (right). This experiment used the same setup as [49], and therefore the optical power densities for 10 mA and 200 mA drive currents are approximately 0.75 and 3 W/cm^2, respectively.

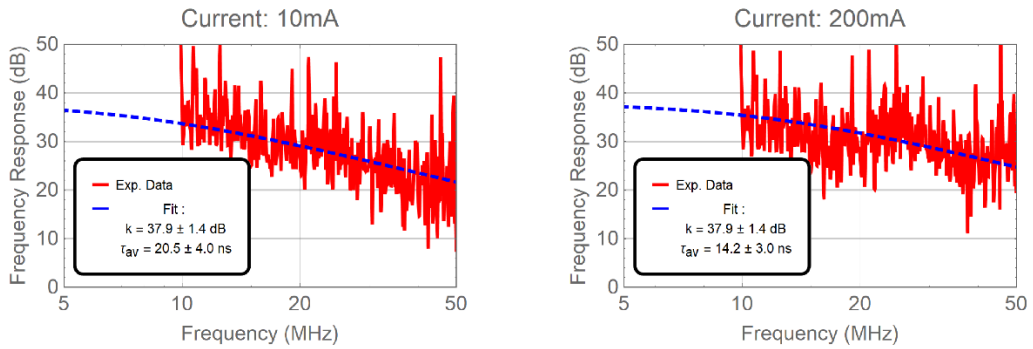

Figure 5-29. Bandwidth measurements of $CsPbBr_3$@Cs_4PbBr_6 crystals-PMMA at 1:2 mass ratio (left: 10 mA; right: 200 mA). Average lifetimes: $\tau_{10\ mA}$ = 20.5±4.0 ns; $\tau_{200\ mA}$ = 14.2±3.0 ns. Frequency responses: $v_{10\ mA}$ = 13.4 MHz; $v_{200\ mA}$ = 19.4 MHz.

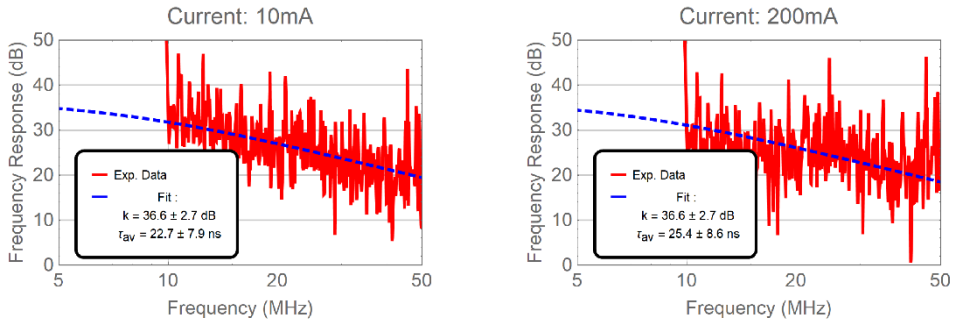

Figure 5-30. Bandwidth measurements of $CsPbBr_3$@Cs_4PbBr_6 crystals-PMMA at 1:3 mass ratio (left: 10 mA; right: 200mA). Average lifetimes: $\tau_{10\ mA}$ = 22.7±7.9 ns; $\tau_{200\ mA}$ = 25.4±8.6 ns. Frequency responses: $v_{10\ mA}$ = 12.1 MHz; $v_{200\ mA}$ = 10.9 MHz.

These measurements suffered from some equipment limitations in the bandwidth availability of the bias-T module (minimum frequency at 10 MHz) and bandwidth availability of the APD (maximum frequency at 40 MHz), which affected the sample size and therefore the accuracy of the fittings.

The average lifetime of these samples was found by fitting the experimental data to Eq. 31. The optical bandwidth was then estimated using Eq. 32. The average lifetime and optical bandwidth for these samples were approximately 20 ns and 15 MHz, respectively (for the detailed values, see Table 5-1). The lifetime values fell 1 to 2 orders of magnitude behind the 0.4 ns observed in single $CsPbBr_3$ QDs [252], most probably due to self-absorption and scattering within the composites, which add noise to the signal response. The results above

are also consistent with those of the state of art using $CsPbBr_3@Cs_4PbBr_6$ in PMMA at a mass ratio of 1:5 [49].

Table 5-1. Frequency response and average lifetime of $CsPbBr_3@Cs_4PbBr_6$ composites for different mass ratios and optical power densities.

		Frequency response, ν (MHz)		Average lifetime, τ (ns)	
	Optical Power density (W/cm^2)	0.75	3	0.75	3
$CsPbBr_3@Cs_4PbBr_6$	1:2	13.4	19.4	20.5	14.2
crystals - PMMA	1:3	12.1	10.9	22.7	25.4
mass ratio	1:5 [49]	18	34	15	7.5

Table 5-1 combines the experimental data from this thesis and data from the state-of-the-art on frequency response and average lifetime of $CsPbBr_3@Cs_4PbBr_6$ composites, for different mass ratios and optical power densities. Although it is difficult to find a trend between the results here obtained and those in the literature, data shows that the range of values obtained in this work fall within the same order of magnitude and margin of error as the previously reported data.

A straightforward comparison is difficult because parameters such as the quality of the crystal and composite vary from synthesis to synthesis. These parameters and small adjustments in the setup affect the optical power density available per crystal in the composite, as well as the self-absorption and scattering within the composite. In turn, these variations and the equipment limitations mentioned in this section affect the final measurements.

5.2.7 Summary on Water Resistant All Inorganic Halide Perovskite Composites for VLC

Motivated by their low manufacturing cost and simple processing, PDMS and PMMA were tested and studied as host matrices for the $CsPbBr_3@Cs_4PbBr_6$ crystals synthesized in this work.

The PDMS samples were not stable upon immersion in water. This finding indicates that water was able to reach the guest $CsPbBr_3$@Cs_4PbBr_6 crystals. On the other hand, PMMA composites showed little to no trace of degradation when immersed in water under vigorous stirring for up to 72 hours.

PMMA was found to be an effective matrix host for $CsPbBr_3$@Cs_4PbBr_6 by enabling moisture and water protection, as any degradation at the surface is mitigated by the extremely low water penetration depth and by the volume of the composite itself.

The bandwidth properties under µLED pumping are also consistent with the state-of-art [49], which shows this approach is viable for robust colour-conversion in VLC applications that already require a certain degree of resistance to water. Moreover, its encapsulation can be easily scaled up, showing potential for macrosized industrial applications, such as colour conversion,

5.3 Conclusion

This chapter has shown the capability of exotic NCs for self-assembling into SPs, which is promising for further optical experiments involving WGMs and FRET. These results are encouraging for further studies on photoluminescence, lasing, and energy transfer profiles of such NCs.

This chapter has also successfully demonstrated a way to encapsulate $CsPbBr_3$@Cs_4PbBr_6 crystals with PMMA to provide a high degree of protection against water and humidity while maintaining bandwidths similar to those in the state-of-art with no exposure to water [49].

While the design, optimal concentration and operation modes of such composites still require further optimization to enable bandwidths closer to the individual $CsPbBr_3$ QDs, this polymer matrix approach to minimize moisture-sensitivity should enable the utilization of the attractive fast color converting properties of $CsPbBr_3$@Cs_4PbBr_6 towards practical applications, such as underwater communications.

Self-assembly of all-inorganic halide perovskite QDs into SPs has already been reported [263] and could possibly be adapted to the Perovskite crystals here studied.

Part III

Conclusion and Outlook

Chapter 6. Conclusion and Future Directions

6.1 Summary of the thesis

Research on semiconductor NCs is broad and yet they still have a lot of hidden potential to show. In that context, the focus of this thesis has been on II-V colloidal quantum dots and related NCs as the building blocks of novel lasers that self-assemble from the bottom up. It also looked at an encapsulation approach for a perovskite quantum dot-based structure resistant to water, which among other applications, could also be used as a robust colour-converter of LEDs.

Chapter 1 started by presenting the motivation for this work, followed by the background on the synthesis of CQDs and a general overview on the relevant physics, including electronic states and optical gain. It covered the current status on the usage of CQDs for lasing applications and discussed the condition for lasing. The concepts behind the process of self-assembly of NCs, utilized in Chapters 2, 3 and 4 [17], [181], was also explained there. The focus of this introductory chapter was placed on Cd-based QDs as this is the material predominantly used in the thesis, and on inorganic perovskite NCs, the family of the material used in the colour converter study of Chapter 5. The basics of CQDs and all-inorganic perovskite NCs as colour-converting material technology for VLC was also summarized.

Chapter 2 demonstrated a new type of microlasers based on the bottom assembly of alloyed core/shell CdSSe/ZnS CQDs. The resulting micron-size SPs, spherical in shape, act as both the gain material and the optical cavity necessary for a laser. It described an in-depth study on the modelling for emission below threshold and the determination of $\langle N \rangle$ in such SPs by analyzing spectra of randomly chosen SPs with different diameters, and drawing a parallelism with the emission of single QDs researched in the literature. SPs had a Q-factor of 294 ± 15 and achieved multimode lasing between the 625 and the 655 nm when pumped above the threshold fluence, which was on average estimated for $\langle N \rangle \approx 2.3$ according to the emission model introduced in this work. Not only were these results consistent with those recently

reported by another group [118], but the analysis could help the characterization of other types of SPs using free space optical excitation. Self-assembly of such NCs can also provide them with unique properties such as mixed electronic states and new luminescence features [32], [158].

In Chapter 3, studies on the blending of CQDs with different bandgaps during the synthesis of SPs have shown the enhancement of characteristics and the addition of new properties to these structures. The addition of higher bandgap CQDs to the synthesis of SPs mitigates self-absorption of red CQDs, which in turn enabled the enhancement of the Q-factor, the increase in cavity size where lasing could be obtained in the given experimental conditions, and the increase of emission intensity in SPs.

For bandgaps of CQDs lower than the energy of the pump photons, multicolour lasing was also observed in SPs. Three lasing regimes were successfully demonstrated in a single SP, as a function of the pump fluence (namely single colour red, single colour yellow and simultaneous dual colour red and yellow). These findings represent important steps towards the design of higher quality CQD microcavities with multicolor lasing capabilities and have great application potential for integrated circuits, imaging, sensing and novel photonic materials [30], [198].

The proof-of-concept of a technique for the manipulation of individual SPs and subsequent integration was demonstrated in Chapter 4 by successfully coupling laser modes of a SP to a waveguide. Here, the TfP technique was covered in detail and shown to be a reliable way of transferring SPs between substates and printing them at a desired location without affecting their emission below and above lasing threshold.

Such results have shown that the transfer printing method is a strong contender for future integrated photonic applications of SPs and SPs have potential for integrated applications, which paves the way to more complex designs.

Chapter 5 comprised the results on the other NCs explored in this thesis, namely $CsPbBr_3@Cs_4PbBr_6$ crystals, Cu-doped QDs, NPLs and TPs. Current all inorganic halide perovskite QDs are sensible to water and would benefit from any sort of protection that could extend their exposure to humidity.

The studies on Cu-doped QDs, NPLs and TPs showed in the first half of Chapter 5 were part of a 3-month internship at NTU, in collaboration with LUMINOUS! led by Prof. Hilmi Volkan

Demir. Here, the self-assembly of different types of semiconductor NCs into SPs was successfully demonstrated as a first step to further exploit the optical properties of these exotic materials with the WGMs of microspheres.

Results suggest that CdSe-based, copper-doped QDs, TPs and rolled NPLs have the ability to self-assemble into well-defined microspheres by using the synthesis recipe of previous chapters. On the other hand, flat-NPLs showed a tendency to stack during such synthesis and did not self-assemble into neat microspheres. This issue was successfully addressed by adding a small percentage of PMMA to the oil phase solution.

Some small shifts in the overall size of the SPs has also been observed between experiments. However, these can be explained by fluctuations in the concentration of surfactant (PVA) and solute (NCs). The evaporation rate of solvent (Chloroform) during the process was non negligible, and this could affect the accuracy of the measurements to estimate the concentration of NCs during the experiment, which in turn will affect the final size of the self-assembled SPs. Nevertheless, the capability of assembling these NCs into SPs is promising for further optical experiments involving WGMs.

The second half of this chapter was dedicated to the investigation of water exposure on perovskites ($CsPbBr_3@Cs_4PbBr_6$) by looking into two different types of polymeric matrices and studying the luminescence of the encapsulated composites prior to and after exposure to water.

The two polymeric matrices chosen for this case study were PDMS and PMMA, due to their low manufacturing cost and simple processing, and they were studied as host matrices for the in-house synthesized $CsPbBr_3@Cs_4PbBr_6$ crystals. Results have shown that PDMS samples were not stable upon immersion in water, indicating that water was able to reach the guest $CsPbBr_3@Cs_4PbBr_6$ crystals. On the other hand, PMMA composites showed little to no trace of degradation when immersed in water under vigorous stirring for up to 3 full days. Such moisture and water protection has shown that PMMA was an effective matrix host for $CsPbBr_3@Cs_4PbBr_6$.

The bandwidth values obtained on PMMA encapsulated samples under µLED pumping were also consistent with the state-of-art [49], and showed that this approach could be viable for robust colour-conversion in VLC applications requiring resistance to water. Its encapsulation

can also be easily scaled up and used for industrial applications, such as LEDs and colour conversion.

While the design, optimal concentration and operation modes of such composites still require further optimization to enable bandwidth values closer to those claimed for $CsPbBr_3$ CQDs, this polymer matrix approach to minimize moisture-sensitivity should enable the utilization of the attractive fast color converting properties of $CsPbBr_3@Cs_4PbBr_6$ towards practical applications, such as underwater communications.

Overall, the research conducted in this thesis has resulted in important progress towards the use, optimization and application of NCs as lasers and for VLC. Nevertheless, these are but a fraction of what could be further explored within these fields.

In the rest of this chapter, further steps are suggested to widen the research. These steps include: (1) further investigation on closed-packed NC assemblies and their inherent properties; (2) Exploration of the use of surface treatments for further enhancement of the Q-factor, to help with the preservation of SPs and exploit the interaction between different functionalisations and WGMs towards sensing applications; (3) Exploration of different synthesis methods and ways of moving SPs between substrates; (4) Implementation of these SPs in real life applications.

6.2 Properties of Nanocrystals and Superparticles

Performances of both perovskite composites and CdSe based SPs seem are affected by self-absorption. Studies on the density of perovskites in composites, and thickness of composites could be explored to find bandwidths closer to the perovskite NCs themselves. Likewise, other types NCs could be tested in SPs to explore ways towards reduction of self-absorption.

In addition to that, they could also be combined with NCs of different types and bandgaps to test energy transfer in this type of oscillators. Particularly in this research, SPs of NCs made in collaboration with LUMINOUS! (Chapter 5) still have their photoluminescent, lasing, and energy transfer profiles to be explored in detail.

The toxicity of NCs must also be considered and studied according to the application. NCs used in this thesis rely on toxic elements and the applications that use them would be safer with toxic free alternatives. InP CQDs may be a good replacement, being only slightly slower

in their temporal response [17]. There is also intense research in search of Pb-free metal halide perovskites that retain the fast response of current perovskite CQDs [17].

Other species of NCs would also be worth considering, such hand their self-assembly into SPs for lasing [264] or mechanosensitive [265] applications.

In addition to the self-assembly method introduced in this thesis, NCs could benefit from other self-assembly methods. Oil-in-oil emulsions have been proven effective to self-assembly the water sensitive all-inorganic halide Perovskite QDs into SPs [263]. Evaporation of droplets directly on a pre-treated substrate can also lead to self-assembly of several different structures, such as microspheres [266], microcubes [266] or microrings [267].

NCs exist in different shapes, sizes, and have a wide array of different properties. Self-assembled SPs using methods such as those mentioned above could enhance properties of NCs and even enable new ones [158].

6.3 Surface Functionalisation

Self-assembled SPs could benefit from ligand exchanges on their surfaces, or on the individual NCs, prior to the self-assembly process. Ligand exchanges to shorter ligands on QDs have already been reported to improve the crystalline and cavity quality of SPs, which in turn decreases the lasing threshold of SPs [122].

Further studies and optimizations on the choice of ligand before or after self-assembly could enable better Q-factors on SPs. Another factor worth having into consideration is the SP surface protection and possible functionalization towards practical applications. Once self-assembled and drop cast on glass, the CdSe-based SPs here studied proved to be quite sturdy and even the TfP process did not seem to have any damaging effect on them.

However, preserving the SPs in solution showed signs of erosion after long periods of time. Studying a way of preventing erosion and stabilizing them in solution for long periods of time would improve their shelf life, which is important for commercial applications. Surface coatings such as thin shell coating of Silica or polymeric materials could improve such stability without hindering the properties of neat SPs [268], [269].

6.4 Manipulation of Supraparticles

To diversify the type of substrates SPs can be transferred onto via TfP, studies on the energy release rates and peeling forces between the μ-stamp, SPs and different substrate materials ought to be done. The need of doing further investigation on the TfP of SPs onto glass substrates was highlighted in Chapter 4.

Ways of facilitating the process of transfer printing onto glass substrate include testing the process at different temperatures and treating the surface of the glass substrate by coating it with a surfactant that favorably changes the energy release rate. Other manipulation and placement techniques of SPs could also be explored. In these experiments, it has been experimentally observed that a SEM is capable of charging and repelling SPs on a Si-wafer substrate, by forcing them to roll away from the beam. Such property could be advantageous and worth exploring for precise positioning of SPs.

Similarly, optical nanomanipulation on solid substrates via optothermally-gated photon nudging could also be a viable option for precise control on flat surfaces by precoating them with a thin film of a suitable surfactant (e.g.: Cetrimonium chloride) and using the pump laser to promote a phase transition on it, which would force the motion and positioning of SPs [270].

One last technique that could also be tested for alignment of SPs is the assisted capillary alignment, which combines hydrophilic and superhydrophobic areas on a substrate for self-alignment [271], [272]. Although this technique is more commonly used to align samples with large surface areas and placed on top of droplets that stay within the hydrophilic areas, this principle should also be viable with SPs. When droplets dry, the sample gets aligned or within the hydrophilic region, thus providing some control over the positioning without the requirement of sophisticated equipment. Alternatively, alignment of SPs could also be attempted by functionalizing their surface with molecules that bind onto molecules of another target surface (e.g. avidin and biotin).

6.5 Supraparticles and Practical Applications

As seen in Chapter 2, self-assembled SPs have a wide range of properties that can be exploited but have yet to be seen in a practical application. They could either be tested in similar sensing applications to other microspheres, such as microspheres embedded or

coated with NCs or fluorescent molecules [116], [123], [273], or bio applications, such as polymeric functionalization coatings for sensitive immunosensors [269].and in vitro or in vivo imaging [122].

Other possibilities include novel applications that take advantage of their mobility and capability both as gain mediums and cavities [30]–[32], [118] and could allow their integration in more complex devices, as demonstrated in Chapter 4.

6.6 Summary

Overall, NC-based devices are still in their early development stages, and although they have enormous potential, there are still obstacles to overcome.

SPs of NCs still lack the technology for electrical pumping, which can put them behind solid state lasers in certain applications. The durability, stability and efficiency of both SPs and composites must also be assured for long run applications. Despite that, these SPs have shown positive results with optical pumping that can be applied within integrated circuitry, imaging and sensing applications in scattering media so it will be interesting to see the steps NCs and their supra-structures will take in the years to come.

Bibliography

[1] D. V. Talapin, J. S. Lee, M. V. Kovalenko, and E. V. Shevchenko, “Prospects of colloidal nanocrystals for electronic and optoelectronic applications,” *Chem. Rev.*, vol. 110, no. 1, pp. 389–458, 2010.

[2] I. L. Medintz, H. T. Uyeda, E. R. Goldman, and H. Mattoussi, “Quantum dot bioconjugates for imaging, labelling and sensing,” *Nat. Mater.*, vol. 4, no. 6, pp. 435–446, 2005.

[3] T. H. Kim *et al.*, “Full-colour quantum dot displays fabricated by transfer printing,” *Nat. Photonics*, vol. 5, no. 3, pp. 176–182, 2011.

[4] V. I. Klimov *et al.*, “Optical gain and stimulated emission in nanocrystal quantum dots,” *Science (80-.).*, vol. 290, no. 5490, pp. 314–317, 2000.

[5] C. Dang, J. Lee, C. Breen, J. S. Steckel, S. Coe-Sullivan, and A. Nurmikko, “Red, green and blue lasing enabled by single-exciton gain in colloidal quantum dot films,” *Nat. Nanotechnol.*, vol. 7, no. 5, pp. 335–339, 2012.

[6] B. Guilhabert *et al.*, “Nanosecond colloidal quantum dot lasers for sensing,” *Opt. Express*, vol. 22, no. 6, p. 7308, 2014.

[7] D. Vasudevan, R. R. Gaddam, A. Trinchi, and I. Cole, “Core-shell quantum dots: Properties and applications,” *J. Alloys Compd.*, vol. 636, no. February, pp. 395–404, 2015.

[8] A. Sahu, A. Garg, and A. Dixit, “A review on quantum dot sensitized solar cells: Past, present and future towards carrier multiplication with a possibility for higher efficiency,” *Sol. Energy*, vol. 203, no. March, pp. 210–239, 2020.

[9] G. Xu, S. Zeng, B. Zhang, M. T. Swihart, K. T. Yong, and P. N. Prasad, “New Generation Cadmium-Free Quantum Dots for Biophotonics and Nanomedicine,” *Chem. Rev.*, vol. 116, no. 19, pp. 12234–12327, 2016.

[10] T. Erdem and H. V. Demir, “Colloidal nanocrystals for quality lighting and displays: Milestones and recent developments,” *Nanophotonics*, vol. 5, no. 1, pp. 74–95, 2016.

[11] J. C. Norman *et al.*, “A review of high-performance quantum dot lasers on silicon,”

IEEE J. Quantum Electron., vol. 55, no. 2, pp. 1–11, 2019.

[12] H. Haas, L. Yin, Y. Wang, and C. Chen, "What is LiFi?," *J. Light. Technol. (Vol. 34, Issue 6, March15, 15 2016)*, vol. 34, no. 6, pp. 1533–1544, 2016.

[13] F. T. Rabouw and C. de Mello Donega, "Excited-State Dynamics in Colloidal Semiconductor Nanocrystals," *Top. Curr. Chem.*, vol. 374, no. 5, pp. 1–30, 2016.

[14] J. Y. Kim, O. Voznyy, D. Zhitomirsky, and E. H. Sargent, "25th anniversary article: Colloidal quantum dot materials and devices: A quarter-century of advances," *Adv. Mater.*, vol. 25, no. 36, pp. 4986–5010, 2013.

[15] A. L. Efros and L. E. Brus, "Nanocrystal Quantum Dots: From Discovery to Modern Development," *ACS Nano*, vol. 15, no. 4, pp. 6192–6210, 2021.

[16] P. Geiregat, D. Van Thourhout, and Z. Hens, "A bright future for colloidal quantum dot lasers," *NPG Asia Mater.*, vol. 11, no. 1, 2019.

[17] Y. Wang and H. Sun, "Advances and prospects of lasers developed from colloidal semiconductor nanostructures," *Prog. Quantum Electron.*, vol. 60, no. May, pp. 1–29, 2018.

[18] S. Nizamoglu, G. Zengin, and H. V. Demir, "Color-converting combinations of nanocrystal emitters for warm-white light generation with high color rendering index," *Appl. Phys. Lett.*, vol. 92, no. 3, 2008.

[19] H. V. Demir, S. Nizamoglu, T. Erdem, E. Mutlugun, N. Gaponik, and A. Eychmüller, "Quantum dot integrated LEDs using photonic and excitonic color conversion," *Nano Today*, vol. 6, no. 6, pp. 632–647, 2011.

[20] J. J. D. McKendry *et al.*, "High-speed visible light communications using individual pixels in a micro light-emitting diode array," *IEEE Photonics Technol. Lett.*, vol. 22, no. 18, pp. 1346–1348, 2010.

[21] R. Ferreira, E. Xie, J. Mckendry, and S. Rajbhandari, "High bandwidth GaN-based micro-LEDs for multi-Gbps visible light communications," *IEEE Photonics Technol. Lett.*, vol. 28, no. 19, p. 1, 2016.

[22] M. F. Leitao *et al.*, "Gb/s Visible Light Communications with Colloidal Quantum Dot Color Converters," *IEEE J. Sel. Top. Quantum Electron.*, vol. 23, no. 5, 2017.

[23] S. Rajbhandari *et al.*, "A review of gallium nitride LEDs for multi- gigabit-per-second visible light data communications," *Semicond. Sci. Technol.*, vol. 32, no. 2, pp. 1–40, 2017.

[24] H. Haas, "A light-connected world," *Phys. World*, vol. 29, no. 8, pp. 29–34, 2016.

[25] D. C. O'Brien, L. Zeng, H. Le-Minh, G. Faulkner, J. W. Walewski, and S. Randel, "Visible Light Communications: Challenges and possibilities," *IEEE Int. Symp. Pers. Indoor Mob. Radio Commun. PIMRC*, pp. 1–5, 2008.

[26] N. Laurand *et al.*, "Colloidal quantum dot nanocomposites for visible wavelength conversion of modulated optical signals," *Opt. Mater. Express*, vol. 2, no. 3, pp. 250–260, 2012.

[27] F. T. Lee-Montiel, P. Li, and P. I. Imoukhuede, "Quantum dot multiplexing for the profiling of cellular receptors," *Nanoscale*, vol. 7, no. 44, pp. 18504–18514, 2015.

[28] A. W. Elshaari *et al.*, "On-chip single photon filtering and multiplexing in hybrid quantum photonic circuits," *Nat. Commun.*, vol. 8, no. 1, pp. 1–8, 2017.

[29] Y. S. Park, W. K. Bae, L. A. Padilha, J. M. Pietryga, and V. I. Klimov, "Effect of the core/shell interface on auger recombination evaluated by single-quantum-dot spectroscopy," *Nano Lett.*, vol. 14, no. 2, pp. 396–402, 2014.

[30] P. U. Alves, N. Laurand, and M. D. Dawson, "Multicolor laser oscillation in a single self-assembled colloidal quantum dot microsphere," *2020 IEEE Photonics Conf. IPC 2020 - Proc.*, pp. 2020–2021, 2020.

[31] P. U. Alves, D. Jevtics, M. J. Strain, M. D. Dawson, and N. Laurand, "Enhancing self-assembled colloidal quantum dot microsphere lasers," *IEEE Photonics Conf.*, pp. 1–2, 2021.

[32] E. Marino *et al.*, "Simultaneous photonic and excitonic coupling in spherical quantum dot supercrystals," *ACS Nano*, vol. 14, no. 10, pp. 13806–13815, 2020.

[33] M. Bayer, "Bridging Two Worlds: Colloidal versus Epitaxial Quantum Dots," *Ann. Phys.*, vol. 531, no. 6, pp. 1–25, 2019.

[34] S. González-Carrero, R. E. Galian, and J. Pérez-Prieto, "Organometal Halide Perovskites: Bulk Low-Dimension Materials and Nanoparticles," *Part. Part. Syst.*

Charact., vol. 32, no. 7, pp. 709–720, 2015.

[35] V. I. Klimov, “Spectral and Dynamical Properties of Multiexcitons in Semiconductor Nanocrystals,” *Annu. Rev. Phys. Chem.*, vol. 58, no. 1, pp. 635–673, 2007.

[36] A. Rogach, “Quantum dots still shining strong 30 years on,” *ACS Nano*, vol. 8, no. 7, pp. 6511–6512, 2014.

[37] A. F. Van Driel, G. Allan, C. Delerue, P. Lodahl, W. L. Vos, and D. Vanmaekelbergh, “Frequency-Dependent Spontaneous Emission Rate from CdSe and CdTe Nanocrystals : Influence of Dark States,” *Phys. Rev. Lett.*, vol. 95, no. 23, pp. 1–4, 2005.

[38] O. Svelto, *Principles of Lasers*, 5th ed. Springer US, 2010.

[39] S. R. D. and K. V. I., “High Efficiency Carrier Multiplication in PbSe Nanocrystals: Implications for Solar Energy Conversion,” *Phys. Rev. Lett.*, vol. 92, no. 18, p. 186601, 2004.

[40] K. Gerasimos and E. H.Sargent, *Colloidal quantum dot optoelectronics and photovoltaics*, no. 2005. Cambridge University Press, 2013.

[41] Z. Deutsch, A. Avidan, I. Pinkas, and D. Oron, “Energetics and dynamics of exciton-exciton interactions in compound colloidal semiconductor quantum dots,” *Phys. Chem. Chem. Phys.*, vol. 13, no. 8, pp. 3210–3219, 2011.

[42] J. Zhang *et al.*, “Low-Dimensional Halide Perovskites and Their Advanced Optoelectronic Applications,” *Nano-Micro Lett.*, vol. 9, no. 3, pp. 1–26, 2017.

[43] L. Protesescu *et al.*, “Nanocrystals of Cesium Lead Halide Perovskites (CsPbX 3 , X = Cl, Br, and I): Novel Optoelectronic Materials Showing Bright Emission with Wide Color Gamut,” *Nano Lett.*, vol. 15, no. 6, pp. 1–5, 2015.

[44] J. Song, J. Li, X. Li, L. Xu, Y. Dong, and H. Zeng, “Quantum Dot Light-Emitting Diodes Based on Inorganic Perovskite Cesium Lead Halides (CsPbX 3),” *Adv. Mater.*, vol. 27, no. 44, pp. 7162–7167, 2015.

[45] Y. Wang, X. Li, J. Song, L. Xiao, H. Zeng, and H. Sun, “All-Inorganic Colloidal Perovskite Quantum Dots : A New Class of Lasing Materials with Favorable Characteristics,” *Adv. Mater.*, vol. 27, no. 44, pp. 7101–7108, 2015.

[46] Y. Wang *et al.*, "Solution-Grown CsPbBr3/Cs4PbBr6Perovskite Nanocomposites: Toward Temperature-Insensitive Optical Gain," *Small*, vol. 13, no. 34, pp. 1–8, 2017.

[47] L. N. Quan *et al.*, "Highly Emissive Green Perovskite Nanocrystals in a Solid State Crystalline Matrix," *Adv. Mater.*, vol. 29, no. 21, pp. 1–6, 2017.

[48] Q. A. Akkerman, A. L. Abdelhady, and L. Manna, "Zero-Dimensional Cesium Lead Halides: History, Properties, and Challenges," *J. Phys. Chem. Lett.*, vol. 9, no. 9, pp. 2326–2337, 2018.

[49] M. F. Leitão *et al.*, "Pump-power-dependence of a CsPbBr3-in-Cs4PbBr6 quantum dot color converter," *Opt. Mater. Express*, vol. 9, no. 8, pp. 3504–3518, 2019.

[50] Q. A. Akkerman, G. Rainò, M. V. Kovalenko, and L. Manna, "Genesis, challenges and opportunities for colloidal lead halide perovskite nanocrystals," *Nat. Mater.*, vol. 17, no. 5, pp. 394–405, 2018.

[51] J. Lim, W. K. Bae, J. Kwak, S. Lee, C. Lee, and K. Char, "Perspective on synthesis, device structures, and printing processes for quantum dot displays," *Opt. Mater. Express*, vol. 2, no. 5, p. 594, 2012.

[52] V. K. Lamer and R. H. Dinegar, "Theory, Production and Mechanism of Formation of Monodispersed Hydrosols," *Am. Chem. Soc.*, vol. 72, no. 11, pp. 4847–4854, 1950.

[53] C. B. Murray, C. R. Kagan, and M. G. Bawendi, "Synthesis and characterization of monodisperse nanocrystals and close-packed nanocrystal assemblies," *Annu. Rev. Mater. Sci.*, vol. 30, no. June 2017, pp. 545–610, 2000.

[54] J. Van Embden, A. S. R. Chesman, and J. J. Jasieniak, "The heat-up synthesis of colloidal nanocrystals," *Chem. Mater.*, vol. 27, no. 7, pp. 2246–2285, 2015.

[55] H. Jung, N. Ahn, and V. I. Klimov, "Prospects and challenges of colloidal quantum dot laser diodes," *Nat. Photonics*, vol. 15, no. 9, pp. 643–655, 2021.

[56] M. S. Silberberg, *Chemistry: The Molecular Nature of Matter and Change with Advanced Topics*, 8th ed. New York: McGraw-Hill Education, 2018.

[57] L. Brus, "Electronic wave functions in semiconductor clusters: Experiment and theory," *J. Phys. Chem.*, vol. 90, no. 12, pp. 2555–2560, 1986.

[58] I. Kang and F. W. Wise, “Electronic structure and optical properties of PbS and PbSe quantum dots,” *J. Opt. Soc. Am. B*, vol. 14, no. 7, pp. 1632–1646, 1997.

[59] J. Johansen, B. Julsgaard, S. Stobbe, J. M. Hvam, and P. Lodahl, “Probing long-lived dark excitons in self-assembled quantum dots,” *Phys. Rev. B - Condens. Matter Mater. Phys.*, vol. 81, no. 8, Feb. 2010.

[60] S. Chen and A. V. Nurmikko, “Coherent Light Emitters From Solution Chemistry: Inorganic II-VI Nanocrystals and Organometallic Perovskites,” *IEEE J. Sel. Top. Quantum Electron.*, vol. 23, no. 5, 2017.

[61] V. I. Klimov, “Optical nonlinearities and ultrafast carrier dynamics in semiconductor nanocrystals,” *J. Phys. Chem. B*, vol. 104, no. 26, pp. 6112–6123, 2000.

[62] M. Grundmann and D. Bimberg, “Theory of random population for quantum dots,” *Phys. Rev. B - Condens. Matter Mater. Phys.*, vol. 55, no. 15, pp. 9740–9745, 1997.

[63] J. Nanda, S. A. Ivanov, M. Achermann, I. Bezel, A. Piryatinski, and V. I. Klimov, “Light amplification in the single-exciton regime using exciton-exciton repulsion in type-II nanocrystal quantum dots,” *J. Phys. Chem. C*, vol. 111, no. 42, pp. 15382–15390, 2007.

[64] K. Thyagarajan and A. Ghatak, *Lasers, Fundamentals and Applications*, 2nd ed. Springer Science+Business Media, 2010.

[65] H. Chang *et al.*, “Ultrastable low-cost colloidal quantum dot microlasers of operative temperature up to 450 K,” *Light Sci. Appl.*, vol. 10, no. 1, 2021.

[66] M. A. Hines and P. Guyot-Sionnest, “Synthesis and characterization of strongly luminescing ZnS-capped CdSe nanocrystals,” *J. Phys. Chem.*, vol. 100, no. 2, pp. 468–471, 1996.

[67] C. B. Murray, C. R. Kagan, and M. G. Bawendi, “Self-organization of CdSe nanocrystallites into three-dimensional quantum dot superlattices,” *Science (80-.).*, vol. 270, no. 5240, pp. 1335–1338, 1995.

[68] A. Cretí, M. Zavelani-Rossi, G. Lanzani, M. Anni, L. Manna, and M. Lomascolo, “Role of the shell thickness in stimulated emission and photoinduced absorption in CdSe core/shell nanorods,” *Phys. Rev. B - Condens. Matter Mater. Phys.*, vol. 73, no. 16,

pp. 3–6, 2006.

[69] B. O. Dabbousi *et al.*, "(CdSe)ZnS core-shell quantum dots: Synthesis and characterization of a size series of highly luminescent nanocrystallites," *J. Phys. Chem. B*, vol. 101, no. 46, pp. 9463–9475, 1997.

[70] R. R. Cooney, S. L. Sewall, K. E. H. Anderson, E. A. Dias, and P. Kambhampati, "Breaking the phonon bottleneck for holes in semiconductor Quantum dots," *Phys. Rev. Lett.*, vol. 98, no. 17, pp. 1–4, 2007.

[71] P. Kambhampati, "Unraveling the structure and dynamics of excitons in semiconductor quantum dots," *Acc. Chem. Res.*, vol. 44, no. 1, pp. 1–13, 2011.

[72] V. I. Klimov and D. W. McBranch, "Femtosecond 1P-to-1S electron relaxation in strongly confined semiconductor nanocrystals," *Phys. Rev. Lett.*, vol. 80, no. 18, pp. 4028–4031, 1998.

[73] V. Klimov, A. Mikhailovsky, D. McBranch, C. Leatherdale, and M. Bawendi, "Mechanisms for intraband energy relaxation in semiconductor quantum dots: The role of electron-hole interactions," *Phys. Rev. B - Condens. Matter Mater. Phys.*, vol. 61, no. 20, pp. R13349–R13352, 2000.

[74] V. I. Klimov, A. A. Mikhailovsky, D. W. McBranch, C. A. Leatherdale, and M. G. Bawendi, "Quantization of multiparticle Auger rates in semiconductor quantum dots," *Science (80-.).*, vol. 287, no. 5455, pp. 1011–1014, 2000.

[75] V. A. Kharchenko and M. Rosen, "Auger relaxation processes in semiconductor nanocrystals and quantum wells," *J. Lumin.*, vol. 70, no. 1-6 SPEC. ISS., pp. 158–169, 1996.

[76] V. I. Klimov, J. A. McGuire, R. D. Schaller, and V. I. Rupasov, "Scaling of multiexciton lifetimes in semiconductor nanocrystals," *Phys. Rev. B - Condens. Matter Mater. Phys.*, vol. 77, no. 19, pp. 1–12, 2008.

[77] H. Htoon, J. A. Hollingsworth, R. Dickerson, and V. I. Klimov, "Effect of zero- to one-dimensional transformation on multiparticle auger recombination in semiconductor quantum rods," *Phys. Rev. Lett.*, vol. 91, no. 22, pp. 1–4, 2003.

[78] M. Tytus, J. Krasnyj, W. Jacak, A. Chuchmaa, W. Donderowicz, and L. Jacak,

"Differences between photoluminescence spectra of type-I and type-II quantum dots," *J. Phys. Conf. Ser.*, vol. 104, no. 1, 2008.

[79] D. Oron, M. Kazes, and U. Banin, "Multiexcitons in type-II colloidal semiconductor quantum dots," *Phys. Rev. B - Condens. Matter Mater. Phys.*, vol. 75, no. 3, pp. 1–7, 2007.

[80] S. A. Ivanov and M. Achermann, "Spectral and dynamic properties of excitons and biexcitons in type-II semiconductor nanocrystals," *ACS Nano*, vol. 4, no. 10, pp. 5994–6000, 2010.

[81] R. Vaxenburg, A. Rodina, E. Lifshitz, and A. L. Efros, "Biexciton Auger Recombination in CdSe/CdS Core/Shell Semiconductor Nanocrystals," *Nano Lett.*, vol. 16, no. 4, pp. 2503–2511, 2016.

[82] J. Kundu, Y. Ghosh, A. M. Dennis, H. Htoon, and J. A. Hollingsworth, "Giant nanocrystal quantum dots: Stable down-conversion phosphors that exploit a large stokes shift and efficient shell-to-core energy relaxation," *Nano Lett.*, vol. 12, no. 6, pp. 3031–3037, 2012.

[83] L. Zhang *et al.*, "Single-Mode Lasing from 'giant' CdSe/CdS Core-Shell Quantum Dots in Distributed Feedback Structures," *ACS Appl. Mater. Interfaces*, vol. 9, no. 15, pp. 13293–13303, 2017.

[84] A. Shabaev, A. V. Rodina, and A. L. Efros, "Fine structure of the band-edge excitons and trions in CdSe/CdS core/shell nanocrystals," *Phys. Rev. B - Condens. Matter Mater. Phys.*, vol. 86, no. 20, pp. 1–14, 2012.

[85] F. García-Santamaría, Y. Chen, J. Vela, R. D. Schaller, J. A. Hollingsworth, and V. I. Klimov, "Suppressed auger recombination in 'Giant' nanocrystals boosts optical gain performance," *Nano Lett.*, vol. 9, no. 10, pp. 3482–3488, 2009.

[86] G. E. Cragg and A. L. Efros, "Suppression of auger processes in confined structures," *Nano Lett.*, vol. 10, no. 1, pp. 313–317, 2010.

[87] J. I. Climente, J. L. Movilla, and J. Planelles, "Auger recombination suppression in nanocrystals with asymmetric electron-hole confinement," *Small*, vol. 8, no. 5, pp. 754–759, 2012.

[88] W. K. Bae *et al.*, "Controlled alloying of the core-shell interface in CdSe/CdS quantum dots for suppression of auger recombination," *ACS Nano*, vol. 7, no. 4, pp. 3411–3419, 2013.

[89] G. Yuan, D. E. Gómez, N. Kirkwood, K. Boldt, and P. Mulvaney, "Two Mechanisms Determine Quantum Dot Blinking," *ACS Nano*, vol. 12, no. 4, pp. 3397–3405, 2018.

[90] Z. Li *et al.*, "Carrier Dynamics in Alloyed Chalcogenide Quantum Dots and Their Light-Emitting Devices," *Adv. Energy Mater.*, vol. 11, no. 40, 2021.

[91] Q. Yuan, T. Wang, P. Yu, H. Zhang, H. Zhang, and W. Ji, "A review on the electroluminescence properties of quantum-dot light-emitting diodes," *Org. Electron.*, vol. 90, no. January, p. 106086, 2021.

[92] V. I. Klimov *et al.*, "Single-exciton optical gain in semiconductor nanocrystals," *Nature*, vol. 447, no. 7143, pp. 441–446, 2007.

[93] S. A. Ivanov *et al.*, "Light amplification using inverted core/shell nanocrystals: Towards lasing in the single-exciton regime," *J. Phys. Chem. B*, vol. 108, no. 30, pp. 10625–10630, 2004.

[94] J. Q. Grim, L. Manna, and I. Moreels, "A sustainable future for photonic colloidal nanocrystals," *Chem. Soc. Rev.*, vol. 44, no. 16, pp. 5897–5914, Aug. 2015.

[95] H. Htoon *et al.*, "Highly emissive multiexcitons in steady-state photoluminescence of individual 'giant' CdSe/CdS Core/Shell Nanocrystals," *Nano Lett.*, vol. 10, no. 7, pp. 2401–2407, 2010.

[96] E. Baghani, S. K. Oleary, I. Fedin, D. V. Talapin, and M. Pelton, "Auger-limited carrier recombination and relaxation in CdSe colloidal quantum wells," *J. Phys. Chem. Lett.*, vol. 6, no. 6, pp. 1032–1036, 2015.

[97] L. T. Kunneman *et al.*, "Bimolecular Auger Recombination of Electron − Hole Pairs in Two-," *J. Phys. Chem. Lett.*, vol. 4, no. 21, pp. 3574–3578, 2013.

[98] B. Guzelturk, Y. Kelestemur, M. Olutas, S. Delikanli, and H. V. Demir, "Amplified spontaneous emission and lasing in colloidal nanoplatelets," *ACS Nano*, vol. 8, no. 7, pp. 6599–6605, 2014.

[99] C. She *et al.*, "Low-threshold stimulated emission using colloidal quantum wells,"

Nano Lett., vol. 14, no. 5, pp. 2772–2777, 2014.

[100] J. Q. Grim *et al.*, “Continuous-wave biexciton lasing at room temperature using solution-processed quantum wells,” *Nat. Nanotechnol.*, vol. 9, no. 11, pp. 891–895, 2014.

[101] A. A. Lutich *et al.*, “Multiexcitonic dual emission in CdSe/CdS tetrapods and nanorods,” *Nano Lett.*, vol. 10, no. 11, pp. 4646–4650, 2010.

[102] Y. Kelestemur, A. F. Cihan, B. Guzelturk, and H. V. Demir, “Type-tunable amplified spontaneous emission from core-seeded CdSe/CdS nanorods controlled by exciton-exciton interaction,” *Nanoscale*, vol. 6, no. 15, pp. 8509–8514, 2014.

[103] Y. Gao *et al.*, “Observation of polarized gain from aligned colloidal nanorods,” *Nanoscale*, vol. 7, no. 15, pp. 6481–6486, 2015.

[104] Y. Liao, G. Xing, N. Mishra, T. C. Sum, and Y. Chan, “Low threshold, amplified spontaneous emission from core-seeded semiconductor nanotetrapods incorporated into a sol-gel matrix,” *Adv. Mater.*, vol. 24, no. 23, 2012.

[105] I. Moreels, G. Rainaó, R. Gomes, Z. Hens, T. Stöferle, and R. F. Mahrt, “Nearly temperature-independent threshold for amplified spontaneous emission in colloidal CdSe/CdS quantum dot-in-rods,” *Adv. Mater.*, vol. 24, no. 35, 2012.

[106] M. Saba *et al.*, “Exciton-exciton interaction and optical cain in colloidal CdSe/CdS Dot/Rod nanocrystals,” *Adv. Mater.*, vol. 21, no. 48, pp. 4942–4946, 2009.

[107] R. Patel, “Quantum Dot Lasers,” UNIVERSITY OF OXFORD, 2017.

[108] L. A. Coldren, S. W. Corzine, and M. L. Mašanović, “Diode Lasers and Photonic Integrated Circuits,” vol. 1, 2017, pp. 565–577.

[109] F. Träger, *Springer Handbook of Lasers and Optics*. 2012.

[110] C. Dang, J. Lee, C. Breen, J. S. Steckel, S. Coe-Sullivan, and A. Nurmikko, “Red, green and blue lasing enabled by single-exciton gain in colloidal quantum dot films,” *Nat. Nanotechnol.*, vol. 7, no. 5, pp. 335–339, 2012.

[111] C. Dang, J. Lee, C. Breen, J. S. Steckel, S. Coe-Sullivan, and A. Nurmikko, “Red, green and blue lasing enabled by single-exciton gain in colloidal quantum dot films,” *Nat.*

Nanotechnol., vol. 7, no. 5, pp. 335–339, 2012.

[112] B. Le Feber, F. Prins, E. De Leo, F. T. Rabouw, and D. J. Norris, "Colloidal-Quantum-Dot Ring Lasers with Active Color Control," *Nano Lett.*, vol. 18, no. 2, pp. 1028–1034, 2018.

[113] V. M. Menon, M. Luberto, N. V. Valappil, and S. Chatterjee, "Lasing from InGaP quantum dots in a spin-coated flexible microcavity," *Opt. Express*, vol. 16, no. 24, p. 19535, 2008.

[114] M. M. Adachi *et al.*, "Microsecond-sustained lasing from colloidal quantum dot solids," *Nat. Commun.*, vol. 6, pp. 6–13, 2015.

[115] C. Foucher, B. Guilhabert, N. Laurand, and M. D. Dawson, "Wavelength-tunable colloidal quantum dot laser on ultra-thin flexible glass," *Appl. Phys. Lett.*, vol. 104, no. 14, pp. 1–5, 2014.

[116] Z. Yuan, Z. Wang, P. Guan, X. Wu, and Y. C. Chen, "Lasing-Encoded Microsensor Driven by Interfacial Cavity Resonance Energy Transfer," *Adv. Opt. Mater.*, vol. 8, no. 7, pp. 1–9, 2020.

[117] C. Grivas *et al.*, "Single-mode tunable laser emission in the single-exciton regime from colloidal nanocrystals," *Nat. Commun.*, vol. 4, no. May, 2013.

[118] F. Montanarella *et al.*, "Lasing Supraparticles Self-Assembled from Nanocrystals," *ACS Nano*, vol. 12, no. 12, pp. 12788–12794, 2018.

[119] A. V. Malko *et al.*, "From amplified spontaneous emission to microring lasing using nanocrystal quantum dot solids," *Appl. Phys. Lett.*, vol. 81, no. 7, pp. 1303–1305, 2002.

[120] Y. Wang *et al.*, "Blue liquid lasers from solution of CdZnS/ZnS ternary alloy quantum dots with quasi-continuous pumping," *Adv. Mater.*, vol. 27, no. 1, pp. 169–175, 2014.

[121] Y. Wang *et al.*, "Unraveling the ultralow threshold stimulated emission from CdZnS/ZnS quantum dot and enabling high-Q microlasers," *Laser Photonics Rev.*, vol. 9, no. 5, pp. 507–516, 2015.

[122] K. H. Kim, P. H. Dannenberg, H. Yan, S. Cho, and S. H. Yun, "Compact Quantum-Dot

Microbeads with Sub-Nanometer Emission Linewidth," *Adv. Funct. Mater.*, vol. 2103413, pp. 1–8, 2021.

[123] J. Schäfer, J. P. Mondia, R. Sharma, Z. H. Lu, and L. J. Wang, "Quantum dot microdrop laser," *Opt. InfoBase Conf. Pap.*, 2008.

[124] Y. Chen *et al.*, "Colloidal quantum dot random laser," *Opt. Express*, vol. 19, no. 4, p. 2996, 2011.

[125] Y. Wang *et al.*, "Stimulated emission and lasing from CdSe/CdS/ZnS core-multi-shell quantum dots by simultaneous three-photon absorption," *Adv. Mater.*, vol. 26, no. 18, pp. 2954–2961, 2014.

[126] C. Gollner *et al.*, "Random Lasing with Systematic Threshold Behavior in Films of CdSe/CdS Core/Thick-Shell Colloidal Quantum Dots," *ACS Nano*, vol. 9, no. 10, pp. 9792–9801, 2015.

[127] Z. Yang, M. Pelton, I. Fedin, D. V. Talapin, and E. Waks, "A room temperature continuous-wave nanolaser using colloidal quantum wells," *Nat. Commun.*, vol. 8, no. 1, 2017.

[128] C. Dang, A. Nurmikko, C. Breen, J. S. Steckel, and S. Coe-Sullivan, "Optical gain and green/red vertical cavity surface emitting lasing from CdSe-based colloidal nanocrystal quantum dot thin films," *Opt. InfoBase Conf. Pap.*, pp. 4–5, 2011.

[129] H. Yang *et al.*, "Enhanced Multiexciton Emission Property in Gradient Alloy Core/Shell CdZnSeS/ZnS Quantum Dots: Balance between Surface Passivation and Strain-Induced Lattice Defect," *J. Phys. Chem. C*, vol. 125, no. 19, pp. 10759–10767, 2021.

[130] Y. Chen *et al.*, "Fabrication and optical characterization of a flexible colloidal quantum dot laser," *Proc. IEEE Conf. Nanotechnol.*, pp. 958–962, 2011.

[131] H. Jung *et al.*, "Tunable colloidal quantum dot distributed feedback lasers integrated on a continuously chirped surface grating," *Nanoscale*, vol. 10, no. 48, pp. 22745–22749, 2018.

[132] V. M. Lavchiev, A. Saeed, D. Pogany, and W. Jantsch, "A quantum dot nanoimprinted DFB laser," *IOP Conf. Ser. Mater. Sci. Eng.*, vol. 6, pp. 6–11, 2009.

[133] E. Lafalce *et al.*, "Robust lasing modes in coupled colloidal quantum dot microdisk pairs using a non-Hermitian exceptional point," *Nat. Commun.*, vol. 10, no. 1, pp. 1–8, 2019.

[134] C. H. Lin *et al.*, "Large-Scale Robust Quantum Dot Microdisk Lasers with Controlled High Quality Cavity Modes," *Adv. Opt. Mater.*, vol. 5, no. 9, 2017.

[135] W. Xie *et al.*, "On-Chip Integrated Quantum-Dot–Silicon-Nitride Microdisk Lasers," *Adv. Mater.*, vol. 29, no. 16, 2017.

[136] P. T. Snee, Y. Chan, D. G. Nocera, and M. G. Bawendi, "Whispering-gallery-mode lasing from a semiconductor nanocrystal/ microsphere resonator composite," *Adv. Mater.*, vol. 17, no. 9, pp. 1131–1136, 2005.

[137] P. U. Alves, N. Laurand, and M. D. Dawson, "Multicolor laser oscillation in a single self-assembled colloidal quantum dot microsphere," *2020 IEEE Photonics Conf. IPC 2020 - Proc.*, pp. 20–21, 2020.

[138] E. Yablonovitch and E. O. Kane, "Correction to 'Reduction of Lasing Threshold Current Density by the Lowering of Valence Band Effective Mass,'" *J. Light. Technol.*, vol. 4, no. 7, p. 961, 1986.

[139] A. R. Adams, "Band Structure engineering for low-threshold high-efficiency semiconductor lasers," *Electron. Lett.*, vol. 22, pp. 249–250, 1986.

[140] F. Fan *et al.*, "Continuous-wave lasing in colloidal quantum dot solids enabled by facet-selective epitaxy," *Nature*, vol. 544, no. 7648, pp. 75–79, 2017.

[141] K. S. Cho *et al.*, "High-performance crosslinked colloidal quantum-dot light-emitting diodes," *Nat. Photonics*, vol. 3, no. 6, pp. 341–345, 2009.

[142] X. Dai, Y. Deng, X. Peng, and Y. Jin, "Quantum-Dot Light-Emitting Diodes for Large-Area Displays: Towards the Dawn of Commercialization," *Adv. Mater.*, vol. 29, no. 14, 2017.

[143] X. Dai *et al.*, "Solution-processed, high-performance light-emitting diodes based on quantum dots," *Nature*, vol. 515, no. 7525, pp. 96–99, 2014.

[144] A. Nurmikko, "What future for quantum dot-based light emitters?," *Nat. Nanotechnol.*, vol. 10, no. 12, pp. 1001–1004, 2015.

[145] J. Lim, Y. S. Park, and V. I. Klimov, "Optical gain in colloidal quantum dots achieved with direct-current electrical pumping," *Nat. Mater.*, vol. 17, no. 1, pp. 42–48, 2018.

[146] J. Roh, Y. S. Park, J. Lim, and V. I. Klimov, "Optically pumped colloidal-quantum-dot lasing in LED-like devices with an integrated optical cavity," *Nat. Commun.*, vol. 11, no. 1, pp. 1–10, 2020.

[147] G. S. He, L. S. Tan, Q. Zheng, and P. N. Prasad, "Multiphoton absorbing materials: Molecular designs, characterizations, and applications," *Chem. Rev.*, vol. 108, no. 4, pp. 1245–1330, 2008.

[148] X. Li *et al.*, "CsPbX3Quantum Dots for Lighting and Displays: Roomerature Synthesis, Photoluminescence Superiorities, Underlying Origins and White Light-Emitting Diodes," *Adv. Funct. Mater.*, vol. 26, no. 15, pp. 2435–2445, 2016.

[149] Y. Wang and H. Sun, "All-Inorganic Metal Halide Perovskite Nanostructures: From Photophysics to Light-Emitting Applications," *Small Methods*, vol. 2, no. 1, pp. 1–27, 2018.

[150] J. Song, J. Li, X. Li, L. Xu, Y. Dong, and H. Zeng, "Quantum Dot Light-Emitting Diodes Based on Inorganic Perovskite Cesium Lead Halides (CsPbX3)," *Adv. Mater.*, vol. 27, no. 44, pp. 7162–7167, 2015.

[151] L. Protesescu *et al.*, "Nanocrystals of Cesium Lead Halide Perovskites (CsPbX3, X = Cl, Br, and I): Novel Optoelectronic Materials Showing Bright Emission with Wide Color Gamut," *Nano Lett.*, vol. 15, no. 6, pp. 3692–3696, 2015.

[152] Y. Wang, X. Li, X. Zhao, L. Xiao, H. Zeng, and H. Sun, "Nonlinear Absorption and Low-Threshold Multiphoton Pumped Stimulated Emission from All-Inorganic Perovskite Nanocrystals," *Nano Lett.*, vol. 16, no. 1, pp. 448–453, 2016.

[153] S. Yakunin *et al.*, "Low-threshold amplified spontaneous emission and lasing from colloidal nanocrystals of caesium lead halide perovskites," *Nat. Commun.*, vol. 6, pp. 1–8, 2015.

[154] S. Yang, Y. Wang, and H. D. Sun, "Advances and Prospects for Whispering Gallery Mode Microcavities," *Adv. Opt. Mater.*, vol. 3, no. 9, pp. 1136–1162, 2015.

[155] Y. Wang, X. Li, V. Nalla, H. Zeng, and H. Sun, "Solution-Processed Low Threshold

Vertical Cavity Surface Emitting Lasers from All-Inorganic Perovskite Nanocrystals," *Adv. Funct. Mater.*, vol. 27, no. 13, pp. 1–7, 2017.

[156] J. A. Castañeda *et al.*, "Efficient Biexciton Interaction in Perovskite Quantum Dots under Weak and Strong Confinement," *ACS Nano*, vol. 10, no. 9, pp. 8603–8609, 2016.

[157] Y. Zhang *et al.*, "Aggregation-Induced Emission Luminogens as Color Converters for Visible-Light Communication," *ACS Appl. Mater. Interfaces*, vol. 10, no. 40, pp. 34418–34426, 2018.

[158] M. A. Boles, M. Engel, and D. V. Talapin, "Self-assembly of colloidal nanocrystals: From intricate structures to functional materials," *Chem. Rev.*, vol. 116, no. 18, pp. 11220–11289, 2016.

[159] R. D. Piner, J. Zhu, F. Xu, and S. Hong, "' Dip-Pen ' Nanolithography," *Science (80-.).*, vol. 283, no. January, pp. 661–664, 1999.

[160] G. Fritz, V. Schädler, N. Willenbacher, and N. J. Wagner, "Electrosteric stabilization of colloidal dispersions," *Langmuir*, vol. 18, no. 16, pp. 6381–6390, 2002.

[161] A. Nag, M. V. Kovalenko, J. S. Lee, W. Liu, B. Spokoyny, and D. V. Talapin, "Metal-free inorganic ligands for colloidal nanocrystals: S2-, HS-, Se2-, HSe-, Te2-, HTe -, TeS32-, OH-, and NH 2- as surface ligands," *J. Am. Chem. Soc.*, vol. 133, no. 27, pp. 10612–10620, 2011.

[162] T. A. Witten and L. M. Sander, "Diffusion-limited aggregation, a kinetic critical phenomenon," *Phys. Rev. Lett.*, vol. 47, no. 19, pp. 1400–1403, 1981.

[163] P. J. Lu, E. Zaccarelli, F. Ciulla, A. B. Schofield, F. Sciortino, and D. A. Weitz, "Gelation of particles with short-range attraction," *Nature*, vol. 453, no. 7194, pp. 499–503, 2008.

[164] S. M. Rupich, E. V. Shevchenko, M. I. Bodnarchuk, B. Lee, and D. V. Talapin, "Size-dependent multiple twinning in nanocrystal superlattices," *J. Am. Chem. Soc.*, vol. 132, no. 1, pp. 289–296, 2010.

[165] D. Luo, C. Yan, and T. Wang, "Interparticle Forces Underlying Nanoparticle Self-Assemblies," *Small*, vol. 11, no. 45, pp. 5984–6008, 2015.

[166] K. J. M. Bishop, C. E. Wilmer, S. Soh, and B. A. Grzybowski, "Nanoscale forces and their uses in self-assembly," *Small*, vol. 5, no. 14, pp. 1600–1630, 2009.

[167] Y. Min, M. Akbulut, K. Kristiansen, Y. Golan, and J. Israelachvili, "The role of interparticle and external forces in nanoparticle assembly," *Nat. Mater.*, vol. 7, no. 7, pp. 527–538, 2008.

[168] T. Wang, X. Wang, D. Lamontagne, Z. Wang, Z. Wang, and Y. C. Cao, "Shape-controlled synthesis of colloidal superparticles from nanocubes," *J. Am. Chem. Soc.*, vol. 134, no. 44, pp. 18225–18228, 2012.

[169] K. Rae *et al.*, "InGaN μLEDs integrated onto colloidal quantum dot functionalized ultra-thin glass," *Opt. Express*, vol. 25, no. 16, p. 19179, 2017.

[170] C. Foucher *et al.*, "Flexible Glass Hybridized Colloidal Quantum Dots for Gb/s Visible Light Communications," *IEEE Photonics J.*, vol. 10, no. 1, pp. 1–11, 2018.

[171] C. H. Yeh, Y. F. Liu, C. W. Chow, Y. Liu, P. Y. Huang, and H. K. Tsang, "Investigation of 4-ASK modulation with digital filtering to increase 20 times of direct modulation speed of white-light LED visible light communication system," *Opt. Express*, vol. 20, no. 15, p. 16218, 2012.

[172] I. Dursun *et al.*, "Perovskite Nanocrystals as a Color Converter for Visible Light Communication," *ACS Photonics*, vol. 3, no. 7, pp. 1150–1156, 2016.

[173] S. Mei *et al.*, "High-Bandwidth White-Light System Combining a Micro-LED with Perovskite Quantum Dots for Visible Light Communication," *ACS Appl. Mater. Interfaces*, vol. 10, no. 6, pp. 5641–5648, 2018.

[174] T. K. and J. W. W. J. Grubor, S. C. J. Lee, K. Langer, "Wireless High-Speed Data Transmission with Phosphorescent White-Light LEDs," in *33rd European Conference and Exhibition of Optical Communication - Post-Deadline Papers (published 2008)*, 2007, pp. 1–2.

[175] Y. D. Zang and J. Zhang, "Optimal scheme of DCO-OFDM for optical frequency-selectivity," *Procedia Comput. Sci.*, vol. 131, pp. 1074–1080, 2018.

[176] W. Hong, T. Li, W. Li, and X. Shi, "Analysis of DCO-OFDM for Indoor Visible Light Communications," *J. Phys. Conf. Ser.*, vol. 1606, no. 1, 2020.

[177] D. Feezell and S. Nakamura, “Invention, development, and status of the blue light-emitting diode, the enabler of solid-state lighting,” *Comptes Rendus Phys.*, vol. 19, no. 3, pp. 113–133, 2018.

[178] J. J. D. Mckendry, E. Gu, N. Mcalinden, N. Laurand, K. Mathieson, and M. D. Dawson, “Micro-LEDs for biomedical applications,” pp. 1–38, 2021.

[179] D. V. Dinh, Z. Quan, B. Roycroft, P. J. Parbrook, and B. Corbett, “GHz bandwidth semipolar (112¯2) InGaN/GaN light-emitting diodes,” *Opt. Lett.*, vol. 41, no. 24, p. 5752, 2016.

[180] H. Haas, “LiFi is a paradigm-shifting 5G technology,” *Rev. Phys.*, vol. 3, no. October 2017, pp. 26–31, 2018.

[181] P. Tian *et al.*, “Micro-LED based optical wireless communications systems,” *Semicond. Semimetals*, vol. 106, pp. 281–321, 2021.

[182] N. Laurand *et al.*, “Colloidal quantum dot nanocomposites for visible wavelength conversion of modulated optical signals,” *Opt. Mater. Express*, vol. 2, no. 3, p. 250, 2012.

[183] H. Chun *et al.*, “LED Based Wavelength Division Multiplexed 10 Gb/s Visible Light Communications,” *J. Light. Technol.*, vol. 34, no. 13, pp. 3047–3052, 2016.

[184] P. Asbeck, “Self-absorption effects on the radiative lifetime in GaAs-GaAlAs double heterostructures,” *J. Appl. Phys.*, vol. 48, no. 2, pp. 820–822, 1977.

[185] A. P. Piquette, M. E. Hannah, and K. C. Mishra, “An Investigation of Self-Absorption and Corresponding Spectral Shift in Phosphors,” *ECS Trans.*, vol. 41, no. 37, pp. 1–9, 2019.

[186] A. M. Smith and S. Nie, “Semiconductor nanocrystals: Structure, properties, and band gap engineering,” *Acc. Chem. Res.*, vol. 43, no. 2, pp. 190–200, 2010.

[187] X. Yuan *et al.*, “Temperature-dependent photoluminescence of inorganic perovskite nanocrystal films,” *RSC Adv.*, vol. 6, no. 82, pp. 78311–78316, 2016.

[188] Y. Wang *et al.*, “Solution-Grown CsPbBr3/Cs4PbBr6 Perovskite Nanocomposites: Toward Temperature-Insensitive Optical Gain,” *Small*, vol. 13, no. 34, pp. 1–8, 2017.

[189] P. P. Manousiadis, K. Yoshida, G. A. Turnbull, and I. D. W. Samuel, "Organic semiconductors for visible light communications," *Philos. Trans. R. Soc. A Math. Phys. Eng. Sci.*, vol. 378, no. 2169, 2020.

[190] H.-Y. LIN, C.-W. SHER, T.-M. C. DAN-HUA HSIEH, XIN-YIN CHEN, HUANG-MING PHILIP CHEN, K.-M. LAU, and H.-C. K. CHYONG-HUA CHEN, CHIEN-CHUNG LIN, "Optical cross-talk reduction in a quantum-dot-based full-color micro-light-emitting-diode display by a lithographic-fabricated photoresist mold," *Photonics Res.*, vol. 5, no. 5, pp. 411–416, 2017.

[191] T. H. Kim *et al.*, "Full-colour quantum dot displays fabricated by transfer printing," *Nat. Photonics*, vol. 5, no. 3, pp. 176–182, 2011.

[192] B. Guilhabert *et al.*, "Integration by self-aligned writing of nanocrystal/epoxy composites on InGaN micro-pixelated light-emitting diodes.," *Opt. Express*, vol. 16, no. 23, pp. 18933–18941, 2008.

[193] J. S. Park *et al.*, "Alternative Patterning Process for Realization of Large-Area, Full-Color, Active Quantum Dot Display," *Nano Lett.*, vol. 16, no. 11, pp. 6946–6953, 2016.

[194] D. Bera, L. Qian, T. K. Tseng, and P. H. Holloway, "Quantum dots and their multimodal applications: A review," *Materials (Basel).*, vol. 3, no. 4, pp. 2260–2345, 2010.

[195] S. Ghimire and V. Biju, "Relations of exciton dynamics in quantum dots to photoluminescence, lasing, and energy harvesting," *J. Photochem. Photobiol. C Photochem. Rev.*, vol. 34, pp. 137–151, 2018.

[196] V. I. Klimov, "Nanocrystal Quantum Dots: From fundamental photophysics to multicolor lasing," *Los Alamos Sci.*, vol. 28, no. 28, pp. 214–220, 2003.

[197] F. Grillot *et al.*, "Physics and applications of quantum dot lasers for silicon photonics," *Nanophotonics*, vol. 9, no. 6, pp. 1271–1286, 2020.

[198] E. Marino *et al.*, "Favoring the Growth of High-Quality, Three-Dimensional Supercrystals of Nanocrystals," *J. Phys. Chem. C*, vol. 124, no. 20, pp. 11256–11264, 2020.

[199] G. C. Righini *et al.*, "Whispering Gallery Mode microresonators: Fundamentals and applications," *Riv. del Nuovo Cim.*, vol. 34, no. 7, pp. 435–488, 2011.

[200] D. Sarid and W. Challener, *Modern Introduction to Surface Plasmons*. Cambridge: Cambridge University Press, 2010.

[201] S. Balac and P. Féron, "Whispering gallery modes volume computation in optical micro-spheres. FOTON, UMR CNRS 6082.," 2014.

[202] Y. Meng, Z. Zhang, H. Yin, and T. Ma, "Automatic detection of particle size distribution by image analysis based on local adaptive canny edge detection and modified circular Hough transform," *Micron*, vol. 106, no. August 2017, pp. 34–41, 2018.

[203] D. Jevtics *et al.*, "Integration of Semiconductor Nanowire Lasers with Polymeric Waveguide Devices on a Mechanically Flexible Substrate," *Nano Lett.*, vol. 17, no. 10, pp. 5990–5994, 2017.

[204] D. B. Dement, M. Puri, and V. E. Ferry, "Determining the Complex Refractive Index of Neat CdSe/CdS Quantum Dot Films," *J. Phys. Chem. C*, vol. 122, no. 37, pp. 21557–21568, 2018.

[205] E. A. Riley, C. M. Hess, and P. J. Reid, "Photoluminescence intermittency from single quantum dots to organic molecules: Emerging themes," *Int. J. Mol. Sci.*, vol. 13, no. 10, pp. 12487–12518, 2012.

[206] M. Abbarchi *et al.*, "Poissonian statistics of excitonic complexes in quantum dots," *J. Appl. Phys.*, vol. 106, no. 5, 2009.

[207] M. Abbarchi *et al.*, "Poissonian excitonic population of single QDs," *Phys. E Low-Dimensional Syst. Nanostructures*, vol. 42, no. 4, pp. 884–886, 2010.

[208] S. H. Abid and S. H. Mohammed, "On The Continuous Poisson Distribution," *Int. J. Data Envel. Anal. *Operations Res.*, vol. 2, no. 1, pp. 7–15, 2016.

[209] N. Kholmicheva, P. Moroz, H. Eckard, G. Jensen, and M. Zamkov, "Energy transfer in quantum dot solids," *ACS Energy Lett.*, vol. 2, no. 1, pp. 154–160, 2017.

[210] Y. Lu *et al.*, "Multicolour laser from a single bandgap-graded CdSSe alloy nanoribbon," *Opt. Express*, vol. 21, no. 19, p. 22314, 2013.

[211] S. Il Park *et al.*, "Printed assemblies of inorganic light-emitting diodes for deformable and semitransparent displays," *Science (80-.).*, vol. 325, no. 5943, pp. 977–981, 2009.

[212] A. J. Trindade *et al.*, "Heterogeneous integration of gallium nitride light-emitting diodes on diamond and silica by transfer printing," *Opt. Express*, vol. 23, no. 7, p. 9329, 2015.

[213] H. J. Kim-Lee, A. Carlson, D. S. Grierson, J. A. Rogers, and K. T. Turner, "Interface mechanics of adhesiveless microtransfer printing processes," *J. Appl. Phys.*, vol. 115, no. 14, 2014.

[214] A. J. Trindade *et al.*, "Nanoscale-accuracy transfer printing of ultra-thin AlInGaN light-emitting diodes onto mechanically flexible substrates," *Appl. Phys. Lett.*, vol. 103, no. 25, 2013.

[215] D. A. B. Miller, "Attojoule Optoelectronics for Low-Energy Information Processing and Communications," *J. Light. Technol.*, vol. 35, no. 3, pp. 346–396, 2017.

[216] N. G. McCrum, C. P. Buckley, and C. B. Bucknall, *Principles of polymer engineering*, vol. 9, no. 1. New York: Oxford University Press Inc., 1988.

[217] X. Feng, M. A. Meitl, A. M. Bowen, Y. Huang, R. G. Nuzzo, and J. A. Rogers, "Competing fracture in kinetically controlled transfer printing," *Langmuir*, vol. 23, no. 25, pp. 12555–12560, 2007.

[218] M. A. Meitl *et al.*, "Transfer printing by kinetic control of adhesion to an elastomeric stamp," *Nat. Mater.*, vol. 5, no. 1, pp. 33–38, 2006.

[219] M. L. Williams, R. F. Landel, and J. D. Ferry, "The Temperature Dependence of Relaxation Mechanisms in Amorphous Polymers and Other Glass-forming Liquids," *J. Am. Chem. Soc.*, vol. 77, no. 14, pp. 3701–3707, 1955.

[220] N. Bamiedakis, J. Chen, R. V. Penty, and I. H. White, "Bandwidth studies on multimode polymer waveguides for ≥ 25 Gb/s optical interconnects," *IEEE Photonics Technol. Lett.*, vol. 26, no. 20, pp. 2004–2007, 2014.

[221] B. Bhola, H. C. Song, H. Tazawa, and W. H. Steier, "Polymer microresonator strain sensors," *IEEE Photonics Technol. Lett.*, vol. 17, no. 4, pp. 867–869, 2005.

[222] P. U. Alves, I. M. Watson, N. Laurand, and M. D. Dawson, "Water Resistant Caesium Lead Bromide Crystal Composites," *2018 Br. Irish Conf. Opt. Photonics, BICOP 2018 - Proc.*, no. December, pp. 12–15, 2019.

[223] A. Sharma, M. Sharma, K. Gungor, M. Olutas, D. Dede, and H. V. Demir, "Near-Infrared-Emitting Five-Monolayer Thick Copper-Doped CdSe Nanoplatelets," *Adv. Opt. Mater.*, vol. 7, no. 22, pp. 1–8, 2019.

[224] M. Sharma *et al.*, "Understanding the Journey of Dopant Copper Ions in Atomically Flat Colloidal Nanocrystals of CdSe Nanoplatelets Using Partial Cation Exchange Reactions," *Chem. Mater.*, vol. 30, no. 10, pp. 3265–3275, 2018.

[225] S. Shendre *et al.*, "Ultrahigh-efficiency aqueous flat nanocrystals of CdSe/CdS@Cd1−xZnxS colloidal core/crown@alloyed-shell quantum wells," *Nanoscale*, vol. 11, no. 1, pp. 301–310, 2019.

[226] M. Sharma *et al.*, "Near-Unity Emitting Copper-Doped Colloidal Semiconductor Quantum Wells for Luminescent Solar Concentrators," *Adv. Mater.*, vol. 29, no. 30, pp. 1–10, 2017.

[227] M. Sharma, S. Delikanli, and H. V. Demir, "Two-Dimensional CdSe-Based Nanoplatelets: Their Heterostructures, Doping, Photophysical Properties, and Applications," *Proc. IEEE*, vol. 108, no. 5, pp. 655–675, 2020.

[228] C. Li and P. Wu, "Cu-doped quantum dots: a new class of near-infrared emitting fluorophores for bioanalysis and bioimaging," *Luminescence*, vol. 34, no. 8, pp. 782–789, 2019.

[229] G. K. Grandhi and R. Viswanatha, "Tunable infrared phosphors using Cu doping in semiconductor nanocrystals: Surface electronic structure evaluation," *J. Phys. Chem. Lett.*, vol. 4, no. 3, pp. 409–415, 2013.

[230] S. Brovelli, C. Galland, R. Viswanatha, and V. I. Klimov, "Tuning radiative recombination in cu-doped nanocrystals via electrochemical control of surface trapping," *Nano Lett.*, vol. 12, no. 8, pp. 4372–4379, 2012.

[231] S. Wageh, A. A. Al-Ghamdi, A. A. Al-Zahrani, and H. Driss, "High quantum yield Cu doped CdSe quantum dots," *Mater. Res. Express*, vol. 6, no. 8, pp. 0–14, 2019.

[232] A. M. Jawaid, S. Chattopadhyay, D. J. Wink, L. E. Page, and P. T. Snee, "Cluster-seeded synthesis of doped CdSe:Cu4 quantum dots," *ACS Nano*, vol. 7, no. 4, pp. 3190–3197, 2013.

[233] N. Mishra, V. G. Vasavi Dutt, and M. P. Arciniegas, "Recent Progress on Metal Chalcogenide Semiconductor Tetrapod-Shaped Colloidal Nanocrystals and their Applications in Optoelectronics," *Chem. Mater.*, vol. 31, no. 22, pp. 9216–9242, 2019.

[234] H. Heo *et al.*, "Assemblies of Colloidal CdSe Tetrapod Nanocrystals with Lengthy Arms for Flexible Thin-Film Transistors," *Nano Lett.*, vol. 17, no. 4, pp. 2433–2439, 2017.

[235] C. L. Choi, H. Li, A. C. K. Olson, P. K. Jain, S. Sivasankar, and A. P. Alivisatos, "Spatially indirect emission in a luminescent nanocrystal molecule," *Nano Lett.*, vol. 11, no. 6, pp. 2358–2362, 2011.

[236] J. Lim *et al.*, "Controlled synthesis of CdSe tetrapods with high morphological uniformity by the persistent kinetic growth and the halide-mediated phase transformation," *Chem. Mater.*, vol. 25, no. 8, pp. 1443–1449, 2013.

[237] Y. Kim *et al.*, "Tailored growth of single-crystalline InP tetrapods," *Nat. Commun.*, vol. 12, no. 1, pp. 1–9, 2021.

[238] M. Olutas, B. Guzelturk, Y. Kelestemur, A. Yeltik, and S. Delikanli, "Lateral Size-Dependent Spontaneous and Stimulated Emission Properties in Colloidal CdSe Nanoplatelets," *ACS Nano*, vol. 9, no. 5, pp. 5041–5050, 2015.

[239] B. Guzelturk, Y. Kelestemur, M. Olutas, S. Delikanli, and H. V. Demir, "Amplified Spontaneous Emission and Lasing in Colloidal Nanoplatelets," *ACS Nano*, vol. 8, no. 7, pp. 6599–6605, 2014.

[240] Y. Altintas *et al.*, "Giant Alloyed Hot Injection Shells Enable Ultralow Optical Gain Threshold in Colloidal Quantum Wells," *ACS Nano*, vol. 13, pp. 10662–10670, 2019.

[241] D. Dede *et al.*, "Highly Stable Multicrown Heterostructures of Type-II Nanoplatelets for Ultralow Threshold Optical Gain," *Chem. Mater.*, vol. 31, pp. 1818–1826, 2019.

[242] O. Erdem *et al.*, "Orientation-Controlled Nonradiative Energy Transfer to Colloidal

Nanoplatelets: Engineering Dipole Orientation Factor," *Nano Lett.*, vol. 19, pp. 4297–4305, 2019.

[243] N. Taghipour *et al.*, "Near-Unity Efficiency Energy Transfer from Colloidal Semiconductor Quantum Wells of CdSe/CdS Nanoplatelets to a Monolayer of MoS2," *ACS Nano*, vol. 12, pp. 8547–8554, 2018.

[244] B. Liu *et al.*, "Light-Emitting Diodes with Cu-Doped Colloidal Quantum Wells : From Ultrapure Green , Tunable Dual-Emission to White Light," *Small*, vol. 15, no. 1901983, pp. 1–9, 2019.

[245] B. Liu, S. Delikanli, Y. Gao, D. Dede, and K. Gungor, "Nano Energy Nanocrystal light-emitting diodes based on type II nanoplatelets," *Nano Energy*, vol. 47, no. February, pp. 115–122, 2018.

[246] Y. Jiang, W. S. Ojo, B. Mahler, X. Xu, B. Abécassis, and B. Dubertret, "Synthesis of CdSe Nanoplatelets without Short-Chain Ligands: Implication for Their Growth Mechanisms," *ACS Omega*, vol. 3, no. 6, pp. 6199–6205, 2018.

[247] D. A. Kurtina, A. V. Garshev, I. S. Vasil'Eva, V. V. Shubin, A. M. Gaskov, and R. B. Vasiliev, "Atomically Thin Population of Colloidal CdSe Nanoplatelets: Growth of Rolled-up Nanosheets and Strong Circular Dichroism Induced by Ligand Exchange," *Chem. Mater.*, vol. 31, no. 23, pp. 9652–9663, 2019.

[248] M. R. Krames *et al.*, "Status and future of high-power light-emitting diodes for solid-state lighting," *IEEE/OSA J. Disp. Technol.*, vol. 3, no. 2, pp. 160–175, 2007.

[249] J. J. Wierer, J. Y. Tsao, and D. S. Sizov, "Comparison between blue lasers and light-emitting diodes for future solid-state lighting," *Laser Photonics Rev.*, vol. 7, no. 6, pp. 963–993, 2013.

[250] L. Wang *et al.*, "Highly efficient narrow-band green and red phosphors enabling wider color-gamut LED backlight for more brilliant displays," *Opt. Express*, vol. 23, no. 22, p. 28707, 2015.

[251] L. Huang *et al.*, "Highly Stable K2SiF6:Mn4+@K2SiF6Composite Phosphor with Narrow Red Emission for White LEDs," *ACS Appl. Mater. Interfaces*, vol. 10, no. 21, pp. 18082–18092, 2018.

[252] M. A. Becker *et al.*, “Bright triplet excitons in caesium lead halide perovskites,” *Nature*, vol. 553, no. 7687, pp. 189–193, 2018.

[253] B. T. Diroll, G. Nedelcu, M. V. Kovalenko, and R. D. Schaller, “High-Temperature Photoluminescence of CsPbX3(X = Cl, Br, I) Nanocrystals,” *Adv. Funct. Mater.*, vol. 27, no. 21, pp. 1–7, 2017.

[254] A. Loiudice, S. Saris, E. Oveisi, D. T. L. Alexander, and R. Buonsanti, “CsPbBr3QD/AlOxInorganic Nanocomposites with Exceptional Stability in Water, Light, and Heat,” *Angew. Chemie - Int. Ed.*, vol. 56, no. 36, pp. 10696–10701, 2017.

[255] J. Ren, X. Dong, G. Zhang, T. Li, and Y. Wang, “Air-stable and water-resistant all-inorganic perovskite quantum dot films for white-light-emitting applications,” *New J. Chem.*, vol. 41, no. 22, pp. 13961–13967, 2017.

[256] L. Gomez, C. De Weerd, J. L. Hueso, and T. Gregorkiewicz, “Color-stable water-dispersed cesium lead halide perovskite nanocrystals,” *Nanoscale*, vol. 9, no. 2, pp. 631–636, 2017.

[257] X. Chen *et al.*, “Centimeter-Sized Cs4PbBr6Crystals with Embedded CsPbBr3Nanocrystals Showing Superior Photoluminescence: Nonstoichiometry Induced Transformation and Light-Emitting Applications,” *Adv. Funct. Mater.*, vol. 28, no. 16, pp. 1–7, 2018.

[258] Newport, “Relation between power bandwidth and optical bandwidth.” [Online]. Available: https://www.newport.com/t/high-speed-detectors.

[259] C. C. Stoumpos *et al.*, “Crystal growth of the perovskite semiconductor CsPbBr3: A new material for high-energy radiation detection,” *Cryst. Growth Des.*, vol. 13, no. 7, pp. 2722–2727, 2013.

[260] S. J. Harley, E. A. Glascoe, and R. S. Maxwell, “Thermodynamic study on dynamic water vapor sorption in sylgard-184,” *J. Phys. Chem. B*, vol. 116, no. 48, pp. 14183–14190, 2012.

[261] P. J. Flory, *Principles of Polymer Chemistry*. Ithaca, New York: Cornell University Press, 1953.

[262] M. Unemori, Y. Matsuya, S. Matsuya, A. Akashi, and A. Akamine, “Water absorption

of poly(methyl methacrylate) containing 4-methacryloxyethyl trimellitic anhydride," *Biomaterials*, vol. 24, no. 8, pp. 1381–1387, 2003.

[263] Y. Tang *et al.*, "Highly Stable Perovskite Supercrystals via Oil-in-Oil Templating," *Nano Lett.*, vol. 20, no. 8, pp. 5997–6004, 2020.

[264] A. Fernandez-Bravo *et al.*, "Continuous-wave upconverting nanoparticle microlasers," *Nat. Nanotechnol.*, vol. 13, no. 7, pp. 572–577, 2018.

[265] C. A. McLellan *et al.*, "Alkaline-earth rare-earth upconverting nanoparticles as bio-compatible mechanical force sensors," *Opt. InfoBase Conf. Pap.*, vol. Part F183-, pp. 2–3, 2020.

[266] S. Schyck, J.-M. Meijer, L. Baldauf, P. Schall, A. V. Petukhov, and L. Rossi, "Self-assembly of colloidal superballs under spherical confinement of a drying droplet," *JCIS Open*, vol. 5, no. October 2021, p. 100037, 2022.

[267] S. Zrig *et al.*, "Self-assembly of nanoparticles from evaporating sessile droplets: Fresh look into the role of particle/substrate interaction," *Langmuir*, vol. 36, no. 39, pp. 11411–11421, 2020.

[268] Y. Kobayashi *et al.*, "Silica-coating of fluorescent polystyrene microspheres by a seeded polymerization technique and their photo-bleaching property," *Colloids Surfaces A Physicochem. Eng. Asp.*, vol. 242, no. 1–3, pp. 47–52, 2004.

[269] S. Soria *et al.*, "High-Q polymer-coated microspheres for immunosensing applications," *Opt. Express*, vol. 17, no. 17, p. 14694, 2009.

[270] J. Li *et al.*, "Optical nanomanipulation on solid substrates via optothermally-gated photon nudging," *Nat. Commun.*, vol. 10, no. 1, pp. 1–9, 2019.

[271] M. Mastrangeli, Q. Zhou, V. Sariola, and P. Lambert, "Surface tension-driven self-alignment," *Soft Matter*, vol. 13, no. 2, pp. 304–327, 2017.

[272] J. Berthier, K. Brakke, S. Mermoz, L. Sanchez, C. Fretigny, and L. Di Cioccio, "Self-alignment of silicon chips on wafers: A numerical investigation of the effect of spreading and wetting," *Sensors and Transducers*, vol. 13, no. SPEC.ISSUE, pp. 44–52, 2011.

[273] J. Yu, E. Lewis, G. Brambilla, and P. Wang, "Temperature sensing performance of

microsphere resonators," *Sensors (Switzerland)*, vol. 18, no. 8, pp. 1–15, 2018.

Part IV

Appendix

A. SPs and Mode Calculation

The calculations of the Transverse Electric (TE) and Transverse Magnetic (TM) electric modes for SPs in this thesis were based on the research report written by Stéphane Balac and Patrice Feron (Stéphane Balac, Patrice Feron. "Whispering gallery modes volume computation in optical micro-spheres". [Research Report] FOTON, UMR CNRS 6082. 2014. Hal-01279396v2).

Wolfram Mathematica™ was used to calculate and plot the WGMs.

From the research report above, the modal equation for TE electric field modes in a microsphere obtained by the Maxwell equations is given by:

$$\underline{\boldsymbol{E}}(r,\theta,\varphi) = A_{i/o}^{TE}\frac{r_l(kr)}{kr}\boldsymbol{X}_{lm}(\theta,\varphi)$$

Where $A_{i/o}^{TE}$ is a term whose value depends on the domain (index i when inside the SP and index o when outside the SP):

$$\begin{cases} A_i^{TE} = 1 \\ A_o^{TE} = -A_i^{TE}\dfrac{k_0}{k_0 N}\dfrac{\psi(l,k_0 NR)}{\zeta(l,k_0 R)} \end{cases}$$

With ψ being related to the Ricatti-Bessel function of first kind (uses "$SphericalBesselJ[]$" in Wolfram Mathematica™):

$$\psi(l,z) = z.SphericalBesselJ[l,z]$$

And ζ to the Ricatti-Bessel function of third kind:

$$\zeta(l,z) = \psi(l,z) + i\chi(l,z)$$

Where χ is associated to Ricatti-Bessel function of second kind (uses "$SphericalBesselY[]$" in Wolfram Mathematica™):

$$\chi(l,z) = -z.SphericalBesselY[l,z]$$

The wavenumber inside the SP, k, depends on the refractive index of the SP, N, and on the wavenumber in vacuum, k_0:

$$k = k_0 N; k_0 = \frac{2\pi}{\lambda_0}$$

The radial term r_l also depends on the domain:

$$r_l(kr) = \begin{cases} \psi(l, k_0 N r)\,, 0 \le r \le R \\ \zeta(l, k_0 r)\,, r > R \end{cases}$$

Where R is the radius of the microsphere.

$X_{lm}(\theta, \varphi)$ corresponds to one of the three vector spherical harmonics ($X_{lm}(\theta, \varphi)$, $Y_l(\theta, \varphi)$, $Z_{lm}(\theta, \varphi)$) and is given by the wedge product between the gradient of the scalar spherical harmonics and the vector $\boldsymbol{r} = \{r, 0, 0\}$:

$$\boldsymbol{X}_{lm}(\theta, \varphi) = \nabla Y_l^m \wedge \boldsymbol{r}$$

The scalar spherical harmonics is given by a Wolfram Mathematica™ function:

$$Y_l^m = SphericalHarmonicY[l, m, \theta, \varphi]$$

And the gradient ∇Y_l^m can be calculated by Wolfram Mathematica™ using the "$Grad[]$" function:

$$\nabla Y_l^m = Grad[SphericalHarmonicY[l, m, \theta, \varphi], \{r, \theta, \varphi\}, "Spherical"]$$

Likewise, the modal equation for TM electric modes is given by:

$$\underline{\boldsymbol{E}}(R, \theta, \varphi) = A_{i/o}^{TM} \left(l(l+1) \frac{r_l(kR)}{k^2 R^2} \boldsymbol{Z}_{lm}(\theta, \varphi) + \frac{r_l{}'(kR)}{kR} \boldsymbol{Y}_{lm}(\theta, \varphi) \right)$$

With:

$$\begin{cases} A_i^{TM} = 1 \\ A_o^{TM} = -A_i^{TM} \dfrac{\psi(l, k_0 N R)}{\zeta(l, k_0 R)} \end{cases}$$

$$r_l(kr) = \begin{cases} \psi(l, k_0 N r)\,, 0 \le r \le R \\ \zeta(l, k_0 r)\,, r > R \end{cases}$$

$$r'_l(z) = \begin{cases} \dfrac{d\psi(l,z)}{dz}, 0 \le r \le R \\ \dfrac{d\zeta(l,z)}{dz}, r > R \end{cases}$$

The other two vector spherical harmonics, $\boldsymbol{Y}_{lm}(\theta,\varphi)$ and $\boldsymbol{Z}_{lm}(\theta,\varphi)$, are given by:

$$\boldsymbol{Y}_{lm}(\theta,\varphi) = r\nabla Y_l^m$$

$$\boldsymbol{Z}_{lm}(\theta,\varphi) = Y_l^m \boldsymbol{e_r} = Y_l^m.\{1,0,0\}$$

Figures A.1 – A6 describe in detail the steps taken to calculate and plot these modes.

```
Modal Equation - Find l

MEl1[λ_, n_, R_] := (2 * Pi * (R + (λ*n)/(2*Pi*n*Sqrt[n^2-1])))/λ - 0.5;

MMl1[λ_, n_, R_] := (2 * Pi * (R + λ/(2*Pi*(n^2)*Sqrt[n^2-1])))/λ - 0.5;

MEl2[λ_, n_, R_] := (n * 2 * Pi * (R + (λ*n)/(2*Pi*n*Sqrt[n^2-1])))/λ - 0.5;

MMl2[λ_, n_, R_] := (n * 2 * Pi * (R + λ/(2*Pi*(n^2)*Sqrt[n^2-1])))/λ - 0.5;

a1 = MEl1[λ, n, R];
b1 = MMl1[λ, n, R];
a2 = MEl2[λ, n, R];
b2 = MMl2[λ, n, R];
Print[a1, " < L_TE < ", a2]
Print[b1, " < L_TM < ", b2]
```

A. 1. These 4 functions define the region of interest for l (first and third for TE modes and second and fourth for TM modes), according to the SP laser emission wavelength (λ), its refractive index, N, and its radius, R.

```
(* Modal function - TE; P = n*)
ME[l_, λ_, n_, R_] := Im[HankelH1[l - 0.5, 2*Pi/λ * R]] / Im[HankelH1[l + 0.5, 2*Pi/λ * R]] - n * BesselJ[l - 0.5, n * 2*Pi/λ * R] / BesselJ[l + 0.5, n * 2*Pi/λ * R] - l * (1/(2*Pi/λ * R) - n/(n * 2*Pi/λ * R));

(* Modal function - ME; P = 1/n *)
MM[l_, λ_, n_, R_] := Im[HankelH1[l - 0.5, 2*Pi/λ * R]] / Im[HankelH1[l + 0.5, 2*Pi/λ * R]] - (1/n) * BesselJ[l - 0.5, n * 2*Pi/λ * R] / BesselJ[l + 0.5, n * 2*Pi/λ * R] - l * (1/(2*Pi/λ * R) - (1/n)/(n * 2*Pi/λ * R));
```

A. 2. Modal functions for TE and TM modes. First they are used to find l in the region of interest by finding values for which the functions are equal to zero within that range and according to the laser emission wavelength of the SP (λ), its refractive index (N), and its radius (R).

```
"Modal Equation - Find λ"
```

```
Modal Equation - Find λ
```

$$\alpha TE[n\_] := \frac{n}{n * \text{Sqrt}[n^2 - 1]};$$

$$\alpha TM[n\_] := \frac{1}{n^2 * \text{Sqrt}[n^2 - 1]};$$

$$ME\lambda 1[findl\_, n\_, R\_] := \frac{2 * Pi * R}{findl + 0.5 - \alpha TE[n]};$$

$$ME\lambda 2[findl\_, n\_, R\_] := \frac{2 * Pi * R * n}{findl + 0.5 - \alpha TE[n] * n};$$

$$MM\lambda 1[findl\_, n\_, R\_] := \frac{2 * Pi * R}{findl + 0.5 - \alpha TM[n]};$$

$$MM\lambda 2[findl\_, n\_, R\_] := \frac{2 * Pi * R * n}{findl + 0.5 - \alpha TM[n] * n};$$

```
c1 = MEλ1[36, n, R];
d1 = MMλ1[35, n, R];
c2 = MEλ2[36, n, R];
d2 = MMλ2[35, n, R];
Print[c1, " < λTE < ", c2]
Print[d1, " < λTM < ", d2]

c21 = MEλ1[27, n, R];
d21 = MMλ1[27, n, R];
c22 = MEλ2[27, n, R];
d22 = MMλ2[27, n, R];
Print[c21, " < λTE < ", c22]
Print[d21, " < λTM < ", d22]
```

A. 3. These 4 functions ($ME\lambda 1; MM\lambda 1;\ ME\lambda 2;\ MM\lambda 2$) define the region of interest for λ (first and third for TE modes and second and fourth for TM modes), according to the list of l numbers found in figure A.2., the refractive index of the SP, N, and its radius, R.

The λ at the resonance frequencies are then found by using the Modal equations in A.2, and by finding the zeros for each l number previously found (e.g. A.4).

The definition in Mathematica™ of the TM and TE electric field modes can be found in A.5.

```
Lpic2e = Plot[{ME[36, λ, n, R], ME[31, λ, n, R], ME[27, λ, n, R]}, {λ, MEλ1[findl, n, R], MEλ2[findl, n, R]},
  LabelStyle → {20, GrayLevel[0]}, PlotRange → {{0.625, 0.645}, {-0.5, 1.5}}, FrameLabel → {"λ (μm)", None},
  Frame → True, FrameTicks → {{{-1, 0, 1}, None}, {{0.630, 0.640}, None}}, GridLines → Automatic,
  PlotLegends → Placed[SwatchLegend[{"l=36; λ=0.629", "l=31; λ=0.634", "l=27; λ=0.639"},
    LegendFunction → (Framed[#, RoundingRadius → 5, Background → White] & )], Scaled[{0.625, 0.625}]], ImageSize → is
```

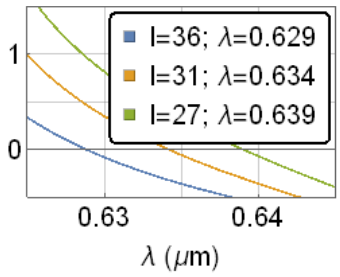

A.4. Plot of the Modal function for TE modes and finding the λ at resonance frequencies (example given for l: 36, 31, 27; R =2.45; N =1.7)

```
(* Electric field, TE mode *)

(* Inside the sphere, ricatti bessel first mode only *)
ψ[l_, z_] := z * SphericalBesselJ[l, z];
dψ[l_, x_] :=
  SphericalBesselJ[l, x] + x (-SphericalBesselJ[l, x]/(2 x) + 1/2 (SphericalBesselJ[-1 + l, x] - SphericalBessel[1 +

(* outside the sphere, ricatti bessel third kind (first + i second) *)
χ[l_, z_] := -z * SphericalBesselY[l, z];
ξ[l_, z_] := ψ[l, z] + I * χ[l, z];
dξ[l_, z_] :=
  SphericalBesselJ[l, z] + z (-SphericalBesselJ[l, z]/(2 z) + 1/2 (SphericalBesselJ[-1 + l, z] - SphericalBessel[1 +
   i SphericalBesselY[l, z] - i z (-SphericalBesselY[l, z]/(2 z) + 1/2 (SphericalBesselY[-1 + l, z] - SphericalBesselY

(* TE complex constant nr i/o the sphere *)
Ai = 1;
A0te[k0_, N_, R_, l_] := -Ai * k0/(k0 * N) * ψ[l, k0 * N * R]/ξ[l, k0 * R]

(* Radial Field - excludes the vectorial harmonic X_lm(Θ,ϕ) *)
EteR[k0_, N_, r_, R_, l_] := Piecewise[{{Ai * ψ[l, k0 * N * r]/(k0 * N * r), 0 < r ≤ R}, {-1 * A0te[k0, N, R, l] * ξ[l, k0 * r]/(k0 * r),
```

```
(* Electric Field *)
(* TE Modes - includes the vectorial harmonic X_lm(θ,ϕ) *)

(* Calculating the vectorial harmonic, X_lm(θ,ϕ) = ∇Y_l^m ∧ r *)
Grad[SphericalHarmonicY[l, m, θ, ϕ], {r, θ, ϕ}, "Spherical"];

GradY[r_, θ_, ϕ_, l_, m_] :=
  {0,
   1/r (m Cot[θ] SphericalHarmonicY[l, m, θ, ϕ] +
      e^(-i ϕ) Sqrt[Gamma[1 + l - m]] Sqrt[Gamma[2 + l + m]] SphericalHarmonicY[l, 1 + m, θ, ϕ] /
       (Sqrt[Gamma[l - m]] Sqrt[Gamma[1 + l + m]])),
   i m Csc[θ] SphericalHarmonicY[l, m, θ, ϕ] / r};

X[r_, θ_, ϕ_, l_, m_] := Cross[GradY[r, θ, ϕ, l, m], {r, 0, 0}]

Ete[r_, θ_, ϕ_, l_, m_, k0_, N_, R_] := EteR[k0, N, r, R, l] * X[r, θ, ϕ, l, m]

(* TM Modes - includes the vectorial harmonic Y_lm(θ,ϕ) = r∇Y_l^m and Z_lm(θ,ϕ) = Y_l^m.{1,0,0} *

Z[l_, m_, θ_, ϕ_] := SphericalHarmonicY[l, m, θ, ϕ] * {1, 0, 0}

Y[r_, l_, m_, θ_, ϕ_] :=
 r *
  {0,
   1/r (m Cot[θ] SphericalHarmonicY[l, m, θ, ϕ] +
      e^(-i ϕ) Sqrt[Gamma[1 + l - m]] Sqrt[Gamma[2 + l + m]] SphericalHarmonicY[l, 1 + m, θ, ϕ] /
       (Sqrt[Gamma[l - m]] Sqrt[Gamma[1 + l + m]])),
   i m Csc[θ] SphericalHarmonicY[l, m, θ, ϕ] / r}

(* TM complex constant nr i/o the sphere *)
Ai = 1;
A0tm[k0_, N_, R_, l_] := -Ai * 1/N^2 * ψ[l, k0*N*R] / ξ[l, k0*R];

(* Electric field inside the sphere - TM*)
Etm[r_, θ_, ϕ_, l_, m_, k0_, N_, R_] :=
 Piecewise[{{Ai * (l (l + 1) * (ψ[l, k0*N*r] / (k0*N*r)^2) * Z[l, m, θ, ϕ] + (dψ[l, k0*N*r] / (k0*N*r)) * Y[r, l, m, θ, ϕ]), 0 < r ≤ R}
   {-A0tm[k0, N, R, l] * (l (l + 1) * (ξ[l, k0*r] / (k0*r)^2) * Z[l, m, θ, ϕ] + (dξ[l, k0*r] / (k0*r)) * Y[r, l, m, θ, ϕ]), r > R}}]
```

A. 5. Definition of the TE and TM electric field modes.

An example of a contour plot of the norm of the real part of the Electric TM mode can be found in A.6.

```
(* TM MODES *)
(* XY - plane *)
(* Θ = 0 *)
Cpic1xyM = ContourPlot[Norm[Re[Etm[Norm[{x, y, 0}], Pi / 2, ArcCos[x / Norm[{x, y, 0}]], 35, 35 - 15, 2 * Pi / 0.633, n, R]]]
  {x, -5, 5}, {y, -5, 5}, RegionFunction → Function[{x, y, z}, 0 ≤ Norm[{x, y, 0}] ≤ R], BoundaryStyle → Red,
  AspectRatio → Automatic, ImageSize → is, LabelStyle → {FontFamily → "Arial", 20, GrayLevel[0]},
  FrameLabel → {"X (μm)", "Y (μm)"}, PlotRange → All]
```

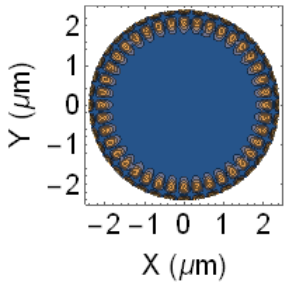

A.6. Electric TM modes (norm of the real component) of a SP with R =2.45; N =1.7; l=35 and m=20.

B. SPs and Emission Model

This annex shows how the emission model of the SPs was obtained from their emission spectra. This analysis used a script written in Wolfram Mathematica™ capable of reading the output data from the spectrometer from an excel file and process it to find the fitting parameters discussed in Chapters 2 and 3 ($\alpha, \beta \; and \; A$). The routines of this script were, step by step:

1. Call the data from the excel file and retrieve (Fig. B1 and B2):
    a. The original list (with background removed) as a vector list with the counts for each wavelength and pump energy:

    $$C_\lambda = \{\left\{\left\{\lambda_1^{E_1};\ counts_{\lambda_1}^{E_1}\right\}, \dots, \left\{\lambda_n^{E_1}; counts_{\lambda_n}^{E_1}\right\}\right\}, \dots, \left\{\dots, \left\{\lambda_n^{E_k}; counts_{\lambda_n}^{E_k}\right\}\right\}\};$$

    b. The below threshold and above threshold lists, as vector lists with the sum of the counts over the lasing modes for each pump energy and microsphere size:

    $$C_E = \{\left\{SP1_{radius};\ E_1\ ;\ \sum_{i=\lambda_{min}}^{\lambda_{max}} counts_{\lambda_i}\right\}, \dots, \left\{SP1_{radius};\ E_k\ ;\ \sum_{i=\lambda_{min}}^{\lambda_{max}} counts_{\lambda_i}\right\}\}$$

    ;

    c. The complete list, as a vector list with the sum of the counts over the lasing modes for each pump energy:

    $$C_{Et} = \{\left\{\ E_1\ ;\ \sum_{i=\lambda_{min}}^{\lambda_{max}} counts_{\lambda_i}\right\}, \dots, \left\{\ E_k\ ;\ \sum_{i=\lambda_{min}}^{\lambda_{max}} counts_{\lambda_i}\right\}\};$$

    d. The lists with the maxima of PL emission for the biexciton and multiexciton emission as a function of the pump energy:

    $$M_E = \{\{E_1\ ; counts_{\lambda_{max}}\}, \dots, \{E_k\ ; counts_{\lambda_{max}}\}\};$$

    e. The lists with the fitted parameters to Gaussian distributions for the biexciton and multiexciton PL emissions and for all the pump energies:

$$M_p = \{\{a_1;\ b_1;\ c_1\}, \ldots, \{a_k;\ b_k;\ c_k\}\}.$$

2. For each microsphere, apply the multi-nonlinear model fit to the expression that describes the emission of a SP (Fig. B3):
    a. First and similarly to QDs, the average number of excitons of a QD in a SP is approximated to a power law trend as a function of the unknown parameters (α, β) and pump energy (E_{pump}):
    $$\langle N \rangle = \beta . E_{pump}^{\alpha}$$
    b. In a QD, the probability of the emission of a photon resulting from the recombination of the nth-exciton follows a Poisson distribution. However, because the total emission of photons taking place in a SP depends on the nth-exciton of each of its QDs, the Poisson probability distribution is used in its continuous form, and gives the probability of the SP to have k excitons for an average number of excitons as a function of the optical pump $\langle N \rangle$. The gamma function, Γ, is predefined in Mathematica™:
    $$P(k; \langle N \rangle) = \frac{\Gamma(k+1, \langle N \rangle)}{\Gamma(k+1)} - \frac{\Gamma(k, \langle N \rangle)}{\Gamma(k)}$$
    c. The multi-nonlinear model fit (Contributed by: Sjoerd Smit, https://resources.wolframcloud.com/FunctionRepository/resources/MultiNonlinearModelFit/) is used to fit the two equations below:
    $$\begin{cases} Data_{630nm} = A.P(k_1; \langle N \rangle), & 1 < k_1 < 2; \\ Data_{580nm} = A.P(k_2; \langle N \rangle), & k_2 > 3; \end{cases}$$
    That correspond to the biexciton and multiexciton emissions, respectively. The intensity of these two emissions can be extracted from the measured spectra at their respective wavelengths ($Data_{630nm}$ and $Data_{580nm}$). Here, the parameter A is assumed to depend on the number of active QDs in the SP and to the coupling efficiency onto the spectrometer. The emission at 630 nm corresponds to the energy of biexciton emission (k_1) and therefore, the average nth-exciton in the SP should sit exclusively between $1 < k_1 < 2$. Likewise, the emission at 580 nm corresponds to the energy of multiexciton emission (k_2) and therefore, the average nth-exciton in the SP should be such that $k_2 > 3$.

```
In[50]:= (* Data processing/ NEEDS SizeALL list *)
DataProc[DataMS_, Nr_, ThresholdPostion_, λmin_, λmax_] :=
 Module[{i, list, n, MS, BckGnd, MSEnergy, MSsize, MSlistBT, MSlistAT, MSlistT, FitExc, SolExc, a1, a1err, b1,
   b1err, a2, a2err, b2, b2err, c2, c2err, d2, d2err, e2, e2err, a, b, c, d, e, x, DataME, DataMEfit, DataEBE, DataEBEfit},
  (* Spectrum/ noise removed *)
  MS = {};
  For[i = 2, i ≤ Dimensions[DataMS][[2]], i++,
   list = TimeSeries[Table[{DataMS[[n]][[1]], DataMS[[n]][[i]]}, {n, 2, Dimensions[DataMS][[1]], 1}]];
   BckGnd = Mean[TimeSeriesWindow[list, {200, 500}]];
   list = list - BckGnd;
   MS = Append[MS, TimeSeries[list]]];

  (* MS energy data/ Units: nJ *)
  MSEnergy = Table[DataMS[[1]][[n]] / Lfreq, {n, 2, Dimensions[DataMS][[2]], 1}] * 10^3;

  (* MS size data (Radius)/ Units: μm *)
  MSsize = SizeAll[[Nr + 1]][[2]] / 2;

  (* Count Integration over Δλ / Units: {μm, nJ, Average counts read per pulse} *)
  MSlistBT = {};
  For[i = 1, i ≤ ThresholdPostion, i++,
   MSlistBT = Append[MSlistBT, {MSsize, MSEnergy[[i]], NIntegrate[MS[[i]][x], {x, λmin, λmax}] / Lfreq}];
  ];
  (* Count Integration over Δλ / Units: {μm, nJ, Average counts read per pulse} *)
  MSlistAT = {};
  For[i = 1 + ThresholdPostion, i < Dimensions[DataMS][[2]], i++,
   MSlistAT = Append[MSlistAT, {MSsize, MSEnergy[[i]], NIntegrate[MS[[i]][x], {x, λmin, λmax}] / Lfreq}];
  ];
  (* Count Integration over Δλ / Units: {nJ, Average counts read per pulse} *)
  MSlistT = {};
  For[i = 1, i ≤ Dimensions[MS][[1]], i++,
   MSlistT = Append[MSlistT, {MSEnergy[[i]], NIntegrate[MS[[i]][x], {x, λmin, λmax}] / Lfreq}];
  ];

  DataME = {};
  DataMEfit = {};
  DataEBE = {};
  DataEBEfit = {};

  For[i = 1, i ≤ Dimensions[MS][[1]], i++,
   (* Exciton/ Biexciton and Multiexciton Peak Fits *)
   FitExc = TimeSeriesInsert[TimeSeriesWindow[TimeSeriesResample[MS[[i]], 0.5], {550, λmin}],
     TimeSeriesWindow[TimeSeriesResample[MS[[i]], 0.5], {λmax, 680}]];
   SolExc = NonlinearModelFit[FitExc, {a * PDF[NormalDistribution[b, c], x] + d * PDF[NormalDistribution[e, c], x],
      0 < a, 575 < b < 595, 8 < c < 25, 0 < d, 620 < e < 665}, {a, {b, 585}, {c, 10}, d, {e, 630}}, x];
   a2 = SolExc["ParameterTable"][[1]][[1]][[2]][[2]];
   a2err = SolExc["ParameterTable"][[1]][[1]][[2]][[3]];
   b2 = SolExc["ParameterTable"][[1]][[1]][[3]][[2]];
   b2err = SolExc["ParameterTable"][[1]][[1]][[3]][[3]];
   c2 = SolExc["ParameterTable"][[1]][[1]][[4]][[2]];
   c2err = SolExc["ParameterTable"][[1]][[1]][[4]][[3]];
   d2 = SolExc["ParameterTable"][[1]][[1]][[5]][[2]];
   d2err = SolExc["ParameterTable"][[1]][[1]][[5]][[3]];
   e2 = SolExc["ParameterTable"][[1]][[1]][[6]][[2]];
   e2err = SolExc["ParameterTable"][[1]][[1]][[6]][[3]];

   DataME = Append[DataME, {MSEnergy[[i]], a2 * PDF[NormalDistribution[b2, c2], b2] / Lfreq}];
   DataMEfit = Append[DataMEfit, {a2, b2, c2}];

   DataEBE = Append[DataEBE, {MSEnergy[[i]], d2 * PDF[NormalDistribution[e2, c2], e2] / Lfreq}];
   DataEBEfit = Append[DataEBEfit, {d2, e2, c2}];

  ];
  (*Print Fitted positions of ME and EBE peaks*)

  Return[{MS, MSlistBT, MSlistAT, MSlistT, TimeSeries[DataME], DataMEfit, TimeSeries[DataEBE], DataEBEfit}];
```

B. 1. Function to call the data of the spectra from the excel file.

```
(* Size data *)
SizeAll = Flatten[Import["C:\\Users\\Admin\\Desktop\\red new beam\\ms size Data.xlsx"], 1];
```

B. 2. Function to call the data of the sizes for each SP (from a different excel file).

```
(* Continuous Poisson *)
PoissonC[k_, x_] := Gamma[1 + k, x] / Gamma[1 + k] - Gamma[k, x] / Gamma[k]

(* Poissonian, v = {k,β,α,Exciton} *)
Poi[x_, v_] := v[[1]] * PoissonC[v[[4]], v[[2]] * (x^v[[3]])];

(* Power law fit *)
PLfit[NPoints_, DataEBE_, DataME_, kinit_, βinit_, αinit_, N1init_, N2init_] :=
  Module[{sol, x, k, β, α, N1, N2, a, aerr, b, berr, c, cerr, d, derr, e, eerr},
   sol = MultiNonlinearModelFit[{Take[DataEBE["Path"], NPoints], Take[DataME["Path"], NPoints]}, <|
      "Expressions" → {Poi[x, {k, β, α, N1}], Poi[x, {k, β, α, N2}]},
      "Constraints" → 0 < k && 0 < β < 5 && 0 < α < 1 && 1 < N1 < 2 && 3 < N2 < 8
      |>, {{k, kinit}, {β, βinit}, {α, αinit}, {N1, N1init}, {N2, N2init}}, {x}];
   a = sol["ParameterTable"][[1]][[1]][[2]][[2]];
   aerr = sol["ParameterTable"][[1]][[1]][[2]][[3]];
   b = sol["ParameterTable"][[1]][[1]][[3]][[2]];
   berr = sol["ParameterTable"][[1]][[1]][[3]][[3]];
   c = sol["ParameterTable"][[1]][[1]][[4]][[2]];
   cerr = sol["ParameterTable"][[1]][[1]][[4]][[3]];
   d = sol["ParameterTable"][[1]][[1]][[5]][[2]];
   derr = sol["ParameterTable"][[1]][[1]][[5]][[3]];
   e = sol["ParameterTable"][[1]][[1]][[6]][[2]];
   eerr = sol["ParameterTable"][[1]][[1]][[6]][[3]];
   Return[{{a, b, c, d}, {aerr, berr, cerr, derr}, {a, b, c, e}, {aerr, berr, cerr, eerr}}]];
```

B. 3. Function to call the data of the sizes for each SP (from a different excel file).

C. Journal Publications

2018 IEEE British and Irish Conference on Optics and Photonics
12-14 December 2018, London

Water Resistant Caesium Lead Bromide Crystal Composites

Pedro Urbano Alves, Ian M. Watson, Nicolas Laurand and Martin D. Dawson
Institute of Photonics, Department of Physics, SUPA, University of Strathclyde
Glasgow, UK
pedro.alves@strath.ac.uk

Abstract — *Water-resistant luminescent polymer composites with $CsPbBr_3$ quantum dots in Cs_4PbBr_6 crystals ($CsPbBr_3$@Cs_4PbBr_6) are reported. These color-converting materials enable a narrow-band green emission with fast dynamics and are therefore a potential alternative to phosphors, mainly for applications that require a fast modulation of light.*

Keywords — Visible Light Communication, Perovskite, Quantum Dot, Semiconductor Nanocrystal, Encapsulation, LED.

I. Introduction

Solid-state lighting and display technologies rely on UV/blue GaN LEDs, or in some special cases laser diodes, to optically pump phosphors [1], [2]. For the purpose of high light quality and/or wide color gamut, a combination of narrow-band red and green phosphors are used [3]. For device processing and operation stability, the phosphors are also required to be heat and water resistant [3], [4]. However, the very long photoluminescence (PL) lifetime of phosphors precludes their utilization in applications requiring high speed modulation of the light, e.g. visible light communications [5], [6].

Colloidal quantum dots (QDs) represent an alternative to phosphors for such applications [6], [7]. QDs are nanoscale semiconductor crystals [8] with high PL quantum efficiency, narrow emission linewidth and typical luminescence lifetimes 10^3 to 10^5 shorter than those of phosphors [7], [9]. Perovskite QDs of composition $CsPbX_3$ (with X a halide ion), demonstrated for the first time 3 years ago [10], are particularly attractive because they have the fastest dynamics of all known QDs [9], [11].

Despite these advantages, QDs have limitations in terms of stability. Several approaches have been reported to improve their thermal stability [12], [13], but their sensitivity to oxygen and moisture continues to be a problem and few solutions have been reported to solve them [13]–[15].

A promising material for narrow-band green color conversion is the so-called $CsPbBr_3$@Cs_4PbBr_6 [16]. It consists of $CsPbBr_3$ QDs formed within the wide band gap material Cs_4PbBr_6, which acts as a matrix for the QDs [17], [18]. As opposed to colloidal QDs, these $CsPbBr_3$ QDs are inherently encapsulated in Cs_4PbBr_6 and have no organic ligands on their surfaces, which is beneficial for thermal and photostability. The band edge emission of such material has been shown to be practically temperature invariant [16]. However, a low cost method to enhance the stability of $CsPbBr_3$@Cs_4PbBr_6 upon water exposure remains a challenge. This work comprises synthesis and analysis of $CsPbBr_3$@Cs_4PbBr_6 crystals, and studies of the luminescence properties of related composite samples when placed in contact with water. A guest-host approach is chosen and two different polymeric materials are studied for the matrix host: poly(methyl methacrylate) (PMMA) and polydimethylsiloxane (PDMS).

II. Materials and Methodology

A. Synthesis of Caesium Lead Bromide Crystals

Stoichiometric amounts of caesium bromide and lead bromide at a 4:1 mole ratio were dissolved together in a minimum quantity of dimethylsulfoxide solvent for the $CsPbBr_3$@Cs_4PbBr_6 preparation. This precursor solution was placed in an open inner vial inside a sealed outer jar containing chloroform. Vapour diffusion of the chloroform into the metal salt solution was complete over about 24 hours and caused formation and precipitation of the crystalline solids. This method follows previously reported preparations, but with chloroform acting as an antisolvent [16]. The collected crystals, with sizes ranging from a few hundreds of µm to mm, were washed with chloroform and dried under atmospheric pressure at 60 ºC (Fig. 1). Manual grinding was done with an agate pestle and mortar.

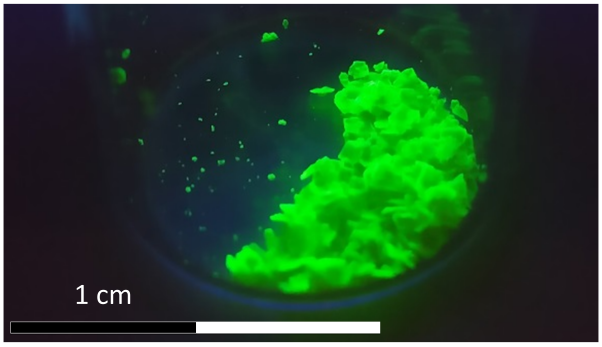

Fig. 1. Synthesized bulk $CsPbBr_3$@Cs_4PbBr_6 crystals under UV illumination.

B. Preparation of Composites

Two PMMA samples were fabricated by dissolving and stirring PMMA (Sigma-Aldrich) in toluene, together with ground $CsPbBr_3$@Cs_4PbBr_6. A mass ratio of 3:1 was used for PMMA and crystals. The solvent was left to evaporate over time, under atmospheric pressure and temperature. One of the PMMA samples, a slab with a thickness of approximately 1 mm, was tested as it was after the PMMA polymerization (*PMMA slab*). The second sample, also a slab with a thickness of approximately 1 mm, was additionally

978-1-5386-7361-4/18/$31.00 ©2018 IEEE

encapsulated in PDMS (*PMMA slab encapsulated in PDMS*).

Two further PDMS samples were prepared by stirring PDMS (Sylgard 184, Dow Corning) with ground $CsPbBr_3@Cs_4PbBr_6$. A mass ratio of 3:1 was used between PDMS and crystals, and a mass ratio of 5:1 between elastomer and curing agent. These composites were cured at 60°C. One of the samples was moulded in the shape of a slab, approximately 1mm thick (*PDMS slab*), and the other in the shape of a thicker composite, approximately 3mm thick (*PDMS thick*). Crystal sedimentation was observed during the preparation of PDMS samples. This led to a heterogeneity in the concentration of $CsPbBr_3@Cs_4PbBr_6$ in the PDMS slab and to a lower concentration of $CsPbBr_3@Cs_4PbBr_6$ in the PDMS thick sample.

C. Phase Analysis of Perovskite Crystals

X-Ray Difraction (XRD) analysis was performed on ground $CsPbBr_3@Cs_4PbBr_6$ crystals using a Bruker D8 Discover diffractometer (GX000915), and copper radiation at a wavelength of 1.5406 Å.

D. Characterization of Composites

A 100×100 μm^2 450 nm-emitting LED was used as pump source to measure the PL of all composites. Two sets of two lenses each (aspheric lenses, Numerical Aperture, NA=0.621 and diameter of 45 mm, Thorlabs) were used to, respectively, image the LED light onto the samples, and to collect the composite's emission onto the detector. A fiber-coupled CCD spectrometer (Ocean Optics, USB 4000; resolution: 2 nm at full width half maximum) was used to acquire the emitted spectral data.

The absorbance was measured by replacing the pump source in the previously described setup by a tungsten halogen lamp (Ocean Optics, HL-2000). Blank composites (i.e. with no $CsPbBr_3@Cs_4PbBr_6$ crystals) of PDMS and PMMA were used as reference samples.

III. Results and Discussion

A. XRD on $CsPbBr_3@Cs_4PbBr_6$ crystals

Fig. 2 shows a powder diffraction pattern from a ground portion of the $CsPbBr_3@Cs_4PbBr_6$ crystal preparation with nominal Cs_4PbBr_6 stoichiometry, compared with a stick-plot representation of the literature pattern of rhombohedral Cs_4PbBr_6 [16]. A log scale has been used for clear presentation of weaker peaks. Positions of stronger peaks from our preparation match those expected from the Cs_4PbBr_6 phase, although there is evidence of preferred orientation effects on relative peak intensities, and one peak attributable to CsBr starting material. Fig. 2 is also labelled with peak positions calculated for cubic, perovskite-phase $CsPbBr_3$ with a lattice constant of 5.84 Å, and there are clear matches for the 100, 110 and 210 reflections. The $CsPbBr_3$ 111 reflection cannot be observed, but is weak in reported powder patterns of bulk material [19]. The findings just discussed are consistent with those of previous authors who have presented XRD evidence for spontaneous formation of $CsPbBr_3$ nanocrystals within a bulk crystalline Cs_4PbBr_6 host, and attributed green luminescence to this nanophase [16]–[18].

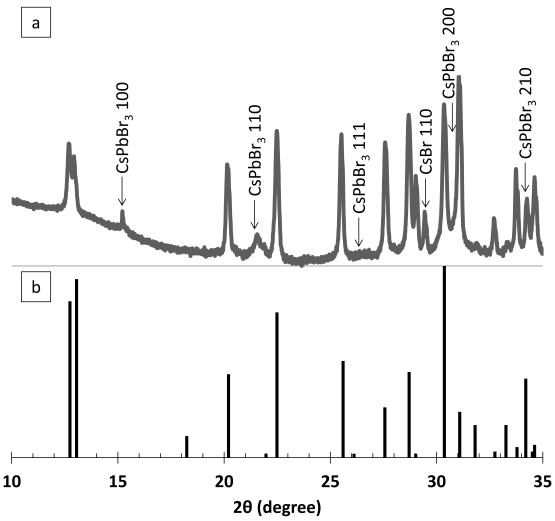

Fig. 2. a) Log-scaled powder XRD pattern from the $CsPbBr_3@Cs_4PbBr_6$ crystal preparation with nominal Cs_4PbBr_6 stoichiometry. The intensity range in the original dataset was 1-100 counts per second. b) Stick plot representation of literature data for the bulk Cs_4PbBr_6 phase, from [16].

B. Polymer/$CsPbBr_3@Cs_4PbBr_6$ Composites

Four different samples, using PMMA or PDMS host matrices, had their PL and absorbance measured before full immersion in deionised water. The PL spectrum of each sample prior to immersion in water can be seen in Fig. 3. There are differences in the initial maximum intensity peaks and respective emission wavelengths between samples. This is explained by intrinsic variations in the concentration of $CsPbBr_3@Cs_4PbBr_6$ crystals and the different thickness of samples. Because the intrinsic PL overlaps with the absorption spectrum, such differences lead to different amounts of reabsorption, hence different intensities and red shifts in the PL spectrum. The *PDMS thick*, which has the least re-absorption, has a PL peak very close to the intrinsic $CsPbBr_3$ emission at 520 nm. The typical PL linewidth is 17 ± 2 nm at full width half maximum. PL and absorbance acquisitions were repeated 1, 4 and 72 hours after the samples had been thoroughly stirred underwater.

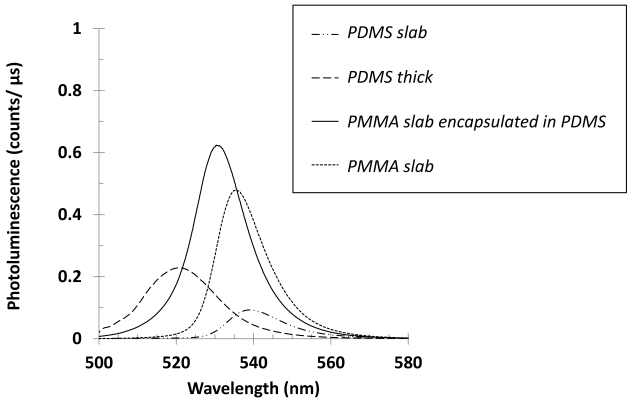

Fig. 3. Photoluminescence measurements of each of the fabricated samples prior to their submersion in water. Pumping was by a 450 nm µLED.

The PL intensity of PMMA composites was constant over time, and its subsequent encapsulation with PDMS showed little to no extra improvement (Fig. 4).

On the other hand, the PDMS samples showed an adverse effect as seen from the PL characteristics after

exposure to water. After 4 hours underwater, the *PDMS slab* (*PDMS thick*) had its PL intensity reduced by almost two orders (one order) of magnitude. These results suggest that water was able to reach and affect most of the crystals in the PDMS samples, despite the hydrophobicity of PDMS.

The shifts of the PL peak wavelength and of the absorption spectrum after 1, 4 and 72-hour-immersion (with respect to the data before immersion) are plotted for all samples in Fig. 5. The PL and absorption of PDMS samples red shifted by approximately 8 nm. This is significant and indicates a reduction of the confinement of the $CsPbBr_3$ QDs. Although superficially suggestive of an increased particle size of the $CsPbBr_3$ QDs, other possibilities are compositional changes to their surface layers and/or adjacent Cs_4PbBr_6 host material. There is a smaller shift for the PMMA samples (1 to 3 nm), very close to the measurement error.

As the wavelength increases, the absorbance decreases for all samples. Its magnitude, however, suggests that samples show scattering, and they become even more strongly scattering after being put into water.

This increase in absorbance after being in contact with water, and a red shift of the emission spectrum, suggest that samples underwent substantial physical and chemical changes while exposed to water. While these effects are negligible in PMMA, PDMS samples presented a significant drop in their PL. A possible explanation might arise from the differences in polymer chain arrangements and consequent water sorption properties between PDMS and PMMA. While PMMA has predominantly linear chains, and forms a dense, glassy microstructure after solvent evaporation, the PDMS used is engineered to partially cross-link during curing, to give an elastomeric end product [20], [21]. This characteristic of PDMS appears to give a microstructure allowing more permeation of water into the composites, and degradation of the luminescent $CsPbBr_3$ QDs. Water permeation in the two polymer hosts have been extensively studied in other contexts, and there is quantitative support for these findings on the relative properties of PDMS [20] and PMMA [22].

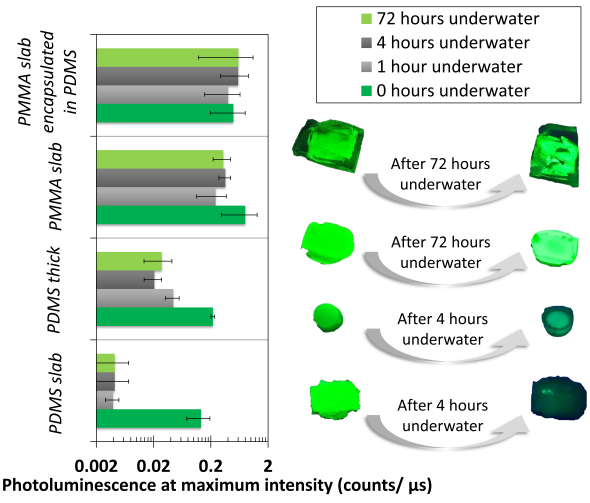

Fig. 4. Photoluminescence at maximum intensity over time, for each of samples studied. Samples are presented in the same order as in the bar plot.

The PL variations over time (Fig. 4) are in agreement with the thickness of the polymer host matrix, and the relative permeability to water just proposed. The *PDMS slab* thickness was small enough to have most of its content of luminescent crystals affected, and its intensity reduced by two orders of magnitude. The *PDMS thick* had its PL peak decreased by one order of magnitude, suggesting that the innermost crystals were more protected against water. PMMA samples showed little to no fluctuation on their maximum intensity PL peaks. Such results suggest that only the crystals exposed on the surface the samples might have been affected, and that crystals are better protected against water when embedded in PMMA.

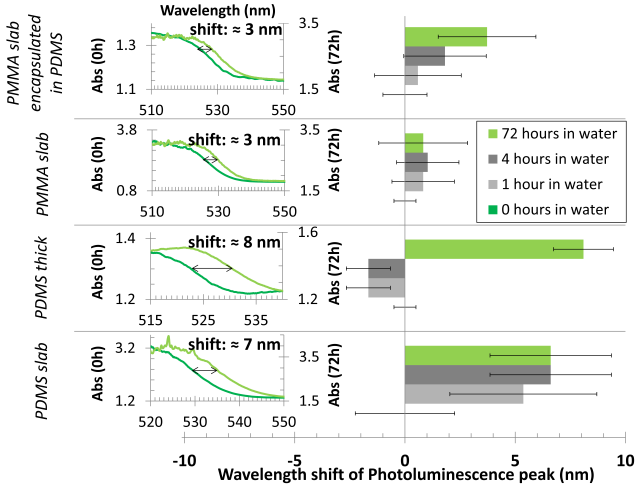

Fig. 5. Shift in wavelength of the photoluminescence peak of each sample after 0, 1, 4 and 72 hour-immersion in water (right) with (left) absorbance spectra before and after immersion in water for 72 hours.

IV. Conclusions

Motivated by their low manufacturing cost and simple processing, PDMS and PMMA were tested and studied as host matrices for the $CsPbBr_3@Cs_4PbBr_6$ crystals synthesized in this work.

The PDMS samples were not stable upon immersion in water. This finding indicates that water was able to reach the guest $CsPbBr_3@Cs_4PbBr_6$ crystals. On the other hand PMMA composites showed little to no trace of degradation when immersed in water under vigorous stirring for up to 72 hours.

PMMA was found in this work to be an effective matrix host for $CsPbBr_3@Cs_4PbBr_6$. Its encapsulation properties show potential for macrosized industrial applications, such as color conversion, where the degradation at the surface is mitigated by the extremely low water penetration depth, and the volume of the composite itself. This polymer matrix approach to minimise moisture-sensitivity should therefore enable the utilisation of the attractive fast color converting properties of $CsPbBr_3@Cs_4PbBr_6$ for practical applications, such as underwater communication.

Acknowledgment

We acknowledge support from the EPSRC Platform Grant EP/P0274X/2. We thank Alan Martin for X-ray powder diffraction, which was performed in the CMAC National Facility, University of Strathclyde Technology and

Innovation Centre, funded with a UKRPIF capital award, SFC ref. H13054, from HEFCE.

Supporting data (dataset) can be found at: http://dx.doi.org/10.15129/fb9f6aa0-26e2-419a-8788-c2b051453108

REFERENCES

[1] M. R. Krames *et al.*, "Status and future of high-power light-emitting diodes for solid-state lighting," *IEEE/OSA J. Disp. Technol.*, vol. 3, no. 2, pp. 160–175, 2007.

[2] J. J. Wierer, J. Y. Tsao, and D. S. Sizov, "Comparison between blue lasers and light-emitting diodes for future solid-state lighting," *Laser Photonics Rev.*, vol. 7, no. 6, pp. 963–993, 2013.

[3] L. Wang *et al.*, "Highly efficient narrow-band green and red phosphors enabling wider color-gamut LED backlight for more brilliant displays," *Opt. Express*, vol. 23, no. 22, p. 28707, 2015.

[4] L. Huang *et al.*, "Highly Stable K_2SiF_6: Mn^{4+}@K_2SiF_6 Composite Phosphor with Narrow Red Emission for White LEDs," *ACS Appl. Mater. Interfaces*, vol. 10, no. 21, pp. 18082–18092, 2018.

[5] D. C. O'Brien, L. Zeng, H. Le-Minh, G. Faulkner, J. W. Walewski, and S. Randel, "Visible Light Communications: Challenges and possibilities," *IEEE Int. Symp. Pers. Indoor Mob. Radio Commun. PIMRC*, pp. 1–5, 2008.

[6] N. Laurand *et al.*, "Colloidal quantum dot nanocomposites for visible wavelength conversion of modulated optical signals," *Opt. Mater. Express*, vol. 2, no. 3, pp. 250–260, 2012.

[7] M. F. Leitao *et al.*, "Gb/s Visible Light Communications with Colloidal Quantum Dot Color Converters," *IEEE J. Sel. Top. Quantum Electron.*, vol. 23, no. 5, 2017.

[8] J. Y. Kim, O. Voznyy, D. Zhitomirsky, and E. H. Sargent, "25th anniversary article: Colloidal quantum dot materials and devices: A quarter-century of advances," *Adv. Mater.*, vol. 25, no. 36, pp. 4986–5010, 2013.

[9] F. T. Rabouw and C. de Mello Donega, "Excited-State Dynamics in Colloidal Semiconductor Nanocrystals," *Top. Curr. Chem.*, vol. 374, no. 5, pp. 1–30, 2016.

[10] L. Protesescu *et al.*, "Nanocrystals of Cesium Lead Halide Perovskites ($CsPbX_3$, X = Cl, Br, and I): Novel Optoelectronic Materials Showing Bright Emission with Wide Color Gamut," *Nano Lett.*, vol. 15, no. 6, pp. 3692–3696, 2015.

[11] M. A. Becker *et al.*, "Bright triplet excitons in caesium lead halide perovskites," *Nature*, vol. 553, no. 7687, pp. 189–193, 2018.

[12] B. T. Diroll, G. Nedelcu, M. V. Kovalenko, and R. D. Schaller, "High-Temperature Photoluminescence of $CsPbX_3$ (X = Cl, Br, I) Nanocrystals," *Adv. Funct. Mater.*, vol. 27, no. 21, pp. 1–7, 2017.

[13] A. Loiudice, S. Saris, E. Oveisi, D. T. L. Alexander, and R. Buonsanti, "$CsPbBr_3$ QD/AlO_x Inorganic Nanocomposites with Exceptional Stability in Water, Light, and Heat," *Angew. Chemie - Int. Ed.*, vol. 56, no. 36, pp. 10696–10701, 2017.

[14] J. Ren, X. Dong, G. Zhang, T. Li, and Y. Wang, "Air-stable and water-resistant all-inorganic perovskite quantum dot films for white-light-emitting applications," *New J. Chem.*, vol. 41, no. 22, pp. 13961–13967, 2017.

[15] L. Gomez, C. De Weerd, J. L. Hueso, and T. Gregorkiewicz, "Color-stable water-dispersed cesium lead halide perovskite nanocrystals," *Nanoscale*, vol. 9, no. 2, pp. 631–636, 2017.

[16] Y. Wang *et al.*, "Solution-Grown $CsPbBr_3$/ Cs_4PbBr_6 Perovskite Nanocomposites: Toward Temperature-Insensitive Optical Gain," *Small*, vol. 13, no. 34, pp. 1–8, 2017.

[17] X. Chen *et al.*, "Centimeter-Sized Cs_4PbBr_6 Crystals with Embedded $CsPbBr_3$ Nanocrystals Showing Superior Photoluminescence: Nonstoichiometry Induced Transformation and Light-Emitting Applications," *Adv. Funct. Mater.*, vol. 28, no. 16, pp. 1–7, 2018.

[18] L. N. Quan *et al.*, "Highly Emissive Green Perovskite Nanocrystals in a Solid State Crystalline Matrix," *Adv. Mater.*, vol. 29, no. 21, pp. 1–6, 2017.

[19] C. C. Stoumpos *et al.*, "Crystal growth of the perovskite semiconductor $CsPbBr_3$: A new material for high-energy radiation detection," *Cryst. Growth Des.*, vol. 13, no. 7, pp. 2722–2727, 2013.

[20] S. J. Harley, E. A. Glascoe, and R. S. Maxwell, "Thermodynamic study on dynamic water vapor sorption in Sylgard-184," *J. Phys. Chem. B*, vol. 116, no. 48, pp. 14183–14190, 2012.

[21] P. J. Flory, *Principles of Polymer Chemistry*. Ithaca, New York: Cornell University Press, pp. 45–52, 1953.

[22] M. Unemori, Y. Matsuya, S. Matsuya, A. Akashi, and A. Akamine, "Water absorption of poly(methyl methacrylate) containing 4-methacryloxyethyl trimellitic anhydride," *Biomaterials*, vol. 24, no. 8, pp. 1381–1387, 2003.

Enhancing self-assembled colloidal quantum dot microsphere lasers

Pedro Urbano Alves, Dimitars Jevtics, Michael J. Strain, Martin D. Dawson, Nicolas Laurand
Institute of Photonics, Department of Physics, SUPA, University of Strathclyde
Glasgow, UK
pedro.alves@strath.ac.uk

***Abstract* — We demonstrate the superior emission properties of a red-emitting self-assembled quantum dot microsphere laser made from a blend of green and red bandgap CdS_xSe_{1-x}/ ZnS quantum dots. The addition of the higher bandgap material reduces self-absorption and improves the Q-factor.**

Keywords — Quantum dots, lasers, nanocrystals, semiconductors, microresonators.

I. Introduction

An optimal design of spherical microresonators requires the tuning of several parameters to minimize the loss of stored energy [1]. In spherical supraparticles (SPs) - self-assembled microspheres of colloidal quantum dots (CQDs) - the parameters that determine their quality factor (Q-factor) not only depend on the shape, size, and average refractive index of the SP, but also on their building blocks - the CQDs. In the solid state, CQDs can suffer from self-absorption, exciton diffusion and nonradiative recombination [2]. In combination, these factors dampen the oscillations of whispering gallery modes and decrease their Q-factor and this has in turn a detrimental effect on the properties of SP lasers. In this work, the addition of higher bandgap CQDs to the fabrication of SPs is studied as a way of preventing such losses. A SP laser blending CQDs of two different bandgaps is shown to operate at higher intensity than, and with a similar threshold to, the equivalent structure without higher bandgap CQDs. Such SP lasers have great application potential for integrated circuits, imaging, sensing and novel photonic materials [3], [4].

II. Materials and Methodology

A. Synthesis of the Supra Particles

An oil-in-water emulsion technique [3], [4] was used to synthesize spherical SPs made of CdS_xSe_{1-x}/ ZnS CQDs with oleic acid ligands. The CQDs were approximately 6.0 ± 0.5 nm in diameter. Two different batches were produced: red SPs made of CQDs emitting at 630 ± 5 nm and SPs with a blend of red and green CQDs at a ratio of 3:1, with the green CQDs emitting at 540 ± 5 nm. Resulting SPs dispersed in water were drop-cast onto a glass substrate and, once the water evaporated, optically-pumped individually.

B. Optical Characterization

SPs were selected and optically pumped one at a time with a 0.76 ns pulse width microchip pulsed laser (λ = 532 nm) at a repetition rate of 7.1 kHz and with a beam spot area of approximately 2.88×10^{-7} cm^2. The beam intensity was controlled by a variable wheel neutral density attenuator and focused on the sample with an objective lens (N PLAN EPI 50×/ 0.75, Leica). A spectrometer (AvaSpec-2048-4-DT, Avantes) was used to acquire the spectral data [4]. The size of the SPs was measured optically with a microscope and verified by the pseudo-Free Spectral Range (pseudo FSR) of their cavities, $\Delta\nu_{n,l}^{\Delta l} \approx \frac{c}{2\pi.N.a}$, where the radius a of a sphere with refractive index N can be expressed by the spacing between two consecutive modes with the same polarization [1]. The Q-factor, $Q = \frac{\lambda}{\Delta\lambda}$, was calculated from the resonance center wavelength, λ, and the resonance peak width at full width half maximum, Δλ, below lasing threshold [1].

III. Results and Discussion

Two SPs (both 6.0 ± 0.5 μm in diameter) were selected from the synthesized batches, one containing exclusively red CQDs (red SP) and the other containing the blend of CQDs (blended SP). These two SPs were then characterized, and their Q-factors and laser intensity transfer functions compared. Emission below and above lasing threshold of the red SP is shown in Fig. 1. The red SP had its Q-factor estimated from the modes highlighted in grey on the normalized emission below threshold and its Fourier transform ($Q \approx 135 \pm 19$). Its lasing threshold is around 12 $mJ.cm^{-2}$ (Fig. 2), but for fluences above 20 $mJ.cm^{-2}$ the emission rolls over, likely due to electron–hole separation, charge diffusion and nonradiative recombination [2]. Micrographs of the red SP below and above threshold are shown in Fig. 3. Emission data above and below lasing threshold for the blended SP are shown in Figs. 4, 5 and 6. The presence of green CQDs reduces the density of red CQDs and therefore diminishes exciton diffusion and self-absorption at the laser transition, leading to an enhanced Q-factor ($Q \approx 340 \pm 60$). The higher Q is also reflected in the lower slope above threshold (Fig. 5). The effect of a lower density of the red CQDs on the modal gain is not only mitigated by the lower exciton diffusion but

This is a peer reviewed, accepted author manuscript of the following research article: Alves, P. U., Jevtics, D., Strain, M. J., Dawson, M. D., & Laurand, N. (2021). Enhancing self-assembled colloidal quantum dot microsphere lasers. In 2021 IEEE Photonics Conference (IPC) (pp. 1-2). IEEE. https://doi.org/10.1109/IPC48725.2021.9592976

also by the fact that green CQD can act as donors. In turn the lasing threshold is not affected significantly (12 – 14 mJ.cm^{-2}), and the SP laser is able operate at higher intensity without rolling over (Fig. 5).

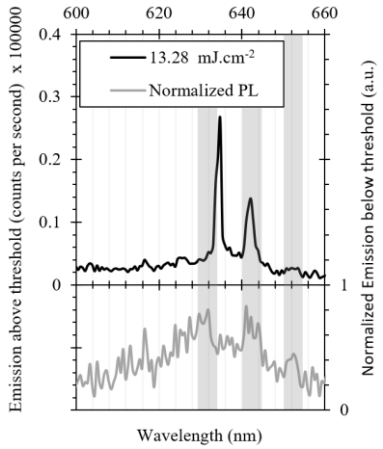

Fig. 1. Emission of the red SP above (13.3 mJ.cm^{-2}) and below (normalized PL) lasing threshold.

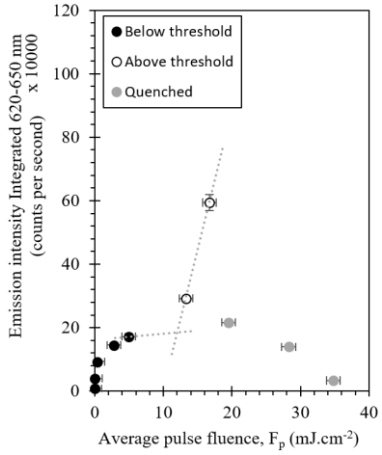

Fig. 2. Laser transfer function of the red SP.

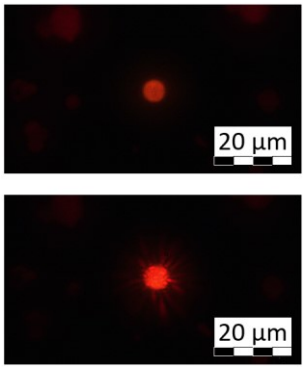

Fig. 3. Microscope images of the red SP below and above lasing threshold.

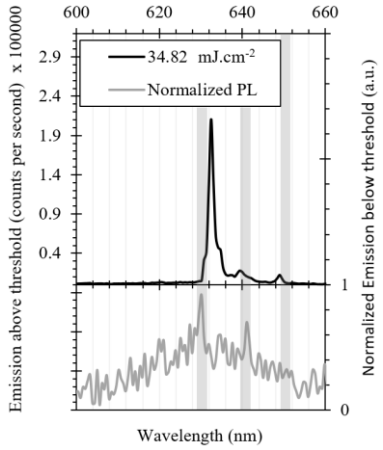

Fig. 4. Emission of the blended SP above (34.8 mJ.cm^{-2}) and below (normalized PL) lasing threshold.

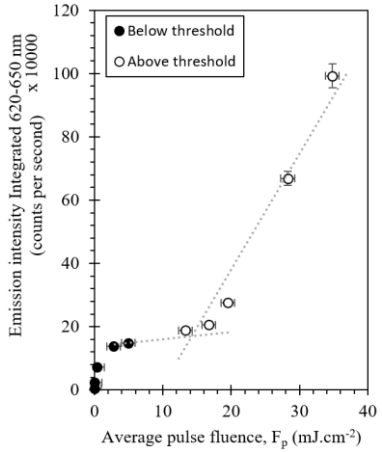

Fig. 5. Laser transfer function of the blended SP.

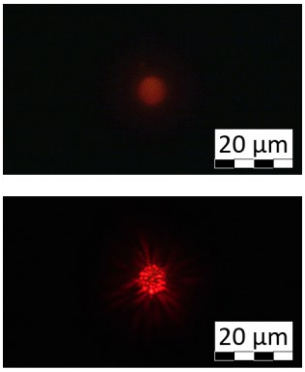

Fig. 6. Microscope images of the blended SP below and above lasing threshold.

IV. Conclusions

Blending CQDs of two different bandgaps has been shown to improve the Q-factor and emission intensity of self-assembled microsphere CQD lasers. This work is an important step towards the design of higher quality CQD microcavities.

Acknowledgment

We acknowledge support from the EPSRC Platform Grant EP/P0274X/2 and the Leverhulme Trust for the Research Leadership Award RL-2019-038. The dataset can be found at: https://doi.org/10.15129/0517de89-0eda-4932-90b9-6655c8035a76.

References

[1] G. C. Righini *et al.*, "Whispering Gallery Mode microresonators: Fundamentals and applications," *Riv. del Nuovo Cim.*, vol. 34, no. 7, pp. 435–488, 2011.

[2] N. Kholmicheva, P. Moroz, H. Eckard, G. Jensen, and M. Zamkov, "Energy transfer in quantum dot solids," *ACS Energy Lett.*, vol. 2, no. 1, pp. 154–160, 2017.

[3] E. Marino *et al.*, "Favoring the Growth of High-Quality, Three-Dimensional Supercrystals of Nanocrystals," *J. Phys. Chem. C*, vol. 124, no. 20, pp. 11256–11264, 2020.

[4] P. U. Alves, N. Laurand, and M. D. Dawson, "Multicolor laser oscillation in a single self-assembled colloidal quantum dot microsphere," *2020 IEEE Photonics Conf. IPC 2020 - Proc.*, pp. 2020–2021, 2020.

Multicolor laser oscillation in a single self-assembled colloidal quantum dot microsphere

Pedro Urbano Alves, Nicolas Laurand and Martin D. Dawson
Institute of Photonics, Department of Physics, SUPA, University of Strathclyde
Glasgow, UK
pedro.alves@strath.ac.uk

***Abstract* — Self-assembled microsphere lasers oscillating simultaneously at more than one wavelength in the visible are reported. The lasers consist of micron-scale supraparticles made of CdS_xSe_{1-x}/ ZnS quantum dots that emit between 585-605 nm and 625-655 nm.**

Keywords — Quantum dots, lasers, nanocrystals, semiconductors, microresonators.

I. Introduction

The advantageous characteristics of colloidal quantum dots (CQDs), including solution processability, near-unity emission quantum yield and tunable emission wavelength, make them attractive for photonic applications. Specifically in terms of laser operation, they have potential in integrated photonics, imaging, sensing and diagnostics [1]. To achieve lasing with CQDs, different types of cavity designs can be used, such as: Fabry-Perot, spherical and micro-ring resonators, vertical cavities implemented with distributed Bragg reflectors, and DFB gratings [1]. While single color laser oscillation has been demonstrated with CQDs, to our knowledge no reports regarding multicolor laser oscillation have been made to date. Such multicolor lasers would pave the way for a broad range of applications including miniature tunable lasers, high density color displays and sensing devices [2]. In this work, advantage of the whispering gallery modes present in spherical supraparticles (SPs) - self-assembled microspheres of CQDs - is taken to demonstrate multicolor lasing in individual SPs.

II. Materials and Methodology

A. Synthesis of the Supra Particles

An oil-in-water emulsion technique [3] was used to synthesize spherical SPs made of CdS_xSe_{1-x}/ ZnS quantum dots. Three different batches were produced: red SPs made of CQDs emitting at ~630 nm; yellow SPs made of CQDs emitting at ~575 nm and SPs with a 50:50 ratio of red and yellow CQDs. Resulting SPs in water were then drop-cast onto a glass substrate and optically-pumped individually for the characterization process. The size dispersion of the synthesised SPs ranged approximately between 1 and 10 µm in diameter (Fig. 1).

B. Optical Characterization

SPs were selected and optically pumped one at a time with a 1.6 ns pulsed frequency-doubled Nd:YAG laser at 532 nm, at a repetition rate of 10 kHz, with a beam spot area of approximately 1.9×10^{-5} cm^2. The beam was attenuated with a variable wheel neutral density attenuator and focused on the sample with an objective lens (4×/ 0.13, Nikon). A spectrometer (AvaSpec-2048-4-DT, Avantes) was used to acquire the spectrum data. The µPhotoluminescence (µPL) setup described above follows the same design as in previous works [4]. The size of the SPs was measured by both optical microscopy and scanning electron microscopy (SEM).

III. Results and Discussion

Two batches of SPs emitting in a single color (red, yellow) were fabricated and characterized, before demonstrating emission at two colors (red and yellow) simultaneously. Fig. 2. and Fig. 3. show the typical emission intensity responses of a red SP laser (630 nm) and a yellow SP laser (575 nm) as a function of the pump fluence, as well as their characteristic photoluminescence below and above threshold. For both single color lasers, the threshold fluence was between 0.5 and 0.7 $mJ.cm^{-2}$. To test if multicolor laser oscillation could be obtained with a single SP, the third batch of SPs was prepared with 50 % of red CQDs and 50 % of yellow CQDs (Fig. 4). Depending on the pump fluence, three laser regimes were observed. In the first regime, the first modes to go above the lasing threshold were in the red band and this happened approximately at the same fluence as their single wavelength counterparts (0.5 to 0.7 $mJ.cm^{-2}$). For the second regime, at around

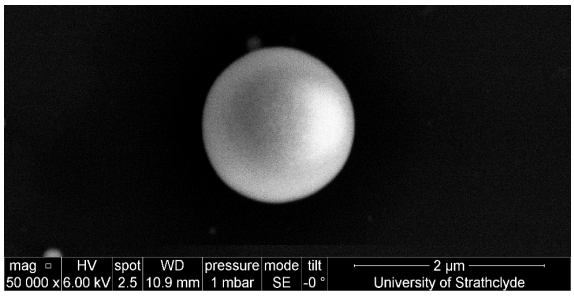

Fig. 1. SEM image of a red SP approximately 1.5 µm in diameter (representative example).

2.0 mJ.cm^{-2}, modes in the yellow band started to oscillate while the modes in the red band started to lose energy. Stable dual color lasing was obtained at approximately 2.4 mJ.cm^{-2} (Fig. 4). The third regime, at higher fluences, had the modes in the yellow band dominating the emission spectrum whilst modes in the red returned to their below threshold state.

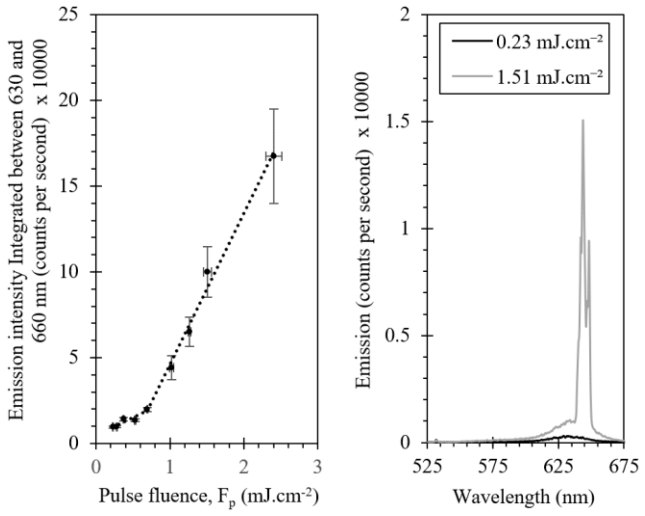

Fig. 2. Laser transfer function of a red SP (diameter: 7.6 µm) and its typical spectrum below and above threshold.

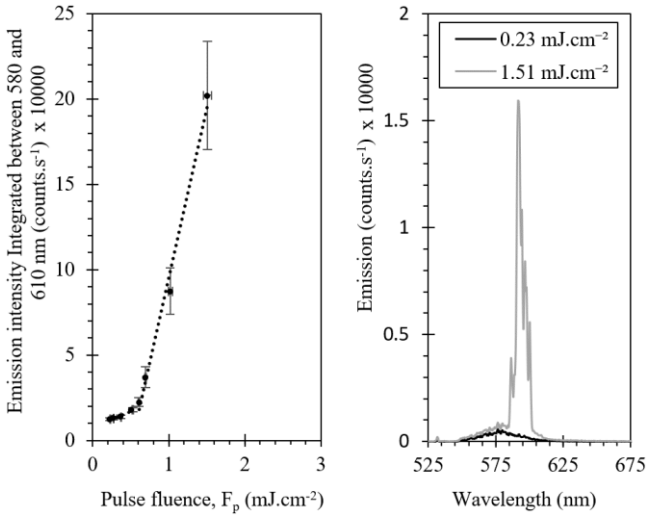

Fig. 3. Laser transfer function of a yellow SP (diameter: 6.8 µm) and its typical spectrum below and above threshold.

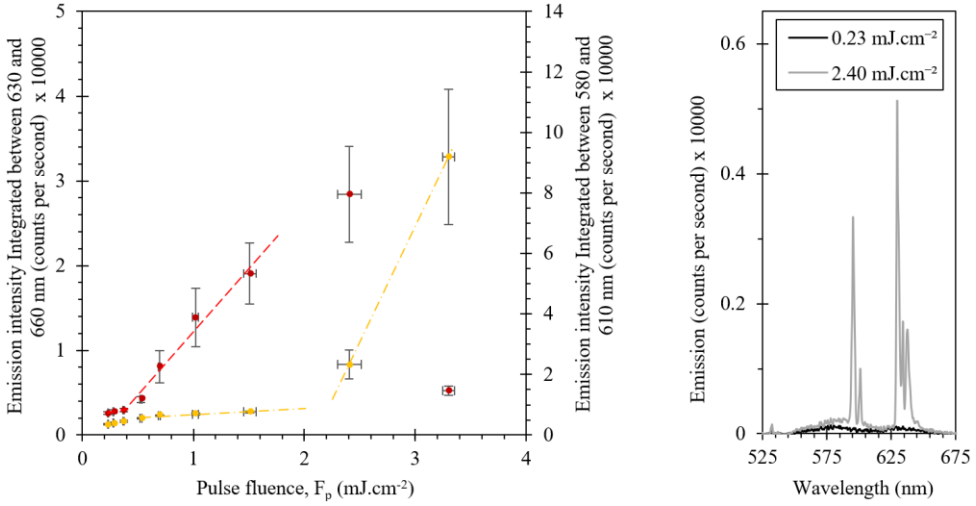

Fig. 4. Laser transfer function of a multicolor SP (diameter: 6.4 µm) and its typical spectrum below and above threshold.

IV. Conclusions

Multicolor lasing in individual self-assembled CQD SPs has been demonstrated. Three lasing regimes were successfully demonstrated in a single SP, as a function of the pump fluence (namely single color red, single color yellow and simultaneous dual color red and yellow). Future work will focus on studying these properties further and demonstrating possible applications.

Acknowledgment

We acknowledge support from the EPSRC Platform Grant EP/P0274X/2. and from R.W. Martin and P.R. Edwards for SEM. Supporting data (dataset) can be found at: https://doi.org/10.15129/66aed63c-684d-48c8-8bf7-6a6595bf4a15.

References

[1] J. Roh, Y. S. Park, J. Lim, and V. I. Klimov, "Optically pumped colloidal-quantum-dot lasing in LED-like devices with an integrated optical cavity," *Nat. Commun.*, vol. 11, no. 1, pp. 1–10, 2020.

[2] Y. Lu *et al.*, "Multicolour laser from a single bandgap-graded CdSSe alloy nanoribbon," *Opt. Express*, vol. 21, no. 19, p. 22314, 2013.

[3] F. Montanarella *et al.*, "Lasing Supraparticles Self-Assembled from Nanocrystals," *ACS Nano*, vol. 12, no. 12, pp. 12788–12794, 2018.

[4] D. Jevtics *et al.*, "Integration of Semiconductor Nanowire Lasers with Polymeric Waveguide Devices on a Mechanically Flexible Substrate," *Nano Lett.*, vol. 17, no. 10, pp. 5990–5994, 2017.